Electrochemically-Mediated Amine Regeneration for Carbon Dioxide Separations

by

Michael C. Stern

B.S. Chemical Engineering
Lehigh University, 2008

M.S. Chemical Engineering Practice
Massachusetts Institute of Technology, 2011

SUBMITTED TO THE DEPARTMENT OF CHEMICAL ENGINEERING IN PARTIAL FULFILLMENT OF THE REQUIREMENTS FOR THE DEGREE OF

DOCTOR OF PHILOSOPHY IN CHEMICAL ENGINEERING
AT THE
MASSACHUSETTS INSTITUTE OF TECHNOLOGY

FEBRURARY 2014

Signature of Author: Signature redacted

Department of Chemical Engineering
October 10th, 2013

Certified by: Signature redacted

T. Alan Hatton
Ralph Landau Professor of Chemical Engineering
Thesis Supervisor

Accepted by: Signature redacted

Patrick S. Doyle
Singapore Research Professor of Chemical Engineering
Chairman, Committee for Graduate Students

Electrochemically-Mediated Amine Regeneration for Carbon Dioxide Separations

by

Michael C. Stern

Submitted to the Department of Chemical Engineering
on October 10th, 2013 in Partial Fulfillment of the
Requirements for the Degree of Doctor of Philosophy
in Chemical Engineering.

ABSTRACT

This thesis describes a new strategy for carbon dioxide (CO_2) separations based on amine sorbents, which are electrochemically-mediated to facilitate the desorption and regeneration steps of the separation cycle. The absorption of CO_2 is accomplished in a similar manner to standard thermal scrubbing techniques. The desorption of the CO_2 from the loaded amines is achieved through the oxidation of a copper metal anode, which generates cupric ions that compete for the amine binding sites. For many amines, the complexation with cupric ions is more favorable than the complexation with CO_2. Reduction of the cupric ions from the amine sorbent onto a separate copper metal cathode regenerates the solution's ability to capture CO_2, completing the capture and release cycle.

The electrochemically-mediated amine regeneration (EMAR) process has several advantages over standard thermal scrubbers. EMAR systems do not require reconfiguration of internal turbine systems for low-pressure steam extraction; this makes EMAR more attractive for the retrofit of existing plants. EMAR systems can also generate CO_2 at elevated pressures, reducing the need for downstream compression.

A thorough evaluation of 13 metals and 14 amines for the EMAR cycle is presented. Based on cost, amine binding strength, and cation reduction potentials, copper was determined to be the best metal for this process. Polyamines, due to their ability to chelate the cupric ions, were identified as the best amines candidates. Ethylenediamine (EDA) and aminoethylethanolamine (AEEA) were investigated experimentally for their thermodynamic and kinetic properties.

For EDA, experiments demonstrated that a system operated at open-circuit could achieve 70% efficiency with respect to a perfectly reversible process. Kinetic experiments and transport modeling are used to extrapolate the performance to a real system operating at closed circuit conditions. A proof-of-concept system was constructed and was capable of separated CO_2 at a rate of 800 sccm/m^2 membrane area with an electrical requirement of 100 kJ/mole CO_2.

Suggestions and specifications for future designs of next generation bench-scale systems are provided. A techno-economic analysis shows the potential of several configurations of industrial scale EMAR systems compared with thermal scrubbing technologies.

Thesis Supervisor: T. Alan Hatton
Title: Ralph Landau Professor of Chemical Engineering

Dedication

To my mother who encouraged me to be myself,

To my father who inspired me to be better,

And to my brother who showed me the way.

Acknowledgements

Professor Hatton: When acknowledging those who supported me through the Ph.D. process, there is none other to thank more than my advisor, Alan. It was clear from the start that our minds thought alike both academically and personally. Academically, Alan gave me the freedom initially to learn (i.e., fail). Once I finally got on the right track, he gave me the freedom to take the research in the directions that interested me the most. This is not to say, however, that Alan has not had a significant impact on the work. He consistently held me to a high standard and repeatedly gave me the push I need to get the tedious but important tasks completed.

Personally, having an advisor with a similar mentality and sense of humor has been invaluable. Alan positive and friendly demeanor encouraged me to be honest and unafraid to offer a dissenting opinion. I think this free exchange of opinions significantly improved the focus of our work and made my work more enjoyable. During my time in his lab, Alan has been sometimes a teacher, a mentor, a boss, but always a friend.

My Committee: Professor Green and Howard Herzog have been extremely helpful during my time at MIT. Howard provided a tremendous amount of perspective about carbon capture and the associated technical challenges. Professor Green was always the most inquisitive member of my committee, for which I am very grateful. Several elements in this thesis can be directly traced back to his influence.

My Labmates: In many ways, both technical and personal, my coworkers have been a great help during my Ph.D. When I started, I learned a tremendous amount from the 'senior member' of the group, Nate Aumock. Both Emily Chang and Fritz Simeon were also great coworkers who helped me tremendously in the lab.

There was no coworker, however, more important than my exceptional friend, Kristin. Sharing the mini office bay with Kristin is something that I will miss terribly. She was also an amazing travel companion during our few work trips to Europe and DC.

My UROPS: I want to thank, and apologize to, the excellent undergrads that tirelessly did my bidding. Michelle Barber, Kali Benevides, Benji Niswonger, Rebecca Han, Michaelann Rodriguez, and Jackie Brew all worked with exceptional dedication despite the poorly designed experiments I asked them to do.

My Friends: My roommates Christy, Andy, Derek, and (previously) Achim have all been essential in providing a wonderful home to come back every night. My 3rd floor lunch buddy Spencer has also been a tremendous source of support. I feel extremely lucky to have found such fun and caring friends who truly give my life balance.

My Family: The debt I owe my family for their love and support is beyond what I could ever repay or fully describe. The unwavering confidence of my whole family, and especially my mother, was essential to my decision to apply to Ph.D. programs. My father and my brother have been excellent role models for my engineering career; I certainly get my interest in science from them. My sister-in-law Nicole and my niece Abby have been wonderful in creating an amazing family atmosphere when I go home to Sudbury. I count my close proximity to my family among one of the great joys in my life.

Table of Contents

Chapter 1

Introduction

Executive Summary

This thesis introduces and investigates a new strategy for carbon dioxide separations called Electrochemically-Mediated Amine Regeneration (EMAR). This technology has the potential to address two severe technological gaps in post-combustion carbon separation technologies: retrofits to existing power plants and application to non-power generating facilities, such as steel, aluminum, and cement plants.

Because EMAR systems are electrically-driven, it is unnecessary to undergo the costly reconfiguration of internal steam turbines when retrofitting an existing power plant. This alleviates a serious complication that makes the deployment of more traditional thermal amine scrubbers unattractive for retrofits. For non-power generating plants where low-pressure steam is unavailable, thermal scrubbers require the additional installation of dedicated natural gas boilers to generate the required steam. These systems operate at low efficiency compared with power plant based systems because they do not pass the steam through a Rankine cycle. Passing the steam through a Rankine cycle extracts most of the energy as electricity before using the low-value heat to operate the thermal scrubber. An EMAR system operates through an electrical connection, and therefore, does not require the natural gas boiler and can operate at a consistent efficiency regardless of the type of plant.

The chemical cycle that defines the EMAR process is developed through modification of an Electrochemically-Mediated Complexation Separation (EMCS) cycle. In an EMCS cycle, the target molecule is selectively absorbed and released by a single redox active carrier species. In the second chapter, a new separations concept, the Electrochemically-Mediated Competitive Complexation Separation (EMCCS) cycle, is introduced. In the EMCCS cycle, the redox active species is separate from

the carrier molecule that binds the target. The redox active species, named the competitor, complexes strongly with the carrier when electrochemically activated. The competitor/carrier complexation releases any bound target molecules and prevents future binding by the target until the redox active competitor is electrochemically deactivated.

The EMAR process is a specific embodiment of an EMCCS cycle, where the carrier is an amine sorbent and the target molecule is carbon dioxide, CO_2. Thirteen different metals are screened for use as the redox active competitor. Oxidation of many metals, especially transition metals, yields cations with sufficient Lewis acidity to compete with carbon dioxide for the amine binding groups. Based on several criteria, including cost, complexation strength with ethylenediamine, and resistance to undesirable oxidation by hydrogen evolution, copper is chosen as the best competitor for an EMAR system. Fourteen different amines, including ethanolamines, amino acids, and polyamines, are screened for use with copper in an EMAR process. After the initial round of screening, which focuses primarily on avoidance of copper salt precipitation, four diamines are chosen as possible EMAR sorbents.

The thermodynamics of the four amines with respect to an EMAR system are investigated in the third chapter by means of a combination of experimentation and modeling. Starting with the fundamental thermodynamics of the process, the maximum achievable efficiencies at zero-flux conditions are determined from combining the pertinent mass action equations with the Nernst equation. Additional inefficiencies from incomplete loading in the absorber and losses due to physical solubility in the sorbent are included in the models. Experiments measured the ability of cupric salts to facilitate CO_2 desorption from the loaded amine sorbents and the required potentials to generate or remove cupric ions at operating conditions. The enthalpy and entropy of the CO_2 binding reaction with EDA is obtained using open-circuit potential measurements of the copper activity at varying temperatures. This method is a cheap and fast technique that had never previously been demonstrated.

The electrochemical kinetics of copper dissolution and deposition is investigated in the 4th chapter using fast galvanostatic pulses. An equivalent circuit model is used to interpret the measured potential responses to the current pulses. The results are compared with a similar investigation of copper

electrochemistry in sulfuric acid systems. The relatively similar reaction rates in the amine solutions compared with sulfuric acid solutions is explained by a new intermediate-stabilized dissociative electron transfer theory. This theory, which is derived from combining a consecutive two-electron transfer process with dissociative electron transfer theory, successfully predicts the trends observed. The addition of chlorides is shown to have a dramatic impact on the electrochemical kinetics. Without chloride ions, the kinetics in CO_2 solutions are prohibitively slow.

The performance of real systems, based on the surface electrochemical kinetics and bulk transport phenomena, is investigated in the 5th chapter. Two configurations of the EMAR system are considered, which include a flat plate electrode system and a porous electrode system. Analytical approaches are taken in both cases substantially reduce the complexity of numerical simulations. Such simplification is necessary for the future implementation of these models in system-wide optimization routines, which may need to run hundreds of iterations to find the optimal design and operating strategy of an EMAR system.

The flat plate electrode system is simplified using the Karman-Pohlhausen integral solution approach. The concentration profile is assumed to be a 3rd order polynomial with a consistent shape within the boundary layer. Based on a set of known boundary conditions, the coefficients can be calculated if the boundary layer thickness is known. To calculate the boundary layer thickness, a shell balance can be performed to relate the current at the surface to the rate of growth of the boundary layer.

The porous electrode system is first simplified by assuming that the isopotential lines are roughly parallel with the direction of flow. This converts the coupled partial differential equations (PDE) to coupled ordinary differential equations (ODE). The coupling refers to the interdependence of the concentration profiles and electrostatic potential profiles, which must be solved simultaneously. By approximating the Butler-Volmer equation as either a single exponential function (valid for large potentials) or as a linear function (valid for small potentials), the coupled ODE's can be converted to a pair of non-linear algebraic equations that are easily solved with minimal computation.

The development and experimental results of a proof-of-concept device are described in the 6th chapter. The proof-of-concept system is the fourth electrochemical CO_2 capture cell constructed, and

lessons learned from the iterative design process are discussed. The proof-of-concept system is tested for its stability, repeatability, Faradaic (current) efficiency, and electrical demand per mole of CO_2 captured. While the system is stable during cyclic or continuous operation for at least 7 hours, reproducibility of the device is poor; this results from the challenges with the device assembly and electrode consistency. The operating efficiencies and electrical demands are promising, especially when considering the system is operated at ambient temperature and pressure, which are far from ideal. There are signs, however, that indicate the electrodes may not be stable over long term operation.

Designs and recommendations for the next generation bench scale system are provided in the 7th chapter. Specifications for the construction of a stacked electrochemical device are provided along with suggestions regarding the peripheral equipment and control strategies required for long term automation. Based on the information from this thesis, a techno-economic assessment is performed for an EMAR systems used to retrofit an existing supercritical coal-fired power plant. The assessment determines the electrical and thermal demands of the EMAR system. The cost of electricity for power plants with EMAR capture systems is compared to those with thermal scrubbers. The assessment shows that an EMAR system can significantly outperform conventional thermal scrubbing systems for retrofit applications.

The next section of the introductory chapter provides motivation for this research. Evidence of climate change due to anthropogenic emissions is presented. Arguments for CO_2 abatement at large point source emitters and the possible technologies capable of such separations are discussed. The importance of technologies for retrofitting existing plants and use at non-power-generating facilities is considered. A description of conventional amine scrubbing, which is the most developed post-combustion CO_2 separation technology, is provided.

The introductory chapter concludes with a technical overview covering amine chemistry, copper electrochemistry, and electrochemical systems, which are helpful, though not necessary, for understanding the analyses in the following chapters. The interactions of amines with CO_2 and copper have been studied separately in extensive detail. The electrochemical kinetics of copper electro-deposition and electro-dissolution have been studied in the contexts of electroplating and corrosion. Transport

phenomena in electrochemical systems have been theoretically and numerical simulated for a variety of battery and fuel cell applications. Electrochemical separation technologies include both facilitated membranes systems and electrochemically-mediated complexation separations. Both types have been previously investigated for CO_2 separations, but have not been adopted due to technical drawbacks.

Climate Change

Since the beginning of the industrial revolution, which dramatically increased the rate of anthropogenic emissions of CO_2, global temperatures have been increasing. Since 1880, the average world temperature has increased by 0.06°C per decade. Since 1970, that rate has nearly tripled to 0.16°C per decade, which is unparalleled in the last 11,000 years.[1,2] This increase has been shown to be highly correlated with the logarithm of CO_2 concentration in the atmosphere. For every doubling of the CO_2 concentration, the average land temperature increases 3°C.[3]

The over 25% increase in atmospheric CO_2 concentrations measured at the Mauna Loa observatory over the past 50 years can be seen in **Figure 1-1**. The increase in global temperatures is expected to produce significant humanitarian crises including famines, floods, and intense storms.[4,5] The National Research Council has recommended a substantial reduction in CO_2 emissions over coming decades to reduce the intensity and impacts of these natural disasters.[6]

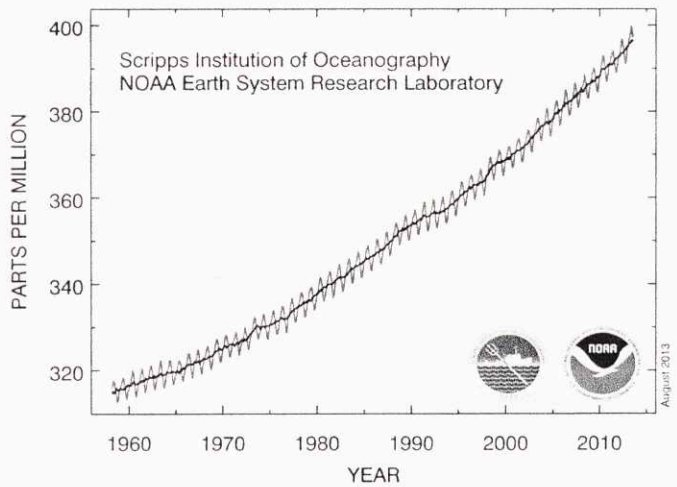

Figure 1-1. Atmospheric CO_2 concentration measured at the Mauna Loa observatory in Hawaii. Figure by Dr. Pieter Tans (NOAA/ESRL) and Dr. Ralph Keeling (Scripps): http://www.esrl.noaa.gov/gmd/ccgg/trends/#mlo_full.

The EPA estimates that in 2010, 40% of the CO_2 emissions in the United States originated from power generation.[7] Despite the recent reduction in natural gas prices, coal will remain as an important fuel for electricity production and is projected to account for 38% of electricity generation in 2035, while the share produced from natural gas will only be 28%.[8,9] Leaders in climate science and governmental policy, including the Intergovernmental Panel on Climate Change and former the U.S. Secretary of Energy, Steven Chu, have identified post-combustion CO_2 capture from coal-fired and gas-fired power plants as a necessary strategy for reducing anthropogenic emissions.[10,11] In addition to the environmental motivations, the depletion of natural CO_2 sources may necessitate CO_2 capture for use in enhanced oil recovery over the next few decades.[12]

While only about 1% of power generating capacity in the United States comes from coal-fired power plants less than 10 years old, approximately 20% of the capacity comes from natural gas plants less than 10 years old with an additional 10% from natural gas plants 11 to 20 years old.[13] With approximately 30% of the current power generating fleet in the US not scheduled for retirement for decades, retrofit technologies are necessary for comprehensive reduction of CO_2 emissions from power plants.

The coal infrastructure in developing countries is both newer and more prevalent with China and India generating 79% and 68% of their electricity from coal, respectively.[14] Over a third of the world's currently installed 1600 GW of coal-fired electricity generating capacity is less than 10 years old.[15] Over the next 20 years, an additional 1,000 GW of coal infrastructure is expected to be constructed, and the fraction that will be constructed with carbon capture capabilities is uncertain. The International Energy Agency, IEA, predicts that to achieve stabilization of global warming, 114 GW of coal-fired capacity will need to be retrofitted with carbon capture technologies.[16] This represents 17% of the total coal-fired capacity that needs to be retrofit.

CO_2 emissions by non-power-generating plants, such as cement, steel, and aluminum are also significant. In 2004, the cement industry was responsible for 3.4% of global CO_2 emissions from fossil fuel combustion.[17] In 1999, it was reported that the steel industry was responsible for 4.6% of global CO_2 emissions.[18] The aluminum industry also contributes approximately 1% of the global CO_2 emissions.[19]

In the next section, a review of carbon capture systems will be provided with specific focus on thermal amine scrubbing, which is the most mature capture technology. The challenges of retrofitting existing plants and non-power-generating plants with thermal scrubbing technology will be discussed.

Carbon Capture Technologies

The current state of the art capture technology is thermal amine scrubbing,[20] which was patented in 1930 by R. R. Bottoms. A diagram of a basic thermal scrubbing process is shown if **Figure 1-2**. Since its invention, significant optimization of the process has occurred. Recently, researchers have tested a variety new amine sorbents, amine sorbent blends, and mixtures with carbonate salts to replace the traditional monoethanolamine (MEA) sorbent.[21–25] Process enhancements such as intercooling in the absorber have also been investigated.[26] Despite the significant improvements to the technology, the parasitic energy requirements of a thermal scrubbing system on a new coal-fired power plant are still dramatic with plant de-ratings between 20% and 30%.[27–29]

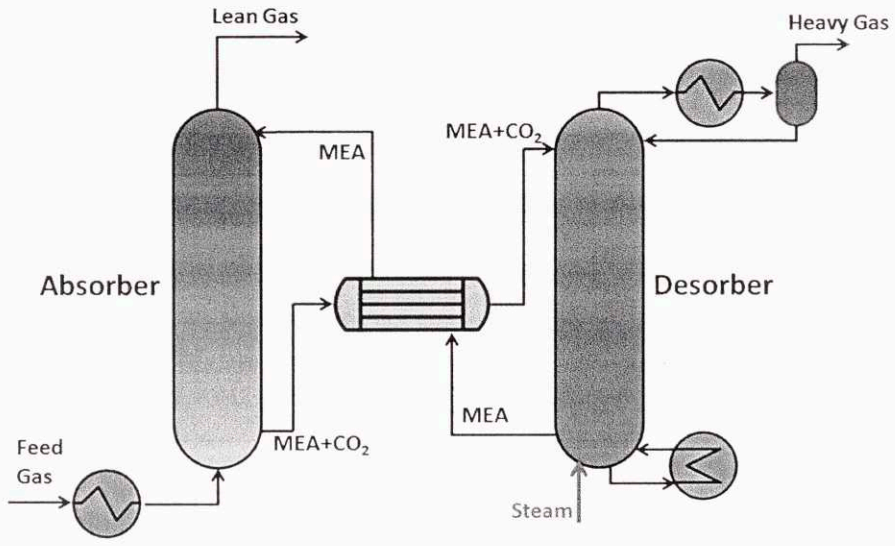

Figure 1-2. Schematic diagram of a simple thermal amine scrubbing unit with an MEA sorbent.

For retrofit systems, de-ratings due to installation of a thermal amine scrubbing capture plant are predicted to be 40% for sub-critical plants.[28,30] In addition to the reduction in efficiency, the capital cost of

the power plant could be increased by as much as 80%.[31] The increase results from difficulties with matching the steam temperatures at available extraction points with the steam requirements of the capture plant. Variants of thermal amine scrubbing using chilled ammonia, rather than MEA, may be able to reduce retrofit de-ratings to 25%, especially when ultra-supercritical (USC) steam turbines are used.[31] USC turbines produce the least CO_2 per MW of electricity, which reduce the requirements for CO_2 capture.

Capture systems that do not require low-pressure steam are being actively investigated as alternatives to thermal amine scrubbing. oxy-fuel combustion,[32,33] membrane separations,[34,35] and vacuum swing absorption[36] all require electrical energy rather than steam.[37] While electricity is a higher value form of energy, the energy requirements are smaller and the capital costs are lower due to the lesser level of heat integration required.

Oxy-fuel systems, which feed pure oxygen into the combustion chamber, require the separation of oxygen from air. This is performed using a cryogenic separation, which is expected to be expensive. For retrofits, the required changes to the plants boiler and steam cycle is minimal, which makes this an attractive technology. Application to natural gas systems is unlikely since the ratio of oxygen required to CO_2 produced is lower, which hinders the process economics.

The simplicity of membrane systems does keep capital costs low, but the low partial pressure of CO_2 in the flue gas (10-15 kPa) does make successful application of a membrane system challenging.[38] Significant research into advanced membrane materials, such as room-temperature ionic liquid membranes, is ongoing.[39,40] Application of membranes for CO_2 capture from natural gas plants is unlikely due to the even lower partial pressure (~5 kPa) of CO_2 in the flue gas. Both oxy-fuel and membrane systems may require a final refrigerated flash separation of the gas to achieve the necessary CO_2 purities to avoid difficulties with compression and transport.[41]

Pre-combustion and chemical looping strategies are also under investigation for use in carbon capture from power plants. Integrated gasification combined cycle (IGCC) plants, where CO_2 can be separated from streams with high CO_2 partial pressures enable the use of physical solvents that have been

proven effective at large scale in natural gas separations.[42] They have also been considered for use with membranes, which can take advantage of the high CO_2 partial pressures.[43] Recently, however, the estimated capital cost of these plants has been revised sharply upward, discouraging the construction of demonstration units.

Chemical looping, in which the CO_2 capture is performed by metal oxides, primarily calcium, in the high temperature combustion chamber, is a promising technology attracting significant attention.[44,45,31] The technology uses low cost sorbents and can be retrofitted onto and existing plant in a way that increases the net plant output, though still with a reduction in efficiency. The main challenge this strategy faces is that it is novel and will take time to develop and mature into an industrial relevant technology. Deactivation of the metal oxide due to carbon deposition is also a concern.

Capture of CO_2 from cement[46] and steel[47,18] plants has been considered, but with significantly less detail than capture from power plants. In one analysis for CO_2 capture from a steel blast furnace exhaust, the entire flue gas would be compressed and then captured using a Selexol process. This has the advantage of using only electrical inputs; since in a steel plant, low pressure steam is not widely available. Compression of the entire flue gas stream, however, may be an unnecessarily costly strategy. Even though steel, cement, and aluminum production account for 9% of global CO_2 emissions, there is no clear strategy for reducing their carbon emissions.

Amine Chemistry

Amines are widely used in a variety of industrial processes and as precursors for the production of many chemicals. The nitrogen atom, which is bound to either hydrogen atoms or alkyl groups, is significant basic due to its lone pair of electrons. The pKa's of amines generally range from 8 to 10 with primary amines (bound to two hydrogen atoms and one alkyl group) being the most basic. Secondary and tertiary amines, which are bound to one and zero protons, respectively, are less basic.

The interactions of amines with CO_2 have been extensively studied because of their common use as acid gas scrubbing sorbents. Unhindered primary and secondary amines will form carbamate salts

when contacted with CO_2, while hindered amines and tertiary amines will form bicarbonate salts.[48,49,22] Example reactions are shown in **Figure 1-3**. Note that two molecules of a primary amine are required to absorb one molecule of CO_2, while only one molecule of a tertiary amine is required to absorb one molecule of CO_2.

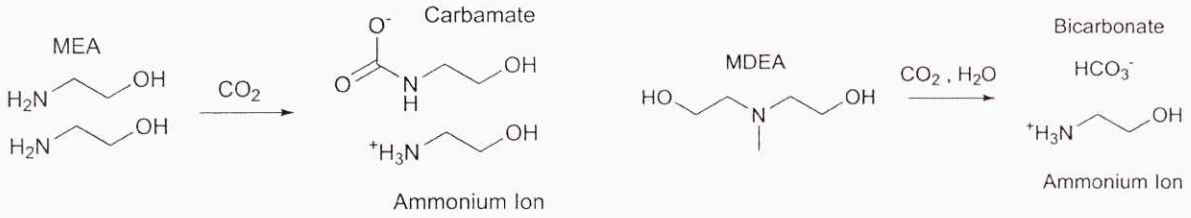

Figure 1-3. (Left) Reaction of two molecules of MEA to form a carbamate ion and an ammonium ion. **(Right)** Reaction of one molecule of MDEA to form a bicarbonate ion and an ammonium ion.

The mechanism of the carbamate formation is generally thought to proceed through a zwitterion intermediate as shown in **Figure 1-4**. Some researchers have also proposed an alternative termolecular mechanism.[50]

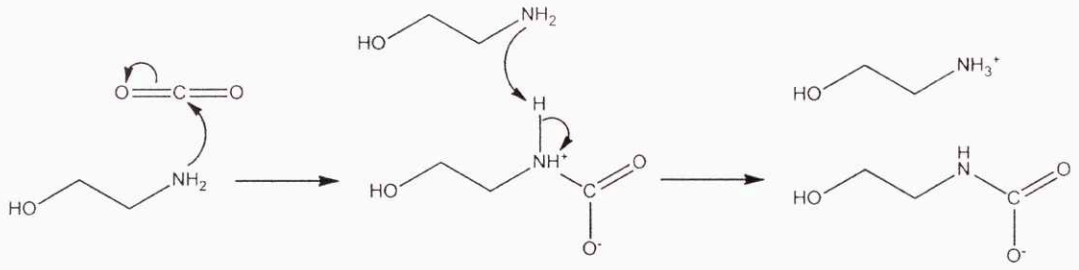

Figure 1-4. Zwitterion mechanism of carbamate formation from CO_2 absorption by MEA.

Experimental measurements and theoretical simulations of CO_2 reactions with amines often focus on obtaining equilibrium CO_2 solubilities, enthalpies of absorption, and reaction kinetics.[51–53] In addition to studies on the most common amines including MEA, diethanolamine (DEA), N-methyldiethanolamine (MDEA), piperazine (PZ), significant experimental results for less common polyamines are also available. As will be demonstrated in Chapter 2, polyamines are the most promising amine for use in an EMAR process due to their ability to strongly chelate metal cations. **Figure 1-5** shows the four polyamines identified as likely EMAR sorbents.

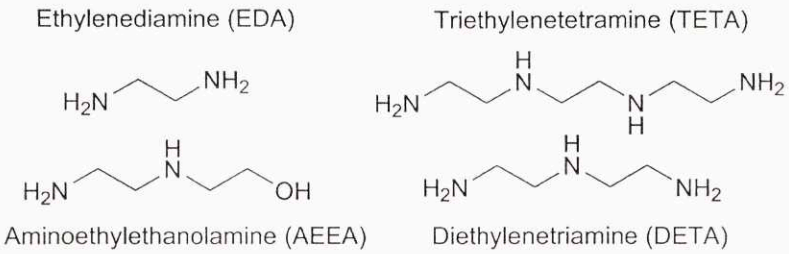

Figure 1-5. Molecular structures of the four polyamines identified as likely EMAR sorbents in Chapter 2.

Ethylenediamine (EDA) has been considered for use in thermal scrubbing systems for CO_2 separation at both the lab scale and at the pilot scale.[54–56] Several kinetic studies have also been performed on CO_2 absorption by EDA.[57,58] Information on the viscosity of aqueous EDA solutions and degradation rates can also be found in literature.[59,60] Ultimately, EDA was not selected as an effective sorbent for the thermal scrubbing of CO_2 because the enthalpy of absorption is too high in the stripper, which necessitates prohibitively high reboiler duties. The reason for the high enthalpy of absorption can be attributed to its ability to chelate CO_2 at low loadings.

Aminoethylethanolamine (AEEA) has also been considered thoroughly for use in CO_2 scrubbing applications.[61–64] AEEA has a slightly lower enthalpy of absorption than EDA or MEA because 50% of its amine groups are secondary. Unlike EDA, the AEEA's enthalpy of CO_2 sorption does not significantly change as the CO_2 loading increases. AEEA also has the benefit of very low vapor pressures do it its hydrophilic functional groups and larger molecular weight, compared to MEA or EDA. Diethylenetriamine[65,66,53] and triethylenetetramine[67,68] also have been examined for CO_2 capture, but in less detail.

The interactions of the amines with copper is equally important to the EMAR process and has been studied extensively, though never before in the presence of CO_2. Amine and copper complexation is important for copper plating,[69,70] copper etching,[71–73] and cupric ion removal applications.[74,75] The stability constant, β, defined in Eq. 1-1, describes the equilibrium of the cupric ion complexed with n ligands, L. The stability constant is equal to the product of all the individual equilibrium constants, K_i.

$$\beta = \frac{\left[CuL_n^{2+}\right]}{\left[Cu^{2+}\right][L]^n} = \frac{\left[CuL^{2+}\right]}{\left[CuL^{2+}\right][L]}\frac{\left[CuL_2^{2+}\right]}{\left[CuL^{2+}\right][L]}\cdots\frac{\left[CuL_n^{2+}\right]}{\left[CuL_{n-1}^{2+}\right][L]} = \prod_{i=1}^{n} K_i \qquad (1\text{-}1)$$

Stability constants for a variety of amines have been calculated using polarography,[76] which measures the apparent half potentials, $E_{1/2}$, as a function of concentration. Using the Nernst equation shown in Eq. 1-2 with the definition of the stability constant from Eq. 1-1, the variation of the potential can be calculated as a function of the copper and ligand concentrations. E_0 is the standard state potential; [Red] and [Ox] are the concentrations of the reduced and oxidized species, respectively. The activity of copper metal is assumed to be unity.

$$E = E_0 - \frac{RT}{nF}\ln\left(\frac{[Red]}{[Ox]}\right) = E_0 - \frac{RT}{nF}\ln\left(\frac{[Cu]}{\left[Cu^{2+}\right]}\right) = E_0 + \frac{RT}{nF}\ln\left(\left[Cu^{2+}\right]\right) \qquad (1\text{-}2)$$

$$E = E_0 + \frac{RT}{nF}\ln\left(\left[Cu^{2+}\right]\right) = E_0 + \frac{RT}{nF}\ln\left(\frac{\left[Cu^{2+}\right]_0}{1+\beta L^n}\right) \qquad (1\text{-}3)$$

In Eq. 1-3, $[Cu^{2+}]_0$ is the total concentration of all cupric ion species. The measured half potential, $E_{1/2}$, is assumed to be equal to the apparent standard state potential, as shown in Eq. 1-4. Note the resemblance of Eq. 1-2 with E_0 and Eq. 1-4 with $E_{1/2}$.

$$E = \left[E_0 - \frac{RT}{nF}\ln\left(1+\beta L^n\right)\right] + \frac{RT}{nF}\ln\left(\left[Cu^{2+}\right]_0\right) = E_{1/2} + \frac{RT}{nF}\ln\left(\left[Cu^{2+}\right]_0\right) \qquad (1\text{-}4)$$

Reliable stability constants for monoamines,[77] ethanolamines,[78] polyamines,[79] and amino acids[80] are all available from polarographic measurements. Spectrophotometric methods are also used for measuring the stability constants of transition metals because the complexation alters the UV-visible absorbance spectrum of the metal.[81,82] In the case of AEEA, spectrophotometric measurements provide additional insight into the underlying mechanism through the analysis of peak shifts.[83]

A pH titration curve can also be used to calculate the stability constants for different amines if the pKa's are known.[84] Measurement of the standard state enthalpy and entropy of the complex formation can

be accomplished by measuring the stability constant at varying temperatures and using the Van't Hoff equation.[85]

The results from literature show that cupric ions generally complex with four sites ligand sites, rather than the six available for most first row transition metals. The cause for the discrepancy is the *d*9 electronic state of the cupric ion that exhibits the Jahn-Teller effect. The Jahn-Teller effect forces the cupric ion complex into an asymmetrical configuration with two elongated bonds, which are generally unreactive. The elongation is required to avoid a degenerate symmetrical state.

The stability constants of cupric ions with polyamines are very high ($10^{16} - 10^{20}$), which indicates why these molecules are excellent at stabilizing copper in the EMAR process. Monoamines and ethanolamines show distinctly lower values. Ammonia and tertiary amines tend to favor the formation of cuprous ions rather than cupric ions.

Electrochemical Kinetics of Copper

The electrochemical kinetics of copper systems have been studied significantly in acidic environments, but only sparsely in basic amine environments. Studies in CO_2-saturated amines have never been previously performed. The study of the electrochemical kinetics of copper has been motivated by the industrially relevant processes of copper deposition, copper etching, and copper corrosion.

Mattsson and Bockris used galvanostatic pulses to examine the electro-dissolution and electro-deposition of copper in sulfuric acid systems.[86] Their results were analyzed by Newman, who showed that the measured potentials correspond well with a two-step mechanism, in which the first oxidation is fast and the second oxidation is slow.[87]

The importance of additives to copper plating baths in order to achieve higher efficiencies has been thoroughly investigated.[88–90] Electro-deposition from alkaline solutions that use amines to stabilize the copper ions is an alternative strategy to deposition from sulfuric acid solutions.[69,91,92]

Copper etching using a MEA solutions showed that even in the absence of oxygen, copper would still be slowly etched, presumably due to hydrogen evolution.[71] Copper corrosion in both alkaline[93,94] and

acidic[95] environments has also been investigated. Significant work has focused on the influence of chloride ions in order to assess corrosion in the ocean.[96,97]

A variety of electrochemical measurement techniques have been used in these investigations to characterize the electrochemical kinetics. The generation of current-potential diagrams and cyclic voltammetry are the most common techniques. Long-duration open-circuit and constant potential measurements have also been used.

Predictions of the effects of chemical reactions coupled with electron transfer were rigorously derived by Saveant and co-workers.[98,99] The derivation was based on the Nobel Prize winning work of Marcus, who theoretically described the rate constants of electrochemical reactions.[100,101] Marcus described the rate of electrochemical reaction in terms of the reorganization energy, λ, which is similar to an activation energy from transition state theory.

$$k_{et} = \frac{k_0}{\sqrt{4\pi\lambda k_b T}} \exp\left[-\frac{\left(\lambda + \Delta G^o\right)^2}{4\lambda k_b T} \right] \tag{1-5}$$

Where:

k_{et} = The electron transfer rate constant

k_0 = A pre-factor based on collision frequency and electronic coupling

ΔG^o = The total Gibb's free energy change for the electron transfer at standard state conditions

k_b = The Boltzmann constant

In most cases, $\lambda >> \Delta G^o$, which leads to the simplified equation shown in Eq. 1-6. Note all of the parameters in front of the exponential function have been lumped into a single pre-exponential term, A.

$$k_{et} = A \exp\left[-\frac{\lambda + 2\Delta G^o}{4k_b T} \right] \tag{1-6}$$

Saveant showed that the impact of a coupled chemical reaction on an electron transfer process would be an increase in the reorganization energy. The reorganization energy with the chemical reaction, λ_C, can be calculated as a function of the dissociation bond energy of the reaction, D_{RX}, and the reorganization energy in the absence of the chemical reaction, λ_0.

$$\lambda_C = \lambda_0 + \frac{D_{RX}}{4} \tag{1-7}$$

In the 4th chapter, this theory will be combined with Newman's concerted electron transfer model of copper electrochemistry in sulfuric acid solutions to predict the copper electrochemical kinetics in amine systems.

Transport Phenomena in Electrochemical Systems

The modeling of porous electrodes was investigated thoroughly by many researchers since the 1960's. The current and potential distribution in a porous electrode with uniform concentration was solved by Euler and Nonnemacher with macroscopic volume averaging of the porous electrode reactions.[102] Newman solved the analogous problem while representing the current with the Tafel approximation; he also used regular perturbation to allow for non-uniform concentration profiles.[103] Posey expanded the models further through incorporation of ion migration in addition to diffusion.[104] Consideration of structural changes in the porous electrode due to dissolution was added by Alkire.[105]

Porous electrode systems with flow have also received a tremendous amount of attention for a variety of applications including deionization,[106] the removal of heavy metals,[107] batteries,[108] and fuel cells. Fleishmann described a metal particle fluidized bed system for the removal of copper from dilute solutions.[109] Most reports focused primarily on the limiting currents of porous electrode systems, which reflect more of a study on transport phenomena than the electrochemical kinetics.[110-113] Many investigators used copper deposition as the experimental chemistry to validate their models.[114] Alkire provided an excellent theoretical analysis of a packed bed electrochemical flow reactor operating below its limiting current.[115]

Tubular and flat plate configurations have also been theoretically and experimentally investigated.[116,117] The majority of these reports also focus on the limiting current of the systems.[118,119] Because of the very inhomogeneous nature of the electrochemical boundary condition, exact analytical models are difficult to achieve. The Tafel approximation, which is used effectively for modeling the

porous electrode systems, fails at the boundary if the concentration drops too low. In cases, where the reaction rates can be defined by the Eyring equation and the electrochemical reactions are first order, the problem can be solved analytically.[120] The effects of gas evolution at a flat electrode surface has also been theoretically considered.[121]

Recently, the wider availability of significant computer power has enabled researchers to perform full numerical simulations of electrochemical systems. Simulations of redox flow batteries, which incorporate the porous electrode reactions and transport phenomena with very few simplifying assumptions, have been performed using multiphysics finite-element modeling in COMSOL.[122–124] Flow batteries with flat plate configurations have also been investigated through numerical simulation.[125] Simulations of lead-acid and lithium-ion batteries, which both involve significant surface chemistry, have been done from microscopic and macroscopic perspectives.[126–129]

In chapter 5, both theoretical and numerical methods will be applied to the copper/amine system, where two amine molecules must react at the surface to form the cupric ion complex. The bimolecular reaction adds significant non-linearity into the problem. An integral approach method is used to model the flat plate geometry.

Electrochemical Separation Technologies

The first electrically induced transport process was demonstrated in 1970 by Ward, who used iron cations to facilitate the transport of nitric oxide across a supported liquid membrane.[130] Since then, several different types of electrical separations have been developed. Capacitive deionization uses the double layer capacitance of high surface area porous electrodes to remove ions from the bulk of a solution.[131] Further research of supported membranes with electrically inducible carriers has led to the development of both high and low temperature carbonate systems for CO_2 transport.[132] Electrochemically-Mediated Complexation Separations (EMCS) were developed by Noble and coworkers for a variety of different separations used redox-active sorbents.[133–135]

Both electrochemical membranes processes and EMCS cycles have been used for CO_2 separations. Winnick and coworkers developed hydrogen-consuming systems and molten carbonate membrane systems for use in space shuttles to prevent CO_2 buildup in the enclosed cabin.[136,132] In the hydrogen system, the hydrogen is oxidized to generate protons that release the CO_2 from carbonates. The use of hydrogen is undesirable since it is dangerous to work with on a space shuttle. The molten carbonate system requires operating temperatures above 500°C, which is also undesirable.

Dubois and Scovazzo made significant progress using quinones for CO_2 concentration from atmospheric concentrations to nearly 1 bar.[137,138] Unfortunately, the quinones were found to be oxygen sensitive, which made them unattractive for separations of CO_2 from air or post-combustion flue gas. Appel developed a binuclear copper complex for use in an EMCS process instead of the quinones, but the molecule was very large and only slightly soluble in water.[139,140] EMCS process were shown to be capable of continuous gas separations by Terry, who demonstrated carbon monoxide separation using cuprous ions.[141]

Several novel electrochemical technologies have been developed recently including the use of bipolar membranes for an electrodialysis type process.[142] Because of the large driving forces that can be applied with electrochemical systems, Eisaman was able to desorb the CO_2 at pressure.[143] Pennline developed a low temperature carbonate fuel cell, which avoids the high temperature challenges of prior molten carbonate designs.[144] Both the low temperature carbonate fuel cell and the bipolar membrane system showed separation energies of 100's of kJ/mole CO_2, which represent efficiencies below 10%. Terry reported efficiencies below 1% for their carbon monoxide separation system. While multiple chemistries have been developed for electrochemical separations, developing an efficient separation system has thus far been unattainable.

Chapter 2

The Electrochemically-Mediated Amine Regeneration (EMAR) Cycle

This chapter describes the concept of an Electrochemically-Mediated Amine Regeneration (EMAR) system for carbon dioxide (CO_2) capture. The chapter begins with a set of general chemistry requirements of a new type of electrochemical scrubbing system based on a capture molecule and a redox active competitive binding agent. The best current EMAR chemistry, polyamines and copper, is then justified through an examination of 13 metals and 14 different amines with copper. Based on the best chosen system, the chemical cycle and a process flow diagram of an EMAR scrubbing system are presented. The chapter concludes with discussion of several advantages specific to EMAR, including the ability to desorb at pressure, achieve lean CO_2 loadings entering the absorber, and "drop-in" integration.

EMAR Chemistry Requirements

In the introduction, previously developed electrochemically-mediated complexation separation (EMCS) strategies were described where the carrier molecule, which binds with the target molecule, is redox active.[141,137,145] By undergoing a redox reaction, the carrier transitions between active and inactive states. A reaction cycle for a generic EMCS process can be seen in Figure **2-1**.

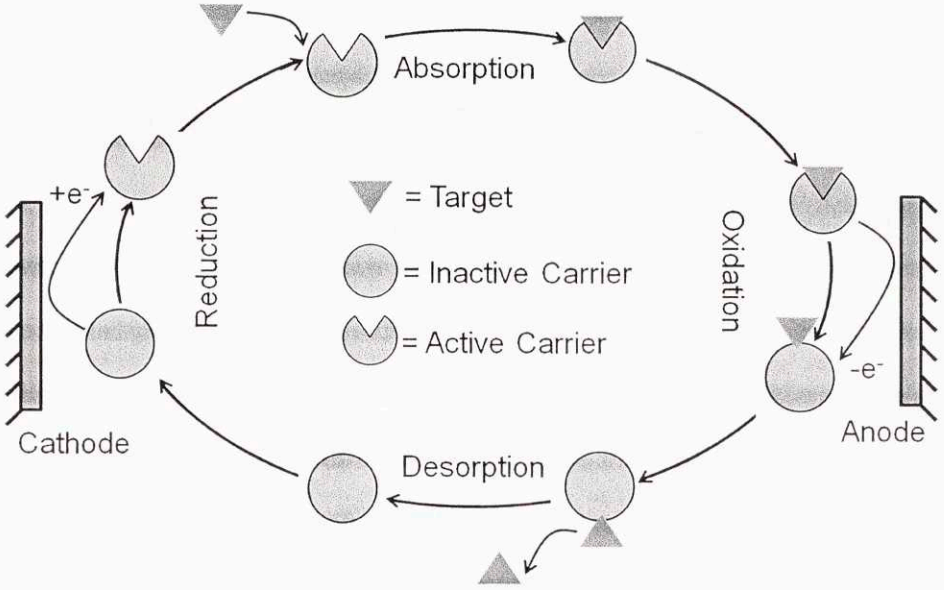

Figure 2-1. Redox capture cycle for an Electrochemically-Mediated Complexation Separation (EMCS) process.

An alternative strategy exists, in which the redox active species and the complexing agent are separate. This will be referred to as an Electrochemically-Mediated Competitive Complexation Separation (EMCCS) process. A reaction cycle for a generic EMCCS process can be seen in **Figure 2-2**.

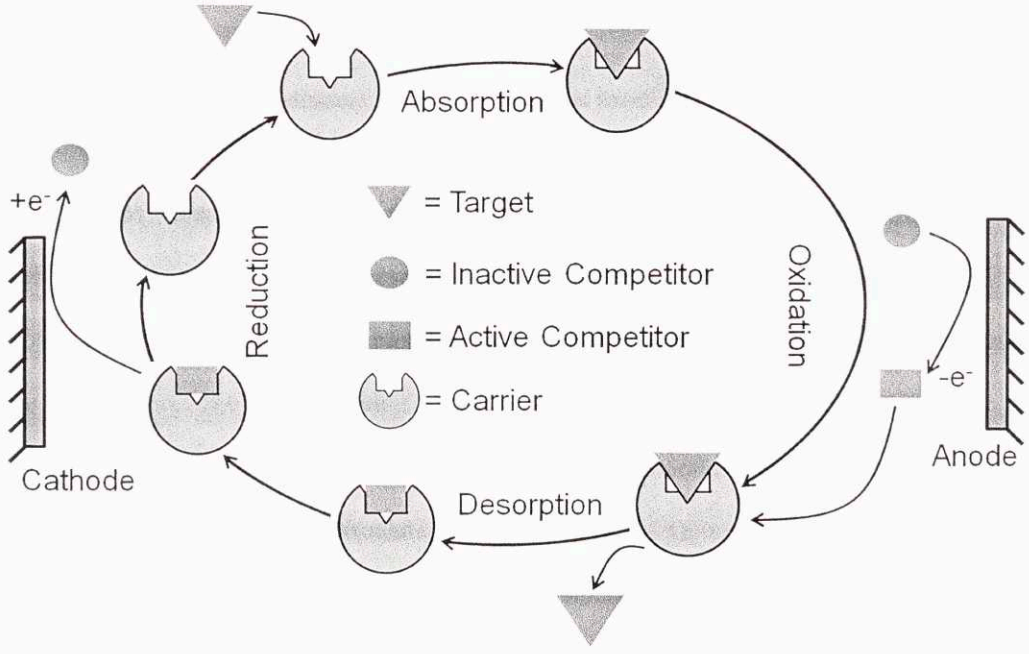

Figure 2-2. Redox capture cycle for an Electrochemically-Mediated Competitive Complexation Separation (EMCCS) process.

The redox active species, known as the competitor in this strategy, modulates the activity of the carrier through competition with the target molecules for the reaction site. When the competitor is in its active redox state, it binds strongly to the carrier, preventing the target molecule from associating. In its inactive redox state, the competitor is inert with respect to the carrier, and the target molecule is free to bind.

Compared with the cycle in Figure **2-1**, the oxidation process in the EMCCS cycle does not directly involve the CO_2 absorbing carrier. Hence, this second strategy is less direct and involves an additional species. EMCCS does, however, possess significant practical benefits for the capture of acidic targets. Many transition metals can be easily switched between their inert metallic state and various cationic states. These cations behave as Lewis acids with varying strengths, based on the specific metal. Lewis acids have been exploited through EMCS to concentrate a variety of ligands, primarily ones with some amount of basicity. These cations, however, are ineffective for capturing acidic targets because of their own inherent acidity. Using the transition metals as a competitor in an EMCCS process, however, allows their redox properties to be exploited for the separation of acidic targets, including acid gases like carbon dioxide or sulfur dioxide. To achieve this, a basic carrier molecule with preference towards the cationic transition metal over the target is required. Additionally, the carrier/cation complex must be electrochemically reversible.

The Electrochemically-Mediated Amine Regeneration (EMAR) process is a subset of EMCCS processes. In the EMAR cycle, the sorbent is an electrochemically-inert amine and the redox agent is a transition metal that can switch between its inert metallic state and its acidic cation form, which competes aggressively with CO_2 for the amines; the displaced CO_2 is released and flashed off as a gas. An example of a possible EMAR system based on copper and ethylenediamine can be seen in **Figure 2-3**. Further explanation of the EMAR process will be provided later in this chapter. The next section, however, will describe how the best possible EMAR chemistries are determined.

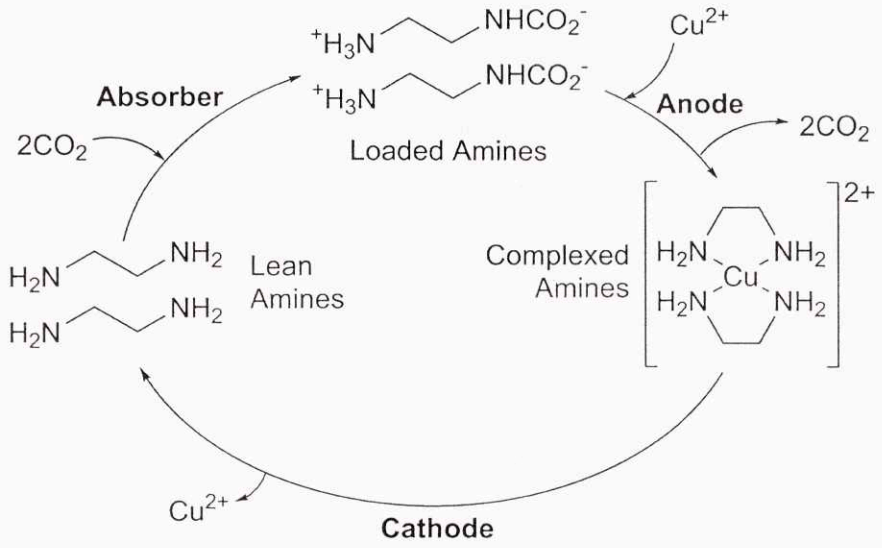

Figure 2-3. An EMAR cycle based on ethylenediamine and copper.

Best Available EMAR Chemistries – Metal

To determine the best combination of metals and amines for an EMAR process, a systematic analysis of most of the first row transition metals along with several other common metals was performed to identify the best possible metals for electrochemically-responsive competition with basic ligands. For this analysis, we used ethylenediamine (EDA) as the hypothetical basic ligand. EDA was chosen because of its known ability to bind CO_2 and the large knowledge base of its complexation chemistry with metal cations.

The first criterion used is cost per mole of metal. With emission rates on the order of 10^7 moles per hour of carbon dioxide for a 500 MW power plant, the system would require roughly 10^7 moles of metal if the material circulated every hour, which is a reasonable estimate. **Figure 2-4** shows approximate capital costs for a 500 MW power plant using an EMAR system based on the 10^7 mole assumption. Vanadium, tin, nickel, and cobalt all would cost significantly more than 10 million dollars, which makes them undesirable candidates. Zinc, manganese, and especially iron, are all inexpensive, and would be excellent candidates based on the capital cost criterion alone.

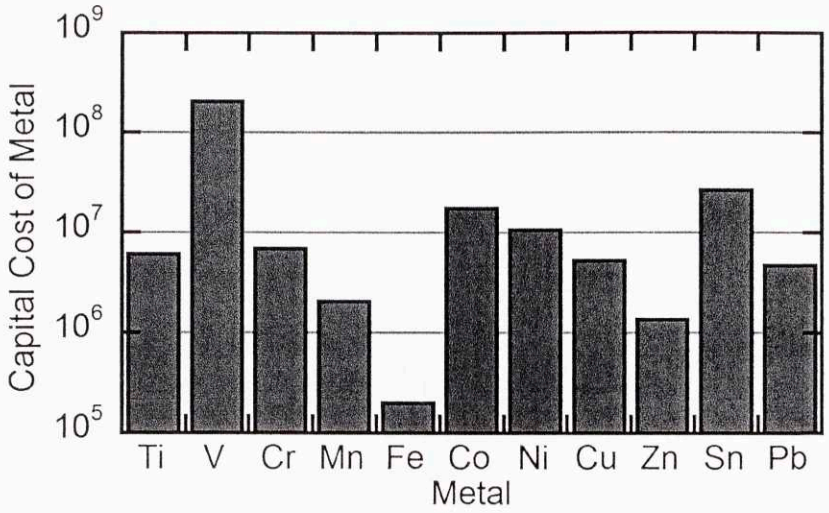

Figure 2-4. Approximate capital cost, in dollars, of different metals for a 500 MW power plant using an EMAR system. Data from http://www.metalprices.com.

The second criteria used is the cation stability constant of complexation with EDA. Some metals have multiple common oxidation states; for these metals, multiple stability constants are reported. A suitable system must possess stronger bonding with the target amine, here assumed to be EDA, than that amine possesses with CO_2. This requirement is mathematically represented in Eq. 2-1.

$$\log(\beta) > n_{ligand} \log\left(K_{CO_2}\right) \tag{2-1}$$

Where β is the stability constant, n_{ligand} is the number of ligands per metal cation, and K_{CO2} is the amine/CO_2 equilibrium constant. At room temperature, the EDA/CO_2 complex has an equilibrium constant of approximately 10^5. This means that for a metal cation to be suitable for this process, it must have stability constant, β, of greater than 10^5 for a single ligand complex, 10^{10} for a double ligand complex, and 10^{15} for a triple ligand complex. **Figure 2-5** compares reported stability constants for single, double, and triple ligand complexes of various metals with EDA. For Fe(III), the values were estimated based on the values for Fe(II) and the ratios of Cr(III)/Cr(II) and Co(III)/Co(II).

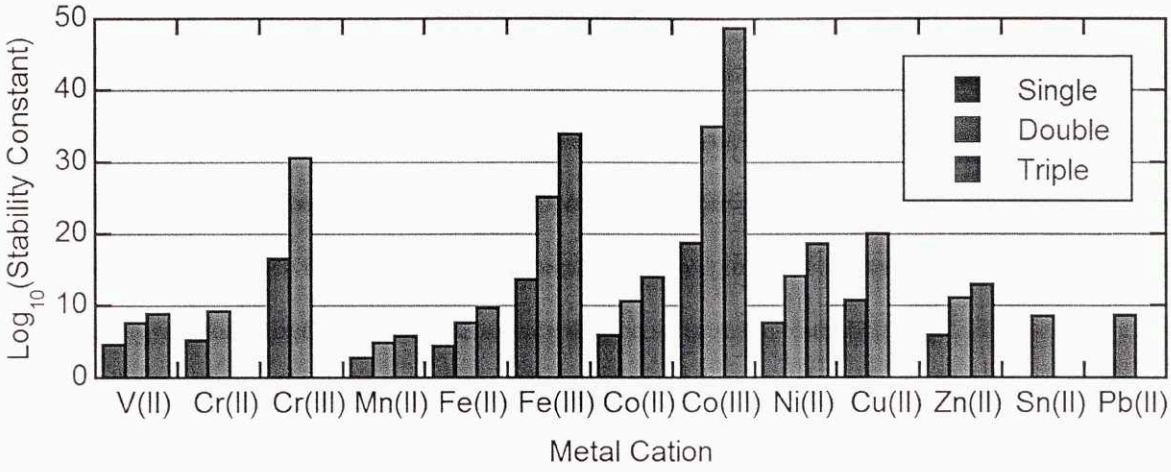

Figure 2-5. Stability constants of single, double, and triple ligand complexes of various transition metal complexes with ethylenediamine. Values for Fe(III) are estimates; the rest were experimentally measured in literature.[146]

Based on the stability constants for ethylenediamine complexes, only Cr(III), Fe(III), Co(II), Co(III), Ni(II), and Cu(II) possess strong enough interactions with amines to successfully operate an EMAR cycle. Of these, chromium (Cr), copper (Cu), and iron (Fe) also met our requirement of keeping the estimated capital cost below 10 million dollars. It should be noted that for cobalt (Co) and iron, application of a reducing potential will first cause the formation of +2 oxidized species based on their reduction potentials. Therefore, while other metals switch between their cation and metallic state, those systems would switch between different cation states.

It is important to consider the stability of the metals to resist oxidation. Oxygen will be present in the flue gas, and metals that are extremely unstable could rust via hydrogen formation. Hydrogen is a common problem in iron-based electrochemical systems, such as iron-air batteries.[147] To assess the stability of a given cation, we look at reduction potentials in systems with and without amines. **Figure 2-6** shows the reduction potentials of the various metals (to a given cation) in both the presence and absence of EDA. High values indicate a lower tendency for oxidation, which is preferable. In all cases, the addition of EDA, which significantly stabilizes the oxidized cation states, lowers the reduction potential.

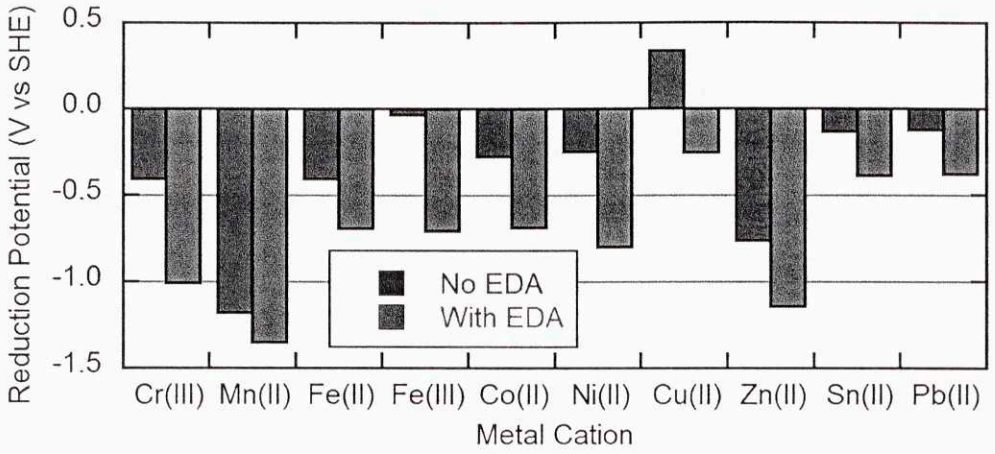

Figure 2-6. Reduction potentials of different metals in the presence and absence of 1 M EDA.

The reduction potentials in EDA, E^0_{EDA}, were calculated by combining published values for reduction, E^0, potentials with the stability constants, β, reported in **Figure 2-5** using Eq. 2-2.

$$E^0_{EDA} = E^0 - \frac{RT}{nF}\ln(\beta) \tag{2-2}$$

Where n is the number of electrons transferred, which is equal to the oxidation state of the specific cation. The half reaction governing hydrogen evolution, which is shown in Eq. 2-3, has a standard reduction potential of -0.83 volts versus the SHE. At the neutral pH's in the EMAR anode, however, the reduction potential will be closer to -0.4 volts.

$$2H_2O + 2e^- \rightleftharpoons H_2 + 2OH^- \tag{2-3}$$

Only copper, tin, and lead possess reduction potentials more positive than -0.4 V in the presence of EDA. The other metals would likely oxidize even in the absence of dissolved oxygen. In the presence of oxygen and the amines, copper, tin, and lead, will still oxidize slowly.

Based on the results from this section, copper is the clear choice for the redox active competitor in an EMAR process. It is relatively low cost, has a strong affinity towards amines, and has the oxidative stability to resist undesirable oxidation through hydrogen evolution, making it the best available candidate. Copper, however, is not without drawbacks. Copper, due to its $d9$ electronic structure (9 electrons in the d-orbital), is subject to the Jahn-Teller effect. As a result, cupric ions only possess four

strong coordination sites, as opposed to Ni^{2+}, which possesses six strong coordination sites. Therefore, while nickel ions can complex with three molecules of EDA, copper ions can only complex with two. For nickel, transferring two electrons could release three molecules of CO_2 (by complexing three molecules of EDA), while transferring two electrons to copper can only release two molecules of CO_2.

Copper, while not as expensive as nickel or several of the other metals, is still expensive at the scale required for a large capture plant. If an EMAR system could be designed with iron instead, the metal cost could be reduced by over an order of magnitude. Unfortunately, iron(II) does not complex amines strongly, and iron(III) precipitates easily in the form of hydroxide salts. Experiments using diethylenetriamine (DETA), which better stabilizes iron(II), returned moderate success at facilitating CO_2 release. **Figure 2-7** shows the variation of CO_2 capacity as a function of metal cation concentration for Cu(II) and Fe(II) with DETA as well as Cu(II) with EDA.

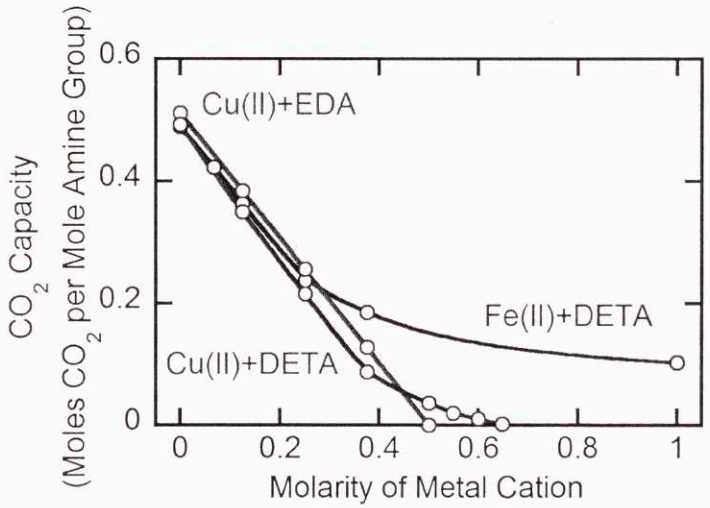

Figure 2-7. CO_2 capacity of amine solutions (per functional group) as a function of metal cation concentration. All solutions are 2 N in amine function group concentration (1 M EDA, 0.67 M DETA).

For low loadings of the metals, adding either copper or iron releases approximately the same amount of CO_2. Because the iron/amine interactions are weak, however, at high loadings the addition of more Fe(II) does not lead to significantly more CO_2 release. This demonstrates the superior qualities of copper for use in an EMAR system in comparison with iron. Additionally, experiments with iron were challenging due

to precipitation and slow kinetics, which are problems that also would hinder application of an iron-based EMAR system.

Having concluded that copper is the best available metal for use in an EMAR process; the next section will focus on selecting the best amines to work with copper.

Best Available EMAR Chemistries – Amine

Fourteen different amines were investigated to identify an optimal set for an EMAR process. **Figure 2-8** shows the chemical structures and abbreviations of each of the amines, which are composed of monoamines (which include both ethanolamines and amino acids), diamines, and polyamines. Full chemical names and additional information can be found in **Table 2-1**. The comments reference their performance in CO_2 capacity measurements, which will be discussed in detail in the Chapter 3.

Table 2-1. List of investigated amines with full chemical names and comments on solution stability.

Abbrev.	Full Chemical Name	Comments
MEA	Monoethanolamine	Precipitate observed during CO_2 capacity measurement
DEA	Diethanolamine	Precipitate observed during CO_2 capacity measurement
MDEA	N-Methyldiethanolamine	Precipitate observed during CO_2 capacity measurement
Gly	Glycine	Precipitate observed during CO_2 capacity measurement
Sar	Sarcosine	CO_2 capacity experiments not performed
Tar	Taurine	CO_2 capacity experiments not performed
EDA	Ethylenediamine	No precipitate observed in target concentration range
dmEDA	N,N-Dimethylethylenediamine	No precipitate observed in target concentration range
deEDA	N,N-Diethylethylenediamine	Precipitate observed during CO_2 capacity measurement
tmEDA	Tetramethylethylenediamine	Amine was too volatile for CO_2 capacity measurement
AEEA	Aminoethylethanolamine	No precipitate observed in target concentration range
DACH	Trans-Diaminocyclohexane	Precipitates immediately when exposed to cupric ions
DETA	Diethylenetriamine	Copper powder formed during CO_2 capacity experiments
TETA	Triethylenetetramine	No precipitate observed in target concentration range

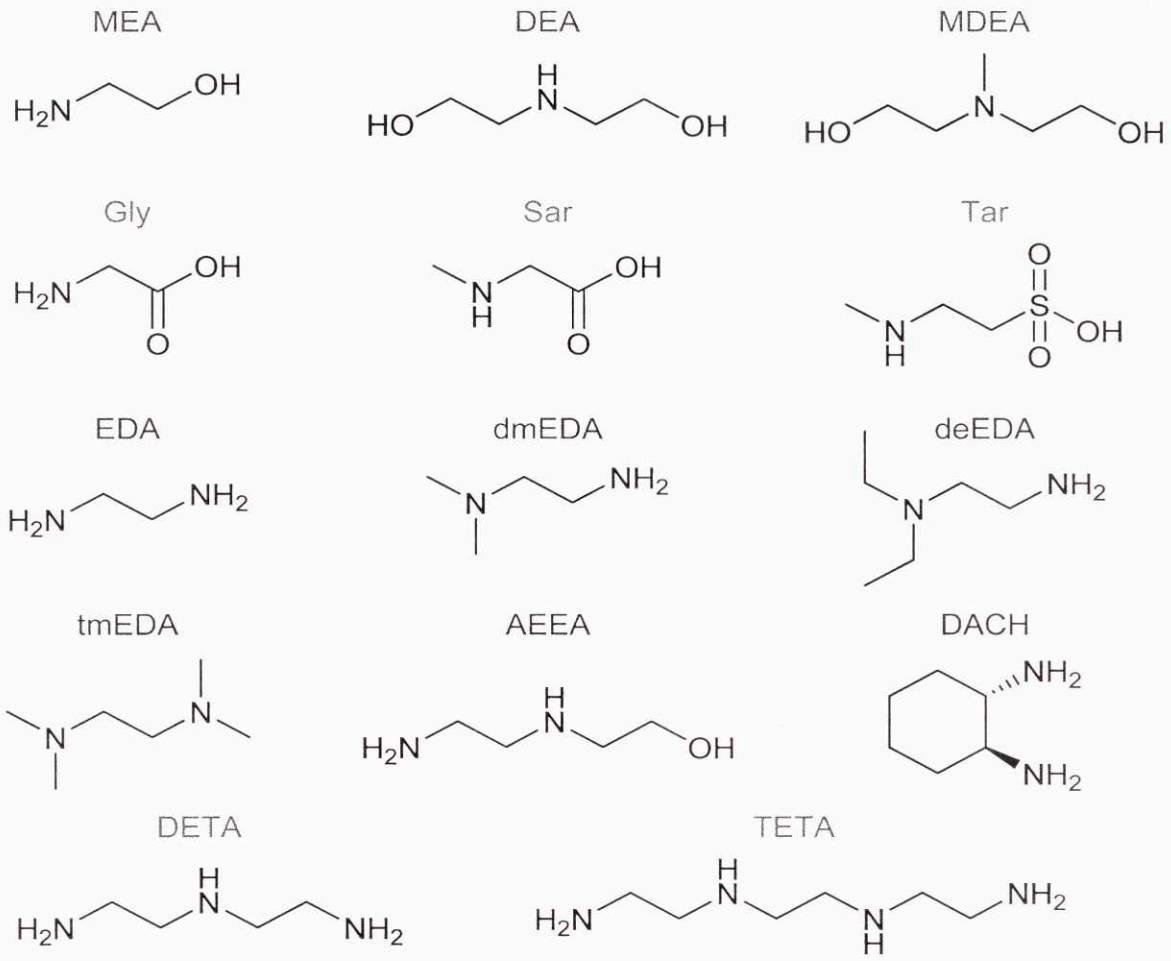

Figure 2-8. Structures and abbreviations of the 14 different amines investigated for use in an EMAR process with copper. The amines consist of enthanolamines (green), amino acids (purple), diamines (blue), and polyamines (red).

Many of the amines precipitated during the experiments, which indicated they were unsuitable for use in an EMAR system. Sarcosine and taurine were not tested for CO_2 capacity. DACH precipitated immediately upon the addition of cupric ions, and was not considered thereafter.

All 14 amines, with the exception of DACH, were tested in cyclic voltammetry experiments under argon and CO_2. The voltammogram experiments were run at 0.1 V/s with 2N of the amine (i.e., the molarity of amine functional groups was 2M), 0.25M copper sulfate ($CuSO_4$), and 1M sodium nitrate ($NaNO_3$). Many of the amines showed cathodic blocking, where the reduction peak was dramatically smaller than the diffusion limitation of the dissolved cupric ions. The cathodic blocking can be explained

by the significant increase in pH near the electrode surface that results from the plating of the cupric ions from the amine complexes. At the high pH, cupric ions precipitate out as copper hydroxide if the amine complexes are insufficiently stable. **Figure 2-9** shows results from the cyclic voltammetry experiments.

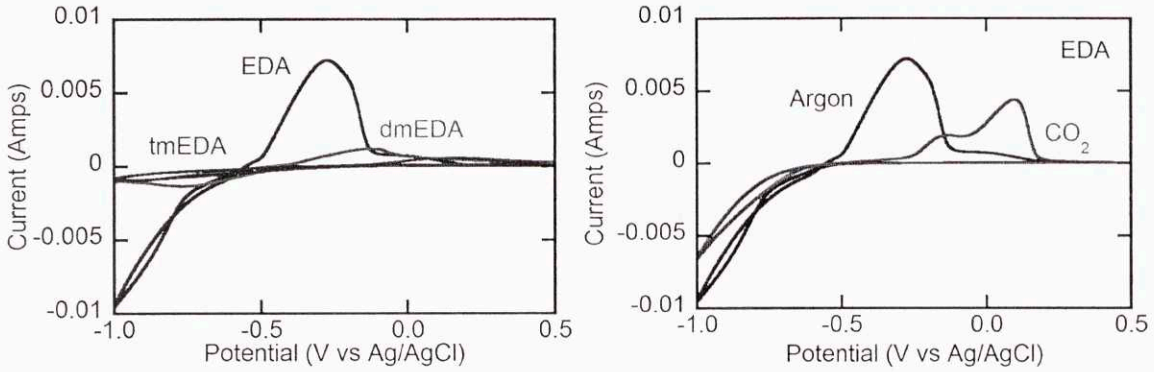

Figure 2-9. (Left) Cyclic voltammograms of different diamines at 0.1 V/s under argon. **(Right)** Cyclic voltammograms of EDA at 0.1 V/s under argon and CO_2. All solutions are 1M amine, 0.25M $CuSO_4$, and 1M $NaNO_3$.

The difference in currents between EDA, dmEDA, and tmEDA is substantial. EDA forms the most stable copper complexes and does not exhibit cathodic blocking behavior. Both dmEDA and tmEDA, however, demonstrate poor cycling. When the experiment is run in a CO_2 saturated environment with EDA, the current is decreased slightly and the reduction and oxidation peaks are separated farther apart. This increased separation is indicative of slower electrode kinetics, which will be discussed further in the Chapter 4. To quantitatively assess the differences in the voltammograms, the total charge passed during the cathodic and anodic processes were calculated, along with their charge ratio, denote A/C. The results of the cyclic voltammetry experiments are tabulated for the 13 amines tested in **Table 2-2.**

The A/C ratio, which would be unity if the amount of cupric ions reduced was exactly equal to the amount of copper oxidized on the following pass, is a good approximation of the plating efficiency of the different systems. The plating efficiency describes what fraction of electrons transferred lead to copper plated on the surface, as opposed to copper powder formed in the bulk of the solution. High currents and the presence of CO_2 appear to negatively affect plating efficiency. The range of efficiencies under argon found for different amines ranged widely from 14% for MDEA to 77% to dmEDA.

Table 2-2. Total cathodic and anodic charging passed during cyclic voltammogram experiments in mA.

	Argon			CO_2		
	Cathodic	**Anodic**	**A/C**	**Cathodic**	**Anodic**	**A/C**
MEA	2.04	0.96	0.47	3.48	1.47	0.42
DEA	1.03	0.45	0.43	3.20	1.52	0.48
MDEA	1.83	0.26	0.14	2.89	1.55	0.54
Gly	1.12	0.85	0.76	1.15	0.52	0.45
Sar	2.56	1.35	0.53	2.27	1.26	0.56
Tar	1.40	0.54	0.38	2.55	0.97	0.38
EDA	3.35	1.98	0.59	2.08	1.12	0.54
dmEDA	0.86	0.66	0.77	1.98	0.68	0.34
deEDA	0.87	0.59	0.68	2.08	1.02	0.49
tmEDA	0.61	0.39	0.63	0.58	0.38	0.65
AEEA	0.86	0.58	0.67	1.68	0.82	0.49
DETA	2.25	1.09	0.48	2.09	0.87	0.41
TETA	0.93	0.68	0.73		N/A	

Based on the stability of the copper amine complexes, which was ascertained through the cyclic voltammetry and CO_2 capacity experiments, it was determined that monoamines were not suitable for EMAR systems because of their tendency to precipitate. Sarcosine and taurine were not fully investigated, but it is unlikely that amino acids would be effective candidates because they tend to only form double-ligand complexes with copper (as opposed to MEA, DEA, or MDEA, that would form quadruple-ligand complexes). Therefore, each molecule of copper oxidized would only release one molecule of CO_2, which translates to 1 molecule of CO_2 per two electrons. In contrast, the ethanolamines, diamines, and polyamines would release 2 molecules of CO_2 per two electrons. The lower CO_2 yield per electron would dramatically increase the required current densities and the associated Ohmic potential losses.

EDA, AEEA, dmEDA, DETA, and TETA all demonstrated sufficient resistance to precipitation. However, due to high volatility, even in aqueous solutions, dmEDA was not considered for further experiments. For the remainder of the chapter, the focus will shift to the description of the overall process with less emphasis on the specific chemistry employed.

The EMAR Process

Figure 2-3 shows the cyclic reaction scheme of an EMAR process with EDA and copper. The scheme consists of three chemical or electrochemical transitions, which take place in an absorber, an anode, and a cathode. A schematic diagram of the EMAR scrubbing process is shown in **Figure 2-10**, which also includes a more detailed view of the electrochemical cell stack. In the scrubbing process, the absorber is analogous to an absorber in a thermal scrubbing system. A pump is placed after the absorber to pressurize the electrochemical cell, which allows for the CO_2 to be exhausted at pressure. The CO_2 is removed in flash tanks placed after the anode sections. The electrodes in the anode and cathode chambers could be either porous copper foam, porous conductive supports plated with copper, or thin channels with copper-plated walls. The membrane could be either an anion exchange membrane or a surfactant coated microporous polyolefin membrane. The electrochemical cells would be stacked in series, similar to a fuel cell stack, to decrease resistive losses. Transport of the anolyte and catholyte solutions will primarily be contained internal to the stack to reduce the piping requirements and equipment footprint.

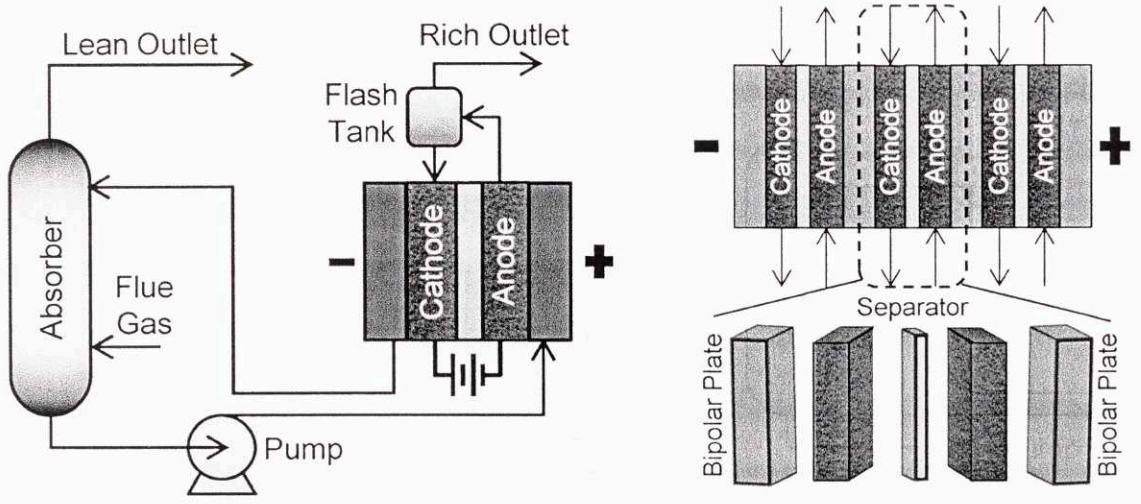

Figure 2-10. (Left) Schematic diagram of an EMAR capture process. **(Right)** A cross-sectional view of the EMAR electrochemical cell stack.

Because CO_2 bubbles are being constantly formed in the anode, several gas/liquid separation steps may be necessary to keep the liquid fraction of the anode stream above 50%. Removing the CO_2 could be accomplished by the aforementioned flash tanks, by inverted bucket separators used commonly for steam

traps, or through a gas permeable membrane separator. While the membrane separator may be more complicated to design, it could be more easily incorporated into a stack structure, which would avoid the need to remove the anolyte solution from the stack. Keeping the liquid in the stack will allow for significantly smaller plant sizes due to the reduction in piping and equipment.

Heat exchanger stack elements, which are commonly found in fuel cell stacks, would also be required to maintain the temperature in the electrochemical stack. As will be discussed in the Chapter 7, the electrochemical stack will cool itself if operated adiabatically.

Figure 2-11 shows a system where the cathode of the electrochemical cell and the absorber are combined. In this coupled-EMAR system, the electrical demands would be reduced because the amines in the cathode would be better stabilized. A coupled system, however, would not be capable of pressurization without the extremely costly compression of the flue gas. A coupled system would also be extremely difficult to design when considering the need for ample gas/liquid contact, low pressure drop, and low electrochemical impedance. For this reason, only the decoupled system will be considered further.

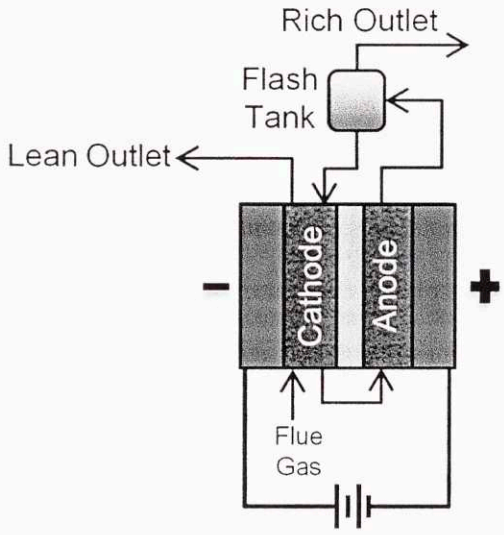

Figure 2-11. Diagram of a coupled EMAR system where the CO_2 absorption occurs in the cathode.

Advantages of EMAR

The EMAR system has several distinct advantages over traditional thermal scrubbing designs. The advantages range from easing installation logistics, reduction in capital costs, to improved operational efficiency.

Desorption at Pressure

EMAR systems possess advantages that reduce the capital costs associated with CO_2 capture. Due to the significantly higher stability of the Cu^{2+}/amine complexes compared to the CO_2/amine complexes, the electrochemical cell can be operated at high pressure, which allows for CO_2 to be removed at high pressure. Assuming the separated CO_2 is intended for geological sequestration, which often requires compression of the CO_2 at the plant to 150 bars, the ability to release at high pressure can dramatically reduce the size of the required compressor train. To quantify the compression work required for CO_2, and the subsequent benefits of high pressure release, we use the Peng-Robinson Equation of State (PR-EOS) shown in Eq. 2-4.[148]

$$P = \frac{RT}{V-b} - \frac{a}{V(V+b)+b(V-b)} \tag{2-4}$$

In Eq. 2-4, a is a function based on temperature and b is a constant. Because EMAR systems are isothermal, we can treat both parameters as constants if we assume a temperature, in this case, 50°C:

$$a = 0.37932\left(\frac{\text{J}}{\text{mol}}\right)\left(\frac{\text{m}^3}{\text{mol}}\right) \qquad b = 2.6664\times10^{-5}\left(\frac{\text{m}^3}{\text{mol}}\right) \tag{2-5}$$

The per mole work required for compression, W_C, can be calculated by integration of the volume as a function of pressure (i.e., the VdP work). Because the PR-EOS is pressure explicit, integration by parts is required to analytically solve the integral as shown in Eq. 2-6.

$$W_C = \int_{P_A}^{P_{out}} VdP = \left[(PV)_{out} - (PV)_A\right] - \int_{V_A}^{V_{out}} PdV$$

$$= (PV)_{out} - (PV)_A - RT\ln\left(\frac{V_{out}-b}{V_A-b}\right) + \frac{a}{2\sqrt{2}b}\ln\left(\frac{\dfrac{1+(V_{out}+b)/\sqrt{2}b}{1-(V_{out}+b)/\sqrt{2}b}}{\dfrac{1+(V_A+b)/\sqrt{2}b}{1-(V_A+b)/\sqrt{2}b}}\right) \quad (2\text{-}6)$$

Assuming a final required pressure, P_{out}, of 150 bar, **Figure 2-12** shows the work required of the compression train as a function of the CO_2 release pressure, P_A, from the anode EMAR system.

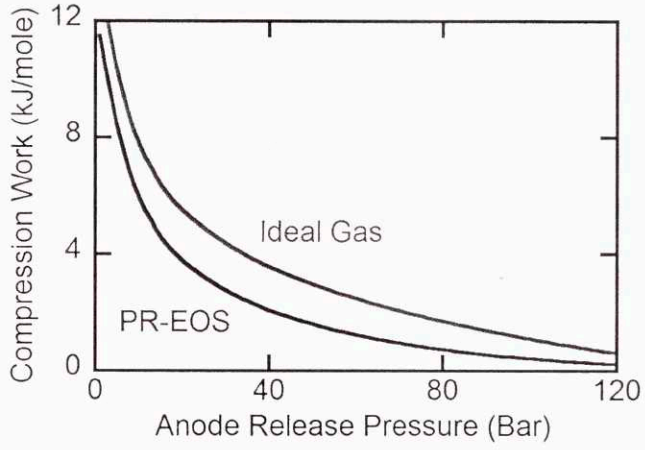

Figure 2-12. Work per mole of CO_2 required of the compression train as a function of the CO_2 release pressure from the anode.

By releasing CO_2 at 10 bar, over 50% of the required compression work can be avoided. This translates to a dramatic reduction in the size of the compression train, and ultimately the associated capital costs. Considering the extremely expensive nature of compressors, this is a significant advantage.

Reduced Absorber Size

The other most capitally expensive unit in the capture plant is the absorber. Many factors contribute to the size of the absorber. The flow rate of the flue gas, which is defined by the design objective, is the primary factor in determining the diameter of the column. The height of the column, however, is very sensitive to the properties of the inlet amine absorbent. The concentration and the CO_2 loading (moles of CO_2

absorbed divided by twice the moles of amine functional groups) affect both the reactivity of the amines and the transport properties (viscosity and diffusivity) of the sorbent solution.

The chemical reaction rate of the amine sorbent will be proportional to the number of unreacted amine sites. Because the reaction is coupled with diffusion in a boundary layer, the square root of the pseudo-first-order reaction rate at the inner boundary (far from the gas phase), is roughly proportional to the enhancement of the flux. This results from the "thick" nature of the boundary layer. The thick boundary layer theory was developed by Smith and Meldon in the 1970's.[149] In a recent paper, Meldon shows strong agreement between the numerical solutions of the larger more complicated systems and the square root approximation.[150] Specifically, it was shown that the enhancement factor, E, which describes the multiplicative increase in flux due to the facilitated transport by the reactive amines, can be approximated with Eq. 2-7.

$$E = \frac{\text{Facilitated transport flux}}{\text{Diffusion only flux}} = \delta \sqrt{\frac{k_1 C_{Am}(\delta)}{D_{Am}}} \tag{2-7}$$

In Eq. 2-7, δ is the thickness of the boundary layer, $C_{Am}(\delta)$ is the concentration of amine functional groups at the far boundary layer, k_1, is the pseudo-first-order reaction rate coefficient, and D_{Am} is the diffusivity of the amine species. In an amine scrubber, the fraction of amines still complexed by CO_2, x_L, is defined in terms of the total amine concentration, C_T, in Eq. 2-8.

$$x_L = \frac{\text{Moles of } CO_2 \text{ in solution}}{\text{Total } CO_2 \text{ capacity}} = \frac{\text{Moles of } CO_2 \text{ in solution}}{(\text{Moles of amine functional groups})/2} = \frac{C_{CO_2}}{C_T/2} \tag{2-8}$$

Eq. 2-7 can be restated based on the definitions of Eq. 2-8 as shown in Eq. 2-9.

$$E = \delta \sqrt{\frac{k_1}{D_{Am}} \left(\frac{(1 - x_L(\delta)) C_T(\delta)}{2} \right)} \tag{2-9}$$

From Eq. 2-9, we see that improved flux occurs when C_T is large and x_L is small. In current thermal scrubbing technologies, incoming values of x_L of 0.4 to 0.5 are common because of the inability to operate at temperatures above 120°C in the desorber. At temperatures any higher, thermal amine

degradation would occur rapidly. For an EMAR system, the competitive desorption strategy should be able to achieve values for x_L at or below 0.1. This will lead to 30% to 40% increase in the enhancement factor, which will lead to an equivalent reduction in column height.

In addition to the concentration and loading of the inlet solution, the diffusivity of the amine species will also affect the absorption rate. Based on thick film theory, the square root of diffusivity should be proportional to the rate of absorption. The Stokes-Einstein equation predicts the diffusivity will be inversely proportional to the viscosity of the solution, which is heavily dependent on both the type of amine, the amine concentration, and the CO_2 loading. The viscosity of a 4M EDA solution approximately doubles upon complete loading with CO_2.

Operating with lower incoming loadings will lead to lower viscosities, and hence higher diffusivities and absorption rates, by lowering the average CO_2 loading in the absorber. The use of polyamine solutions, which were determined to be the ideal choice for EMAR systems, will also allow for high CO_2 loading at relatively low amine mass fractions of the sorbent solution. For example, a 4M EDA solution, which is approximately 24% amine by mass, possesses the same CO_2 capacity of an 8M MEA solution, which is 48% amine by mass. Furthermore, since the desorption process in an EMAR system recovers a higher fraction of the CO_2, the molar flow rate of the amine sorbents can be reduced by an additional 30% to 40%.

Similar to the reduction in compressor duty, the reductions in absorber size and sorbent flow rate represent a significant savings in equipment capital for an EMAR system versus a traditional thermal scrubber.

Polyamine Utilization

Polyamines, which have been previously considered for CO_2 thermal scrubbing applications, have not been widely adopted, with the exception of piperazine.[151] The rigidity of piperazine leads to significantly different behavior compared to the more flexible linear molecules studied earlier this chapter. EDA, AEEA, DETA, and TETA can chelate cupric ions and, to a lesser extent, CO_2. Piperazine, however,

cannot distort its ring structure to become a bidentate ligand, and hence behaves more similarly to monoamines. It has been observed that the enthalpy of CO_2 sorption for EDA is very loading dependent. One hypothesis is that EDA undergoes a sequential CO_2 absorption mechanism, where CO_2 is initially chelated. **Figure 2-13** shows possible mechanisms for sequential absorption for piperazine and EDA.

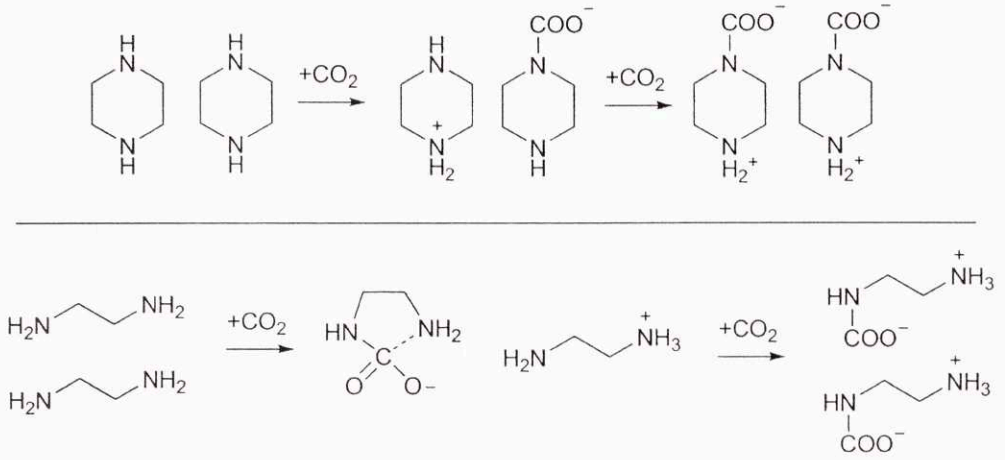

Figure 2-13. (Top) Two-step CO_2 absorption mechanism for piperazie. **(Bottom)** Two-step CO_2 absorption mechanism for EDA.

For piperazine, as well as any other primary or secondary amine that is unable to form chelate complexes, the interactions with CO_2 will not vary appreciably until the amount of absorbed CO_2 exceeds the 1:2 ratio of CO_2 to amine functional groups. Below that ratio, carbamate formation will dominate, and secondary interactions will be negligible.

For polyamines, however, chelated complexes will form. For example, after the first molecule of CO_2 is absorbed by an EDA sorbent, one molecule will chelate the acidic carbon. After the second molecule of CO_2 is absorbed, which corresponds to loadings above 50%, there are no remaining amine groups with accessible lone pairs to chelate the carbons. The result of this is an enthalpy of sorption that decreases as the CO_2 loading increases. This behavior has been observed by Zhou, who reported a formula for the enthalpy of CO_2 sorption, ΔH_{CO2}, as a function of CO_2 loading. The formula is reproduced in Eq. 2-10.[54]

$$\frac{\left(-\Delta H_{CO_2}\right)}{R} = \left(-16300 + 7800 x_L\right) \tag{2-10}$$

In Eq. 2-10, which is based on measurements from 40°C to 100°C, R, is the universal gas constant. Analysis of this equation shows the enthalpy of sorption varies from 136 kJ/mole at zero loading to 71 kJ/mole when fully loaded with CO_2. MEA, for comparison, displays a nearly constant enthalpy of sorption of 82 kJ/mole at 40°C from loadings of 0 to 0.5 mole CO_2 per mole MEA. Even AEEA does not display an appreciable change in sorption enthalpy with loading, presumably because the secondary amine group is too weak to appreciably contribute to the stability of the CO_2 complex.

When considering a thermal stripping system, it is undesirable to use amines with high enthalpies of sorption in the stripper because that translates to large reboiler duties. For most amines, the heat of sorption increases significant with temperature. MEA, for example, increases from 82 kJ/mole at 40°C to over 100 kJ/mole at 120°C. This has been attributed to the change in the enthalpies of acid dissociation, which are inherently coupled with carbamate formation. EDA would be an exceptionally poor choice for a thermal stripping process because not only does the enthalpy increase due to the increase in temperature, but the release of CO_2 in the stripper will further raise the enthalpy of sorption. Not surprisingly, pilot plant experiments for a thermal scrubbing system using EDA found that the system required prohibitively high heat duties.

These CO_2 loading and thermal dependencies, however, are unimportant in an EMAR system, which should be operated in nearly isothermal conditions and high CO_2 partial pressures in the anode. While the CO_2 loading fraction does decrease in the anode due to the addition of cupric ions, the amine which are not complexed with copper retain a high CO_2 loading, thereby retaining the low enthalpy of sorption. As a result, the EMAR system should be capable of utilizing EDA, which is a low cost and high capacity sorbent with fast kinetics.

Ease of Implementation

Due to the electrically-driven, rather than steam-driven, nature of the EMAR system, it does not require any internal reconfiguration of the existing plant. For non-power generated plants, such as cement, aluminum, or steel plants, EMAR could be easily installed using electricity from the power-grid, whereas

as steam-driven system would require the additional installation of a natural gas boiler to produce the steam.

The current fleet of coal-fired power plants, natural gas combined cycle plants, and cement, aluminum, and steel plants, all of which were not designed to incorporate carbon capture technologies, create a large demand for capture technologies which do not require upstream plant integration. The EMAR capture process offers a "drop-in" solution, which could be installed almost anywhere. Smaller-scale applications like generation of CO_2 for use in bio-fuel or bio-chemical production or removal of CO_2 from confined spaces is also possible.

Conclusions from EMAR Chemistry Development

- The EMCCS cycle enables the combination of transition metals with excellent electrochemical properties and amine sorbents with excellent CO_2 absorption properties to create the EMAR capture strategy.
- Polyamines with copper is the most effective EMAR chemistry currently available.
- While MEA did not prevent copper salt precipitation in 2M solutions at 50°C, it still warrants further study because of its prevalence in traditional thermal scrubbing applications. Higher temperatures may prevent precipitation.
- EMAR possesses several logistical and operational advantages including drop-in integration and desorption at pressure.

Chapter 3

Thermodynamics of EMAR

This chapter describes, both theoretically and experimentally, the thermodynamics limits of efficiency of an EMAR system. The theoretical calculations are based on the cycle and process described in the previous chapter, which contains some inherent inefficiency. The extent of the inefficiency is heavily dependent on several fundamental reaction equilibria and solution properties, all of which are temperature dependent. Measurements of these properties are achieved through a series of experiments; the theory and results of these experiments are described. Use of the measured property values in the theoretical models demonstrates that systems with 70% open-circuit efficiency should be attainable at reasonable operating conditions.

Efficiency of Ideal Systems

The generic EMAR cycle is based on three reactions, shown in Eq. 3-1, that occur in the absorber, the anode, and the cathode, respectively.

$$\begin{aligned} &\mathrm{Am(aq)} + m\mathrm{CO_2(g)} \rightleftharpoons \mathrm{Am(CO_2)_m(aq)} \\ &\frac{2}{m}\mathrm{Am(CO_2)_m(aq)} + \mathrm{Cu(s)} \rightleftharpoons \mathrm{CuAm^{2+}_{2/m}(aq)} + 2\mathrm{CO_2(g)} + 2\mathrm{e^-} \\ &\mathrm{CuAm^{2+}_{2/m}(aq)} + 2\mathrm{e^-} \rightleftharpoons \mathrm{Cu(s)} + \frac{2}{m}\mathrm{Am(aq)} \end{aligned} \tag{3-1}$$

'Am' represents a generic amine molecule and m is the number of CO_2 molecules captured per sorbent molecule, which is equal to the number of amine functional groups in the sorbent molecule divided by 2. The formation of bicarbonate is neglected due to the significant preference for carbamate formation by the primary and secondary amines. The two thermodynamic parameters that define the three reactions (of which only two are linearly independent) are the CO_2 binding constant of the first reaction, K_{CO2}, and the

stability constant of the amine complexation of the third reaction, β. The parameters K_{CO2} and β are defined in Eqs. 3-2 and 3-3, respectively.

$$K_{CO_2} = \frac{[\mathrm{Am(CO_2)_m}]}{[\mathrm{Am}]}\left(\frac{P_0}{P_{CO_2}}\right)^m \tag{3-2}$$

$$\beta = \frac{\left[\mathrm{CuAm}_{2/m}^{2+}\right]C_0^{2/m}}{\left[\mathrm{Cu}^{2+}\right][\mathrm{Am}]^{2/m}} \tag{3-3}$$

In these definitions, unit activity coefficients have been assumed. P_0 and C_0 represent standard state pressure and concentration, respectively.

Calculation of the Open-Circuit Potential

To determine the effects of amines and CO_2 on copper chemistry, we start with the Nernst equation for the Cu/Cu^{2+} redox couple; the formula is shown in Eq. 3-4.

$$E = E^0 + \frac{RT}{nF}\ln\left(\frac{\mathrm{Cu}^{2+}}{C_0}\right) \tag{3-4}$$

The open-circuit potential, E, is a function of the standard state potential, E^0, and the concentration of uncomplexed cupric ions. By combining the Nernst equation for copper oxidation with the definitions for K_{CO2} and β, the open-circuit potentials of the Cu/Cu^{2+} system with amines and CO_2 can be derived and is shown in Eq. 3-5.

$$E = E^0 + \frac{RT}{nF}\left[\ln\left(\frac{\mathrm{Cu}_0^{2+}}{C_0}\right) - \ln\left(1 + \frac{\beta}{C_0^{2/m}}\left[\frac{\mathrm{Am}_0 - (2/m)\mathrm{Cu}_0^{2+}}{1 + K_{CO_2}\left(P_{CO_2}/P_0\right)^m}\right]^{2/m}\right)\right] \tag{3-5}$$

Cu_0^{2+} is the total concentration of cupric ions in all forms and Am_0 is the total concentration of amines in all forms. The numerator expression in the square brackets of the second natural log represents the concentration of non-copper complexed amines. When the denominator is included, it represents the fraction of amine complexed by neither copper nor CO_2. The sum of the two natural log terms represents

the natural log of the uncomplexed copper concentration. It is implicit in this derivation that the copper/amine complex is significantly more favorable than the CO_2/amine complex.

The open-circuit potential difference between anodic conditions with a CO_2 partial pressure of P_A and cathodic conditions with no CO_2 present is obtained as the difference between the two corresponding potentials given by Eq. 3-5 with the appropriate pressures. If the solutions in the anode and cathode chambers have the same total cupric ion and amine concentrations, the difference in open-circuit potential can be represented by Eq. 3-6.

$$\Delta E = E_{anode} - E_{cathode} = \frac{RT}{mF} \ln \left[1 + K_{CO_2} \left(\frac{P_A}{P_0} \right)^m \right] \tag{3-6}$$

To arrive at Eq. 3-6, it has again been assumed that $\beta >> (K_{CO2})^{2/m}$. Since values for the stability constant are greater than 10^{18} for many polyamines, this assumption is valid. Eq. 3-6 demonstrates that the potential difference is solely a function of the CO_2 partial pressure, P_A, and the binding constant, K_{CO2}.

To convert the potential difference calculated in Eq. 3-6 to the work of separation per mole of CO_2, the charge required to separate one mole of CO_2 must be calculated. Based on the reactions shown in Eq. 3-1, one electron is required per molecule of CO_2, but, at equilibrium with finite values for K_{CO2}, not all amine molecules entering the anode will be complexed with CO_2. The inefficiencies, which exist even at equilibrium conditions (i.e., are not kinetic), from finite absorption and physical solubility must be included to properly calculate the total work of separation.

Calculation of Equilibrium Inefficiencies

The CO_2 loading fraction of the amines not complexed with copper, x_c, can be calculated through rearrangement of Eq. 3-2 with inclusion of a mass balance. At the liquid outlet of the absorber, the loading fraction, which is function of the flue gas partial pressure of CO_2, P_F, is shown in Eq. 3-7.

$$x_c = \frac{K_{CO_2} P_F^m}{P_0^m + K_{CO_2} P_F^m} \tag{3-7}$$

An additional inefficiency is caused by the physical solubility of CO_2 in the aqueous solution. Since the partial pressure of CO_2 in the anode may be considerably higher than the partial pressure in the absorber, some CO_2 will be retained in the solution even after the addition of cupric ions. The fraction of chemically bound CO_2 that is retained after desorption, x_p, calculated is calculated in Eq. 3-8 in terms of the Henry's coefficient, H_{CO2} and the molar volume of the solution, v_m.

$$x_p = \frac{P_A - P_F}{m H_{CO_2} v_m x_c \mathrm{Am}_0} \tag{3-8}$$

P_A and P_F refer to the anode and flue gas partial pressure of CO_2, respectively. If an additional flash stage were used to recover the CO_2 at atmospheric pressure rather than at the anode pressure, then P_A could be replaced with the ambient pressure in Eq. 3-8. Adding a second flash stage, however, would necessitate repressurizing the sorbent before sending it back to the cathode to avoid large pressure differences across the membrane.

Calculation of the Work and Efficiency of CO_2 Separation

By allowing for the inefficiencies caused by the incomplete conversion of amines at equilibrium in the absorber and the physical solubility of CO_2 in the aqueous solution, we can calculate the open-circuit work of separation of the EMAR system by combining Eqs. 3-6 to 3-8 and multiplying by Faraday's constant. The work of separation of CO_2, W_{CO2}, in an EMAR system at zero flux conditions is shown in Eq. 3-9.

$$W_{CO_2} = \frac{1}{x_c\left(1-x_p\right)} \frac{RT}{m} \ln\left[1 + K_{CO_2}\left(\frac{P_A}{P_0}\right)^m\right] \tag{3-9}$$

For a system with negligible physical solubility and large values of K_{CO2}, Eq. 3-9 becomes independent of m. This is not surprising since the number of amine groups per molecule should not limit the efficiency of the system.

The thermodynamic efficiency of the process, ε, obtained from the thermodynamically reversible work for a perfect separation divided by the actual work, is then given by Eq. 3-10.

$$\varepsilon = \left(\frac{K_{CO_2} P_F^m}{P_0^m + K_{CO_2} P_F^m} - \frac{P_A - P_F}{m H_{CO_2} v_m x_c \, \mathrm{Am}_0} \right) \frac{\ln\left(\frac{P_A}{P_0}\right) - \frac{P_0 - P_F}{P_F} \ln\left(1 - \frac{P_F}{P_0}\right)}{\frac{1}{m} \ln\left[1 + K_{CO_2}\left(\frac{P_A}{P_0}\right)^m\right]} \qquad (3\text{-}10)$$

The inherent irreversibilities of this process, which cause the efficiency in Eq. 3-10 to always be less than unity, are the instantaneous changes in the partial pressure of CO_2 between the absorber, the anode, and the cathode. Inclusion of x_c, which accounts for below unity CO_2 loading of the sorbent exiting the absorber, is necessary for a well-behaved efficiency function. If that factor were not added, Eq. 3-10 could yield efficiencies greater than one for small values of K_{CO2}, which would be physically unreasonable.

Figure 3-1 shows efficiency as a function of K_{CO2} for a diamine (m = 1) solution at 60°C with different anode pressures based on Eq. 3-10 with Am_0 = 4M and a flue gas CO_2 partial pressure of 0.15 bar. The efficiencies reflect the best possible efficiency achievable at equilibrium conditions. These values do not reflect the losses that will be associated with system dynamics. The highest efficiencies are obtained between 5 to 15 bars of pressure in the anode. Pressures beyond 15 bars lower the efficiency because of the increased physical solubility of CO_2 under these conditions.[153,154]

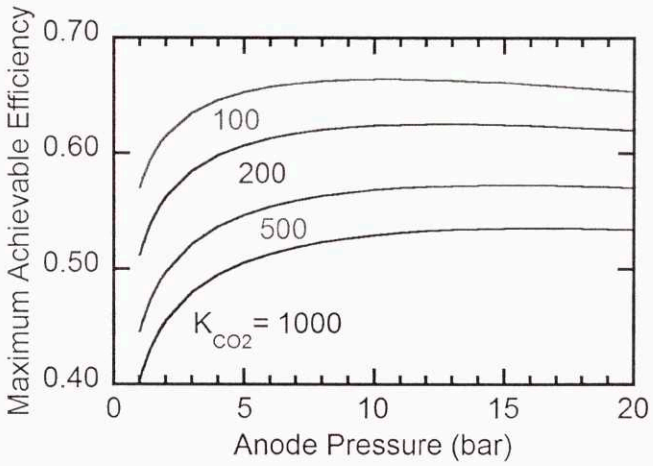

Figure 3-1. Maximum achievable efficiencies (versus a reversible process) for a diamine system at 60°C as a function of the anode pressure and the CO_2 binding constant, K_{CO2}.

The ideal range for K_{CO2} is from 100 to 500. Above 500, **Figure 3-1** shows that the best achievable efficiency drops to 55% or less. Below 100, the loadings achieved in the absorber will be quite low leading to large circulation rates of the sorbent. At optimal conditions, efficiencies between 60% and 70% can be obtained. Systems with lower flue gas CO_2 partial pressures, which would be found in the flue gas of a natural gas plant, could achieve open-circuit efficiencies over 70%.

Eq. 3-10 is based on the idealized scheme shown in Eq. 3-1. The formalism is convenient for demonstrating calculation of the maximum achievable efficiencies of the system in terms of fundamental thermodynamic parameters and will be used to model the EDA process. This approach could be applied to any scheme, though a closed-form solution may not be possible for more complicated reaction sequences. A derivation of the required work for amines that do not follow Eq. 3-1 based on measureable parameters is necessary to effectively compare different amines based on experiments.

Generalized Work and Efficiency Equations

Many amines will not follow the scheme in Eq. 3-1. Amines with a mixture of different primary, secondary, or tertiary amine groups, such as AEEA, DETA, and TETA, would have a more complex reaction scheme including multiple CO_2 containing adducts. Some amines, like amino acids salts, possess non-amine functional groups that can interact with the cupric ions to form different complexes. The scheme also neglects the possibility of bicarbonate formation, which is especially important for hindered and tertiary amines.

When deriving a more general form, both x_c and ΔE are left to be experimentally measured rather than expressed in terms of thermodynamic parameters, such as K_{CO2}. For a generalized system, the work of CO_2 separation and corresponding efficiency can be calculated with Eqs. 3-11 and 3-12, respectively.

$$W_{CO_2} = \frac{F\langle \Delta E \rangle}{x_c\left(1-x_p\right)} = \frac{F\langle \Delta E \rangle}{x_c - \dfrac{P_A - P_F}{m H_{CO_2} v_m x_c \mathrm{Am}_0}} \tag{3-11}$$

$$\varepsilon = \frac{RT}{F\langle \Delta E \rangle}\left(x_c - \frac{P_A - P_F}{m H_{CO_2} v_m x_c \mathrm{Am}_0} \right)\left[\ln\left(\frac{P_A}{P_0}\right) - \frac{P_0 - P_F}{P_F}\ln\left(1-\frac{P_F}{P_0}\right)\right] \tag{3-12}$$

As will be shown later in this chapter, x_c and the average potential difference, $<\Delta E>$, can be measured experimentally to determine the maximum achievable efficiencies for any amine under a given set of conditions. For EDA, it will be shown that Eqs. 3-10 and 3-12 are in agreement. With Eq. 3-10, however, a wide range of operating conditions can be evaluated with only a small set of data. Values for x_c and $<\Delta E>$ can be predicted from any temperature or pressure if the enthalpy and entropy of sorption is known.

Amine Utilization

An important advantage of the EMAR system is its high amine utilization, U_A, which is the fraction of amines that are used in each cycle around the system based on a carbamate mechanism, *i.e.*, one molecule of CO_2 per two amine functional groups. U_A is defined in terms of the molar flow rate of the amine sorbent, n_{CO2}, and the volumetric flow rate, Q, is Eq. 3-13.

$$U_A = \frac{1}{m} \frac{n_{CO_2}}{\mathrm{Am}_0 Q} \tag{3-13}$$

Based on previous definitions, the molar flow rate is defined in Eq. 3-14.

$$n_{CO_2} = x_c \left(1 - x_p\right) m Q \, \mathrm{Am}_0 \tag{3-14}$$

Combination of Eqs. 3-13 and 3-14 yields Eq. 3-15.

$$U_A = x_c \left(1 - x_p\right) \tag{3-15}$$

By inclusion of Eqs. 3-7 and 3-8, the amine utilization is calculated using known thermodynamic properties and system parameters in Eq. 3-16.

$$U_A = \frac{K_{CO_2} P_F^m}{P_0^m + K_{CO_2} P_F^m} - \frac{P_A - P_F}{m H_{CO_2} v_m x_c \, \mathrm{Am}_0} \tag{3-16}$$

The amine utilization depends on the CO_2 capacity and the work of separation depends on the CO_2 capacity and average potential difference. These parameters vary with the chosen amine and are strong functions of temperature with only a slight dependence on electrolyte composition or pressure. As described in the next section, these parameters have been measured experimentally and the maximum achievable efficiencies at 50°C are estimated using Eq. 3-12. The efficiency of an EDA system is also

estimated for a wider range of operating conditions using Eq. 3-10 with a temperature dependent function for K_{CO2} based on its standard state enthalpy and entropy.

Experimental Techniques for Thermodynamic Analysis

CO_2 Capacity Measurements

CO_2 capacity measurements were performed using 50 mL round bottom flasks. The flasks were filled with 40 mL of a given solution. The solutions were 2 N amine solutions with varying amounts of copper salt added. 1 M KNO_3 was added as a supporting electrolyte, though because these were not electrochemical experiments, its presence was unimportant. The setup is shown in **Figure 3-2**.

An inlet gas feed, which could contain N_2, CO_2, or a blend, and a gas outlet were built into the #4 rubber stopper used to close the 24/40 ground glass joint on the top of the round bottom flask. The rubber stopper was secured in place with parafilm. The inlet gas feel was connected to a tube that plunged most of the way into the flask, such that the gas bubbled through the solution before exiting. The outlet had no such tube to prevent liquid from exiting the flask. A Teflon-coated rounded stir-bar was used during all the experiments to vigorously stir the solutions at 500 rpm. The temperature of the flask was controlled by submerging all but the top of the flask in a temperature-controlled mineral oil bath.

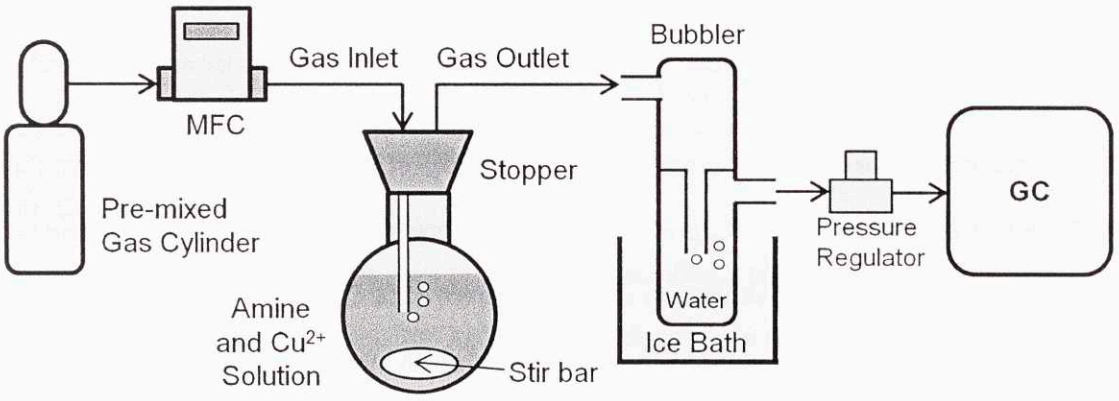

Figure 3-2. Schematic diagram of the experimental setup for CO_2 capacity measurements.

The gas outlet then led to a water bubbler that was submerged in an ice bath to condense out as much water and amine from the gas phase as possible. From there the solution went to a back pressure regulator

that maintained the flask at approximately 0.1 bar above atmospheric pressure. After the regulator, the gas traveled to a Varian CP-3800 Gas Chromatogram (GC) to measure its composition. The GC has a gas injection port that takes a small amount of gas for analysis. Details of the GC setup are:

- Method Filename: *Mike_noFIDslow_slow*
- Temperature: 40°C
- Sweep Gas: Helium
- Sweep Gas Pressure: P(t=0) = 15 psi *then* P(t>0.01) = 27.2 psi with dP/dt = 100 psi/min
- Injection at t = 0.05 minutes
- Detector: TCD (70°C , Filament temp = 120°C , range=0.5 , time constant = fast)

Sequences of runs were setup using the Galaxie software, which allowed for measurements about every 80 seconds. For each measurement, the software was used to automatically calculate the peak areas of the CO_2 and N_2 peaks. Those values were then exported to text files, which were later processed through a Matlab code.

Because CO_2 and N_2 have different thermal conductivities, the ratio of the peak heights was not exactly equal to the ratio of moles in the gas. To convert the CO_2 area fraction determined by the software, f_A, to the actual gas mole fraction, f_M, Eq. 9-1 was used.

$$f_m = \frac{f_A}{f_A + R_{TCD}(1 - f_A)} \qquad \text{Where } f_A = \frac{[\text{Area } CO_2]}{[\text{Area } CO_2] + R_{cut}[\text{Area } N_2]} \tag{3-17}$$

$$R_{TCD} = 1.1581 \quad , \quad R_{cut} = 1.0134$$

R_{TCD} accounts for the discrepancy in the thermal conductivities of the two gases. R_{cut} accounts for the small fraction of the nitrogen peak that gets cutoff due to the appearance of the CO_2 peak. These values were obtained through fitting and calibration using a premixed 15% CO_2 gas. These values agreed well with other mixes prepared by mixing pure CO_2 and N_2 streams with mass flow controllers.

To perform the capacity experiments, 15% CO_2 balance N_2 gas was flown through an Aalborg 0 to 50 sccm CO_2 mass flow controller. The actual flow rate of the gas mixture could be calculated by multiplying the measured value by 1.298. The target measured value was 50 sccm, which led to an actual

flow rate of 64.9 sccm (9.7 sccm CO_2). Prior to the experiment, N_2, was always used to purge all of the lines of any remaining CO_2. An example of the results from an experiment are shown in **Figure 3-3**.

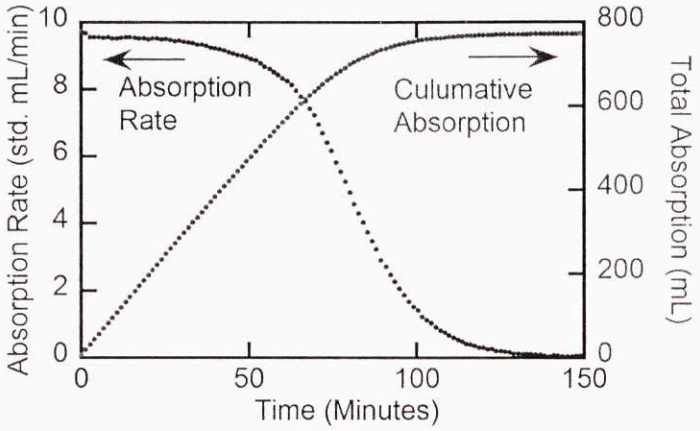

Figure 3-3. Results for a CO_2 capacity measurement run for 1M EDA with 0.125 M $Cu(NO_3)_2$ and 1M KNO_3 at 50°C.

When calculating the net CO_2 absorbed by the amines, the dead volume of the flask, lines, and physical solubility were subtracted out. For a 1M KNO_3 system at 50°C, this was measured to be 18.9 mL.

UV-Visible Spectra Measurements

The UV-Visible absorbance solutions were prepared with 10 mM $Cu(NO_3)_2$ and varying amine concentrations ranging from 30 to 120 mN. CO_2 saturated solutions were prepared by pre-saturating a concentrated amine solution then diluting it and adding the $Cu(NO_3)_2$. Measurements were taken with an Evolution 220 spectrophotometer from Thermo-Scientific in a quart cuvette with a path length of 1 cm. The respective amine/electrolyte solution with no copper was used as the blank.

Open-Circuit Experiments

Open-circuit potential measurements were made using a VersaStat 3 potentiostat from Princeton Applied Sciences. Results are with respect to a Ag/AgCl reference electrode in 3M NaCl solution (0.209 V versus SHE). The working electrode was a copper wire (note a counter is not necessary for open-circuit measurements). The setup can be seen in **Figure 3-4**.

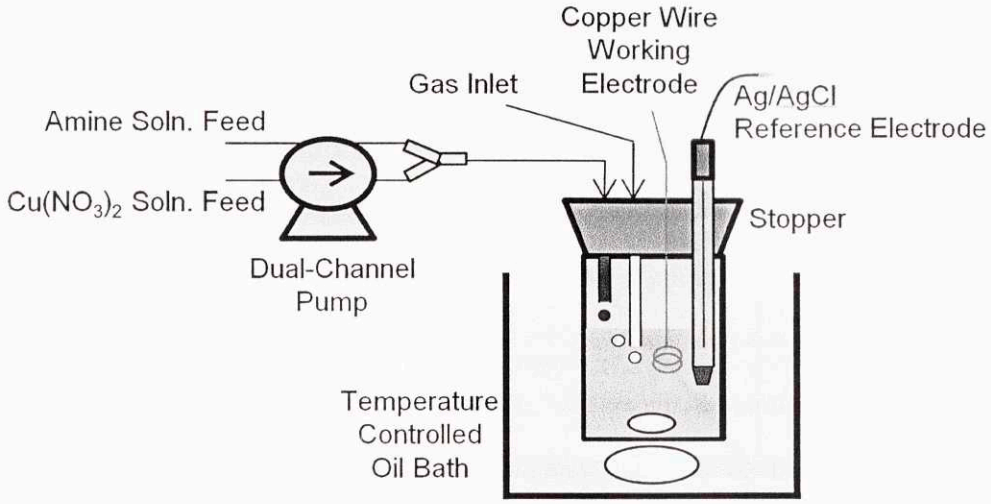

Figure 3-4. Schematic diagram of experimental setup for open-circuit potential measurements.

The starting solution was 5 mL of 10 mM $Cu(NO_3)_2$ with a 2 N amine solution and 1 M $NaNO_3$. Measurements spanning the range of copper loadings with constant amine concentration were performed by repeated injections of equal amounts of a 4N amine and 2M $NaNO_3$ solution and a 2M $Cu(NO_3)_2$ solution followed by a measurement for each new composition. An example of the raw data can be seen in **Figure 3-5**.

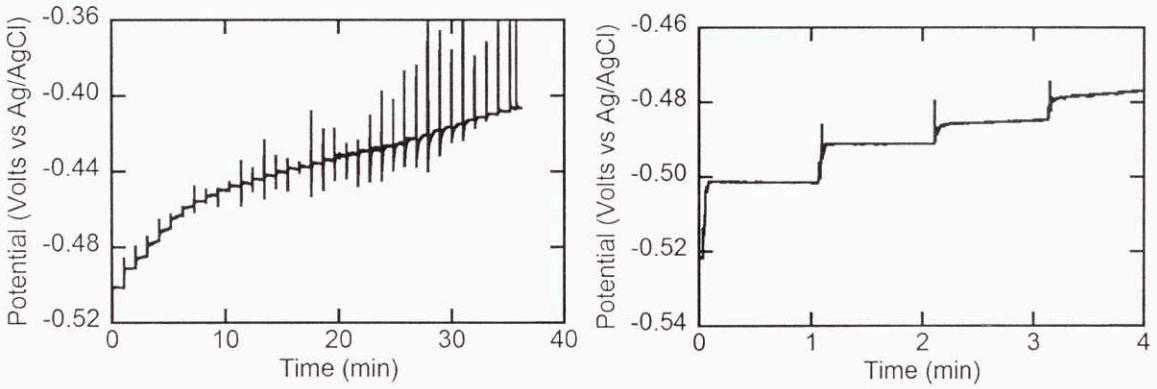

Figure 3-5. Plots showing raw data taken from open-circuit potential measurements of an EDA solution at 50°C under argon.

For measurements representing cathodic conditions, the system was kept under argon and an equilibration time of 60 seconds was given between injections. For measurements representing anodic conditions, the system was kept under pure CO_2 at atmospheric pressure and 240 seconds of equilibration time was given

between injections. The solutions were gently stirred at all times. Temperature was controlled by submerging the electrochemical cell in a temperature controlled oil bath.

The solution was contained in a standard VC-2 cell from BASi Analytical Instruments, which is designed for measurements of 5 to 10 mL samples. A modified #4 rubber stopper was used as the cell top. The working electrode, reference electrode, gas inlet, and liquid inlet were all connected through the rubber stopper. Injections were performed using a Masterflex pump with a dual-channel head programmed with an automatic interval injection program.

Efficiency of Real Systems

As described in the Chapter 2, fourteen different amines were originally considered for use in the EMAR process, including monoamines, amino acids, and polyamines. The ability of the polyamines to chelate copper ions and form stable copper complexes without the precipitation of salts that plagued the other amine candidates, especially in the presence of CO_2, argued for the selection of these polyamines for the EMAR process. The four amines shown in **Figure 3-6** were deemed the most promising and used for the initial experimental study described in this section.

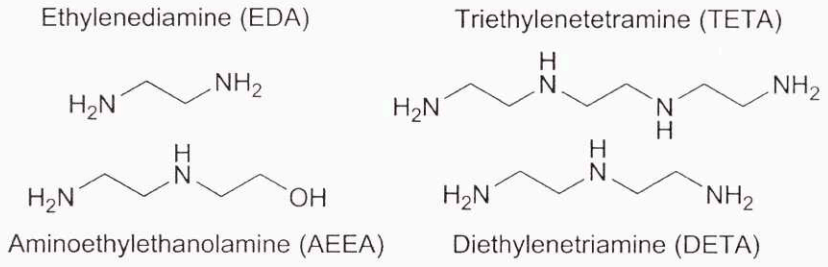

Figure 3-6. Structures of amines investigated in this chapter.

Carbon Dioxide Capacity Measurements

The CO_2 capacities of the four amines were determined at various copper loadings. Based on the assumption that the copper complex formation is significantly stronger than the CO_2 binding, the CO_2 loading, Θ, defined as the total moles of absorbed CO_2, $[CO_2]_{total,}$ relative to the full capacity of the amines for binding CO_2, $m\mathrm{Am}_0$, is expected to be a linear function of the copper loading, η, *i.e.*,

$$\Theta = \frac{x_c}{2}(1-\eta) \qquad \left(\Theta = \frac{1}{m}\frac{[CO_2]_{total}}{Am_0} \quad , \quad \eta = \frac{2}{m}\frac{Cu_0^{2+}}{Am_0} \right) \tag{3-18}$$

The copper loading is defined similarly to the CO_2 loading, except that the total capacity of the amines for copper is just half that for CO_2. The use of loading, rather than concentration, allows for easier comparison of the behavior of different polyamines. The CO_2 loading fraction in the absence of cupric ions, x_c, is given by 2Θ as the copper loading approaches zero.

$$x_c = 2\Theta(\eta \to 0) \tag{3-19}$$

The CO_2 capacity of the different amines as a function of copper loading was measured at 50°C using a 15% CO_2 gas mixture; a detailed description of the experimental method can be found in the Appendix. The results shown in **Figure 3-7** are in excellent agreement with Eq. 3-17 for EDA, TETA, and AEEA.

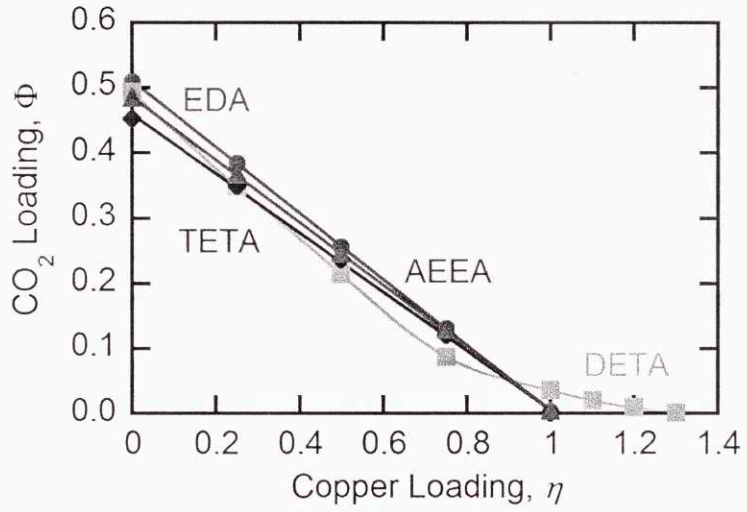

Figure 3-7. Equilibrium CO_2 capacity data of amine solutions as a function of copper loading at 50°C contacted with 15% CO_2 gas stream. Lines are linear fits for EDA, AEEA, and TETA, and a spline for DETA.

The y-intercept values for DETA, TETA, and AEEA below 0.5 indicate that the sorbents are not fully loaded with CO_2 at 50°C, *i.e.*, $x_c < 1.0$; this incomplete loading can be attributed to the presence of unreacted secondary amine groups. The intercept for EDA, which has no secondary amines, is above 0.5 owing to the formation of a small quantity of bicarbonate, as is commonly observed for primary amines such as MEA.

Of the four amines tested, EDA shows the highest CO_2 capacity. The loading of EDA with CO_2 as a function of copper loading was also determined at 70°C; the value of x_c was observed to drop from 1.02 at 50°C to 0.92 at 70°C showing the expected significant temperature dependence of the CO_2 reactions with this amine (data not shown). The loading results correspond well with previous literature reports for EDA[54] and AEEA,[61] indicating that the slight differences in conditions from a thermal system, such as the presence of nitrate salts, are inconsequential for CO_2 capacities.

The significant deviation of DETA's CO_2 loading from Eq. 3-17 suggests that one or more of the assumptions is incorrect for this triamine. **Figure 3-7** shows that at low loadings, DETA follows a linear trend with a slightly steeper slope than observed with the other amines. Previous studies have shown that at low copper loadings, DETA complexes cupric ions with a 2:1 ratio and may interact with up to 6 sites.[155,76] The presence of 2:1 complexes is supported by the breakdown of the linear trend at around η = 2/3, which corresponds to a 2:1 ratio of DETA to Cu^{2+} molecules. The slope of the DETA curve at low loadings indicates that each cupric ion disrupts the CO_2 absorption of approximately 4.5 amine sites.

At loadings higher than 0.67, the complexes begin converting from the 2:1, where some CO_2 affinity remains, to 1:1 complexes where the DETA is more tightly bound and no CO_2 can be absorbed. At η = 4/3, all of the DETA is complexed at the 1:1 ratio, which, as can be seen in **Figure 3-7**, leads to complete CO_2 desorption.

UV-Visible Spectroscopy

The ratio of copper to amine species within the complexes under different copper loadings and in the presence and absence of CO_2 was investigated by UV-Visible absorbance spectrophotometry. Details of

the experimental procedure can be found in the Appendix. Spectra for the four amines are shown in

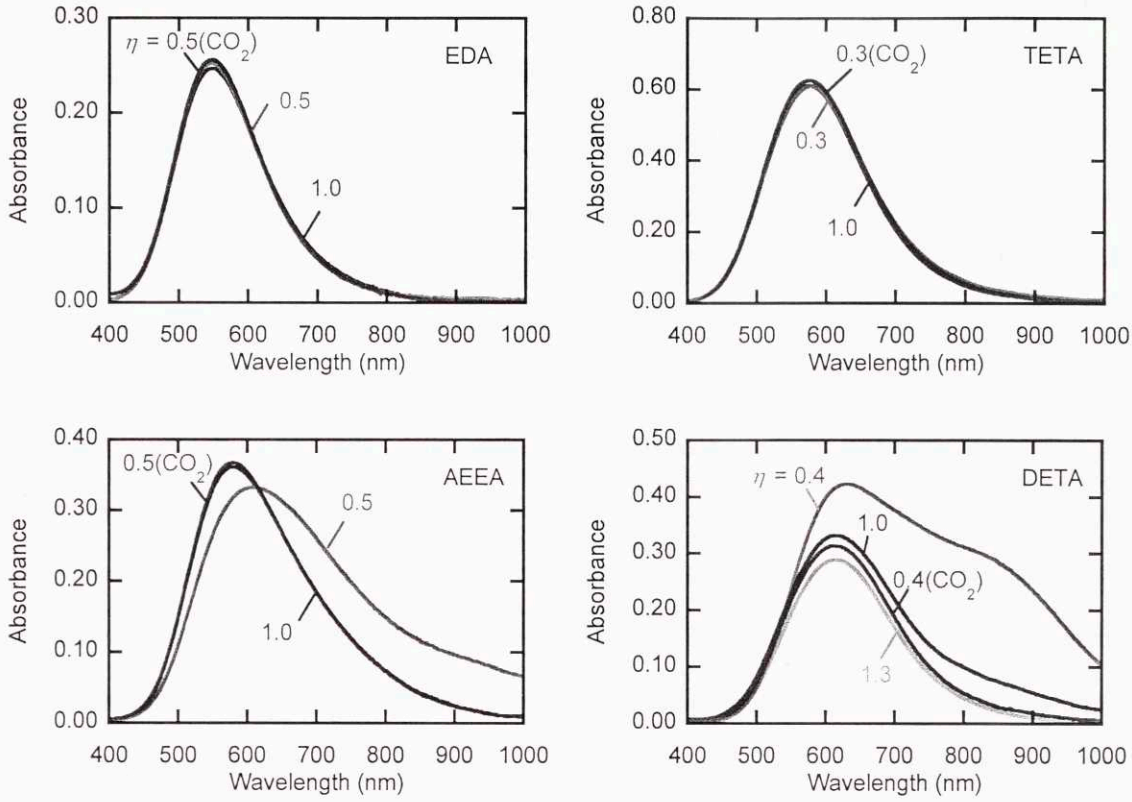

Figure 3-8 under conditions of full copper loading ($\eta = 1$), and excess amine conditions ($\eta < 1$) with and without CO_2. For DETA, an additional spectrum is shown where equimolar amounts of cupric ions and DETA are present ($\eta = 4/3$). Spectroscopic data are widely available in the literature for amine/copper complexes in the absence of CO_2, and show that cupric ions usually interact with four amine functional groups.[156,83]

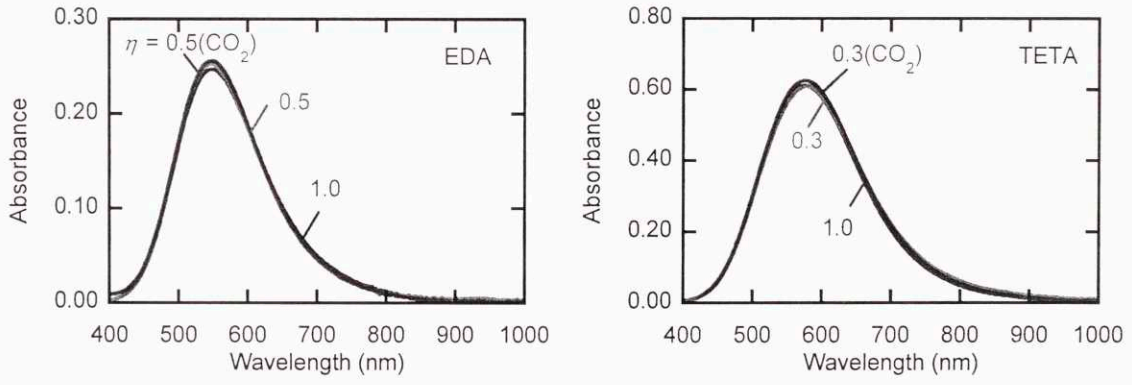

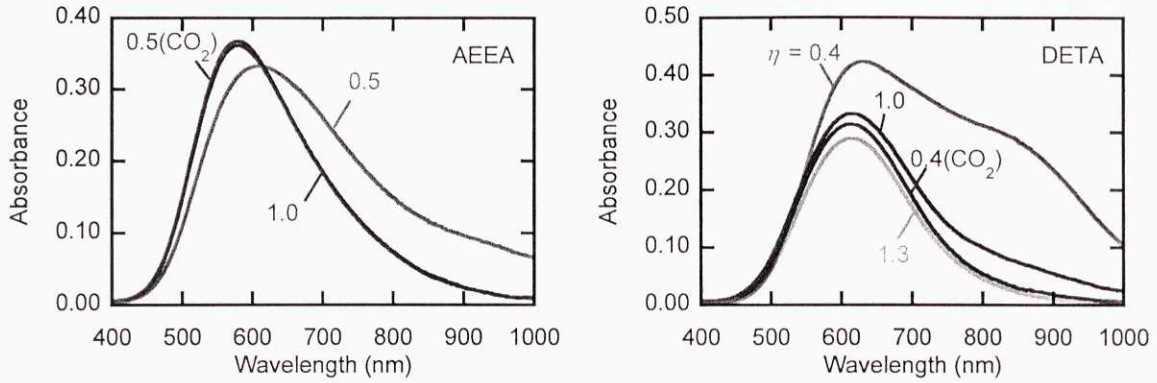

Figure 3-8. UV-Visible absorption spectra for EDA, TETA, AEEA, and DETA under different copper loadings and in the presence and absence of CO_2. Numbers represent the copper loading for each curve.

For EDA and TETA, the 4:1 amine functional group to copper complex is dominant as long as the copper loading is not greater than 1. Upon addition of CO_2, no discernible shifts in the spectra occur, confirming the assumption that the copper complexation is significantly more favorable than CO_2 binding for EDA and TETA.

For AEEA, the spectrum does vary with copper loading in the absence of CO_2. Previous investigations show that at high amine to copper ratios, the alcohol group deprotonates to form different complexes.[83] When saturated with CO_2 or when copper loading equals 1, the spectra are nearly identical. This indicates that the presence of CO_2 causes the formation of the 2:1 AEEA to Cu^{2+} complexes and inhibits deprotonation of the alcohol group, most likely due to the significantly reduced pH that results from CO_2 saturation.

For DETA with excess amine ($\eta = 0.4$), a significant shoulder is observed between 800 and 900 nm. The presence of CO_2 causes the disappearance of the shoulder and the corresponding spectrum instead resembles the curve for $\eta = 1.3$. This indicates a significant change in the complex being formed and supports the capacity results, which demonstrated the disruption of 4.5 amine sites per cupric ion and not 5 or 6, which would be expected based on the types of complexes that form in the absence of CO_2.[85]

Open-Circuit Potential Measurements

The CO_2 capacity measurements demonstrate that the CO_2 release can be controlled by modulation of the cupric ion concentration in the solution. Measurements of the open-circuit potential differences between a copper electrode under anodic and cathodic conditions provide an estimate of the energy requirements for cupric ion generation and removal under low flux conditions. We can estimate the efficiency of the separation using Eq. 3-12 with the value of x_c determined in the capacity experiments and the potential difference, $<\Delta E>$, obtained from the open-circuit experiments. Overpotentials due to electrochemical kinetics at the electrodes and concentration polarization in the solution will be included in Chapters 4 and 5, respectively. A detailed description of the open-circuit experiments can be found in the Appendix.

The open-circuit potentials of a copper electrode in 2N amine solutions under argon solutions with 1M $NaNO_3$ as a function of cupric ion loading are shown in **Figure 3-9**. Cupric ion concentration was controlled through the addition of cupric nitrate, $Cu(NO_3)_2$.

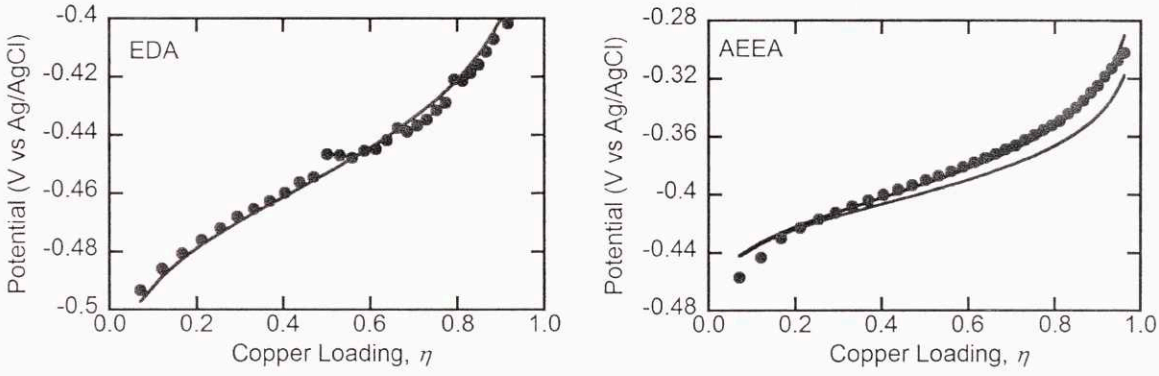

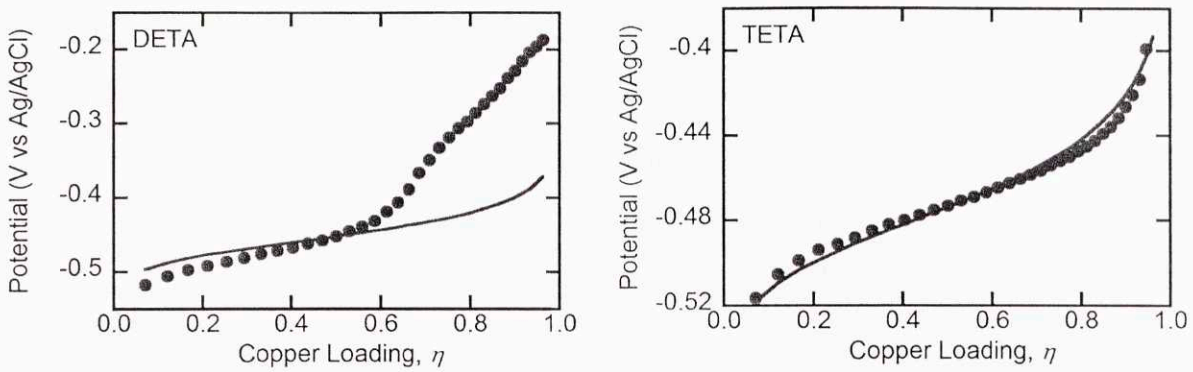

Figure 3-9. Open-circuit potentials of copper in 2N amine solutions with varying copper loadings. The solid red lines are defined in Eq. 3-19. The blue line is defined by Eq. 3-20.

The solid red lines in **Figure 3-9** represents are defined by Eq. 3-19 with β as the lone fitted parameter.

$$E = E^0 + \frac{RT}{nF}\left[\ln\left(\frac{Cu_0^{2+}}{C_0}\right) - \ln(\beta) - \frac{2}{m}\ln\left(\frac{Am_0 - (2/m)Cu_0^{2+}}{C_0}\right)\right] \tag{3-20}$$

This model equation can be derived readily by combining Eqs. 3-3 and 3-4, and invoking the assumption that $\beta >> 1$. The standard state is defined as a one molar solution of cupric ions with no amines present. The corresponding value for E^0 with respect to the 3M NaCl Ag/AgCl reference electrode (0.209 volts versus SHE) is -0.131 volts. Using this model, we determined the value of the stability constant of EDA at 50°C to be 1.8×10^{18}, which agrees well with literature value of 3.0×10^{18} at 49°C estimated from the results of Cotton and Harris.[85]

While Eq. 3-19 is effective at modeling the open-circuit potential dependence on copper loading, the equation fails for both AEEA and DETA due to their more complex reaction mechanisms. For AEEA, where the pH affects its ability to chelate copper with its hydroxyl group, there is an additional dependence on the amount of free amine in the solution that is not captured in Eq. 3-19. Eq. 3-20 allows for a second fitted parameter, ω, to increase the flexibility of the model to account for such phenomena.

$$E = E^0 + \frac{RT}{nF}\left[\ln\left(\frac{Cu_0^{2+}}{C_0}\right) - \ln(\beta) - \omega\ln\left(\frac{Am_0 - (2/m)Cu_0^{2+}}{C_0}\right)\right] \tag{3-21}$$

The blue line in the AEEA plot of **Figure 3-9** is derived from Eq. 3-20 with $\omega = 2.6$. If $\omega = 2$, Eq. 3-20 would be equivalent to Eq. 3-19. **Table 3-1** shows fitting results for open-circuit experiments performed at 50°C with 1M $NaNO_3$ for each of the four amines both under argon and CO_2.

Table 3-1. Fitting results from open-circuit potential measurements.

	Argon			CO_2			K_{CO2}**
	β (3-19)	β (3-20)	ω	β (3-19)	β (3-20)	ω	
EDA	1.64E+18	1.47E+18	1.91	1.29E+12	1.11E+12	1.87	1127
AEEA	1.52E+16	3.20E+16	2.61	3.96E+10	5.05E+10	2.20	620
DETA*	3.47E+18	1.65E+20	6.01	1.34E+11	6.54E+11	3.65	5092
TETA	2.93E+19	2.94E+19	2.00	7.93E+13	7.93E+13	2.26	608

* DETA fit only from $\eta = 0$ to $\eta = 0.67$

** K_{CO2} calculated from Eq. 3-21

For EDA, TETA, and AEEA under CO_2, the values of ω are close to two, indicating that Eq. 3-19 is an effective model. For DETA and AEEA under argon, Eq. 3-19 is not valid. These findings agree with the previous spectroscopic and CO_2 capacity results and observations from literature. The values for K_{CO2} in **Table 3-1** are calculated with Eq. 3-21. This can be quickly derived comparing Eq. 3-5 and Eq. 3-19 with the assumption that $K_{CO2} >> 1$. The results are only strictly valid for systems that follow Eq. 3-19.

$$K_{CO_2} = \sqrt{\frac{\beta_{Ar}}{\beta_{CO_2}}} \tag{3-22}$$

In Eq. 3-21, β_{Ar} and β_{CO2} represent the values of β under environments of argon and CO_2, respectively. AEEA and TETA demonstrate significantly lower binding affinity for CO_2 because half their amine groups are secondary. The surprisingly high K_{CO2} value for DETA is most likely caused by the inability of Eq. 3-21 to appropriately handle the DETA's different complexation mechanism.

The open-circuit copper potentials of the amine solution in the presence and absence of CO_2 are shown as a function of copper loading in **Figure 3-10**. These blue and red curves represent the anodic and cathodic conditions, respectively, of an EMAR process that desorbs at 1 atmosphere. The top x-axis shows the state of charge (SOC) of the system, in units of Coulombs, calculated from Eq. 3-22. A larger state of charge indicates a more oxidized system.

$$\text{State of Charge} = SOC = 2F\,\text{Cu}_0^{2+} = mF\text{Am}_0\eta \tag{3-23}$$

The area between the anodic and cathodic curves based on the SOC x-axis equals the work of a single cycle, in direct electrochemical analogy with the well-known cycle areas in PV and TS diagrams.

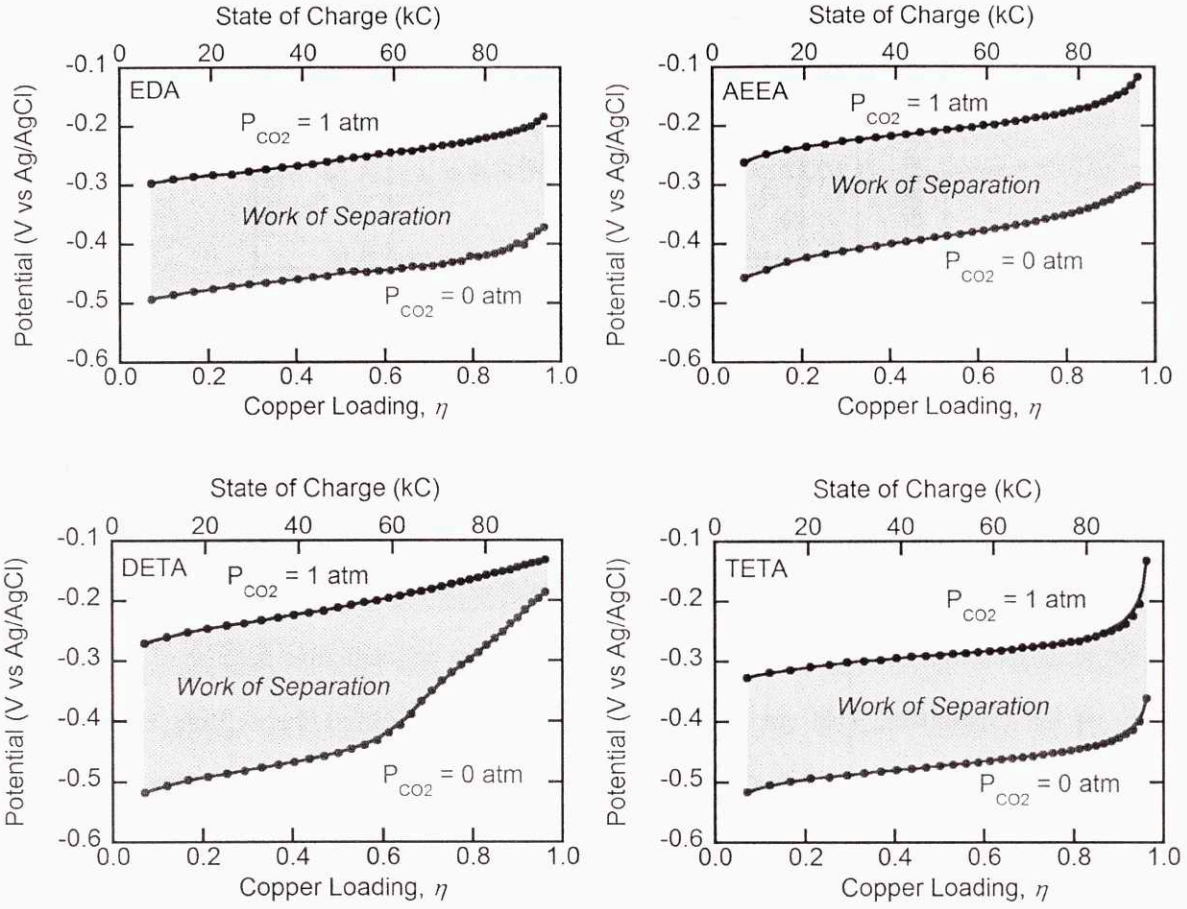

Figure 3-10. Open-circuit potential plots as a function of copper loading and state of charge. Areas defined by the top x-axis represent the work of separation of an EMAR cycle.

The average potential difference, used in Eq. 3-12, can be obtained from **Figure 3-10** as the average distance between the two curves. Mathematically, the average potential is defined in Eq. 3-23, in which SOC_{MAX} and SOC_{MIN} refer to the maximum and minimum states of charge in the system, respectively.

$$\langle \Delta E \rangle = \frac{1}{(SOC_{MAX} - SOC_{MIN})} \int_{SOC_{MIN}}^{SOC_{MAX}} (E_{anode} - E_{cathode})\, dSOC \tag{3-24}$$

Figure 3-11 compiles the results from **Figure 3-10** and shows the differences in anodic and cathodic potentials for the four amines as a function of copper loading.

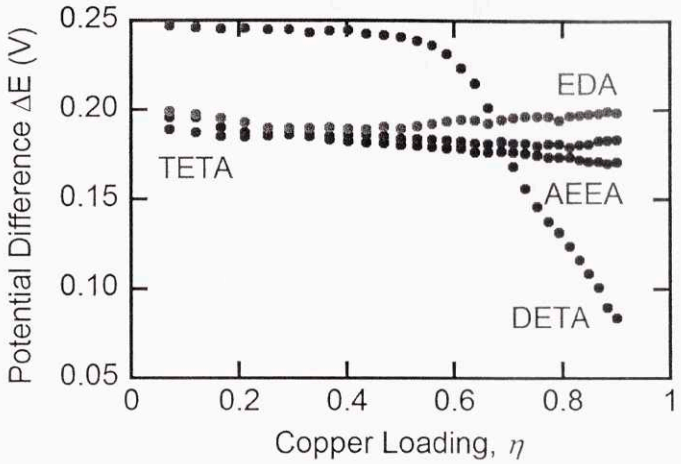

Figure 3-11. Open-circuit potential differences for EDA, TETA, AEEA, and DETA as a function of copper loading.

The potential differences for EDA and TETA are relatively constant, and show no clear variations over the copper loading range. AEEA, however, shows a noticeable decrease in the potential difference with increasing copper loading because the pH, and thus the stability constant, decreased in the absence of CO_2 but not in its presence. In the presence of CO_2, the pH changes are negligible because of the buffering ability of the carbamates. This can be seen in the decrease of values for ω from argon to CO_2 environments for AEEA in **Table 3-1**. By contrast, pH changes do not affect the stability constants of EDA and TETA since they do not have alcohol groups that can deprotonate.

DETA shows a dramatic drop in potential difference at loadings greater than 0.67 owing to the previously discussed transition from a 2:1 DETA to Cu^{2+} binding regime, where CO_2 has a dramatic effect on the copper complex, to the 1:1 binding regime, where the presence of CO_2 is less impactful.

Effects of Chloride Salts

The significant interactions between cupric and, especially, cupreous ions with chloride ions is well documented. Open-circuit potential measurements were taken with 1M NaCl in lieu of the 1M $NaNO_3$ electrolyte. The results, shown in **Figure 3-12**, demonstrate that chloride salts may have some mild effects, but do not significantly alter the thermodynamics of an EDA system. Further measurements would be required to determine if the slight 10 to 20 mV shifts in the curves are statistically significant.

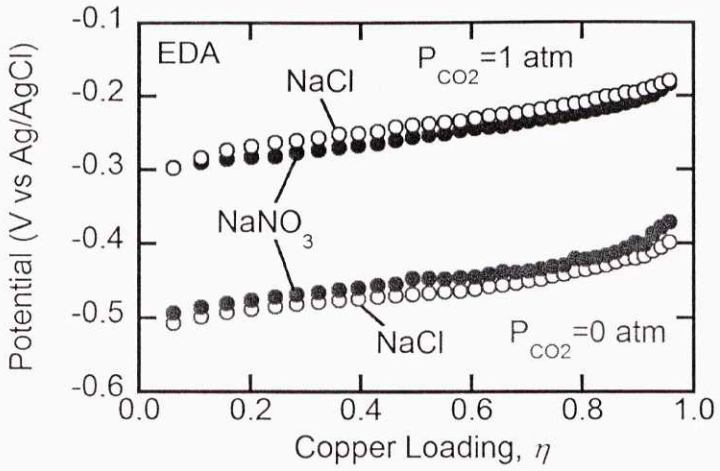

Figure 3-12. Comparison of open-circuit measurements in an EDA system with different electrolytes: 1M $NaNO_3$ (closed circles) and 1M NaCl (open-circles).

Experimentally-Derived Efficiency of CO_2 Separation

The efficiency of an open-circuit EMAR process is tabulated in **Table 3-2** for each of the four amines at 50°C, and for EDA at 70°C. The tabulated efficiencies were calculated from Eq. 3-12 with parameters estimated experimentally through Eqs. 3-18 and 3-23, and under the assumption of desorption at 1 atmosphere of pressure and absorption from a 15% CO_2 flue gas. The efficiency is based on removal of 100% of the CO_2 from the flue gas.

Table 3-2. Predicted open-circuit performance of an EMAR system using different amines with 1 atm CO_2 desorption and 15% CO_2 flue gas.

Amine	x_c [a]	x_p	$\langle \Delta E \rangle$ [b]	W_{CO2} [c]	ε_{rev} [d]
EDA (70°C)	0.93 ± 0.03	0.003	0.142	14.7	0.54
EDA (50°C)	1.02 ± 0.01	0.004	0.194	18.4	0.41
AEEA (50°C)	0.98 ± 0.01	0.004	0.180	17.9	0.42
TETA (50°C)	0.92 ± 0.02	0.005	0.183	19.2	0.39
DETA (50°C)[e]	1.08 ± 0.09	0.004	0.238	21.4	0.35

[a] Calculated from Eq. 17. [b] In units of volts. [c] Calculated from Eq. 11 in units of kJ/mole. [d] Calculated from Eq. 12. [e] For η equals 0 to 0.67.

Table 3-2 shows that at 70°C, an EMAR system using EDA as the amine sorbent should be able to achieve 54% efficiency under open-circuit conditions. This represents a work of separation, W_{CO2}, of 15 kJ/mole as calculated by Eq. 3-11. At lower temperatures, the efficiency drops to 41% and is relatively similar for EDA, AEEA, and TETA, ranging from 39% to 42%. The efficiency loss due to the physical solubility of the CO_2 is negligible in every case because of the low desorption pressure. While the

absorption capacity for CO_2 does drop by about 10% at the higher temperature for EDA, the open-circuit potential required drops by 20%, making the higher temperature more efficient. The importance of operating temperature is highlighted clearly by **Table 3-2**. To obtain estimates of efficiency for a wider range of conditions, we will combine Eq. 3-10 with the temperature dependence of K_{CO2} for EDA.

Analysis of EDA Thermodynamics

With the aid of Eq. 3-4, it is possible to relate the open-circuit potential difference to the CO_2 binding constant, K_{CO2}, which is sufficient to predict the system-wide efficiency under different absorption and desorption partial pressures. This approach, however, can only be applied rigorously to EDA, which follows the simple reaction mechanism shown in Eq. 3-1 at flue gas conditions. The equilibrium constant can also be used to calculate the free energy of the CO_2 absorption reaction via Eq. 3-6, which can be rearranged into Eq. 3-24 to solve for K_{CO2} as a function the standard state free energy of sorption, ΔG_{CO2}^{0} where it is recognized that for EDA, $m = 1$.

$$K_{CO_2} = \exp\left(\frac{-\Delta G^0_{CO_2}}{RT}\right) = \frac{P_0}{P_{CO_2}}\left[\exp\left(\frac{F\Delta E}{RT}\right) - 1\right] \tag{3-25}$$

To predict the performance of an EDA system over a range of temperatures, the standard state enthalpies and entropies of reaction must be known. These quantities can be extracted from measurements of the open-circuit potential difference over a range of temperatures. **Figure 3-13** shows the potential difference values for an EDA system from 50°C to 80°C.

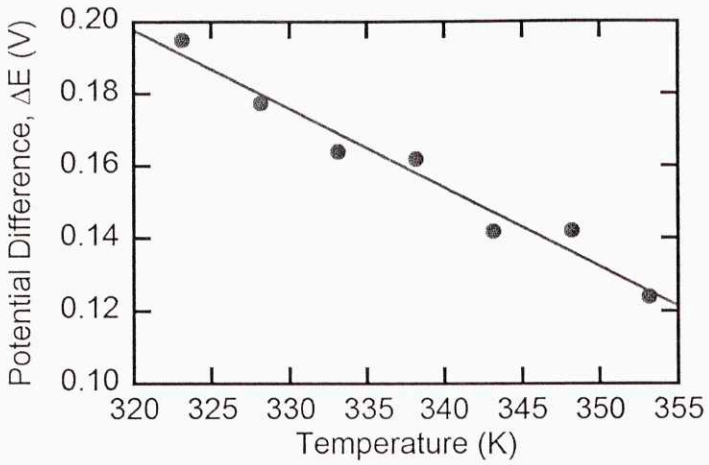

Figure 3-13. Average open-circuit potential difference between anodic (P_{CO2} = 1 atm) and cathodic (P_{CO2} = 0) conditions as a function of temperature for an EDA system with 1M EDA, 1M $NaNO_3$.

If it is assumed that $K_{CO2}P_{CO2}/P_0 >> 1$, then manipulation of Eq. 3-24 and expression of the free energy in terms of the enthalpy, ΔH^0, and entropy, ΔS^0, yields a linear relationship, shown in Eq. 3-25, between the potential difference and the temperature at constant pressure.[148,87]

$$\Delta E = \frac{RT}{F}\ln\left(\frac{P_{CO_2}}{P_0}\right) - \frac{\Delta G^0_{CO_2}}{F} = \frac{RT}{F}\ln\left(\frac{P_{CO_2}}{P_0}\right) - \frac{\Delta H^0}{F} + R\frac{\Delta S^0}{F} \tag{3-26}$$

Note that for an ideal EDA system, the potential difference should not be a function of copper loading, and hence ΔE and $<\Delta E>$ are analogous. Assuming the standard state enthalpy and entropy are not functions of temperature, we can differentiate all terms with respect to temperature to yield Eq. 3-26.

$$\frac{d\Delta E}{dT} = \frac{\Delta S^0}{F} + \frac{R}{F}\ln\left(\frac{P_{CO_2}}{P_0}\right) \tag{3-27}$$

Through rearrangement at constant pressure, Eq. 3-27 shows that the entropy of the CO_2 sorption reaction can be determined from the derivative of the difference in potentials with respect to temperature.

$$\Delta S^0 = F\frac{d\Delta E}{dT} - R\ln\left(\frac{P_{CO_2}}{P_0}\right) \tag{3-28}$$

The value of the derivative can be obtained through linear regression of the data in **Figure 3-13**. The enthalpy can then be calculated using Eq. 3-28 in terms of this derivative and the potential difference itself. This result can also be obtained easily through the Gibbs-Helmholtz equation.

$$\Delta H^0 = FT\frac{d\Delta E}{dT} - F\Delta E \tag{3-29}$$

In using Eq. 3-28 to obtain a temperature independent enthalpy, values for ΔH^0 would have to be calculated at each temperature and then averaged. Using the data in **Figure 3-13**, Eq. 3-28 yields an enthalpy of sorption of 86.4 $\pm$ 1.1 kJ/mole CO_2, which agrees with data reported by Zhou.[54]

Using these experimentally determined thermodynamic parameters, we can calculate the expected value of K_{CO2} over the relevant operational range of temperatures, which is shown in Figure **3-14**. The tan area represents the 95% confidence interval based on using a Student t-distribution to calculate the uncertainty of ΔE as a function of temperature using standard linear regression techniques.

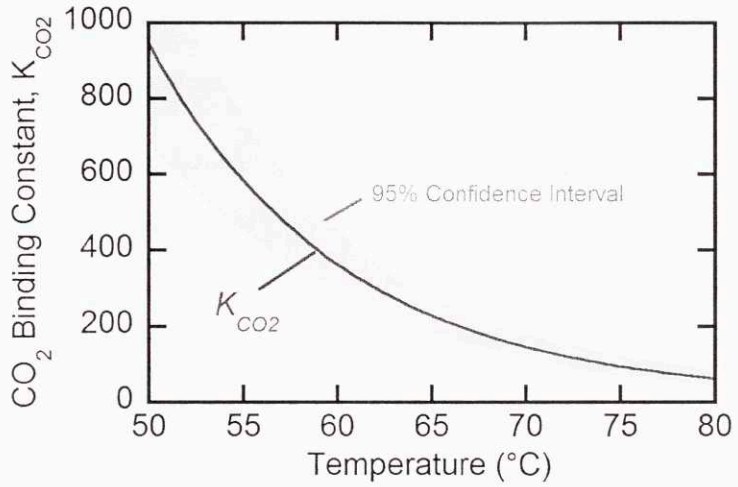

Figure 3-14. Expected value of the CO_2 equilibrium binding constant for EDA as a function of temperature. The tan area represents the 95% confidence interval based on a Student t-distribution.

At 50°C, the expected value for K_{CO2} is 947, which is in reasonable agreement with the estimate of 1127 in **Table 3-1**. The expected values of K_{CO2} can also be used with Eq. 3-10 to predict efficiencies at 50°C and 70°C, the temperatures at which experimental data are reported in **Table 3-2**. The calculated efficiencies are 0.41 at 50°C and 0.54 at 70°C are in excellent agreement with the measured values. These results demonstrate that this model can effectively predict performance over the relevant operational range for EDA. The model does not rely on the absorption capacity measurements previously used to calculate x_c but instead uses the predicted values of K_{CO2} to calculate x_c through Eq. 3-7. The ability to

predict K_{CO2} allows the calculation of efficiency under any set of flue gas conditions, electrochemical cell temperature, and desorption pressure based on simple and inexpensive electrochemical experiments.

This represents the first time copper activity measurements have been used for calculation of amine/CO_2 sorption equilibria and the corresponding thermodynamic parameters. These copper activity measurements, which are significantly cheaper and easier to run than are alternative methods, provide slightly different information than obtained from traditional barium salt titrations. Titrations measure the total dissolved CO_2, whereas the copper activity indicates the fraction of uncomplexed amines. In many cases this information will be analogous; however, there may be some cases where a combination of the two methods can lead to an improved understanding of the CO_2 complexed species.

Optimal EMAR Operating Conditions

With the model developed in Eq. 3-10 and the experimentally determined thermodynamic parameters for K_{CO2}, the EDA system efficiency can be calculated for a wide range of temperatures, desorption pressures, and flue gas compositions.

Figure 3-15 shows the efficiency from 50°C to 80°C and from 1 to 18 bar of desorption pressure for a 15% CO_2 flue gas, which is representative of a coal-fired power plant. **Figure 3-16** shows the same efficiency calculations for a plant with a 5% CO_2 flue gas, which is representative of a natural gas combined cycle (NGCC) plant. The efficiencies for the NGCC case are uniformly higher, but the amine utilization (shown by the black contour lines) is lower. Lower operating temperatures will also be preferable in a natural gas plant.

While the efficiency will be lowered by kinetic losses and auxiliary equipment power demands, initial efficiencies for the coal plant, with an amine utilization of 0.9, of 69% at 8 bars and 76°C and 63% at atmospheric pressure and 80°C, are encouraging. A comparable MEA process would have a theoretical efficiency of 62% assuming absorption at 60°C and regeneration at 120°C.

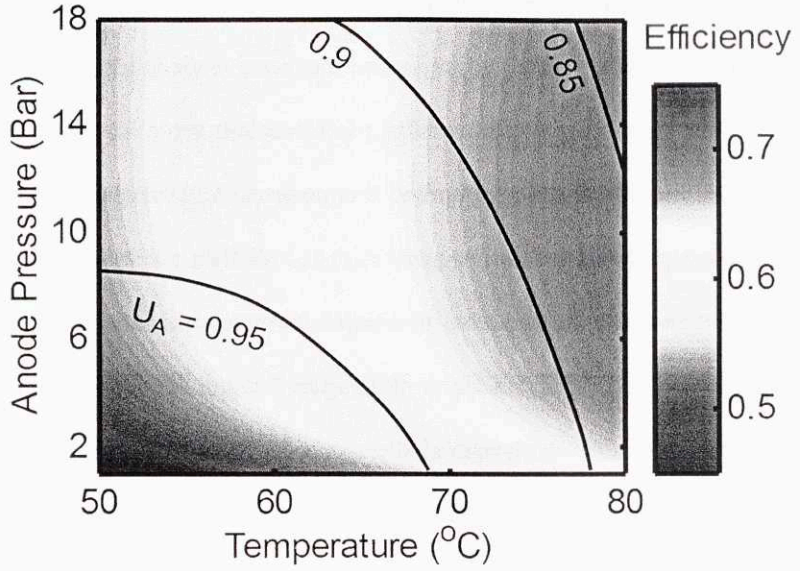

Figure 3-15. Open-circuit efficiency of the EMAR system with a 15% CO_2 flue gas based on experimentally derived K_{CO2} values and Eq. 3-10. Black lines are contours of amine utilization, U_A, from Eq. 3-16.

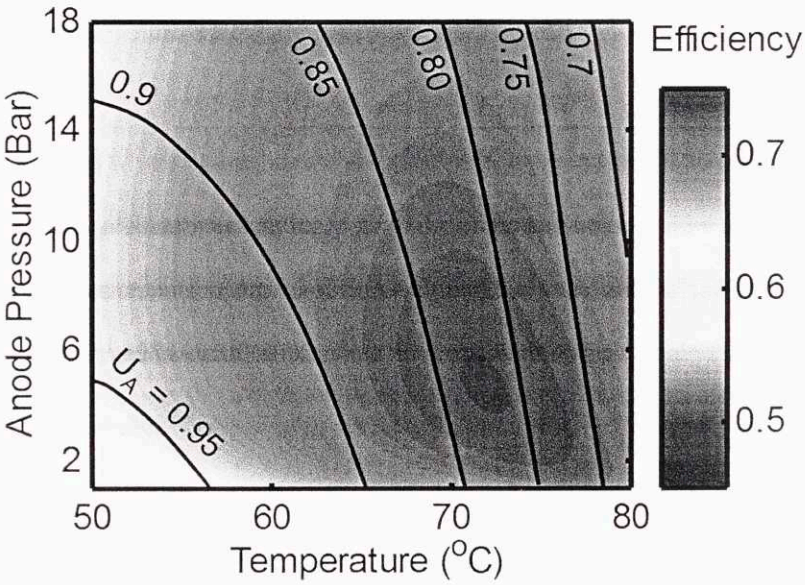

Figure 3-16. Open-circuit efficiency of the EMAR system with a 5% CO_2 flue gas based on experimentally derived K_{CO2} values and Eq. 3-10. Black lines are contours of amine utilization, U_A, from Eq. 3-16.

Conclusions of EMAR Thermodynamics

- The performance of a decoupled EMAR system is heavily dependent on the strength of CO_2 binding, and not dependent on the stability constant for copper complexation.
    - A system that follows the scheme in Eq. 3-1 has an efficiency defined by Eq. 3-10.
    - A general definition of efficiency, applicable to almost any system is found in Eq. 3-12.
- Based on Eq. 3-10, systems with efficiencies around 70% with respect to a fully-reversible process are achievable.
- Experimental results show that EDA, AEEA, and TETA, all show a linear dependence between CO_2 capacity and copper loading, as expected.
- Experimental results show that the difference in potential from anodic to cathodic conditions is relatively constant for EDA, AEEA, and TETA, as expected.
- At 50°C and ambient pressure, EDA, AEEA, and TETA, can operate at 40% efficiency at open-circuit. At 70°C and ambient pressure, EDA can operate above 50% efficiency.
- Based on the calculated thermodynamic parameters for EDA, the open-circuit efficiency at any set of conditions can be calculated. Efficiencies near 70% are achievable at realistic operating conditions.
- The standard state enthalpy and entropy of CO_2 sorption for EDA was obtained using copper activity experiments, demonstrating a measurement technique never previously attempted for any amine.

A significant fraction of the figures and analysis in this chapter is adapted with the permission of the Royal Society of Chemistry.[152]

Chapter 4

Electrochemical Kinetics of EMAR

This chapter describes the characterization of the required electrode overpotentials as a function of current density for different sorbent compositions and operating conditions. This does not account for concentration overpotentials due to transport limitations or overpotentials due to the Ohmic resistance of the solution or membrane. As was discussed in the introduction, only limited work has been done to characterize the kinetics of copper in amine solutions, and the effects of CO_2 saturation has never been previously considered.[71,69]

The chapter begins with a discussion on different analytical strategies for measuring kinetics. Following previous studies in literature on copper kinetics in acidic systems, fast galvanostatic pulses were chosen. A detailed description of how the dynamics of the pulses are analyzed is then provided.

Before showing the experimental results, a thorough theoretical analysis of copper electrochemistry in amine systems is presented to provide context for the results. The analysis is based heavily on Butler-Volmer kinetics and dissociative electron transfer theory. The analysis argues that despite the significantly increased activation energy due to strong ligand complexation, the dramatically stabilized transition state should lead to relatively similar kinetics in acid and amine based systems.

The results begin with a comparison of kinetics of copper dissolution and deposition in amine solutions and in previously studied sulfuric acid solutions. The kinetics in CO_2 saturated solutions are shown to be significantly slower in solutions with non-complexing salts. In solutions with chloride salts, however, CO_2 saturation does not make a large difference to the kinetics. The presence of chlorides also improves the kinetics in AEEA and TETA solutions, but is unimportant in EDA systems. Under argon, EDA shows the lowest overpotentials. In the CO_2-saturated solutions, AEEA outperforms EDA.

Measurement Strategies

There exist many methods for measuring the kinetics of electrochemical processes including dynamic and static potential techniques. Cyclic voltammetry, and more generally linear-sweep voltammetry, are commonly used dynamic potential methods for the measurement the kinetics of electrochemical systems. Cyclic voltammograms were used in the 2nd Chapter during the assessment of amines for EMAR systems. While qualitative arguments can be easily obtained, quantitative results are often difficult to obtain from these methods due to the complexity of the dynamic boundary condition on the electrode surface. Some exact solution strategies do exist for simple reaction schemes.[157–159] Numerical modeling of these systems, while possible, is challenging and simulation results are often not unique representations of the data. For example, Nicholson showed the similarity in curves of processes with slow kinetics and with uncompensated resistances; decoupling these effects is difficult.[160]

Another powerful dynamic potential method is Electrochemical Impedance Spectroscopy (EIS).[161] EIS measures the complex impedance of a system at different frequencies and potentials. Many system parameters, which are especially important in complete electrochemical systems including fuel cells and batteries, can be quickly measured using EIS.[162] These include solution resistance, double-layer capacitances, and electron transfer resistances.[163] This technique, however, is more suited for the analysis of prototype systems rather than analytical kinetic measurements. EIS results are shown for the bench-scale system in Chapter 6.

Various forms of static potential measurements, where the voltage is kept constant for the duration of the experiments, are used for kinetic measurements. Convective methods, such as rotating disk electrodes[164] and channel electrodes,[165] use systems with well-defined geometries such that the fluid dynamics problem can be solved precisely. This allows for the Sherwood number to be calculated for any combination of flow conditions and surface currents. For example, in a rotating disk setup, for any given rotational velocity and current, the concentration profile can be precisely calculated. Most importantly, the concentration of the electrochemically active species at the surface is known.

Use of the rotating disk electrode for measuring the electrochemical kinetics of copper in amine solutions was unsuccessful because it required the plating of copper onto the glassy carbon surface before each measurement. The copper, however, often fell off the electrode due to shear stress or simply dissolved during the course of the experiment. Getting uniform plating on the surface was also challenging. In the future, these experiments may be more successful with a solid copper rotating disk electrode, which would alleviate the need for plating.

Pulse experiments, which can last anywhere from milliseconds to seconds, have the advantage of being fast, but are unable to measure slow-dynamic processes.[166] For example, if an electrode surface changes over the course of seconds or minutes of operation, pulse experiments would be an ineffective strategy for investigating that phenomenon since experiments last only a few seconds at most. The advantage of this approach, however, is that the electrode surface remains unchanged during a set of experiments because so little charge is passed due to the short pulse lengths.

Previous investigations into the electrochemical kinetics of copper in sulfuric acid systems used galvanostatic pulse voltammetry, where constant current pulses are applied.[86] The method was simple and effective. Therefore, it was chosen to investigate the electrochemical kinetics of copper in amine solutions with and without CO_2 saturation.

Methodology for Galvanostatic Pulse Experiments

The electrochemical experiments were performed using a three electrode setup controlled by a potentiostat. A Princeton Applied Science VersaStat 3 potentiostat was used for all pulse experiments and a VersaStat 4 potentiostat was used for impedance spectroscopy experiments. The working electrode was a 3.1 mm diameter rod of copper alloy 101 (99.99% copper). The length of the copper rod was sheathed by heat-shrink FEP insulation, which was then wrapped with a copper mesh that acted as the reference electrode. Another layer of insulation was placed around the reference electrode, which was covered by another layer of copper mesh that acted as the counter electrode. This construction was chosen to minimize uncompensated resistances between the reference and the working electrode by minimizing the

distance between all the electrodes. The three electrodes were held in place by setting them in a modified number 4 rubber stopper. Sketches and pictures of the setup can be seen in **Figure 4-1**.

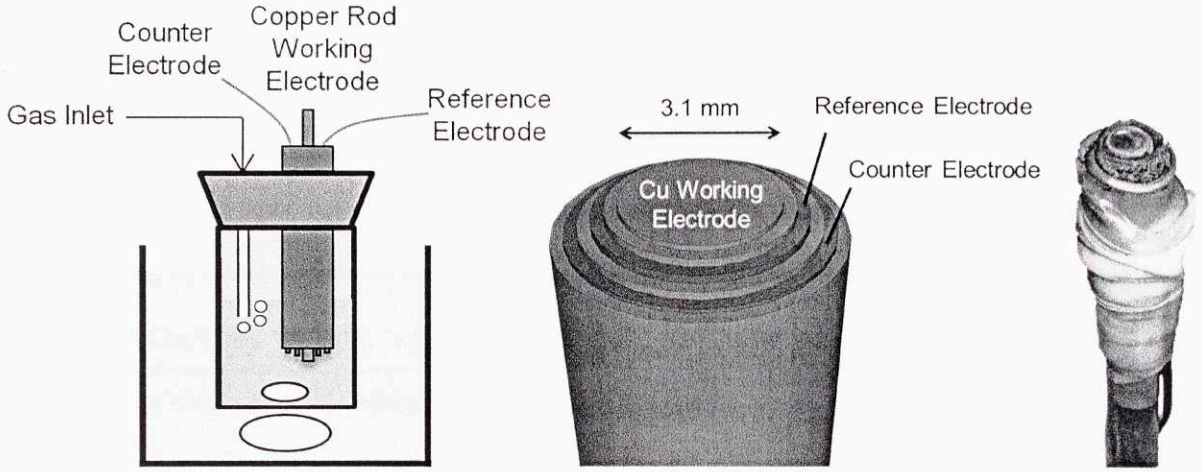

Figure 4-1. (Left) A schematic diagram of the experimental setup for kinetics experiments. **(Center)** A schematic drawing of the electrodes. **(Right)** A picture of the electrodes.

The electrochemical kinetics of copper deposition and dissolution were investigated with constant-current pulses from 1250 A/m^2 to 0.25 A/m^2. Cathodic pulses were always performed before anodic pulses. **Figure 4-2** shows results from a 55°C run of a 0.5M H_2SO_4 with 0.25M $CuSO_4$ experiment under argon. Note that one to ten seconds of delay was given in between each pulse, but is not shown in the figures.

Pulses were performed in order starting with the highest current densities. The length of the pulse was related to the current density. Experiments with current densities at and above 125 A/m^2 had pulse lengths of 0.01 seconds. For pulses at or below 100 A/m^2, the total applied charge density was kept constant at 1.25 C/m^2. Therefore, lower current densities had progressively longer pulse lengths with a maximum length of 5 seconds for the 0.25 A/m^2 pulses.

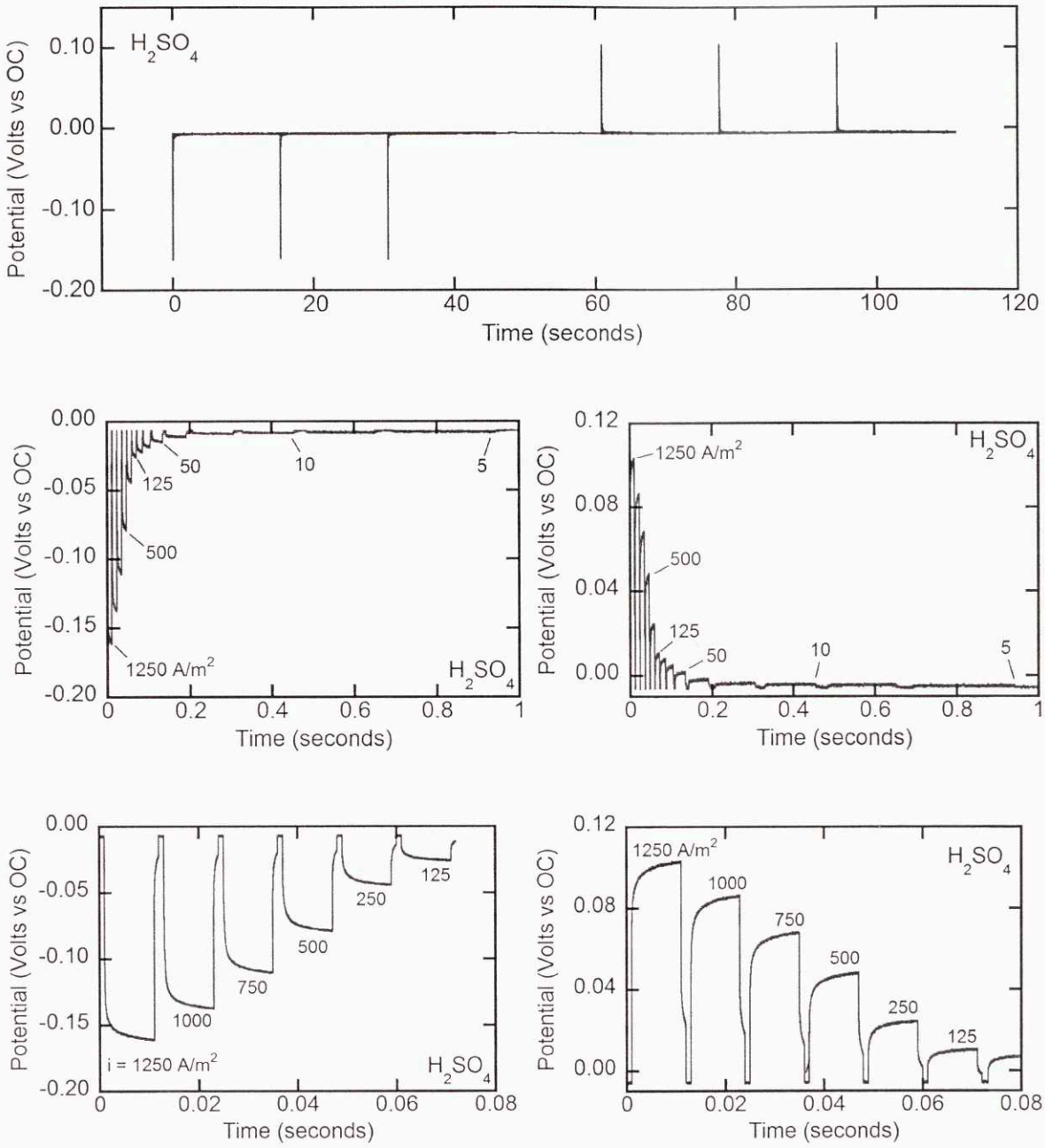

Figure 4-2. (Top) Plot of an entire kinetic pulse experiment including 3 cathodic and 3 anodic sets of 20 pulses each. **(Middle)** Plot of the first 14 cathodic pulses (Left) and first 14 anodic pulses (Right). **(Bottom)** Plot of the first 6 cathodic pulses (Left) and first 6 anodic pulses (Right). Numbers represent current densities of the pulses in A/m^2.

Before a set of pulses were performed, the electrode was removed from the solution and polished using 20 μm polishing paper. The electrode was the electroplated in the solution at 15 A/m^2 for 10 minutes. For experiments under inert atmosphere, argon was bubbled into the cell during both the pulsing

and the electroplating steps. For experiments under CO_2, the solutions were saturated for 15 minutes prior to plating and the CO_2 was bubbled in for the duration of the plating and pulse experiments. All experiments used 10 mL of solution and were gently stirred. Temperature was controlled through submerging the electrochemical cell in a temperature regulated oil bath. For each pulse, 1000 data points were taken.

Due to the large number of different parameters varied, it was not possible to take enough measurements of each set of conditions to obtain individual confidence intervals. One condition, 1M EDA with 0.25M $Cu(NO_3)_2$ with 1M $NaNO_3$ under argon at 55°C, was repeated eight times. The standard deviation of a single experiment was approximately 20% of the average. Since most experiments were performed two or three times at least, this leads to a standard deviation of the reported averages of about 15% of the average. This level of error can be considered consistent through all of the reported data.

It was challenging to keep results from drifting from week to week while running the kinetics experiments. It appeared that the results were extremely sensitive to the polishing process and if a new piece of polishing paper was used. Other methods of polishing, such as using abrasive slurries instead of polishing paper, may yield more consistent results. It was also observed that repeated experiments with acid solutions would lower the measured exchange current density of the electrode by around 25 percent. Once several experiments were again performed in amine solutions, the measured exchange current density would increase again.

Dynamic Analysis of Pulse Experiment Data

An example of the data obtained for a single constant current cathodic pulse is shown in **Figure 4-3**. During the first millisecond of the experiment, the change in potential is significant due to the solution resistance and double-layer capacitance.

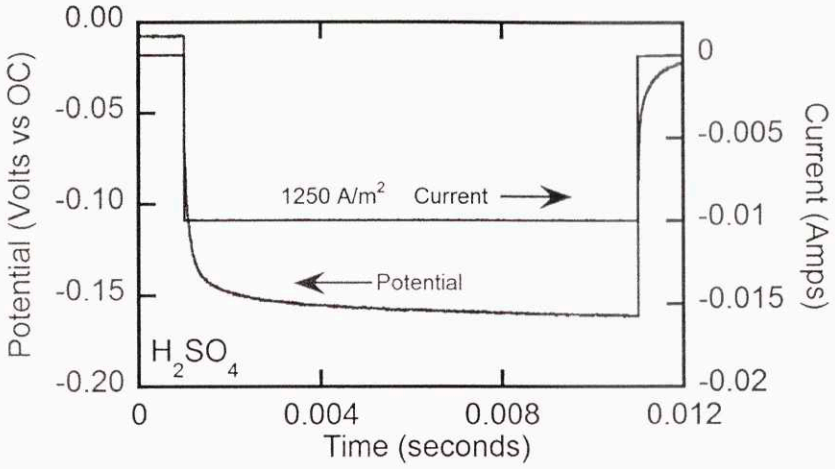

Figure 4-3. Current and potential as a function of time for a single galvanostatic pulse in a 0.5M H_2SO_4 and 0.25M $CuSO_4$ solution under argon at 55°C with a 3.1 mm Cu electrode.

The dynamics of the galvanostatic pulses were assumed to follow the representative RC circuit shown in the top circuit of **Figure 4-4**. In this circuit, R_u is the uncompensated resistance of the solution and C_{DL} is the double layer capacitance. R_1, R_2, and C_2 represent the non-constant resistance of charge transfer for the electro-deposition or electro-dissolution reactions. This circuit was chosen because it models the commonly observed uncompensated resistance and double layer capacitance, while allowing the charge transfer resistance to be described by a sigmoidal function.

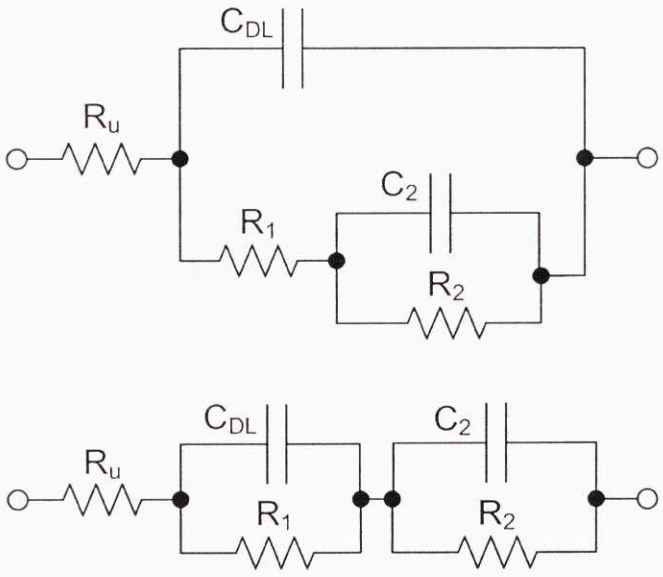

Figure 4-4. Equivalent RC circuits used to model the dynamic behavior of the galvanostatic pulses.

Intuitively, C_2 can be thought of as the consumption or creation of either an intermediate species or an oxidized surface layer, which then leads to a change in the resistance (from R_1 to $R_1 + R_2$) with a time constant of $\tau_2 = R_2C_2$.

If we assume that $R_1C_{DL} << R_2C_2$, then we can safely decouple the two parallel RC elements resulting in the bottom circuit of **Figure 4-4**. The voltage response for a constant current pulse of this circuit is shown in Eq. 4-1.

$$V(t) = i\left[R_u + R_1\left(1-\exp\left(-\frac{t}{R_1C_{DL}}\right)\right) + R_2\left(1-\exp\left(-\frac{t}{R_2C_2}\right)\right)\right] \tag{4-1}$$

Based on previous work and confirmed in this study, the double layer capacitances are typically around 10^{-4} F/cm^2 with resistances on the order of 10 Ω. With an electrode of 0.08 cm^2, the middle term in Eq. 4-1 has an RC time constant of approximately 0.1 milliseconds. Therefore, at short times (below 0.05 millisecond), the uncompensated resistance and capacitive effects are dominant and the first and middle terms can be linearized to yield a linear dependence of voltage on time.

$$V\left(t \le 50\ \mu s\right) = i\left[R_u + \frac{t}{C_{DL}}\right] \tag{4-2}$$

Using Eq. 4-2, the uncompensated resistance and capacitance values for each set of pulses are estimated from the short time data for the pulses with current densities over 250 A/m^2. **Figure 4-5** shows the short time linear resistances for a typical set of high current density pulses for a 1N H_2SO_4 solution with 0.25 M $CuSO_4$ at 55°C. Uncompensated resistance values obtained through this method were confirmed using impedance spectroscopy.

The linear fits in **Figure 4-5** show excellent precision in measuring the uncompensated resistance (the y-intercept) for both anodic and cathodic pulses. The precision of the capacitance measurements is less robust, but still sufficient. The accuracy of the capacitance measurements is also less important, since the effects of the double layer charging are only relevant during the first millisecond of operation.

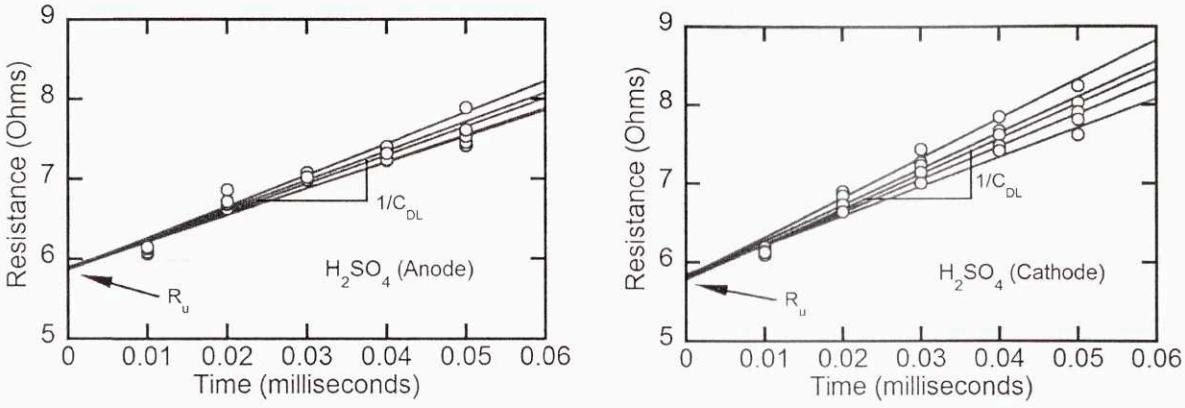

Figure 4-5. Dynamic resistances of anodic (left) and cathodic (right) galvanostatic pulses at short times. Lines represent fit using Eq. 4-2.

For each pulse, the values of R_1, R_2, and C_2 were then fit using Eq. 4-1, using the results obtained for R_u and C_{DL}. **Figure 4-6** shows the time dependent resistances for a typical set of high current density pulses for a 1N H_2SO_4 solution with 0.25 M $CuSO_4$ at 55°C with the uncompensated resistance, R_u, already subtracted out.

Both anodic and cathodic pulses show sufficient approach towards steady state during the 0.01 second pulses. The capacitive effects make a dramatic impact only during the initial one or two milliseconds. Limitations due to diffusional transport are not observed even at 1250 A/m^2.

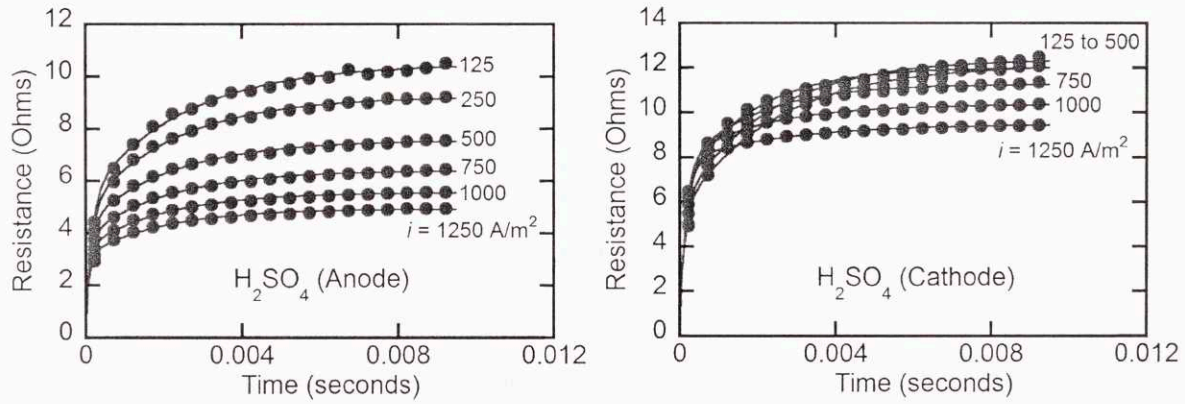

Figure 4-6. Dynamic resistances of anodic (left) and cathodic (right) galvanostatic pulses with the uncompensated resistance already removed. Only 2% of data points shown. Lines represent fit using Eq. 4-1.

The pseudo steady-state overpotentials for each pulse, which will be used for all of the I/V results, are calculated by extrapolation of Eq. 4-1 at infinite time after subtraction of the uncompensated resistance,

$$V(t \to \infty) = i\left(R_1 + R_2\right) \tag{4-3}$$

where R_1 and R_2 are obtained through the curve fitting procedure described above.

To ensure operation within a non-transport limited regime, the limiting current density as a function of time can be calculated based on the well-known similarity solution for semi-infinite diffusion.[167] Eq. 4-4 shows the limiting current, i_{Limit}, which equals the limiting Cu^{2+} flux multiplied by $2F$.

$$i_{Limit} = 2F\left(\frac{D}{\pi t}\right)^{1/2} C_0 \tag{4-4}$$

Integration of Eq. 4-4 over time, yields the total transported charge, Q_{Limit}, of a diffusion limited system as a function of the pulse length as shown in Eq. 4-5.

$$Q_{Limit} = 4F\left(\frac{Dt}{\pi}\right)^{1/2} C_0 \tag{4-5}$$

The copper ion complex diffusivity can be estimated by literature reports of copper sulfate diffusivity is water.[168] Based on an estimated cupric ion complex diffusivity of 10^{-9} m^2/s and a copper concentration of 0.25M, the maximum ratio of charge transferred during a pulse to diffusion limited charge is 0.07 for the 1250 A/m^2 pulse. Experiments at low temperatures, which could have slower diffusivities, and experiments with different copper concentrations could have higher ratios; in general, it was assumed that transport limitations were not significant under these conditions.

Before the results of the galvanostatic pulse experiments are discussed, an examination of electrochemical kinetic theory for systems with intermediate reactions and sequential electron transfers will be presented.

Kinetic Theory Applied to Copper/Amine Systems

Standard Butler-Volmer Approach

The simplest way to interpret the current/potential results from the pulse experiments is with the standard Butler-Volmer equation shown in Eq. 4-6.[87]

$$i = i_0\left[\exp\left(\frac{(1-\alpha)nF}{RT}\eta\right) - \exp\left(\frac{-\alpha nF}{RT}\eta\right)\right] \tag{4-6}$$

An example the results from the pulse experiments fit with Eq. 4-6 can be seen in **Figure 4-7.**

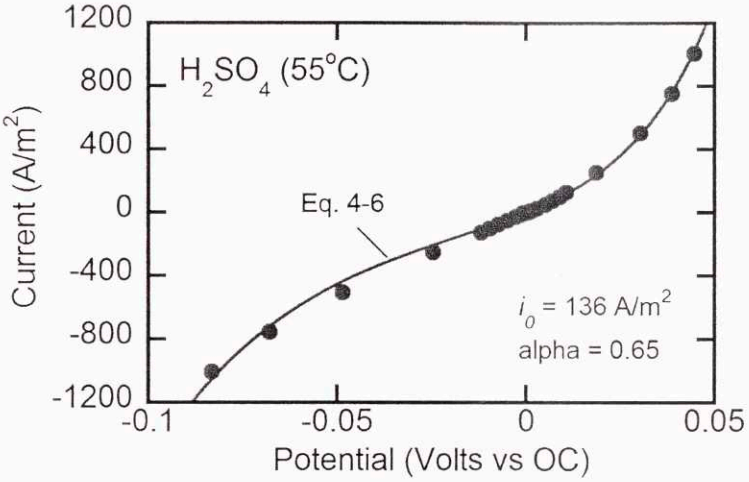

Figure 4-7. Current density as a function of overpotential for a 0.25M $CuSO_4$ and 0.5M H_2SO_4 solution at 55°C fit with Eq. 4-6.

In Eq. 4-6, i_0 is the exchange current density, α is electron transfer coefficient and η is the overpotential. The exchange current density, i_0, is defined as a function of the electron transfer coefficient in Eq. 4-7.

$$i_0 = nF\kappa_0[\mathrm{Red}]^{\alpha}[\mathrm{Ox}]^{1-\alpha} \tag{4-7}$$

where [Red] and [Ox] are the surface concentrations of the reduced and oxidized species, respectively, and κ_0 is a constant based on the rate constants of the different forward and reverse processes. The exchange current densities can be derived from the reaction rate equations for both systems:

$$\begin{aligned} i_0^{ACID} &= 2F\kappa_0^{ACID}\left[\mathrm{Cu}^{2+}\right]^{1-\alpha} \\ i_0^{EDA} &= 2F\kappa_0^{EDA}[\mathrm{EDA}]^{2\alpha}\left[\mathrm{Cu(EDA)}_2^{2+}\right]^{1-\alpha} \end{aligned} \tag{4-8}$$

For low overpotentials, a linear approximation of the exponentials in Eq. 4-6 leads to a simple linear current potential relationship.

$$i\left(\eta < {RT}/{2F}\right) \approx i_0 \frac{2F}{RT}\eta \tag{4-9}$$

Dissociative Electron Transfer Theory

The effects of the amine complexation of the copper ions on the electrochemical kinetics can be accounted for through use of Dissociative Electron Transfer (DET) theory.[98] DET theory, developed by Saveant and coworkers is based heavily on the Marcus-Hush electron transfer theory. For an electrochemical reaction coupled with a complex formation, DET theory predicts an increase in the reorganization energy λ, of one fourth of the bond dissociation energy, D_{RX}. We will assume that the bond dissociation energy is equal to the negative of the reaction enthalpy, ΔH^0.

$$\lambda_{DET} = \lambda_0 + \frac{1}{4} D_{RX} \tag{4-10}$$

Here, λ_{DET} represents the reorganization energy for a dissociative electron transfer and λ_0 is the reorganization energy in the absence of the complexation. The reorganization energy can be assumed analogous to a standard kinetic activation energy for the exchange current density, i_0.

$$i_0 \propto \exp\left(\frac{-\lambda_{DET}}{RT}\right) = \exp\left(\frac{-\lambda_0}{RT}\right)\exp\left(\frac{-D_{RX}}{4RT}\right) \tag{4-11}$$

Eq. 4-11 shows that systems with strong complexation should display significantly hindered kinetics. Based on the approximately 100 kJ/mole reaction enthalpy of the copper/EDA complex,[146] the kinetics would be expected to diminish by 4 orders of magnitude compared to the acid system. This significantly overestimates the difference based on the data shown later. The discrepancy results from the implicit assumption that the electron transfers are simultaneous.

Sequential Electron Transfers

The Butler-Volmer equation in Eq. 4-6, when applied to a two-electron transfer process, does not account for intermediates between the electron transfers, but rather assumes a simultaneous process. Newman has

showed, through referencing data taken by Mattsson and Bockris, that copper electrochemistry in sulfuric acid systems can be interpreted as sequential transfers with a cuprous ion intermediate.[87,86] Furthermore, Newman assumes the reaction between copper metal and the cuprous intermediate is fast, and therefore, at equilibrium. For the acid system, Newman defined the rate equations as:

$$i_2^{ACID} = k_{a2} e^{\frac{(1-\alpha_2)F}{RT}V} - k_{c2}\left[\mathrm{Cu}^+\right] e^{\frac{-\alpha_2 F}{RT}V} \tag{4-12}$$

$$i_3^{ACID} = k_{a3}\left[\mathrm{Cu}^+\right] e^{\frac{(1-\alpha_3)F}{RT}V} - k_{c3}\left[\mathrm{Cu}^{2+}\right] e^{\frac{-\alpha_3 F}{RT}V} \tag{4-13}$$

The analogous equations for an EDA system are quite similar. If we assume a cuprous ion intermediate of the form, $Cu(EDA)^+$, the rate equations are:

$$i_2^{EDA} = k_{a2}[\mathrm{EDA}] e^{\frac{(1-\alpha_2)F}{RT}V} - k_{c2}\left[\mathrm{Cu(EDA)}^+\right] e^{\frac{-\alpha_2 F}{RT}V} \tag{4-14}$$

$$i_3^{EDA} = k_{a3}\left[\mathrm{Cu(EDA)}^+\right][\mathrm{EDA}] e^{\frac{(1-\alpha_3)F}{RT}V} - k_{c3}\left[\mathrm{Cu(EDA)}_2^{2+}\right] e^{\frac{-\alpha_3 F}{RT}V} \tag{4-15}$$

For the acid system, Newman derived the solution for the current as a function of the overpotential,

$$i^{ACID} = i_0\left(e^{(2-\alpha_3)\frac{F\eta}{RT}} - e^{-\alpha_3\frac{F\eta}{RT}}\right) \qquad \text{where} \quad i_0 = 2Fk_{c3}\left(\frac{k_{a3}k_{a2}}{k_{c3}k_{c2}}\right)^{\alpha_3/2}\left[\mathrm{Cu}^{2+}\right]^{(2-\alpha_3)/2} \tag{4-16}$$

Eqs. 4-6 and 4-16 are analogous if $\alpha = \alpha_3/2$. If the electrochemical reaction described in Eq. 4-13 is elementary ($\alpha_3 = 0.5$), then it would be expected that the using the simple Butler-Volmer model in Eq. 4-6 would yield an overall electron transfer coefficients, α, near 0.25. This has been shown previously to be accurate for the acid systems and agrees with our results for amine systems. The experimental observation of faster anodic kinetics, compared to the cathodic process, results from the intermediate mechanism of the sequential electron transfers.

The analogous solution for the EDA case follows closely the solution for the acid system:

$$i^{EDA} = i_0\left(e^{(2-\alpha_3)\frac{F\eta}{RT}} - e^{-\alpha_3\frac{F\eta}{RT}}\right) \qquad \text{where} \quad i_0 = 2Fk_{c3}\left(\frac{k_{a3}k_{a2}}{k_{c3}k_{c2}}\right)^{\alpha_3/2}[\mathrm{EDA}]^{\alpha_3}\left[\mathrm{Cu(EDA)}_2^{2+}\right]^{(2-\alpha_3)/2} \tag{4-17}$$

It is important to note that the rate constants, k_{ij}, are not the same for the acid and EDA systems. It is, however, possible to compare the ratios of k_{a2}/k_{c2} if we follow Newman's assumption that the kinetics of the first electrochemical reaction is fast enough to be in equilibrium. For the acid system the equilibrium assumption yields,

$$\left(\frac{k_{a2}}{k_{c2}}\right)_{ACID} = \left[\mathrm{Cu}^{+}\right] e^{-FV/RT} \tag{4-18}$$

For the EDA case, we find a similar solution.

$$\left(\frac{k_{a2}}{k_{c2}}\right)_{EDA} = \frac{\left[\mathrm{Cu(EDA)}^{+}\right]}{[\mathrm{EDA}]} e^{-FV/RT} \tag{4-19}$$

The ratio of the results from Eqs. 4-18 and 4-19 define the mass action equation for the complexation of the intermediate cuprous ion by EDA with a free energy of $\Delta G_1^{\,0}$.

$$\left(\frac{k_{a2}}{k_{c2}}\right)_{EDA} \Big/ \left(\frac{k_{a2}}{k_{c2}}\right)_{ACID} = \frac{\left[\mathrm{Cu(EDA)}^{+}\right]}{[\mathrm{EDA}]\left[\mathrm{Cu}^{+}\right]} = \exp\left(\frac{-\Delta G_1^0}{RT}\right) = \exp\left(\frac{-\Delta H_1^0}{RT}\right)\exp\left(\frac{\Delta S_1^0}{R}\right) \tag{4-20}$$

We can also take the ratio of the remaining rate constants and relate those using DET theory using the enthalpy of reaction for the second EDA molecule to the singly complexed cupric ion, $\Delta H_2^{\,0}$.

$$\frac{\left[\left(k_{c3}\right)^{1-\alpha_3/2}\left(k_{a3}\right)^{\alpha_3/2}\right]_{EDA}}{\left[\left(k_{c3}\right)^{1-\alpha_3/2}\left(k_{a3}\right)^{\alpha_3/2}\right]_{ACID}} = \frac{e^{-\lambda_0/RT} e^{\Delta H_2^0/4RT}}{e^{-\lambda_0/RT}} = \exp\left(\frac{\Delta H_2^0}{4RT}\right) \tag{4-21}$$

The ratio of the exchange current densities for the EDA and acid systems can be approximated through use of Eqs. 4-16, 4-17, 4-20, and 4-21.

$$\frac{i_0^{EDA}}{i_0^{ACID}} = \frac{[\mathrm{EDA}]^{\alpha_3}\left[\mathrm{Cu(EDA)}_2^{2+}\right]^{(2-\alpha_3)/2}}{\left[\mathrm{Cu}^{2+}\right]^{(2-\alpha_3)/2}} \exp\left[\frac{1}{2RT}\left(\frac{\Delta H_2^0}{2} - \alpha_3 \Delta H_1^0\right)\right] \exp\left[\frac{\alpha_3}{2}\frac{\Delta S_1^0}{R}\right] \tag{4-22}$$

The exponential term in Eq. 4-22 shows that the relative reaction rates of the EDA system compared with the acid system are based heavily on the relative values of $\Delta H_1^{\,0}$ and $\Delta H_2^{\,0}$. If $\Delta H_1^{\,0} \approx \Delta H_2^{\,0}$, then the

exchange current densities would be approximately equal for the EDA and acid systems since the value of the electron transfer coefficient, α_3, should be approximately equal to one half. Based on the results of Cotton and Harris, the difference in enthalpies, $\Delta H_2^0 - \Delta H_1^0 = 3$ kJ/mole. Therefore, the exponent of the first exponential function will be positive. As temperature increases, Eq. 4-22 predicts the ratio of EDA to acid exchange current densities will decrease.

It should be noted that this derivation makes several significant simplifying assumptions. It assumes that the change in reorganization energy due to solvation is equivalent in both systems. It also assumes that the complexation of the cuprous ion is fast enough to maintain the equilibrium assumption of the first redox couple; our results suggest this assumption may not be valid at high current densities in some cases.

The important concept developed in this model is that the electrochemical kinetics for a two-electron dissociative electron transfer process with a stabilized intermediate are influenced by the added reorganization energy of the bond formation and the increased stability of the intermediate species. Consideration of both phenomena, which are competitive by nature, is necessary to reasonably estimate kinetics of copper in aqueous amine solutions.

Based on this theoretical framework, it is possible to explain the behavior of EDA, AEEA, and TETA systems with different copper loadings and temperatures as well as the effects of carbon dioxide saturation and chloride addition.

Galvanostatic Pulse Results

Comparison of Kinetics in H_2SO_4 and EDA Solutions

Figure 4-8 shows the current as a function of overpotential at 25°C for 0.25 M Cu^{2+} in a 1 N sulfuric acid solution and a 1 M EDA solution with 1 M $NaNO_3$ as the inert electrolyte. The Butler-Volmer (BV) equation, Eq. 4-6, and its linearized form, Eq. 4-9, are used to model both systems.

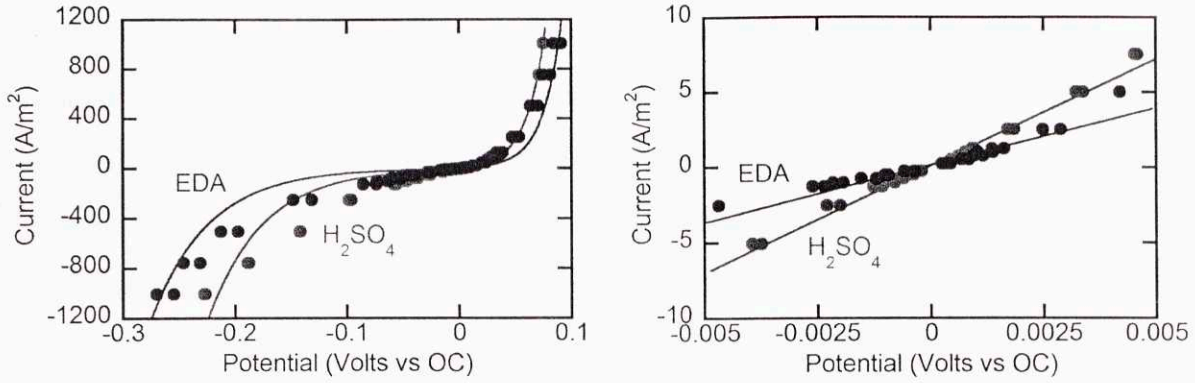

Figure 4-8. Current density as a function of overpotential for 0.25M copper salt in aqueous EDA and sulfuric acid solutions at 25°C under argon. Lines are fits to the Butler-Volmer equation in Eq. 4-6 (Left) and Eq. 4-9 (Right).

For both acid and EDA solutions, the anodic reaction is more facile. The exchange current density, i_0, can be calculated from either non-linear least squares fitting of the full-range of data with the BV equation from Eq. 4-6, or the low potential data, shown in the right plot of **Figure 4-8**, using Eq. 4-9. Using the BV equation, which is similar to using the Tafel slopes, provides information over a more relevant range of current densities and provides more consistent results. **Table 4-1** compares the results for the acid and EDA systems at 25°C under argon.

Table 4-1. Exchange current densities and electron transfer coefficients of acid and EDA systems at 25°C.

	H_2SO_4			EDA		
	Trial 1	**Trial 2**	**Average**	**Trial 1**	**Trial 2**	**Average**
i_0 **(4-6)***	13.2	13.5	13.4	5.7	8.2	6.9
α **(4-6)**	0.26	0.26	0.26	0.25	0.25	0.25
i_0 **(4-9)****	19.2	18.2	18.7	10.3	10.3	10.3

* Calculated with Eq. 4-6. In units of A/m^2.
** Calculated with Eq. 4-9. In units of A/m^2.

The full-range exchange current density is slightly higher for the acid system than the EDA system. At low current densities, however, the exchange current densities are closer. Both systems demonstrated electron transfer coefficients near 0.25, in agreement with the theory of a fast cuprous intermediate. The relatively small disparity between the exchange current densities of the H_2SO_4 and EDA solutions suggests that the competing effects of cuprous ion stabilization and increased reorganization energy, shown in Eq. 4-22, are nearly balanced, as predicted.

The acid system yielded full-range exchange current densities around 13 A/m^2 and an electron transfer coefficient of 0.26, which is in good agreement with previous results by Mattsson and Bockris of 7 A/m^2 and 0.28, respectively, for 0.15M $CuSO_4$ in 1N H_2SO_4.[86] The low-potential current density results, however, were significantly higher than those reported previously. This difference is most likely due to the quantity of data in the chosen low potential range. The slopes in **Figure 4-8** were determined by 13 data points from -5 to 5 mV, while Mattsson and Bockris showed 5 data points from -15 to 15 mV in an example from their study.

The Effect of Temperature

The temperature of operation significantly affects the electrochemical kinetics of both the acid and EDA systems. **Figure 4-9** shows current versus potential data for the EDA system at 25°C, 45°C, and 65°C.

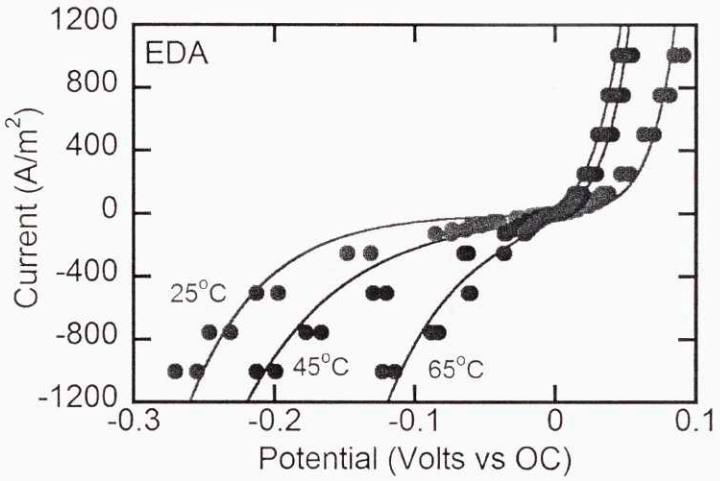

Figure 4-9. Current density as a function of overpotential for 0.25M $Cu(NO_3)_2$ in 1M EDA solutions with 1M $NaNO_3$ under argon at 25°C, 45°C, and 65°C. Lines fit using the BV equation from Eq. 4-6.

As the temperature increases, the exchange current densities increase rapidly, leading to smaller overpotentials. The shape of the curves and the tendency for lower anodic overpotentials than cathodic overpotentials remains constant through increasing temperatures.

The kinetics of both EDA and H_2SO_4 systems were measured from 25°C to 75°C; the exchange current densities and electron transfer coefficients, as functions of temperature, are shown in **Figure 4-10** and tabulated in **Table 4-2**.

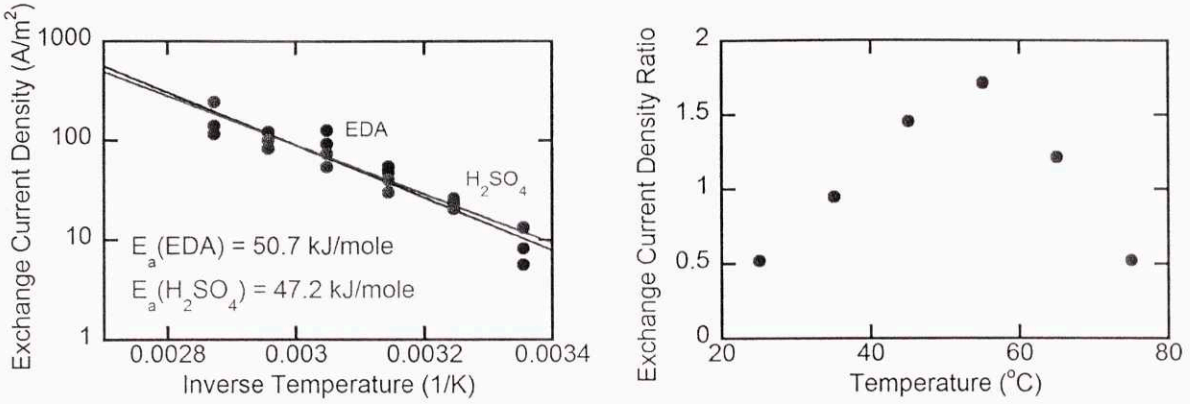

Figure 4-10. (Left) Exchange current density as a function of temperature for EDA and acid solutions under argon. **(Right)** Ratio of exchange current densities as a function of temperature (EDA/H_2SO_4).

The ratio of exchange current densities increases as predicted by Eq. 4-22 until 55°C. The plateauing of EDA exchange current densities at high temperatures has been repeated observed, and may indicate the transition in the rate limiting step of the mechanism. The low temperature dependence of the kinetics at high temperatures suggests the new rate limiting process has a low activation energy. A transport (i.e., diffusion) limitation is plausible.

Table 4-2. Measured exchange current densities and electron transfer coefficients of EDA and H_2SO_4 systems with 0.25M copper salts as a function of temperature.

	Temp (°C)	25	35	45	55	65	75
H_2SO_4	i_0 (4-6)*	13.4	23.8	35.4	64.3	92.2	246.3
	α (4-6)	0.26	0.26	0.29	0.29	0.28	0.33
	i_0 (4-9)**	18.7	28.9	33.9	47.1	55.1	78.1
EDA	i_0 (4-6)*	6.9	22.5	51.5	110.3	112.3	128.7
	α (4-6)	0.25	0.21	0.20	0.24	0.28	0.30
	i_0 (4-9)**	10.3	15.6	26.9	31.5	39.9	47.5

* Calculated with Eq. 4-6. In units of A/m^2. ** Calculated with Eq. 4-9. In units of A/m^2.

Through measurement of the exchange current density as a function of temperature, the activation energy, E_a, of the electrochemical reaction can be obtained with Eq. 4-23.

$$E_a = -R\frac{d\ln(i_0)}{d(1/T)} \tag{4-23}$$

For a simple dissociative electron transfer process, the addition of a concerted chemical reaction with the electron transfer would increase the activation energy as shown in Eq. 4-10. **Figure 4-10**, however, shows

that the activation energies of the acid and EDA systems are quite similar at 47.2 and 50.7 kJ/mole, respectively. For the dissociative electron transfer mechanism with sequential electron transfers, differentiation of the logarithm of the exchange current density ratio from Eq. 4-22 with respect to inverse temperature explains the similarity in the activation energies.

$$E_a^{EDA} - E_a^{ACID} = -R\frac{d\left[\ln\left(i_0^{EDA}/i_0^{ACID}\right)\right]}{d(1/T)} = -\frac{1}{2}\left(\frac{\Delta H_2^0}{2} - \alpha_3 \Delta H_1^0\right) \tag{4-24}$$

Since the standard state enthalpy, ΔH_1^0, of the intermediate complexation is nearly equal to that of the enthalpy of the second complexation of the cupric ion, ΔH_2^0, the difference in activation energies is small.

Kinetics in CO_2 Saturated Solutions

Figure 4-11 shows results for the EDA system under argon, 50% saturated with CO_2, and fully saturated with CO_2. The 50% solution was achieved by mixing equal volumes of CO_2-free solution and CO_2 saturated solution. The cathodic process has been significantly hindered in both the 50% and fully loaded solutions. The exchange current densities, based on fitting the Butler-Volmer equation, have been reduced by nearly two orders of magnitude. The results are tabulated in

Table 4-3.

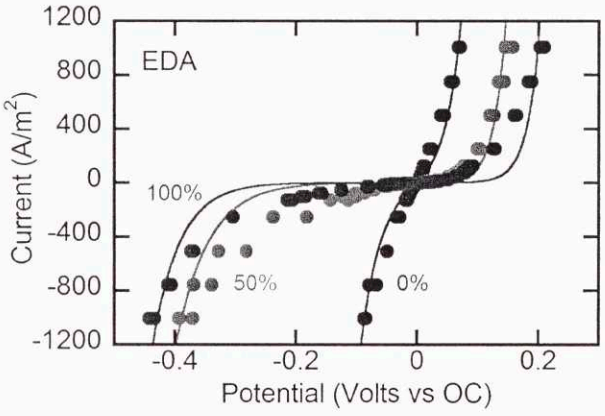

Figure 4-11. Current density as a function of overpotential for a 1M EDA solution with 0.25M $Cu(NO_3)_2$ and 1M $NaNO_3$ at 55°C with CO_2 loadings of 0% (blue), 50% (orange), and 100% (green). Lines are based on fits to Eq. 4-6.

Table 4-3. Exchange current densities and electron transfer coefficients of a 1M EDA system with 0.25M $Cu(NO_3)_2$ and 1M $NaNO_3$ at 55°C with different CO_2 loadings.

CO_2 Loading	0%	50%	100%	100%/0%
i_0 (4-6)*	104.5	0.56	0.15	0.0014
α (4-6)	0.35	0.28	0.31	0.88
i_0 (4-9)**	50.3	4.02	1.66	0.033

* Calculated with Eq. 4-6. In units of A/m^2.
** Calculated with Eq. 4-9. In units of A/m^2.

To apply the derivation resulting in Eq. 4-22, adjustments must be made to account for the presence of CO_2. Because the vast majority of EDA molecules are complexed with CO_2, we must include the relevant mass action equation describing CO_2 absorption:

$$\frac{[\text{EDA-CO}_2]}{[\text{EDA}]}\frac{P_0}{P_{CO_2}} = \exp\left(\frac{-\Delta G^0_{CO_2}}{RT}\right) \tag{4-25}$$

where ΔG^0_{CO2} is the free energy of CO_2 absorption, P_{CO2} is the partial pressure of carbon dioxide, and P_0 is the standard state pressure. Through inclusion of Eq. 4-25 in Eq. 4-22, the effects of CO_2 saturation can be observed.

$$\frac{i_0^{EDA+CO_2}}{i_0^{ACID}} = \left(\frac{P_0}{P_{CO_2}}\right)^{\alpha_3} \frac{[\text{EDA}]_0^{\alpha_3}\left[\text{Cu(EDA)}_2^{2+}\right]^{(2-\alpha_3)/2}}{\left[\text{Cu}^{2+}\right]^{(2-\alpha_3)/2}} \exp\left[\frac{1}{2RT}\left(\frac{\Delta H_2^0}{2} - \alpha_3\Delta G_1^0 + 2\alpha_3\Delta G^0_{CO_2}\right)\right] \tag{4-26}$$

where $[EDA]_0$ is the concentration of all non-copper complexed EDA species. Comparing the exchange current density of an EDA system with and without CO_2, we find:

$$\frac{i_0^{EDA+CO_2}}{i_0^{EDA}} = \left(\frac{P_0}{P_{CO_2}}\right)^{\alpha_3} \exp\left[\frac{\alpha_3\Delta G^0_{CO_2}}{RT}\right] \tag{4-27}$$

Based on our previous work that calculated the standard state enthalpy and entropy of CO_2 absorption by EDA to be -86.4 kJ/mole and -210 J/mole/K, respectively, the free energy of CO_2 absorption can be calculated at any temperature. At 55°C, the free energy would be -17.3 kJ/mole; this leads to a ratio of exchange current densities for unsaturated systems over CO_2-saturated systems of 0.04 (assuming α_3 = 0.5).

Comparison of the exchange current densities, through fitting the BV equation, Eq. 4-6, over the entire range of current densities, yields a value thirty times lower than expected. However, comparison of the exchange current densities as measured by the slope at low overpotentials as described by Eq. 4-9, gives a ratio of 0.03, which is in good agreement with the theory. This suggests that the kinetics of EDA/CO_2 complex formation or breaking may become limiting at high reaction rates. If the kinetics of the CO_2 complexation with EDA is not fast, then the equilibrium expression in Eq. 4-25 does not accurately represent the concentration of free EDA species during the pulses with high current densities.

The significantly hindered kinetics at 50% loading is not surprising; at 50% loading, each EDA molecule is still complexed with either a proton or a carbamate group, which would need to be released before the molecule could complex the cupric ion.

It was observed that the copper working electrode showed signs of oxide formation after running pulse experiments in CO_2 saturated solutions. The formation of passivating films may also explain the slower than expected kinetics at high current densities. With CO_2 equilibrium binding constants of 10^6 at room temperature and an EDA/Copper stability constant of 10^{19}, the effective stability constant, given by Eq. 3-21, would be 10^7. This would lead to an uncomplexed copper activity of about 10^{-7}. The formation of cupric hydroxide, $Cu(OH)_2$, shown in Eq. 4-26, has a solubility product, K_{SP}, of 5.6×10^{-20}.[169]

$$K_{SP} = \left[Cu^{2+}\right]\left[OH^-\right]^2 = \frac{Cu_0^{2+}}{1+\beta[EDA]_0^2}\left[OH^-\right]^2 \tag{4-28}$$

For CO_2-saturated solution, which will have a pH of around 7, the reaction quotient for the precipitation of copper hydroxide will be just under the solubility product. This suggests that during fast anodic pulses, where the copper concentration may increase rapidly at the surface, precipitation may occur. Cupric hydroxide, once formed, will eventually convert to the more stable cupric oxide, CuO.

The Effect of Chloride Salts

Chloride salts are known to complex with copper salts, specifically cuprous ions. Since the intermediate complex is hypothesized to be a cuprous species, adding chlorides is expected to have a significant effect

on the kinetics. It was shown in Chapter 3, however, that chloride salts do not significantly affect the thermodynamics of EDA/Copper systems.

Figure 4-12 shows the current/potential curves for EDA systems with $NaNO_3$ and NaCl salts under argon and in CO_2-saturated systems. While the chloride salts do not significantly impact the kinetics in systems under argon, the effect is dramatic in the presence of CO_2.

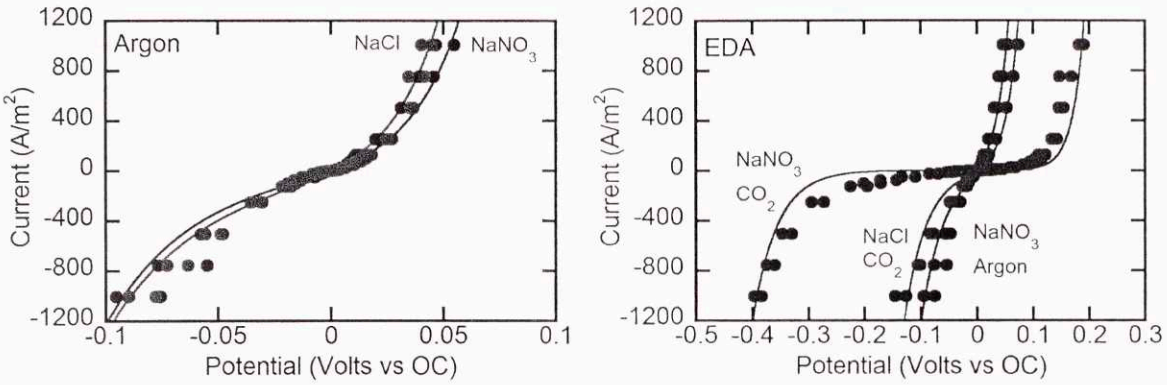

Figure 4-12. Current density as a function of overpotential for 1M EDA solutions with 0.25M $Cu(NO_3)_2$ and either 1M $NaNO_3$ (blue and green) or 1M NaCl (red and grey) under either argon (blue and red) or CO_2 (green and grey) at 55°C. Lines represent least squares fits to Eq. 4-6.

Table 4-4 shows that the addition of chloride ions to a CO_2-saturated system increases the exchange current density from 0.1% to 37% of its unsaturated value. The dramatic increase in the exchange current densities of CO_2-saturated systems with NaCl solutions indicates a different reaction mechanism than in CO_2-saturated $NaNO_3$ solutions.

Table 4-4. Exchange current densities and electron transfer coefficients for 1M EDA solutions with 0.25M $Cu(NO_3)_2$ and either 1M $NaNO_3$ (blue and green) or 1M NaCl (red and grey) under either argon or CO_2 at 55°C.

	Argon		CO_2		CO_2/Ar	
	$NaNO_3$	NaCl	$NaNO_3$	NaCl	$NaNO_3$	NaCl
i_0 (4-6)*	104.5	105.5	0.15	39.1	0.0014	0.37
α (4-6)	0.35	0.37	0.31	0.35	0.89	0.95
i_0 (4-9)**	50.3	32.5	1.66	36.4	0.033	1.12

* Calculated with Eq. 4-6. In units of A/m^2. ** Calculated with Eq. 4-9. In units of A/m^2.

The rate limiting step in NaCl solutions does not appear to be highly correlated to the saturation state of the EDA molecules. One hypothetical scheme, shown in Eq. 4-29, would be a disproportionation mechanism, limited by the initial generation of a cuprous chloride species.

$$Cu + xCl^- \rightleftharpoons CuCl_x^{1-x} + e^-$$
$$2CuCl_x^{1-x} + 2EDA \rightleftharpoons Cu(EDA)_2^{2+} + 2xCl^- + Cu \quad (4\text{-}29)$$

In this mechanism, the amine complexation is only indirectly involved with the electron transfer, and hence, CO_2-saturation would be less influential towards the kinetics. A drawback of this mechanism, however, is that it allows for copper generation in the bulk of the solution during anodic reactions. The generation of copper powder, predominately from anode, has been observed during the bench-scale experiments. Operation of the bench-scale system with NaCl electrolytes did appear to increase the generation of copper powder in the anode, supporting the scheme in Eq. 4-29. Further details of the bench-scale results are provided in Chapter 6.

The stoichiometric parameter, x, is Eq. 4-29 can be ascertained by measurements with varying NaCl concentrations in a CO_2-saturated system. The results, shown in **Figure 4-13**, indicate a linear dependence of the exchange current density on the concentration of NaCl. This suggests the stoichiometric parameter, x, is equal to 1; therefore, cuprous chloride, CuCl, appears to be the dominate intermediate in CO_2-saturated systems with NaCl electrolyte.

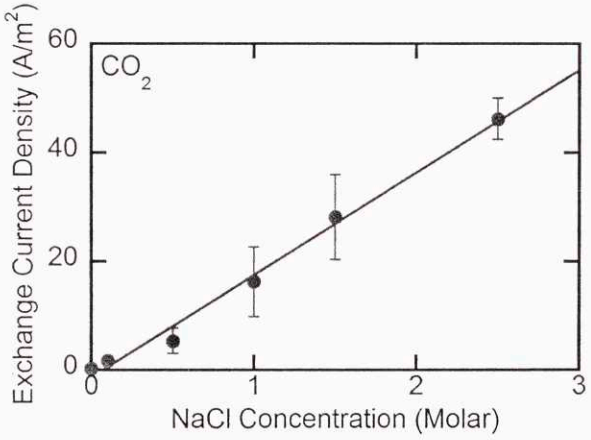

Figure 4-13. Exchange current density, i_0, as a function of NaCl concentration in a CO_2-saturated 1M EDA solution with 0.25M copper salt (either $Cu(NO_3)_2$ or $CuCl_2$). Solutions with less than 1M NaCl also contained 1M $NaNO_3$ to maintain high ionic strength. Exchange current densities were fit using Eq. 4-6.

It was observed that after experiments with NaCl containing solutions, the copper electrode surface appeared brighter, with no signs of copper oxides. This could be an alternative explanation to the

improved kinetics with incorporation of NaCl. However, it would not effectively explain the improved kinetics of 2.5M NaCl solutions over 1M NaCl solutions, since they both appeared to effectively eliminate copper oxide formation.

Kinetics in Different Polyamines

The electrochemical kinetics of aqueous solutions with two additional polyamines, aminoethylethanolamine (AEEA) and triethylenetetramine (TETA), were also investigated.

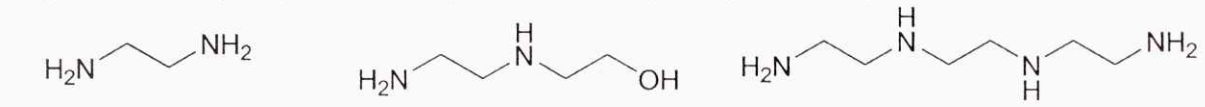

Figure 4-14. Chemical structures of polyamines investigated for electrochemical kinetics.

Half of the amine groups in both AEEA and TETA are less reactive secondary amines; this leads to weaker complexation of the cuprous intermediate, cupric ions, and CO_2. The competing effects of a lower activation energy with a less stable intermediate makes it unclear whether these amines would be expected to display faster or slower kinetics.

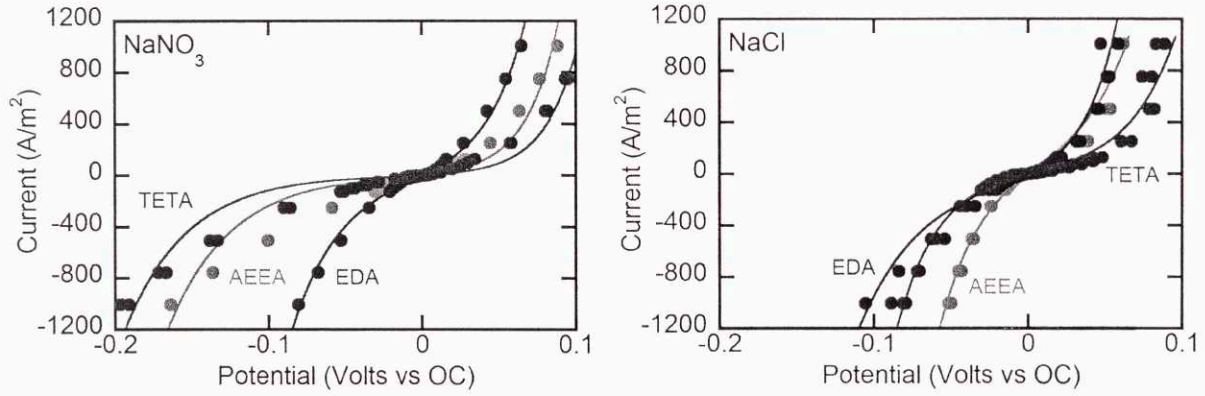

Figure 4-15. Current density as a function of overpotential for amine solutions with 0.25M $Cu(NO_3)_2$ and either 1M $NaNO_3$ (left) or 1M NaCl (right) under argon at 55°C.

Figure 4-15 shows that the kinetics of the three amines follow the order of EDA > AEEA > TETA under argon with 1M $NaNO_3$. All three amines follow a similar current potential curve defined by an electron transfer coefficient below 0.5, which implies lower anodic overpotentials than cathodic overpotentials.

With NaCl as the electrolyte, however, the order of the exchange current density switches to AEEA > EDA > TETA. While EDA shows no significant increase in its exchange current density with NaCl rather than $NaNO_3$, AEEA and TETA show approximately a four-fold increase with the chloride based electrolyte. Furthermore, the shape of the current/potential curves changes drastically with NaCl. As shown in **Table 4-5**, the electron transfer coefficients, α, increase from 0.37 and 0.35 to 0.56 and 0.53 for AEEA and TETA, respectively. This indicates that, unlike EDA, the chloride mechanism shown in Eq. 4-29 may be dominant in AEEA and TETA solutions even when under argon.

Table 4-5. Exchange current densities and electron transfer coefficients for different amines with 0.25M $Cu(NO_3)_2$ and either 1M $NaNO_3$ or 1M NaCl under argon at 55°C.

Amine	**EDA**			**AEEA**			**TETA**		
Anion	NO_3^-	Cl^-	NO_3^-/Cl^-	NO_3^-	Cl^-	NO_3^-/Cl^-	NO_3^-	Cl^-	NO_3^-/Cl^-
i_0 **(4-6)***	104.5	105.5	0.99	34.6	132.5	0.26	9.6	49.6	0.19
α **(4-6)**	0.35	0.37	0.96	0.37	0.56	0.66	0.35	0.53	0.66
i_0 **(4-9)****	50.3	32.5	1.55	35.8	47.4	0.76	16.7	15.3	1.09

* Calculated with Eq. 4-6. In units of A/m^2.
** Calculated with Eq. 4-9. In units of A/m^2.

AEEA respond similarly to EDA when saturated with CO_2. In the absence of NaCl, its exchange current density drops dramatically. In the presence of NaCl, the exchange current density returns to its non-saturated value. **Figure 4-16** shows the CO_2 saturated performance of EDA and AEEA with $NaNO_3$ and EDA, AEEA, and TETA with NaCl. The kinetics of CO_2-saturated TETA was not measured with $NaNO_3$.

In the presence of CO_2, AEEA displays the fastest electrochemical kinetics. The improvement of AEEA, with respect to EDA, under CO_2 is not surprising, and is predicted by Eq. 4-27. Since AEEA, has a lower free energy of CO_2 sorption, its kinetics will be hindered less than EDA.

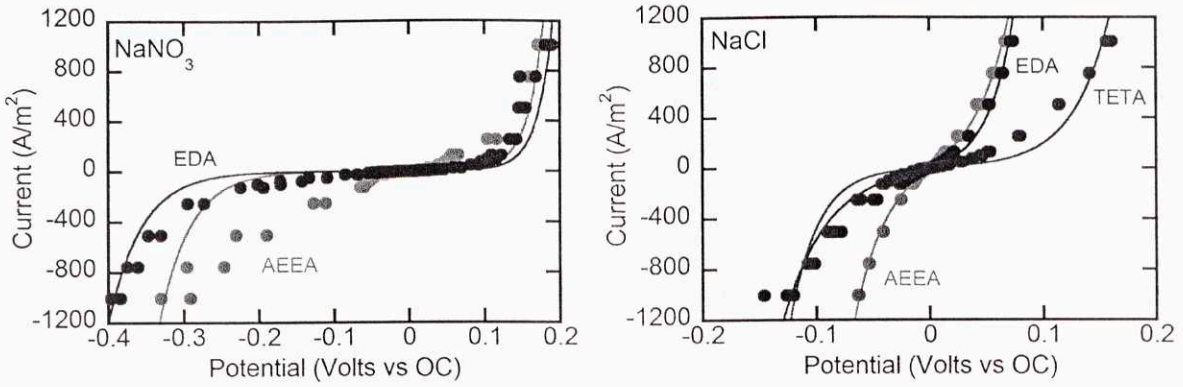

Figure 4-16. Current density as a function of overpotential for different amines saturated with CO_2 with 0.25M $Cu(NO_3)_2$ either 1M $NaNO_3$ (left) or 1M NaCl (right) at 55°C.

It is difficult to interpret the relative change for TETA, with respect to the two diamines, because the mechanism would go through a different intermediate cuprous species. In chloride environments, the significant shift of the electron transfer coefficient of both AEEA and TETA under argon and CO_2, indicates that they are both switching to a chloride-based mechanism. The mechanism does appear to still be dependent on the amine since the exchange current densities vary widely between the two amines.

Table 4-6. Exchange current densities and electron transfer coefficients for different amines with 0.25M $Cu(NO_3)_2$ and either 1M $NaNO_3$ or 1M NaCl under CO_2 at 55°C.

Amine	**EDA**			**AEEA**			**TETA**
Anion	**NO_3^-**	**Cl^-**	**NO_3^-/ Cl^-**	**NO_3^-**	**Cl^-**	**NO_3^-/ Cl^-**	**Cl^-**
i_0* (4-6)	0.15	39.1	0.004	0.44	121.4	0.004	8.89
***α* (4-6)**	0.31	0.35	0.89	0.36	0.59	0.61	0.57
i_0* (4-9)*	1.66	36.4	0.05	5.03	51.9	0.10	11.4

* Calculated with Eq. 4-6. In units of A/m^2.
** Calculated with Eq. 4-9. In units of A/m^2.

The Effect of Copper and Amine Concentrations

Eq. 4-17 shows that the exchange current density should be a function of the copper and amine concentration. Based on an electron transfer coefficient, α_3, of 0.5 (equivalently, α = 0.25), Eq. 4-30 shows how the exchange current density varies as a function of the copper loading, x_{Cu}.

$$i_0 \propto \sqrt{2(1-x_{Cu})}\,(x_{Cu})^{3/4} \qquad x_{Cu} = 2\frac{\text{Total } Cu^{2+} \text{ concentration}}{\text{Total EDA Concentration}} \tag{4-30}$$

The copper loading that maximizes the exchange current density for a given total EDA concentration can be calculated by taking the derivative of Eq. 4-30 with respect to x_{Cu}.

$$\frac{d\,i_0}{d\,x_{Cu}} \propto \frac{3-5x_{Cu}}{\sqrt[4]{x_{Cu}}\sqrt{2(1-x_{Cu})}} \xrightarrow{x_{Cu}=3/5} 0 \tag{4-31}$$

Through examination of the numerator of Eq. 4-31, the root of 3/5 can be determined. However, as shown in **Figure 4-17**, the exchange current density does not follow this behavior exactly. The exchange current density values obtained through Eqs. 4-6 and 4-9 loosely follow the expected pattern of a maximum around medium loadings and low values at low or high loadings. The exchange current densities fit with Eq. 4-6, only encompass data taken from -100 to 100 A/m^2 to avoid the problems of transport limitation.

The lines in **Figure 4-17** are obtained through least-squares fitting of the exchange current densities to Eq. 4-17 with two free parameters: a coefficient and α_3. For both curves, the optimized value for α_3 was found to be 0.95 (α = 0.47). Based on all the kinetic results reported for EDA at 55°C in the previous sections, the value for α_3 was expected to be closer to 0.7 (α = 0.35).

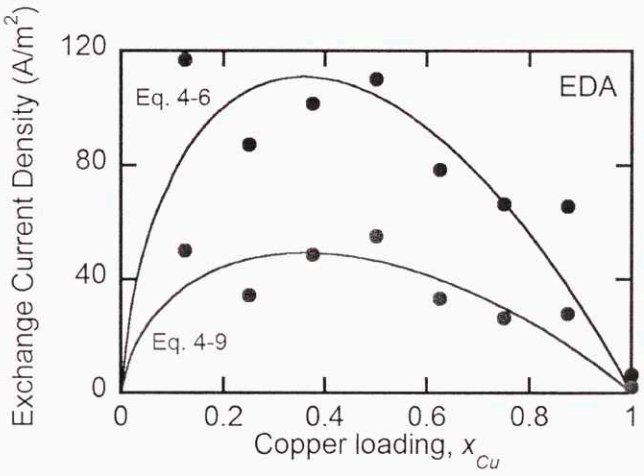

Figure 4-17. Exchange current density as a function of copper loading for 1M EDA solutions with 1M $NaNO_3$ under argon at 55°C. Values obtained from fits to Eqs. 4-6 and 4-9. Lines are least-squared fits to Eq. 4-17.

One explanation that can account for the difference in measured α_3 values is the effect of EDA concentration on the copper surface. If high concentrations of EDA leads to more reactive surface (presumably because oxides are less likely to form), then an exaggerated value for α_3 would be expected.

To test this hypothesis, two sets of experiments were performed: one at constant copper concentration with varying excess amine concentration, [EDA], and one at constant amine excess, with varying copper concentration, [Cu]. The results of the two experiments can be seen in **Figure 4-18**.

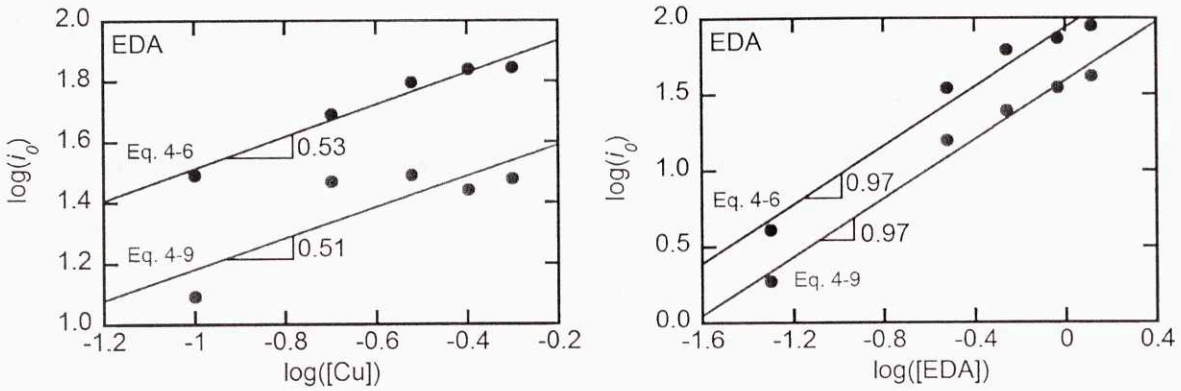

Figure 4-18. (Left) Log of the exchange current density as a function of $Cu(NO_3)_2$ concentration in a 0.5M EDA solution with 1M $NaNO_3$ under argon at 55°C. **(Right)** Log of the exchange current density as a function of excess EDA in a 0.1M $Cu(NO_3)_2$ solution with 1M $NaNO_3$ under argon at 55°C. Lines represent standard linear regressions.

The results are plotted in log-log plots because Eq. 4-17 predicts a linear relationships between $\log(i_0)$ and $\log([Cu])$ and $\log(i_0)$ and $\log([EDA])$. Eq. 4-32 shows the logarithmic form of the exchange current density from Eq. 4-17 with the front terms combined into an arbitrary constant, A. Through linear regressions, values of α_3 can be obtained.

$$\log(i_0) = \log(A) + \alpha_3 \log([EDA]) + \frac{2-\alpha_3}{2} \log([Cu]) \tag{4-32}$$

The results from **Figure 4-18** yield consistent values of α_3 of about 1 for both plots, in agreement with the results obtained from **Figure 4-17**, but different than the values obtained through fits of the current/potential curves using Eq. 4-6.

These conflicting results highlight the complexity of the system, where the concentration of EDA and Cu^{2+} may not only affect the kinetics through their role as reactants but also due their role in controlling the surface composition.

Pulse Dynamics

Because the data was analyzed through fitting of to the equivalent circuit shown in **Figure 4-4**, the dynamics can be investigated in addition to the steady-state values. In previous investigations of acid systems, it was reported that the pulse lengths needed to be long enough to deposit or remove several monolayers on the surface. In our analysis of both acid and amine systems, pulse lengths needed to be long enough to deposit or remove from 1 to 5 coulombs/m^2 in order to reach a steady state. This represents a few angstroms of deposition. Considering the 1.4 Å Van der Waals radii for copper, this agrees with the previous reports. Pulses with large cathodic currents required the most charge to equilibrate.

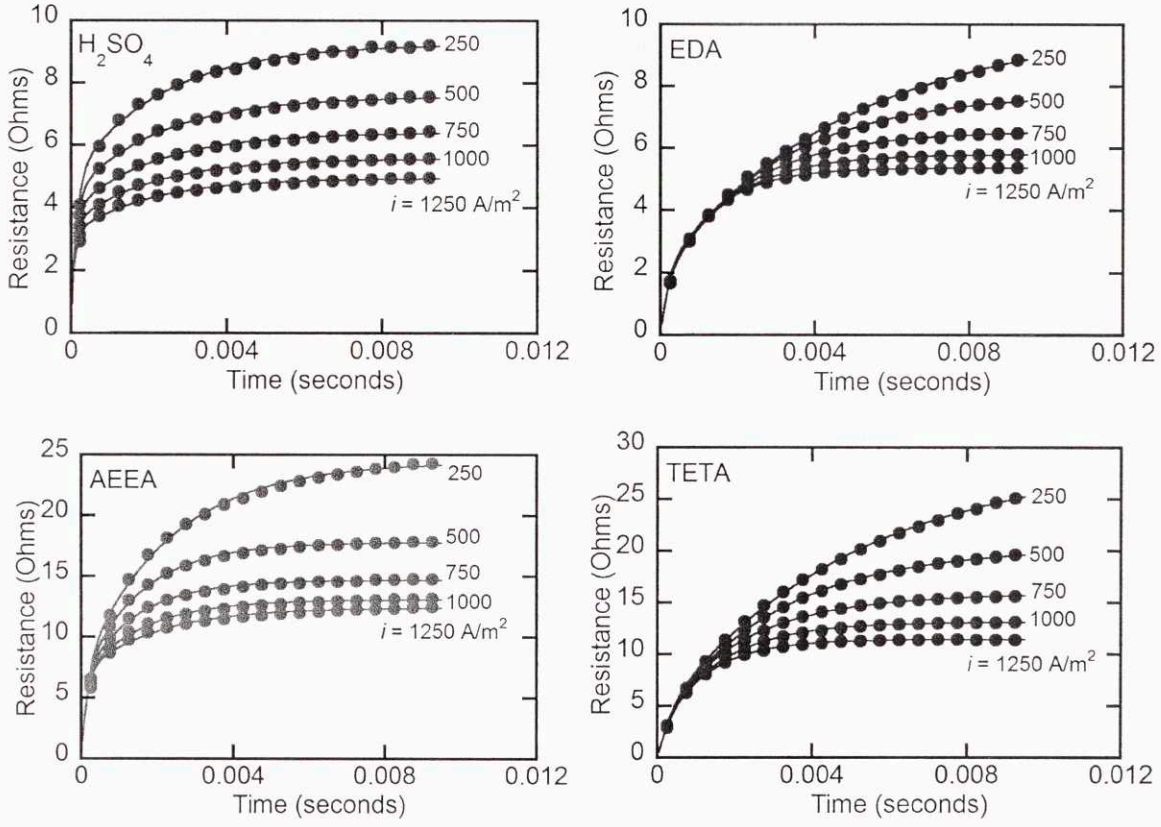

Figure 4-19. Anodic pulses of acid and amine systems at 55°C under argon. Only 2% of data points are shown. Lines represent least-square fits to the equivalent RC circuit model in Eq. 4-1.

Uncompensated resistances ranged from 5 to 10 ohms based on the temperature and electrolyte concentration. Acid systems, systems with nitrate salts, and systems under argon tended to have lower

uncompensated resistances. Capacitance values typically ranged from 50 to 100 $\mu F/cm^2$ for most systems. Acid systems, systems with chloride salts, and CO_2 saturated systems tended to have lower capacitances.

Because of the lower capacitance in acidic systems, the shape of the pulses differs significantly from the shape in amine systems. **Figure 4-19** shows pulses from acid, EDA, AEEA, and TETA systems. AEEA shows distinctly less capacitance (a steeper initial slope) than the other amines systems. Interactions between the surface and the hydroxyl groups in AEEA could be reducing the ability of ions to populate the double-layer.

Conclusions from Copper/EDA/CO_2 Kinetics

- While there exist many possible strategies for measuring the electrochemical kinetics of amine systems, galvanostatic pulse experiments were chosen for this study due to its prior success investigating copper kinetics in sulfuric acid systems.
- An equivalent circuit model was developed for analyzing the dynamic pulse experiments.
- Through application of Dissociative Electron Transfer (DET) theory to a sequential electron transfer mechanism with a stabilized intermediate, the similar kinetics between acid and amine systems was successful explained.
- The effects of temperature, electrolyte, CO_2 saturation, and reaction concentrations were investigated for three different amines. AEEA showed the best performance in CO_2-saturated systems, while EDA performed the best in systems under argon.
- Further investigation is required to determine if the addition of chloride salts, which significantly improves kinetics in CO_2-saturated systems, leads to unacceptable copper power formation in the solution. Without chlorides, the kinetics of CO_2-saturated systems are prohibitively slow and would require unacceptable overpotentials.

Chapter 5

Transport Modeling of EMAR

This chapter describes the development of analytical and numerical models for EMAR systems that specifically focus on mass transport phenomena. Flat plate electrode systems and systems with porous electrodes are both considered. In the flat plate electrode system, boundary layer development causes a significant decrease in transport if the solution is not remixed sufficiently. In the porous electrode system, careful consideration of the variation of the electrostatic potential through the electrode is required to accurately assess the current distribution. The models show that the porous electrode system is superior in terms of requiring lower overpotentials. Based on the most recent kinetic data, flat plate electrode systems will most likely operate at electrode overpotentials of near 100 mV per electrode, whereas porous systems could operate at near 50 mV per electrode for membrane current densities of 500 A/m^2.

The benchmark chemistry for these analyses will be based on the results for ethylenediamine with sodium chloride electrolyte from the previous two chapters. **Table 5-1** shows the pertinent data for the temperature dependent kinetics and thermodynamics. The same kinetics will be assumed for unsaturated and CO_2-saturated solutions. Thermodynamic and kinetic parameter values are given at 55°C but can be converted to different temperatures using the Arrhenius equation and the given reaction enthalpy or activation energy, respectively. A representative diffusion coefficient is also given, which is assumed valid for the cupric ions and amine molecules. A total amine concentration of 2M EDA was chosen because it would require a similar sorbent flow rate as a 7M MEA thermal scrubber.

Table 5-1. Thermodynamic, kinetic, and system parameters used in transport analysis based on results from Chapters 3 and 4. Values given at 55°C.

Name	Symbol	Value	Unit
CO_2 Sorption Equilibrium Coefficient	K_{CO2}	600	
Enthalpy of CO_2 Sorption	ΔH	-85	kJ/mole
Exchange Current Density	i_0	100	A/m^2
Electron Transfer Coefficient	α	0.35	
Activation Energy	E_a	50	kJ/mole
Diffusion Coefficient	D	10^{-9}	m^2/s
Total Amine Concentration	Am_0	2	mol/dm^3

Analytical Modeling of a Flat Plate System

Flat Plate Electrodes

Preliminary investigation into the overall performance of an EMAR system with flat plate electrodes has been done using an integral solution method to solve the partial differential equation resulting from the diffusion equation. In the solution, the fluid flow is assumed to be a fully-developed parabolic flow between two infinitely wide flat plates. The mass transport boundary layer is assumed to develop from the initial point ($x = 0$) over the course of the entire length of the plates ($x = L$). The length, L, can be imagined as the length before a turn in a serpentine channel design. The thickness of the channel, H, and the width of the channel, W, can be related to the length by: $L >> W >> H$. **Figure 5-1** shows schematic diagrams of a serpentine design of an EMAR flow channel.

The boundary condition at the electrode surface describes the $Cu(EDA)_2^{2+}$ complexes being generated or consumed (and EDA is either being consumed or generated). The surface flux is calculated using the previously introduced Butler-Volmer equation. The reaction at the surface causes the formation of a diffusion boundary layer, $\delta(x)$. To solve this problem, the Karman-Pohlhausen integral approach is used.[167,170] This method assumes the shape of the concentration profile within the boundary layer remains consistent through the whole boundary layer. The advantages of the integral approach are that the non-linear boundary conditions and profiles can be included without simplification. Most other analytical techniques require the application of the Leveque approximation, which linearizes the velocity profile and limits applicability to very small boundary layers.[167]

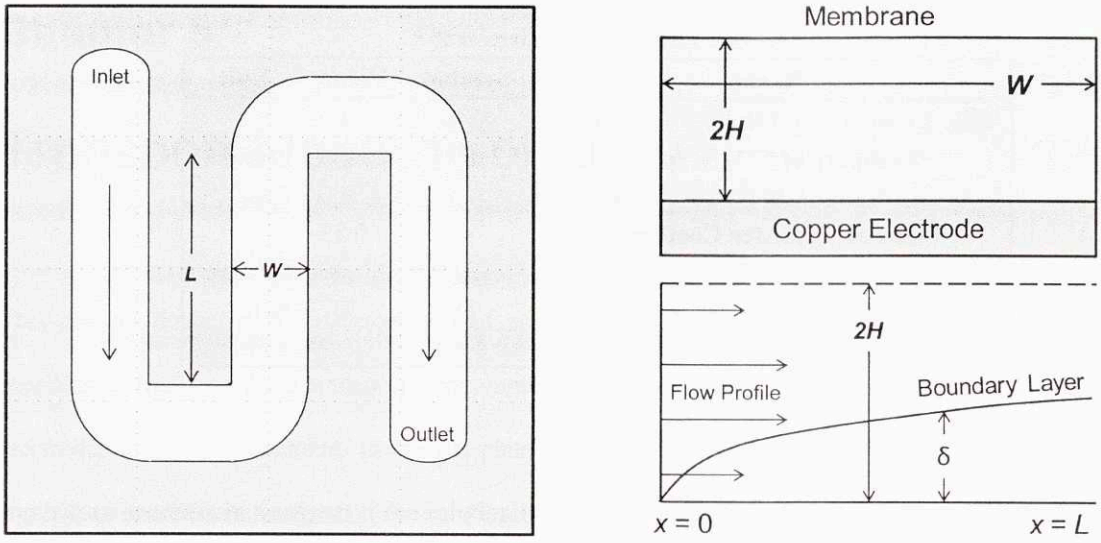

Figure 5-1. (Left) Diagram of a hypothetical flow designs for an EMAR system with flat plate electrodes. **(Top Right)** H-W cross-section of the channel. **(Bottom Right)** H-L cross-sectional view of the flow channel showing the parabolic flow profile and the boundary layer development.

The general diffusion equation defining the problem, for each species j, is:

$$u_x(y)\frac{\partial C_j}{\partial x} = D_j \frac{\partial^2 C_j}{\partial y^2} \quad , \quad C_j(x=0,y) = C_j^{Bulk} \quad , \quad \left.\frac{\partial C_j}{\partial y}\right|_{y=0} = -v_j \frac{i}{nFD_j} \quad , \quad \left.\frac{\partial C_j}{\partial y}\right|_{y=2H} = 0 \qquad (5\text{-}1)$$

Where

y = the spatial distance perpendicular from the electrode surface.

$u_x(y)$ = Solution velocity in the x direction as a function of y.

C_j = Concentration of species j.

C_j^{Bulk} = Initial and bulk concentration of species j.

D_j = Diffusivity of species j.

v_j = Stoichiometric coefficient of species j for the reaction at the copper electrode boundary.

i = current density at the electrode boundary.

Note that $y = 0$ represents the electrode surface and $y = 2H$ represents the membrane wall. This problem can be simplified through the use of non-dimensional parameters,

$$\left(2\eta - \eta^2\right)\frac{\partial \Theta_j}{\partial \xi} = \frac{\partial^2 \Theta_j}{\partial \eta^2} \quad , \quad \Theta_j(\xi = 0, \eta) = \Theta_j^{Bulk} \quad , \quad \left.\frac{\partial \Theta_j}{\partial \eta}\right|_{\eta=0} = -v_j \Psi \quad , \quad \left.\frac{\partial \Theta_j}{\partial \eta}\right|_{\eta=2} = 0 \qquad (5\text{-}2)$$

Where

$$\Theta_j = \frac{C_j}{C^0} \quad , \quad \eta = \frac{y}{H} \quad , \quad \xi = \frac{x}{Pe\,H} \quad , \quad \Psi_0 = \frac{i_0 H}{nFDC^0} \quad , \quad \Psi = \Psi_0 \frac{i}{i_0} \quad , \quad Pe = \frac{3}{2}\frac{UH}{D} \tag{5-3}$$

To simplify the problem we will assume that the diffusivities are all approximately equal. With equal diffusivities, C^0 can be defined such that the concentration of all states of EDA is $3C^0$ everywhere. Therefore,

$$[\mathrm{EDA}] + 2\left[\mathrm{Cu(EDA)}_2^{2+}\right] = 3C^0 \qquad \text{For all x,y} \tag{5-4}$$

We can then define the precise form of the Butler-Volmer equation as a function of Θ. Eq. 5-5 is derived by starting with Eq. 4-6, and then accounting for the difference in the actual surface concentrations from the standard state concentrations. Finally, the equation is made non-dimensional by application of the definitions in Eq. 5-3.

$$\begin{aligned} i &= i_0\left[\left(\frac{C_{EDA}}{C^0}\right)^2 \exp\left((1-\alpha)\frac{2F}{RT}\left(E-E^0\right)\right) - 2\left(\frac{C_{Cu}}{C^0}\right)\exp\left(-\alpha\frac{2F}{RT}\left(E-E^0\right)\right)\right] \\ &= i_0\left[\left(2\frac{C^0-C_{Cu}}{C^0}\right)^2 \exp\left((1-\alpha)\frac{2F}{RT}\left(E-E^0\right)\right) - 2\left(\frac{C_{Cu}}{C^0}\right)\exp\left(-\alpha\frac{2F}{RT}\left(E-E^0\right)\right)\right] \\ &= i_0\left[4(1-\Theta)^2\exp\left((1-\alpha)\phi\right) - 2\Theta\exp\left(-\alpha\phi\right)\right] \qquad \phi = \frac{2F}{RT}\left(E-E^0\right) \\ \Psi &= \Psi_0\left[4(1-\Theta)^2\exp\left((1-\alpha)\phi\right) - 2\Theta\exp\left(-\alpha\phi\right)\right] \end{aligned} \tag{5-5}$$

Where

C_{Cu} = Concentration the $Cu(EDA)_2^{2+}$ complex.

C_{EDA} = Concentration EDA.

Θ = Dimensionless concentration of the $Cu(EDA)_2^{2+}$ complex.

ϕ = The dimensionless potential.

E^0 = The standard state potential, where $E^0 = \frac{RT}{2F}\left[\ln C^{bulk} - 2\ln\left(3C^0 - 2C^{bulk}\right)\right]$

Now with the problem sufficiently defined, we can apply the integral approach to solve for the required potential based on the input parameters. We will use a fourth-order polynomial expression to describe the

concentration profile throughout the boundary layer. We will use the boundary conditions from Eq. 5-2 along with an additional constraint that the second derivative is zero at the electrode surface. This additional boundary condition is necessary (though not unique) to satisfy all of the unknowns of the polynomial function.

$$\Theta(s) = a_0 + a_1 s + a_2 s^2 \tag{5-6}$$

$$\Theta(1) = \Theta^{bulk} \quad , \quad \left.\frac{d\Theta}{ds}\right|_{s=0} = -\delta\Psi \quad , \quad \left.\frac{d^2\Theta}{ds^2}\right|_{s=0} = 0 \quad , \quad \left.\frac{d\Theta}{ds}\right|_{s=1} = 0 \quad , \quad s = \frac{\eta}{\delta}$$

Where δ is the dimensionless boundary layer thickness, which is a function of x, and s is the fractional vertical position in the boundary layer. Note that we have implicitly assumed that a definitive boundary layer exists, outside of which, the concentration is constant. An exact closed-form solution for $\Theta(s)$ can be obtained.

$$a_0 = \Theta_b + \frac{\Psi\delta}{2} \quad , \quad a_1 = -\Psi\delta \quad , \quad a_2 = \frac{\Psi\delta}{2} \tag{5-7}$$

$$\Psi = \frac{12 - 8\Theta_b + e^{-\phi}}{4\delta} + \frac{2e^{-\alpha\phi} + \sqrt{4e^{-2\alpha\phi} + \Psi_0^2\delta^2 e^{-\phi}\left(e^{-\phi} + 24\right) + \Psi_0\delta e^{-\alpha\phi}\left(4e^{-\phi} + 48 - 32\Theta_b\right)}}{4\Psi_0\delta^2}$$

From this solution, the profile and flux can be determined only if the boundary layer thickness, δ, is known. For boundary layer thickness of 2% (blue), 5% (green), and 10% (red) of the channel thickness, the surface concentrations, $\Theta(s = 0)$, and fluxes, Ψ, can be determined, as shown in **Figure 5-2**.

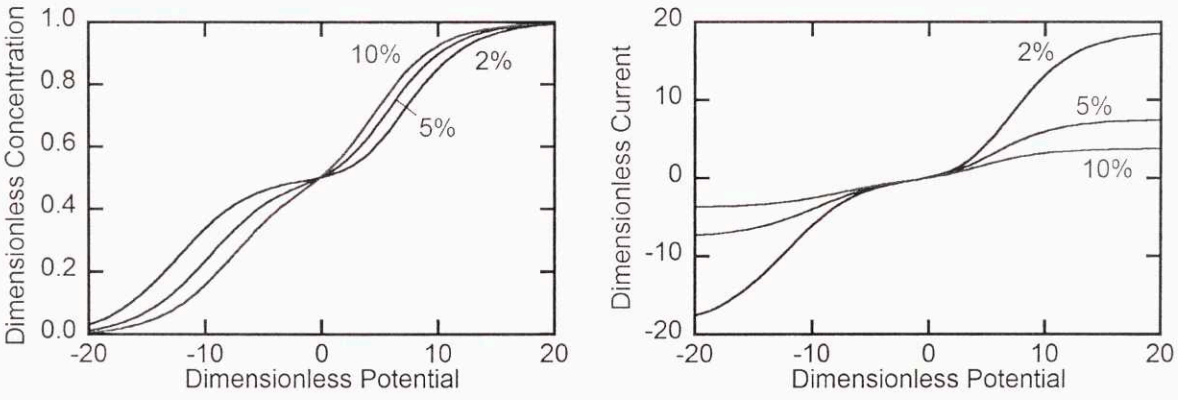

Figure 5-2. Dimensionless surface concentration (left) and dimensionless surface flux (right) as calculated through the integral solution strategy as a function of applied dimensionless potential for different boundary layer thicknesses.

Calculation of δ as a function of the axial position, ξ, can be achieved through consideration of a relationship between boundary layer growth, horizontal convective flux, and surface flux (current).

We start by vertically integrating the convective flux, Π, (the velocity multiplied by the concentration) over the entire boundary layer in Eq. 5-8.

$$\int_0^2 \left(2\eta-\eta^2\right)\Theta d\eta = \int_0^1 \delta^2\left(2s-\delta s^2\right)\Theta ds + \int_\delta^2 \left(2\eta-\eta^2\right)\Theta^{bulk} d\eta = \Pi \tag{5-8}$$

We can then take the derivative of the total convective flux with respect to the boundary layer thickness:

$$\frac{d}{d\delta}\left(\int_0^1 \delta^2\left(2s-\delta s^2\right)\Theta ds\right) = \frac{\text{Change in convective flux}}{\text{Change in boundary layer thickness}} \tag{5-9}$$

A simple shell balance on the growth of the boundary layer yields:

$$\frac{d\Pi}{d\xi} = \Psi \tag{5-10}$$

By multiplying both sides of Eq. 5-10 with $d\xi/d\delta$, we find:

$$\frac{d\xi}{d\delta}\frac{d\Pi}{d\xi} = \frac{d\Pi}{d\delta} = \Psi\frac{d\xi}{d\delta} \tag{5-11}$$

Rearrangement yields:

$$\frac{d\delta}{d\xi} = \Psi\left(\frac{d\Pi}{d\xi}\right)^{-1} \tag{5-12}$$

The term on the right hand side of Eq. 5-12 can be solved for analytically.

$$\frac{d\delta}{d\xi} = \frac{120\left[2e^{-\alpha\phi} - \sigma_1 e^{-(1+\alpha)\phi} + \Psi_0\delta\left(12-8\Theta_b+e^{-\phi}\right)\right]\delta^{-2}}{2\Psi_0\delta\left(120+10e^{-\phi}-80\Theta_b-36\delta-3\delta e^{-\phi}+24\delta\Theta_b\right)+\left(\delta^2\sigma_2-5\delta\sigma_2+4\delta\sigma_1-10\sigma_1+20e^{\phi}-8\delta e^{\phi}\right)e^{-(1+\alpha)\phi}}$$

$$\text{where} \quad \sigma_1 = \sqrt{4e^{2\phi} + \Psi_0^2 \delta^2 e^{2\alpha\phi}\left(1+24e^{\phi}\right) + 4\Psi_0 \delta e^{\alpha\phi} e^{2\phi}\left(12 - 8\Theta_b + e^{-\phi}\right)} \tag{5-13}$$

$$\text{where} \quad \sigma_2 = \frac{4\Psi_0 e^{\alpha\phi} e^{2\phi}\left(12 - 8\Theta_b + e^{-\phi}\right) + 2\Psi_0^2 \delta e^{2\alpha\phi}\left(1+24e^{\phi}\right)}{\sigma_1}$$

Calculation of the propagation of the boundary layer through integration is simple once the expression in Eq. 5-13 is obtained. It is, however, easier to solve for $\xi(\delta)$ based on the form of Eq. 5-13.

$$\xi(\delta) = \int_0^{\delta} \frac{d\xi}{d\delta'}(\delta')d\delta' \tag{5-14}$$

The integral in Eq. 5-15 is computed numerically because no closed-form analytical solution could be found. The integration is fast in comparison to a full finite element or finite difference solution to the problem posed in Eq. 5-2. When the profile for the boundary layer is solved, and hence the function $\delta(\xi)$, or its inverse, is known, the flux at every lateral position can be solved using Eq. 5-7. The averaged surface flux over the total remix length, L, is given by,

$$\Psi_{ave} = \frac{1}{\xi_{max}} \int_0^{\xi_{max}} \Psi(\xi) d\xi \qquad \xi_{max} = \frac{L}{Pe\,H} \tag{5-15}$$

To determine the energy consumption of the system, we will use the following values:

$H = 1\text{ mm}$, $C^0 = 1\text{ M}$, $C^{bulk} = 0.75\text{ M}$, $D = 10^{-9}\text{ m}^2/\text{s}$, $i_0 = 100\text{ A/m}^2$, $\alpha = 0.35$
$U = 0.1\text{ m/s}$, $Pe = 1.5\times10^5$, $\Psi_0 = 0.26$, $L = 0.1\text{ m}$, $\xi^{max} = 6.7\times10^{-4}$, $\Theta^{bulk} = 0.75$

Based on these values, the propagation of the boundary layer and the flux can be calculated. Assuming a desired current density of 500 A/m^2, the desired value of Ψ can be calculated knowing Ψ_0 and i_0.

$$\Psi = \Psi_0 \frac{i}{i_0} = (0.26)\frac{500\text{ A/m}^2}{50\text{ A/m}^2} = 2.6 \tag{5-16}$$

To determine the required potential, ϕ, to obtain the desired flux, the results can be calculated for a range of potential values. The left plot of **Figure 5-3** shows the propagation of the boundary layer in the anode for a range of dimensionless potentials. While higher potentials, which produce higher fluxes at the surface, do generate slightly thicker boundary layers, the differences in the boundary layer propagation

are small. This suggests that a single representative curve can be used effectively to represent the boundary layer thickness as a function of dimensionless position, $\delta(\xi)$. This would allow calculation of the flux as a function of position without the need to perform any integrals. In our results, the error from using a representative curve, $\delta(\xi) = 2.7\xi^{1/3}$, is under 2%.

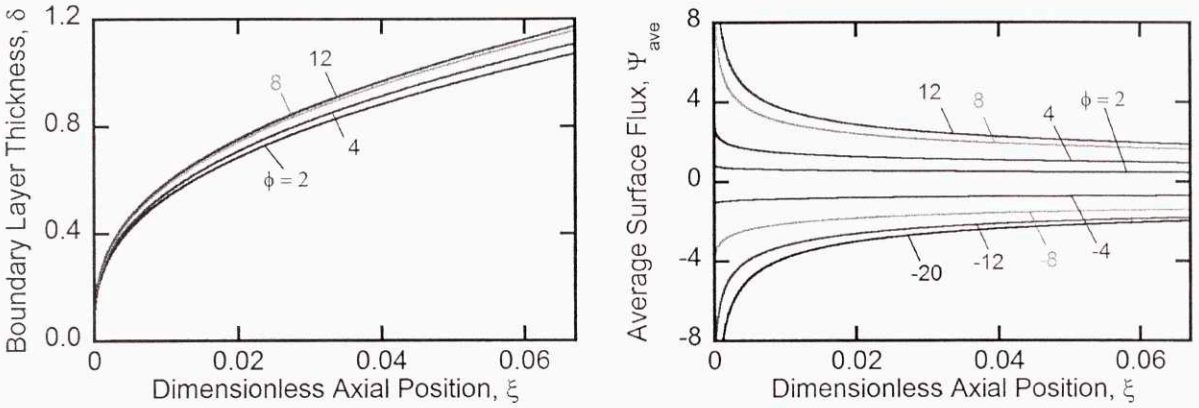

Figure 5-3. (Left) Dimensionless boundary layer thickness, δ, as a function of dimensionless axial position. **(Right)** Average dimensionless flux as a function of axial position.

Figure 5-3 shows the averaged dimensionless current as a function of position for a range of different anodic and cathodic potentials. Because of the small electron transfer coefficient, α, anodic currents are higher for a given magnitude of potential. For dimensionless anodic overpotentials greater than 2 dimensionless cathodic potentials more negative than -4, transport limitations significantly hinder the system performance. Maintaining values of the maximum dimensionless position less than 0.005 is essential for avoiding diffusion limitations.

The anodic results in **Figure 5-3** are compared with the similarity solution by Leveque[167] and numerical simulation in **Figure 5-4**. The Leveque solution assumes that only transport is limiting; hence, it should be equivalent to the other approaches at high potentials. The numerical solution is performed through the method of lines where the vertical coordinate is approximated with finite differences discretization and the lateral coordinate is solved through the coupled solution of the finite difference points with an implicit ODE solver.

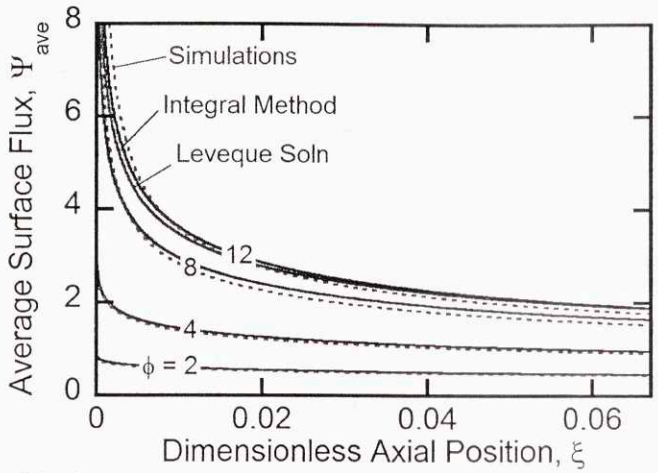

Figure 5-4. Comparison of the integral approach with numerical simulations and the Leveque similarity solution. Labels represent dimensionless potentials.

The conclusions that can be drawn from this derivation are that significant progress can be made in determining the transport limitations of this system with closed-form solutions based on an integral approach. Instead needing to solve a partial differential equation, which can be computationally intensive, the integral method requires only the solution of a single ODE (Eq. 5-12) and some algebra, which has been done computationally. Based on these preliminary results, current densities, up to 500 A/m^2, are possible with combined electrode overpotentials below 200 mV the dimensionless remixing length is kept low. The minimum possible overpotential for a system with no transport limitations would be 50 mV for the anodic side and 92 mV for the cathodic side.

Analytical Modeling of a Porous Electrode System

If electrode potentials below 100 mV per electrode are required, porous electrodes can be used to increase the effective electrode surface area. To model this system, a volume averaged approach is used to incorporate the reactions at the porous electrode as a volume generation term. Ohmic potential drops within the electrodes' pores are included in this model in order to accurately predict how the current density is distributed across the thickness of the porous electrode. The system is assumed to be well-mixed in the lateral direction (y direction). This assumption can be validated, as will be shown. Because

of the increased dispersion in porous media, and the bulk reaction as opposed to a surface reaction, the well-mixed assumption is reasonable. A diagram of the model can be seen in the **Figure 5-5**.

Analogous derivations have been performed for similar systems with different chemistries.[102,103] Application of the solution to model the performance of a full EMAR system has not, however, been done before. Inclusion of lateral concentration gradients has been done in literature through a perturbation approach by Newman. The impact of changing electrode morphology has been investigated by Alkire.[105] At high current densities, the addition of a diffusion resistance from the bulk to the electrode surface may also be required.[108]

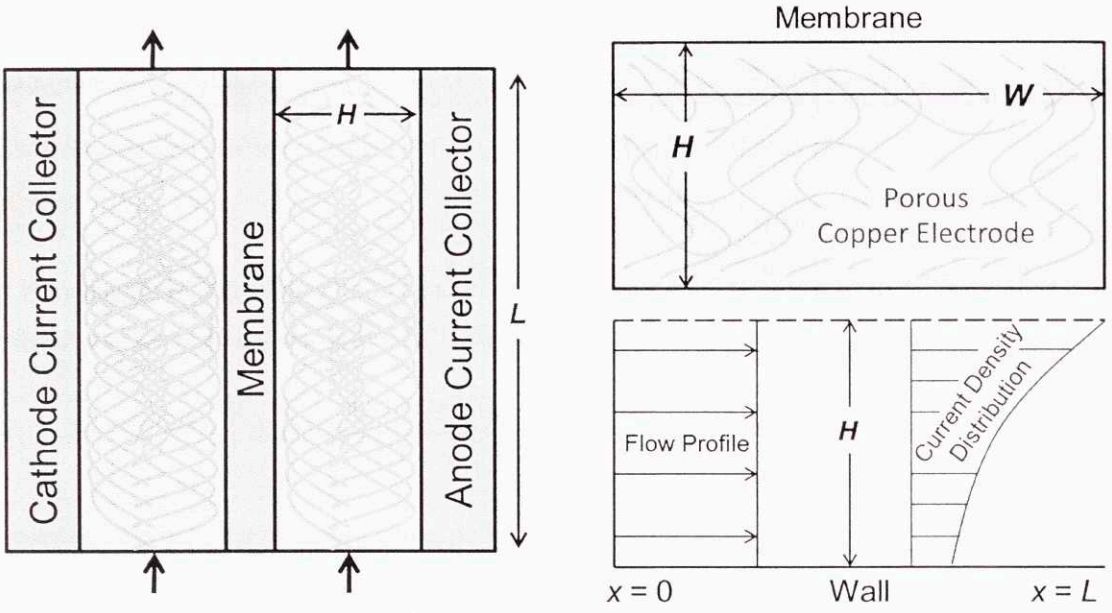

Figure 5-5. (Left) Diagram of the porous electrode flow system including both the anode and cathode sides. **(Top Right)** H-W cross-section of the channel. **(Bottom Right)** H-L cross-sectional view showing the flow profile and current density distribution.

Figure 5-4 shows the assumption of plug flow through the porous media. It also highlights the expected trend that the current density is highest near the membrane and drops off towards to wall. This occurs because current near the wall requires an equivalent ionic current to transfer ions through the solution to the membrane to maintain electro-neutrality. This incurs a higher Ohmic potential loss near the wall since the distance the ions must migrate is farther.

In the previous derivation for flat plates, calculation of the concentration gradients was the primary challenge; in the porous electrode systems we will initially assume the concentration gradients are negligible and focus on the gradient of the electrostatic potential laterally through the electrode. Where in the flat plate electrode problem we defined the voltage and calculated the current, for the porous electrode system, we will define the current density and calculate the required potential.

We start by considering only one side of the total electrochemical cell, either the anode or the cathode. At the membrane at some length down the device, x, there will be some predefined ionic current, j_M. We will define ionic currents with j and electronic currents with i. If we assume that the iso-potential lines are nearly parallel with the direction of fluid flow, then it follows that the ionic flux through the membrane will equal the integral of electronic fluxes in the perpendicular cross-section.

$$j_M(x) = S\int_0^H i(x,y)dy \tag{5-17}$$

Where S is the specific surface area of the porous electrode in units of inverse length. More generally, the ionic flux at any lateral position, y, can be calculated as,

$$j(x,y) = S\int_0^y i(x,y')dy' \tag{5-18}$$

The variation in the electrostatic potential, Φ, can be obtained through the differential form of Ohm's law.

$$\frac{\partial \Phi}{\partial y} = \frac{j}{\kappa} \tag{5-19}$$

Where κ represents the solution conductivity and is assumed constant through the system. Eqs. 5-18 and 5-19 can then be further related by describing the current, i, as a function of the electrostatic potential.

$$i = i_0\left[\exp\left((1-\alpha)\frac{2F}{RT}\left(\Phi - E^0\right)\right) - \exp\left(-\alpha\frac{2F}{RT}\left(\Phi - E^0\right)\right)\right] \tag{5-20}$$

In Eq. 5-20, both i_0 and E_0 will be functions of the reactant concentration. Combining Eqs. 5-18 to 5-20, we obtain a second order differential equation describing the system.

$$\frac{d^2\phi}{d\eta^2} = \frac{2Fi_0SH^2}{RT\kappa}\left[\exp\left((1-\alpha)\phi\right) - \exp\left(-\alpha\phi\right)\right] \qquad \text{Where} \quad \phi = \frac{2F}{RT}\left(\Phi - E^0\right) \quad , \quad \eta = \frac{y}{H} \tag{5-21}$$

Where it has been implicitly assumed that the variation in φ in the x direction happens only due to the different concentrations. In the y direction we have assumed constant concentration. The boundary conditions for this problem are the ionic fluxes at the current collector wall ($\eta = 0$) and at the membrane ($\eta = 1$).

$$j(\eta = 0) = \frac{\kappa RT}{2FH}\left.\frac{d\phi}{d\eta}\right|_{\eta=0} = 0 \quad , \quad j(\eta = 1) = \frac{\kappa RT}{2FH}\left.\frac{d\phi}{d\eta}\right|_{\eta=1} = j_M \tag{5-22}$$

To numerically solve this second order non-linear ODE, boundary value solving techniques like the shooting method or finite difference would be required due to the dual Neumann boundary conditions. Analytically, we can continue through definition of a new function, $\Gamma = d\varphi/d\eta$.

$$\Gamma = \frac{d\phi}{d\eta} = \frac{2FH}{\kappa RT} j \qquad , \qquad \Gamma\frac{d\Gamma}{d\phi} = \frac{d^2\phi}{d\eta^2} \tag{5-23}$$

Application of these definitions to Eq. 5-21 and the definition of $\varphi(\eta = 0) = \varphi_0$ yields,

$$\int_0^{\Gamma(\eta)} \Gamma d\Gamma = \frac{2Fi_0SH^2}{RT\kappa}\int_{\phi_0}^{\phi(\eta)} \left[\exp\left((1-\alpha)\phi\right) - \exp\left(-\alpha\phi\right)\right] \; d\phi \tag{5-24}$$

If we extend this out over the entire range, defining $\Gamma(\eta = 1) = \Gamma_M$, we obtain:

$$\frac{\Gamma_M^2}{4}\frac{RT\kappa}{Fi_0SH^2} = \frac{e^{(1-\alpha)(\phi_M-\phi_0)}-1}{1-\alpha}e^{(1-\alpha)\phi_0} + \frac{e^{-\alpha(\phi_M-\phi_0)}-1}{\alpha}e^{-\alpha\phi_0} \tag{5-25}$$

We can combine this with the definition from Eq. 5-23 and the result in Eq. 5-24,

$$\int_0^1 d\phi = \phi_M - \phi_0 = \int_0^1 \Gamma d\eta = \pm 2\left(\frac{Fi_0SH^2}{RT\kappa}\right)^{1/2}\int_0^1 \left(\frac{e^{(1-\alpha)(\phi(\eta)-\phi_0)}-1}{1-\alpha}e^{(1-\alpha)\phi_0} + \frac{e^{-\alpha(\phi(\eta)-\phi_0)}-1}{\alpha}e^{-\alpha\phi_0}\right)^{1/2} d\eta \tag{5-26}$$

With Eqs. 5-25 and 5-26, we have two equations and two unknowns, φ_M and φ_0. Solving the coupled ODE's allows for calculation of the flux and potential at every lateral location. Unfortunately, due to the complexity of the problem, a numerical approach is required.

The Tafel Solution (High Overpotentials)

If we assume large potentials (the Tafel approximation), such that only one of the exponential terms in Eq. 5-20 is significant, the analytical derivation can proceed further. Rewriting Eq. 5-26 based on this assumption with limits from 0 to η, we obtain:

$$\phi(\eta)-\phi_0 = 2\left(\frac{Fi_0SH^2}{RT\kappa}\right)^{1/2}\left(\frac{e^{(1-\alpha)\phi_0}}{1-\alpha}\right)^{1/2}\int_0^{\eta}\left(e^{(1-\alpha)(\phi(\eta')-\phi_0)}-1\right)^{1/2}d\eta' \tag{5-27}$$

Note that we have assumed $\varphi_M > \varphi_0 > 1$, which is true for the anode. This integral equation can be solved through differentiation of both sides with respect to η.

$$\frac{d\phi}{\sqrt{e^{(1-\alpha)(\phi(\eta)-\phi_0)}-1}} = \frac{2\arctan\left(\sqrt{e^{(1-\alpha)(\phi(\eta)-\phi_0)}-1}\right)}{1-\alpha} = 2\left(\frac{Fi_0SH^2}{RT\kappa}\right)^{1/2}\left(\frac{e^{(1-\alpha)\phi_0}}{1-\alpha}\right)^{1/2}\eta \tag{5-28}$$

Solving for $\varphi(\eta)$, we obtain,

$$\phi(\eta) = \phi_0 + \frac{1}{1-\alpha}\ln\left(\tan^2\left[\left(\frac{Fi_0SH^2}{RT\kappa}\right)^{1/2}\left((1-\alpha)e^{(1-\alpha)\phi_0}\right)^{1/2}\eta\right]+1\right) \tag{5-29}$$

Due to the sensitivity of the tangent function, it is clear that the term in the square brackets cannot equal more than $\pi/2$, or else the solution will fail. This would indicate that the result is only valid if $4Fi_0SH^2(1-\alpha) < \pi^2RT\kappa$. To obtain a second equation, we use the same Tafel assumption on Eq. 5-25, and solve for $\varphi(\eta)$,

$$\phi(\eta) = \phi_0 + \frac{1}{1-\alpha}\ln\left(\frac{\Gamma^2(\eta)}{4}\frac{RT\kappa}{Fi_0SH^2}\frac{1-\alpha}{e^{(1-\alpha)\phi_0}}+1\right) \tag{5-30}$$

Taking both Eqs. 5-29 and 5-30 to their limits of $\eta = 1$ yields two non-linear algebraic equations with two unknowns. Rearranging both equations and solving for φ_0 yields a single self-consistent equation.

$$\phi_0 = -\frac{1}{1-\alpha}\ln\left(4\frac{Fi_0SH^2}{\Gamma_M^2RT\kappa(1-\alpha)}\tan^2\left[\left(\frac{Fi_0SH^2}{RT\kappa}\right)^{1/2}\left((1-\alpha)e^{(1-\alpha)\phi_0}\right)^{1/2}\right]\right) \tag{5-31}$$

Using Eqs. 5-30 and 5-31, an accurate estimate of the required potentials can be readily obtained without significant numerical difficulty. Instead of needing to simulate two coupled ODE's, the entire system can be modeled easily with the calculation of one self-consistent non-linear algebraic equation. If lateral concentration gradients can be ignored, this solution acts as a lower bound for the required potential.

Figure 5-6 shows the distribution of overpotential, current density, and ionic flux as a function of lateral position. It can be seen that the distribution of current is more uniform on the cathodic side, which indicates that after many cycles, the distribution of copper in the porous electrode might shift. Specifically, the copper will tend to migrate away from the membrane.

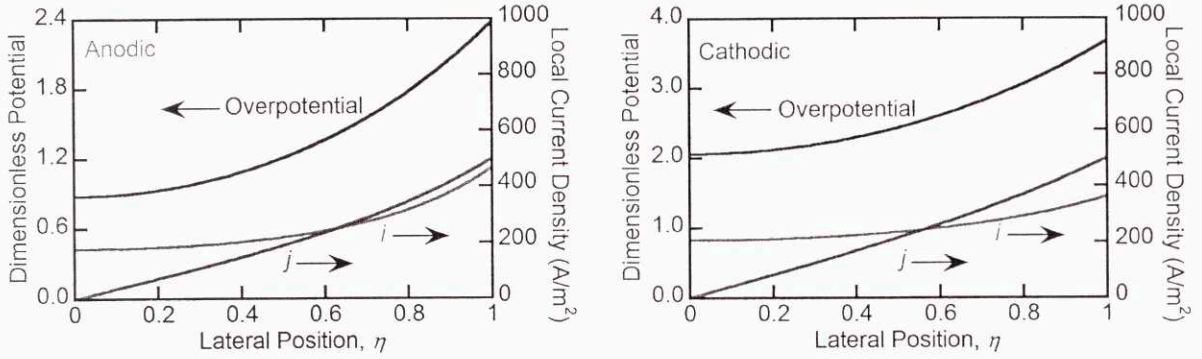

Figure 5-6. Overpotential, current, and ionic flux as a function of lateral position for a system operating at 500 A/m^2. Values calculated using the Tafel model. Other parameter values used can be found in the next section.

The Linear Solution (Low Overpotentials)

If however, we desire an upper bound to the required potential. We can solve the problem assuming a small required potential. To do this, the small-potential linear form of the Butler-Volmer equation (Eq. 4-9) is used to represent the current. This approximation, however, is only valid at low overpotentials. The linear form is a very poor approximation of the true exponential function if the magnitude of the exponent is greater than unity.

$$i = i_0 \phi \qquad \text{Only valid for: } |\phi| < 1 \tag{5-32}$$

Based on this definition, Eq. 5-21 simplifies to,

$$\frac{d^2\phi}{d\eta^2} = \frac{2Fi_0SH^2}{RT\kappa}\phi \qquad \left.\frac{d\phi}{d\eta}\right|_{\eta=0} = 0 \qquad \left.\frac{d\phi}{d\eta}\right|_{\eta=1} = \frac{2FH}{\kappa RT} j_m \tag{5-33}$$

This solution to this can be found easily as the sum of hyperbolic functions. Application of the boundary conditions yields,

$$\phi = \frac{2F}{\kappa RT}\frac{j_M H}{\lambda}\frac{\cosh(\lambda\eta)}{\sinh(\lambda)} \qquad \text{Where} \quad \lambda = \sqrt{\frac{2Fi_0 SH^2}{RT\kappa}} \tag{5-34}$$

The most important parameter to determine is the potential at the membrane, since that is equal to the applied potential in the cell. This is because the potential at the membrane surface experiences no Ohmic potential loss due to ion transport in the solution.

$$\phi_M = \frac{2F}{\kappa RT}\frac{j_M H}{\lambda}\coth(\lambda) \tag{5-35}$$

It is important to note that the system is linear with respect to the membrane current density, j_M. This means that doubling the desired flux doubles the required potential. The required potential can be calculated based on a set of realistic operating parameters.

$$H = 2 \text{ mm} \quad , \quad i_0 = 100 \text{ A/m}^2 \quad , \quad \alpha = 0.35 \quad , \quad S = 1000 \text{ m}^{-1}$$
$$\kappa = 20\frac{1}{\Omega \text{ m}} \quad , \quad T = 323.15 \text{ K} \quad , \quad \lambda = 1.20$$

Based on these above values we find that the membrane potential equals,

$$\phi_M = 0.0072 j_M \tag{5-36}$$

Considering the limits stated in Eq. 5-32, the linear solution is only valid for $j_M < 140$ A/m^2 under these conditions. More generally, the limit of j_M for a valid solution can be defined as:

$$j_M < \frac{\kappa RT\lambda}{2FH}\tanh(\lambda) \tag{5-37}$$

We can compare the results of the Tafel solution (Eqs. 5-30 and 5-31) with the results of the linear approximation shown in Eq. 5-35 using the parameter values stated above. **Figure 5-7** shows a comparison of total predicted overpotentials (the sum of anodic and cathodic) as function of the membrane current density.

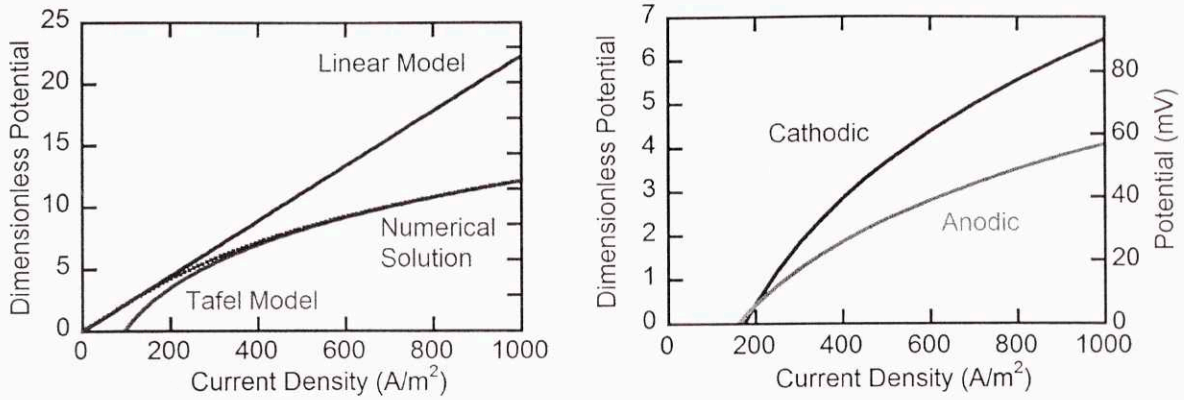

Figure 5-7. (Left) Required total overpotential as a function of current density for the linear and Tafel models and the numerical solution. **(Right)** Cathodic and anodic contributions to the total overpotential for the Tafel model.

The linear solution shows the linear profile as expected. The Tafel solution shows non-physical behavior below 100 A/m^2 due to the poor validity of the Tafel assumption in that region. Above 400 A/m^2, the Tafel model is an accurate approximation to the real solution, and represents the lower bound to the exact solution of the overpotential. The linear model, similarly, provides an effective upper bound.

Assuming no concentration gradients, the linear solution and the Tafel solutions represent precise upper and lower bounds to the system overpotentials. Based on the results, a porous electrode system could achieve current densities up to 1000 A/m^2 with overpotentials well below 100 mV per electrode. Even at 2000 A/m^2, the total overpotential is only 200 mV. This represents at least a four-fold current increase over the flat-plate electrode system. The breakdown of the anodic and cathodic contributions to the total overpotential for the Tafel solutions is also shown in **Figure 5-7**. For the linear solution, the contributions of the two sides are equal.

Lateral Concentration Gradients

All of these results have been with the assumption of no lateral concentration gradients. To consider the prevalence of lateral concentration gradients, we start with a shell balance on a differential lateral element with thickness, Δy. The thickness of the vertical element is Δx and there is a plug flow velocity in the vertical direction of U_x. Assuming steady-state, we obtain,

$$0 = \Delta y U_x \left(C(x) - C(x+\Delta x)\right) + D\Delta x \left(\left.\frac{dC}{dy}\right|_y - \left.\frac{dC}{dy}\right|_{y+\Delta y} \right) + \\ 2Fi_0 S \Delta x \Delta y \left[\exp\left((1-\alpha)\frac{2F}{RT}\left(\Phi - E^0\right)\right) - \exp\left(-\alpha \frac{2F}{RT}\left(\Phi - E^0\right)\right)\right] \tag{5-38}$$

By taking the limit of infinitesimal elements, we find,

$$-U_x \frac{\partial C}{\partial x} = D\frac{\partial^2 C}{\partial y^2} + \frac{i_0 S}{2F}\left[\exp\left((1-\alpha)\frac{2F}{RT}\left(\Phi - E^0\right)\right) - \exp\left(-\alpha \frac{2F}{RT}\left(\Phi - E^0\right)\right)\right] \tag{5-39}$$

In the previous derivations for the porous electrodes, we have assumed the diffusive term is negligible. To assess the importance of the terms, we switch to the non-dimensional form.

$$Pe\frac{\partial \Theta}{\partial \xi} = \frac{\partial^2 \Theta}{\partial \eta^2} + \Psi_0 \left[\exp\left((1-\alpha)\phi\right) - \exp\left(-\alpha\phi\right)\right] \tag{5-40}$$

$$Pe = \frac{U_x H}{D}\frac{H}{L} \quad , \quad \xi = \frac{x}{L} \quad , \quad \eta = \frac{y}{H} \quad , \quad \Psi_0 = \frac{i_0 S H^2}{2FDC^0} \quad , \quad \phi = \frac{2F}{RT}\left(\Phi - E^0\right)$$

To examine the formation of the concentration gradient, we must consider the gradient in the current density across the system. To do this, we differentiate both sides of the equation by η. For simplicity we will use the linear approximation of the current term from Eq. 5-32.

$$Pe\frac{\partial^2 \Theta}{\partial \eta \partial \xi} = \frac{\partial^3 \Theta}{\partial \eta^3} + \Psi_0 \frac{\partial \phi}{\partial \eta} \; Pe\frac{\partial^2 \Theta}{\partial \eta \partial \xi} = \frac{\partial^3 \Theta}{\partial \eta^3} + \Psi_0 \frac{\partial \phi}{\partial \eta} \tag{5-41}$$

Through substitution of the derivative of the potential with the value at the membrane described by Eq. 5-33, we obtain,

$$Pe\frac{\partial^2 \Theta}{\partial \eta \partial \xi} = \frac{\partial^3 \Theta}{\partial \eta^3} + \Psi_0 \frac{2FH}{\kappa RT} j_m \tag{5-42}$$

The coefficient of the generation term, Λ, is thus:

$$\Lambda = \Psi_0 \frac{2FH}{\kappa RT} j_m = \sqrt{\frac{2i_0 SFH^2}{\kappa RT}} \frac{H j_M}{2FDC^0} \tag{5-43}$$

A value of $\Lambda > 1$ indicates that the current density gradient is forming a concentration gradient faster than diffusion can dissipate that gradient. In a porous electrode system, we must consider that the effective dispersion in the porous medium will be about an order of magnitude higher than the molecular diffusivity. Thus, using a value of $D=10^{-8}$, we find $\Lambda=0.001 j_M$. Therefore, for membrane current densities below 1000 A/m^2, we find the concentration gradients should be mild, validating the above derivations. This result, however, is very sensitive to the electrode thickness, H. For channels thicker than a few millimeters, significant concentration gradients will form.

Full-System Modeling

To extend the results for the flat plate or porous electrode systems, the solutions must be applied to an entire system accounting for the change in concentrations and loadings along the x-direction. The primary effect of the varying concentration is change in i_0, but some secondary parameters, such as the diffusivity and conductivity, can also be affected. In full-system modeling, additional inefficiencies such as those mentioned in the thermodynamics chapter can be included. Ohmic potential drops due to membrane resistance should also be included. Finally, electrical power requirements of auxiliary pumps and compressors can also be added for a truly detailed analysis as will be shown in Chapter 7.

Full-system modeling is necessary to determine the range of copper loading desired in the system. As was shown in the kinetics chapter, high copper loadings lead to poor kinetics (i.e., small exchange current densities). Under these conditions the required potentials will rapidly increase, lowering overall efficiency. Eq. 5-44 shows the dependences of the exchange current density, i_0, on the free amine concentration, [EDA], and the cupric ion concentration, [Cu], reported in the kinetics chapter.

$$i_0 \propto C_{EDA} C_{Cu}^{1/2} \propto (1 - x_{Cu})(x_{Cu})^{1/2} \tag{5-44}$$

We can plot the required potential according to the porous electrode model as a function of copper loading, x_{Cu}. From 0 to 5% loading and from 90 to 100% loading, the required potentials rise quickly. **Figure 5-8** shows the required dimensionless potential to maintain a constant 500 A/m^2 membrane current density for both the flat plate and porous electrode geometries.

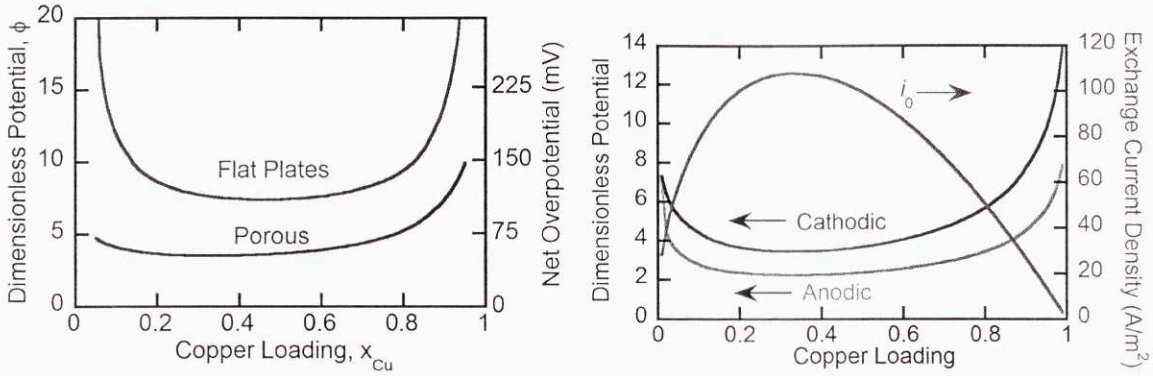

Figure 5-8. (Left) Required potential as a function of copper loading for a porous electrode system based on the Linear and Tafel models. **(Right)** Cathodic overpotential, anodic overpotential, and the exchange current density as a function of copper loadings based on the Tafel model and Eq. 5-44.

Conclusions from Transport Modeling

- Flat plate electrode systems should be capable of operating at overpotentials below 100 mV per electrode. This is 40% greater than the value required for a system with no transport limitations. Further gains can be achieved through increasing exchange current densities or lowering the desired current density.
- Porous electrode systems should be capable of operating at overpotentials below 50 mV per electrode. While they are clearly superior to flat plates, porous electrodes due pose greater operational challenges, most notably, the entrapment of bubbles within their pores.
- Both systems may have issues with non-uniform deposition and dissolution, leading to instability of the electrodes over time. Flat plate systems will have currents that vary over the length of the electrode, while porous electrodes will also have variations laterally.
- Both flat plate and porous electrode systems are sensitive to the exchange current density, which in turn is sensitive to the copper loading. Full system models are necessary to identify the ideal range of copper loadings. At the extremes of copper loading, required potentials rise quickly.
- Analytical models, which highlight important dimensionless groups of parameters, are extremely useful for the initial analysis and design of EMAR systems.

Chapter 6

Bench-Scale Demonstration of EMAR

Based on the thermodynamic, kinetic, and transport analyses of the previous three chapters, the EMAR system should be capable of CO_2 separation, and under the right conditions, efficient separation. In this chapter, the results from a proof-of-concept device will be presented and discussed. The small prototype system was designed to capture up to 10 mL/min of CO_2, but does possess several shortcomings. The system only operates at ambient pressure and temperature, which are rather far from the ideal operating conditions of approximately 70°C and at least 5 bar. Even with the non-optimized design, the system did successful demonstrate the ability of an EMAR device to capture CO_2.

The primary performance metrics were Faradaic efficiency and the work of separation. Faradaic efficiencies reached an impressive 80% in some experiments, and could increase further with an optimized system. The work of separation ranged from 20 kJ/mole at low fluxes to about 100 kJ/mole at fluxes relevant for real-world application.

Important design issues, including the use of porous electrodes and chloride salts, were investigated with the bench-scale system. The performance of porous electrode systems started quite high, but decayed over time due to bubble entrapment in the electrodes. Chloride-based salts did reduce the required operating potentials, but also lowered the Faradaic efficiency, caused noticeable copper powder generation in the anode, and corroded the aluminum chassis. The below unity Faradaic efficiency indicates undesirable crossover of certain species across the membrane with either salt.

The lessons learned in the device construction were invaluable for the development of future systems. In the next chapter, the development next-generation experimental setups and industrial-scale system will be considered. The geometry, materials, and peripherals of future experimental and industrial EMAR designs are based on heavily on the successes and failures of the proof-of-concept system.

Electrochemical Cells Design

Progression of Electrochemical Cells

The proof-of-concept system, which will be the primary focus of this chapter, was the fourth-generation electrochemical cell designed for electrochemical CO_2 capture. The primary material of construction for the four systems progressed from PVC, to polypropylene, to polycarbonate, to aluminum. The polycarbonate system slowly swelled due to the aqueous amine solutions, and was not a stable construction material. The PVC system was tested with a different chemistry, and, therefore, its long-term stability with aqueous amine solutions is unknown. Both the polypropylene and aluminum systems are indefinitely stable in aqueous amine solutions. In the presence of chlorides, however, the aluminum will undergo galvanic corrosion if contacting copper.

The second generation system, while well-constructed, chemically-resistant, and water-tight, has a poor geometry for electrochemical flow reactions. Pictures of the disassembled cell with and without the porous glassy carbon electrode can be seen in **Figure 6-1**. A picture of the assembled cell and a schematic diagram of the device can be seen in Figure 6-2. The flow channel is 1/2" deep, which is far too deep for effective use of the electrode. As was shown in the previous chapter's discussion of transport in porous electrode systems, Ohmic potential drops across a porous electrode are significant. While the 2nd generation system might boast an impressive total electrode surface area, only 25% of it is useful.

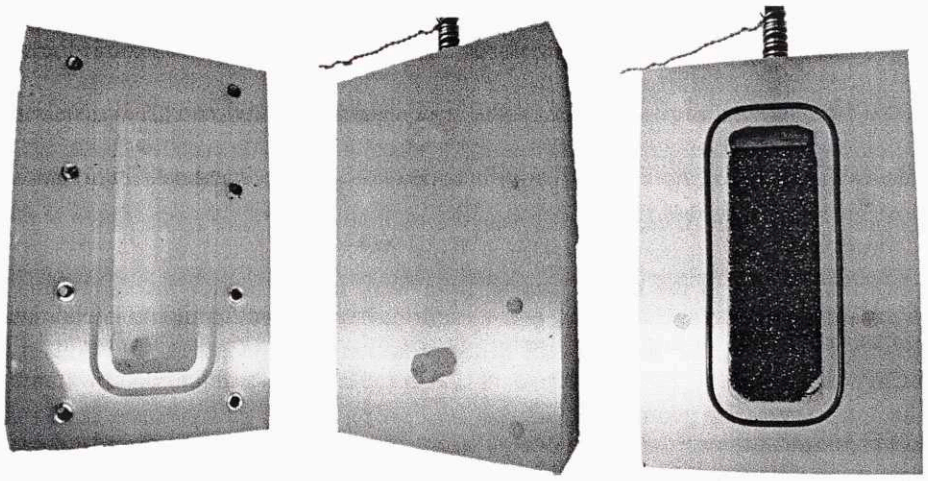

Figure 6-1. Pictures of the second generation electrochemical flow cell with and without the porous electrode.

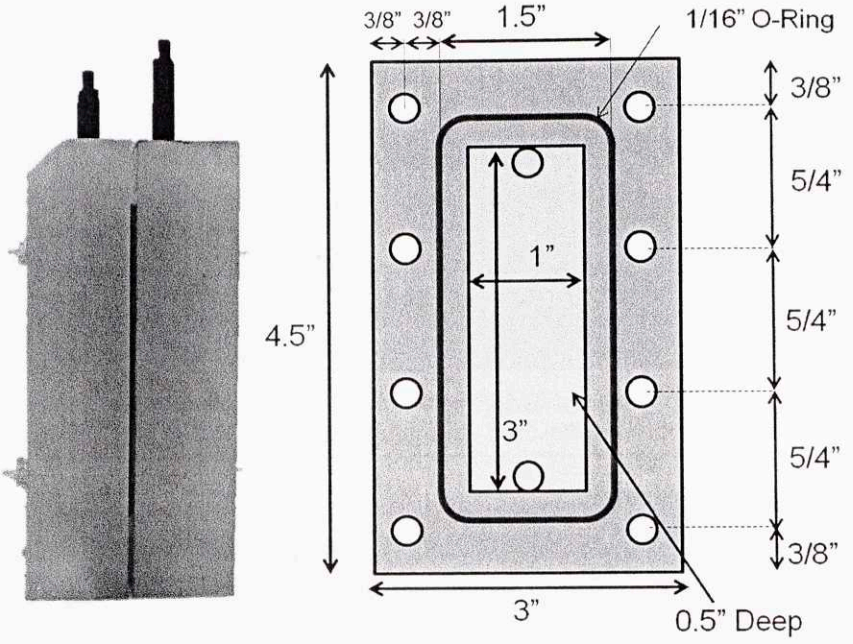

Figure 6-2. (Left) Side-view picture of the assembled cell. **(Right)** Schematic diagram of the cell.

EMAR 3

The third generation system was designed and constructed effectively. Unfortunately, due to the use of polycarbonate, which was chosen for its transparency, the system lacked stability over long experiments. **Figure 6-3** shows a schematic diagram used for the fabrication of the third generation device. Each side of the polycarbonate chassis had 14 bolt holes (designed for size 6-32 bolts) around the outside to allow for tight assembly of the system. Inside those bolt holes was a thin channel cut 0.0825" deep for a 3/32" silicone O-ring (#169). Inside the O-ring channel, a large area was milled to create the flow channel for the system. In the 1/4" deep section, a 1/8" thick copper plate would be placed. Once the plate was in, the entire flow area would be 1/8" inch deep.

This system was originally designed for use with 1/8" porous copper electrodes that would sit in the 1/8" inch flow channel. Not shown in the diagram are the holes drilled at the ends of the flow channel for inlet and outlet flows. Those holes were tapped with size 10 screw threading for the attachment of female Luer Lock fittings. Another hole was also drilled in the center of the chassis to allow for an electrical connection to the copper plate through the back of the system.

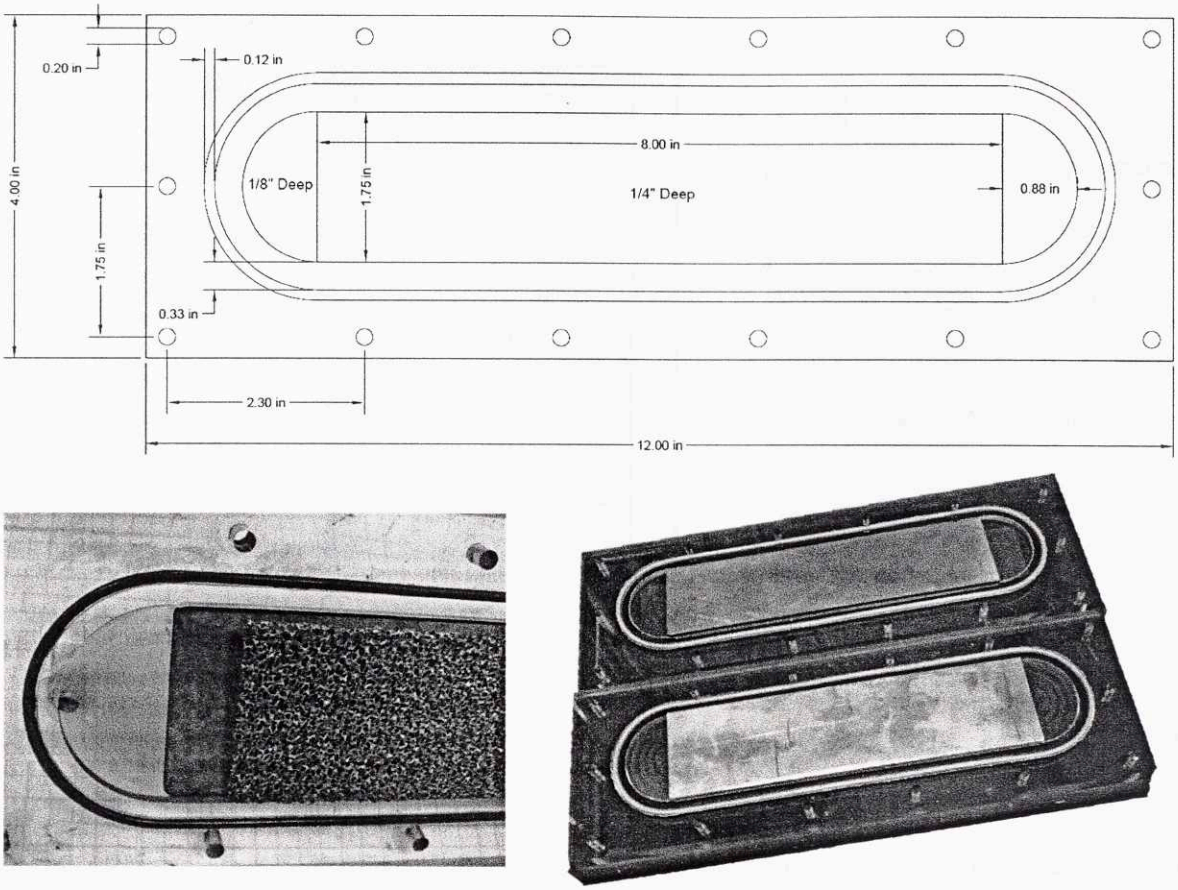

Figure 6-3. (Top) Schematic diagram of the 3rd generation EMAR flow system. **(Left)** Picture of the system with the porous copper electrode. **(Right)** Picture of both sides of the device with just the copper plates.

While its useful life was short, the system did not leak and was effective. The third generation device initially demonstrated the ability to inflate a balloon with captured CO_2 using an EMAR system. Pictures of those initial experiments can be seen in **Figure 6-4**. Another shortcoming of this system was the difficulty of electrically connecting the electrode to an external power supply. A hole was drilled in the center of the chassis to connect to the 1/8" copper plate; this however, was difficult to do accomplish without leaks.

One important difference between the 3rd and 4th generation systems was that Nafion was used as the membrane with the 3rd generation system. A picture of the membrane after operation can be seen in **Figure 6-5**. Note the significant discoloration due to impregnation with the copper/amine complexes. Despite the coloring, the membrane did appear to be stable and was effective.

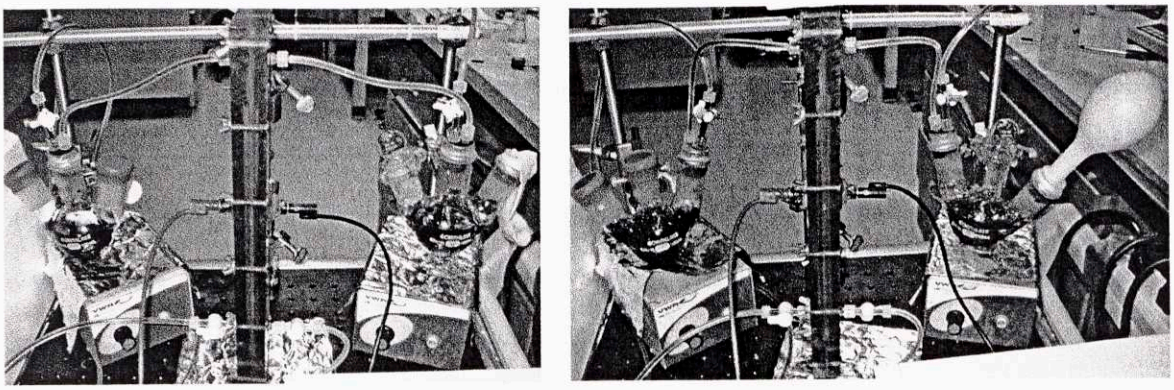

Figure 6-4. Pictures during the operation of the 3rd generation EMAR system at the start of the experiments (left) and after an hour of operating the system (right). The balloon has been inflated with the captured CO_2.

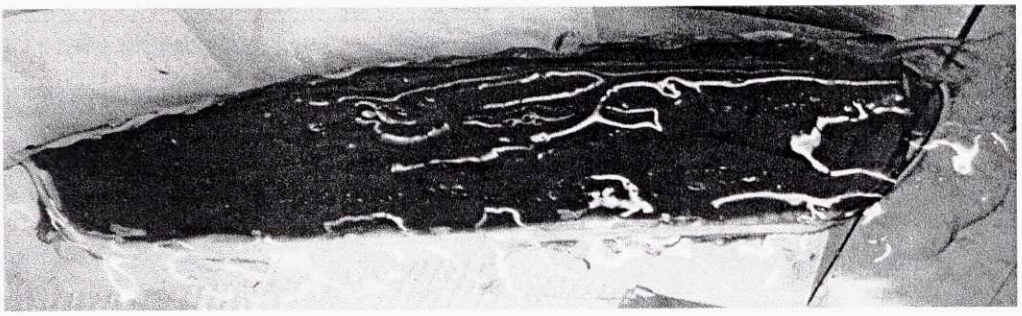

Figure 6-5. Picture of the Nafion membrane used in the 3rd generation EMAR system after operation.

EMAR 4

The fourth generation electrochemical cell, EMAR 4, will be the focus for the remainder of the chapter. The design emphasized ease of construction, versatility of the flow geometry, and stability. The initial design also included the ability measure electrode overpotentials with open-circuit copper wires. A detailed schematic of the EMAR 4 aluminum chassis used for fabrication can be found in Figure **6-6**. The aluminum chassis pieces are constructed from 1/2" thick aluminum plates.

The holes drilled around the outside of the aluminum plates are bolt holes. The two aluminum plates are pressed together through bolt and nut assembly. In the previous generation plastic systems, one side of the chassis had threaded bolt holes, which led to quicker and easier assembly of the device. This strategy was not used because of fears that this would lead to a short circuit of the two sides of the chassis via an electrical connection through the bolt. By using bolt and nut assembly, electrically insulating washers could be placed to insulate the nut and bolt from the aluminum chassis plates.

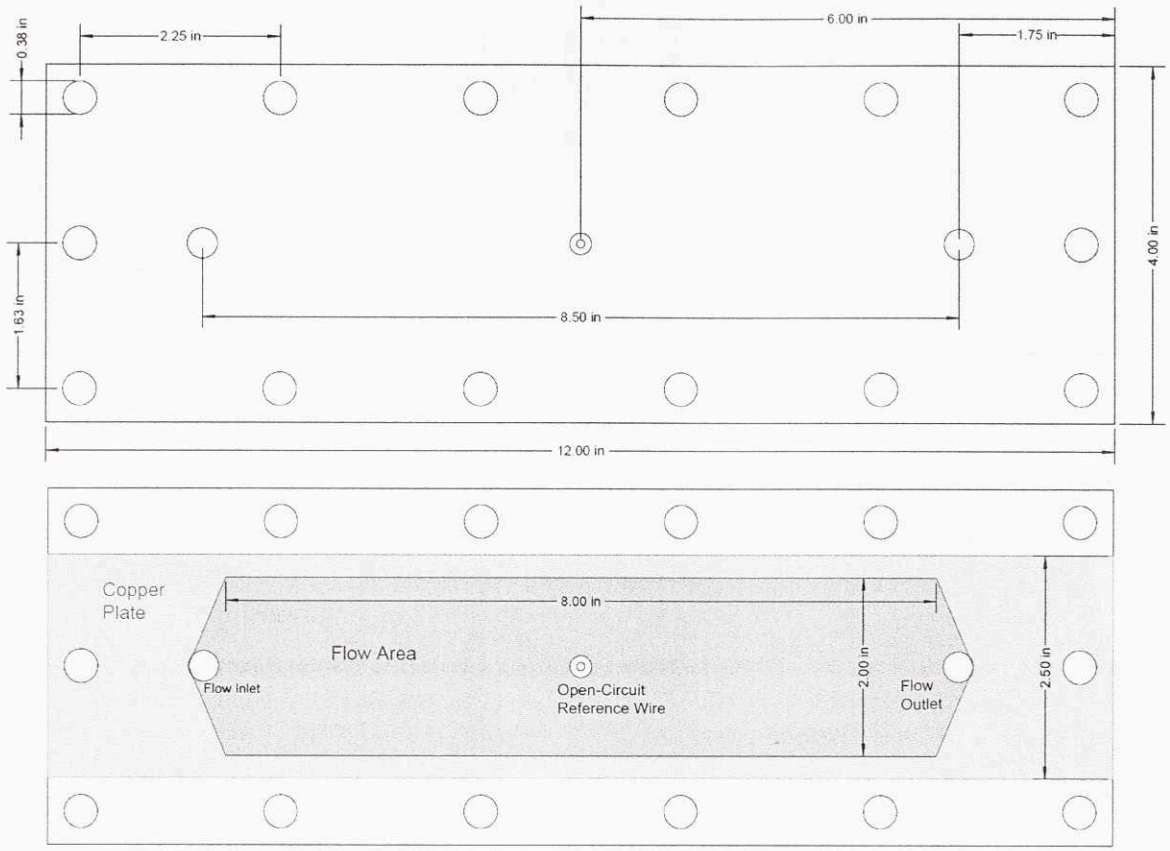

Figure 6-6. (Top) Schematic diagram of the aluminum chassis pieces for the EMAR 4 electrochemical flow cell. **(Bottom)** Chassis piece diagram with the copper plate and flow area highlighted. The flow area is created from a gasket (not shown) placed on top of the copper plate with a cutout in the shape of the flow area.

Holes were drilled in the side of each plate to allow for the electrical connections via banana clips. One advantage of the aluminum chassis is that it can also be used as a current collector. Instead of connecting the power supply to the copper electrodes, the connection can be made to the aluminum instead, which is more accessible and less fragile. As will be discussed later, however, connecting two metals with significantly different oxidation potentials does create an environment predisposed to galvanic corrosion.

The two holes at the ends of the flow channels are the inlet and outlet of the working fluid. The holes in the aluminum were tapped to create 1/8" NPT threads. Polypropylene or Kynar fittings that convert 1/8" NPT to male Luer Lock were inserted into the plates through the threaded inlet and outlet holes. This allowed for easy connection of EMAR 4 to the liquid distribution system, which was constructed from PVC Tygon tubing with barbed fittings.

The hole in the center of the aluminum chassis was tapped to create a 1/16" NPT threading. This allowed for a small 1/16" NPT to 1/16" barbed fitting to be connected from the outside of the chassis. A copper wire was passed through the fitting to rest just inside the device. This wire was insulated from the main copper electrodes by a small piece of Teflon tubing to allow for the measurement of electrode overpotentials. The overpotential would be equal to the difference in potentials of the main electrode and the copper wire.

The main copper electrodes are 1/16" thick plates of copper alloy 101 (99.99% copper) with holes punched in the same positions as the chassis holes. The bolt holes on the sides of the chassis are not duplicated on the copper plate, however, because the aluminum and copper do not overlap on the sides. The lack of overlap on the sides is because the copper is only 2.5" wide, while the aluminum is 4" wide. The two bolt holes that are centered at the top and bottom of the device are punched through the copper plate.

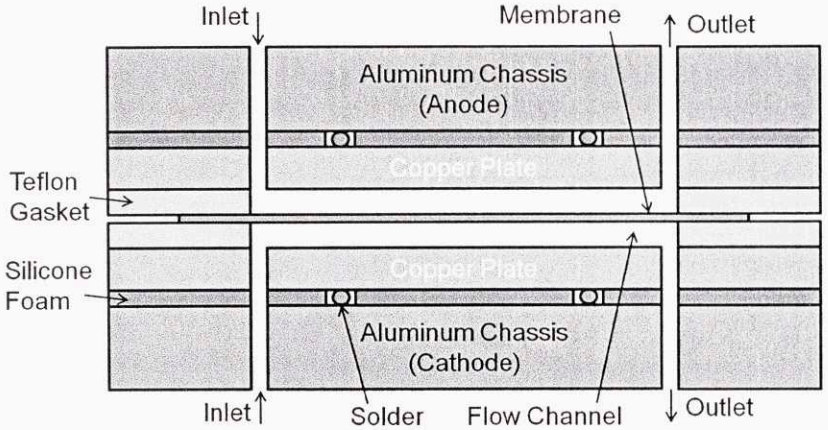

Figure 6-7. Cross-sectional view of EMAR 4 showing the aluminum, foam, copper, gasket, and membrane construction. The open-circuit reference wire is omitted from the diagram.

One challenge in this construction was the space between the aluminum and copper plate. It was difficult to prevent liquid from settling in the small gaps between the two pieces of metal. This problem was addressed by putting a highly compressible sheet of closed-cell silicone foam in between the copper plate and the chassis. This, however, eliminated the electrical connection between the chassis and the copper plate, which was one advantage of using a metal for the chassis. This problem was solved by cutting out

two square sections of foam and placing solder between the copper and aluminum in those sections. A schematic diagram of the chassis, foam, and copper construction is shown in **Figure 6-7**.

Flow Channel and Membrane Design

To create the flow channels for the aqueous working fluid, silicone or Teflon gaskets were placed on top of the copper plate electrodes. When operating with porous copper electrodes, 1/8" silicone gaskets were used. When operating with flat plate electrodes, a 1/32" gasket was use to promote high flow rates and reduce mass transfer limitations. The shape of the flow channel was controlled by the shape of the cutout of the gasket. A picture of a 1/32" silicone gaskets can be seen in **Figure 6-8**. The 2" x 8" shape created a membrane surface area of approximately 103 cm^2. Compared with the O-ring construction of the two previous generation systems, the gasket design was far more prone to leaking.

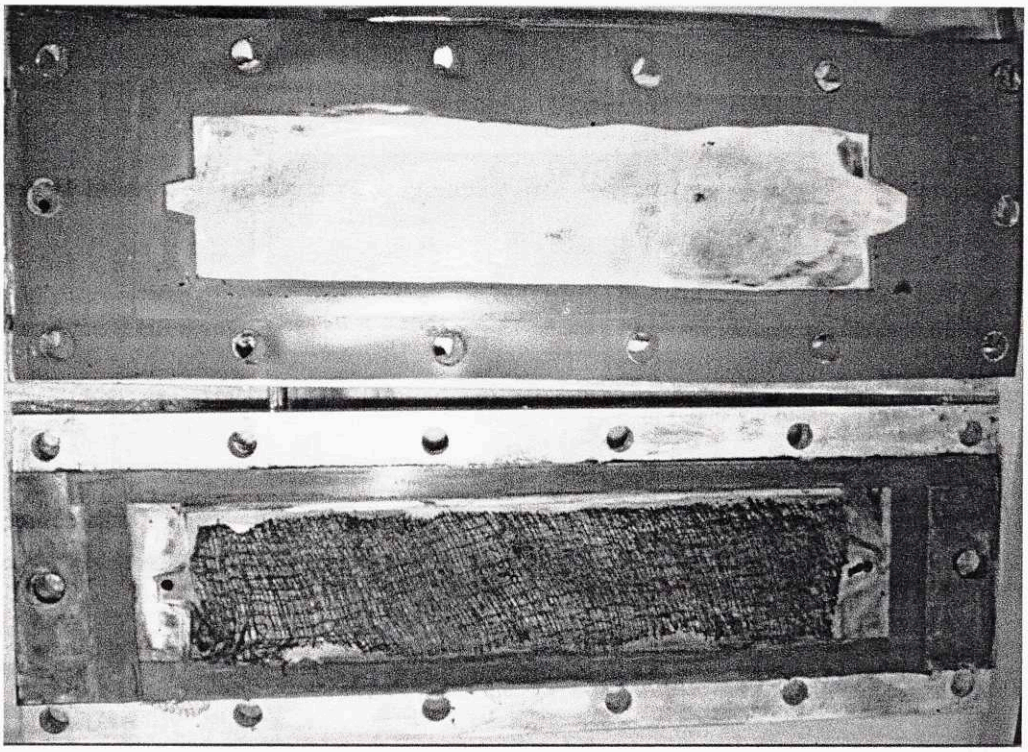

Figure 6-8. (Top) A silicone gasket sitting on top of a Celgard membrane. **(Bottom)** The EMAR chassis and copper plate with cheesecloth on top. The purple color is from contact with the amine and copper complexes.

The membrane was placed in between the gaskets from each side of the device to prevent convection and diffusion between the anode and cathode chambers. The membranes used were Celgard® 3501

surfactant-coated porous polypropylene membranes. These membranes do allow migration of ions, which maintains electro-neutrality through the device. A consistent challenge was preventing the membrane from touching the copper plate electrodes directly. If the membrane was in direct contact with the electrode, copper would grow through the membrane during operation leading to a short circuit. A picture of this is seen in **Figure 6-9**.

Many strategies were attempted to prevent direct contact between the membrane and electrode. The most successful was placing fabric between the membrane and the electrode. Both cheesecloth and butter muslin were effective. Putting a Teflon mesh between the membrane and electrode prevented transport to the electrode, which caused copper salts to precipitate on the electrode surface; these salts built up until they completely inactivated the electrode surface. The hydrophobicity of the Teflon is what caused it to fail compared to the hydrophilic fabrics.

While the fabrics did allow the system to operate without short circuits, it did noticeably affect the current distribution. When observing the copper plates after operation, the deposition and dissolution patterns showed the highest current densities on the outside edges of the flow area. This is because the fabric blocked flow through the center of the flow channel. **Figure 6-9** shows that the addition of felt spacers significantly affects the distribution of current across the surface of the electrode during operation. The inability to use the entire flow area effectively represents the greatest flaw of the EMAR 4 device.

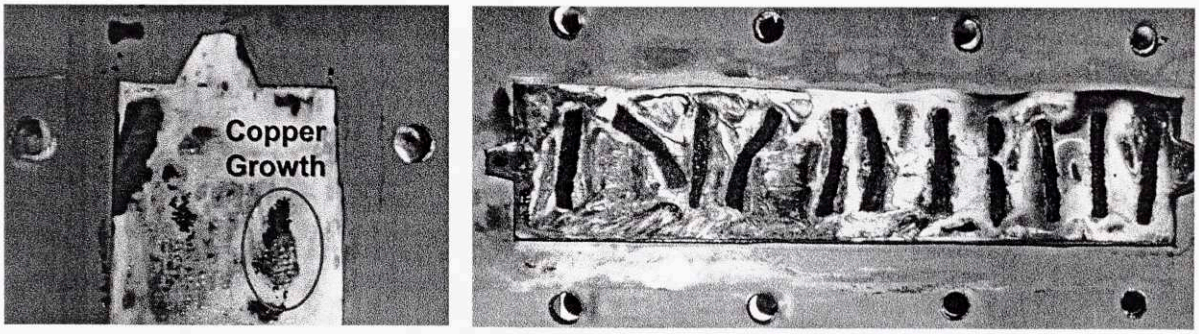

Figure 6-9. (Left) Picture of the membrane after operation showing significant copper growth through the membrane. **(Right)** Picture showing the copper electrode surface after operation with felt spacers designed to prevent membrane contact with the electrode.

Full System Design

The electrochemical cell described in the previous section is only one of several pieces of equipment required for an electrochemical scrubbing process. The other main units are the CO_2 absorption vessel and the gas/liquid separator. Minor peripherals include the pump, the power supply, and the measurement and control units. A simplified schematic and a picture of the entire setup can be seen in **Figure 6-10**.

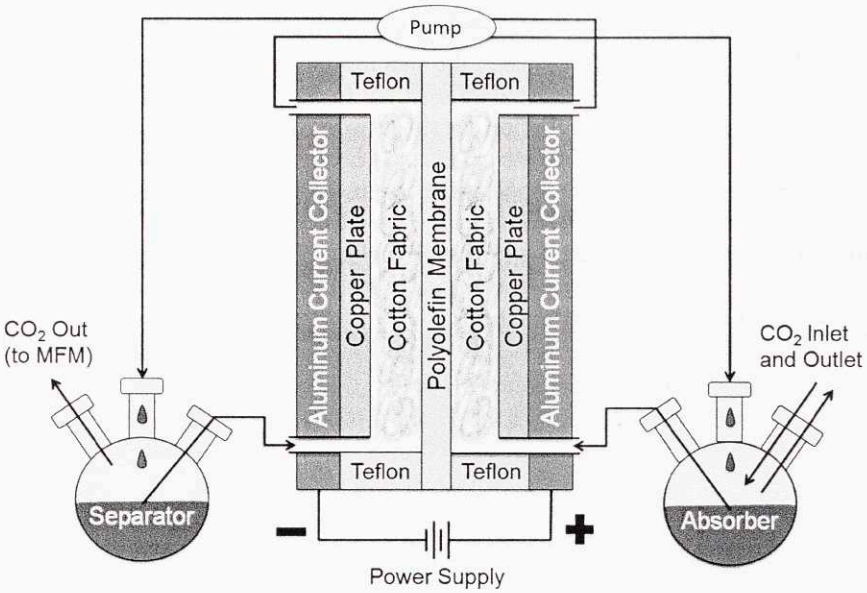

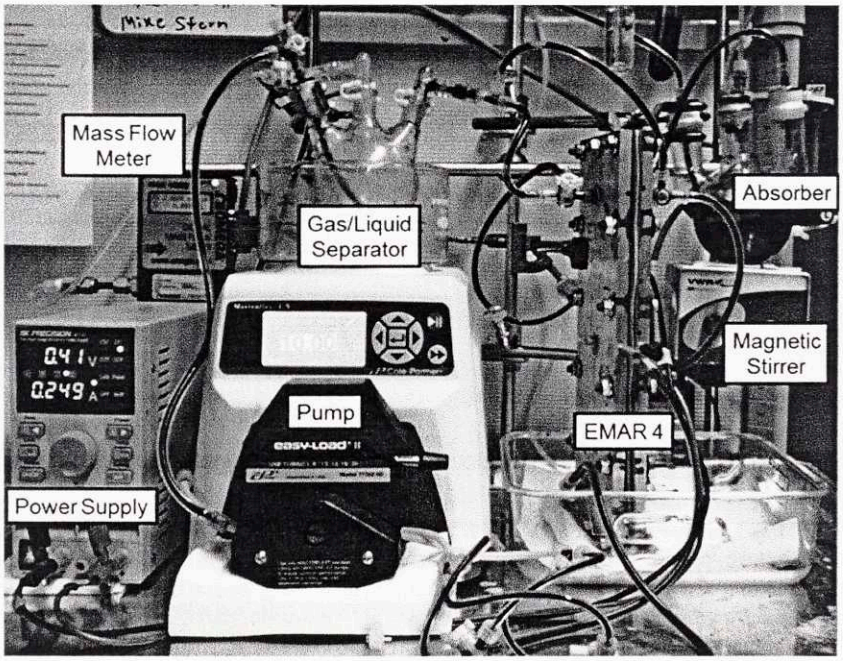

Figure 6-10. (Top) Diagram of the EMAR bench scale setup. **(Bottom)** Picture of the actual setup.

Absorption Vessel

The purpose of the CO_2 absorption vessel is to re-saturate the sorbent solution with CO_2 after it has been partially regenerated in the cathode of the EMAR cell. In the proof-of-concept system, the absorption was done at room temperature and near ambient pressure. Due to downstream measurement devices, the pressure may have been elevated over ambient by several kilopascals. Two types of vessels were investigated for use as the absorber: a packed column and a stirred flask. Pictures of both vessels can be seen in **Figure 6-11**.

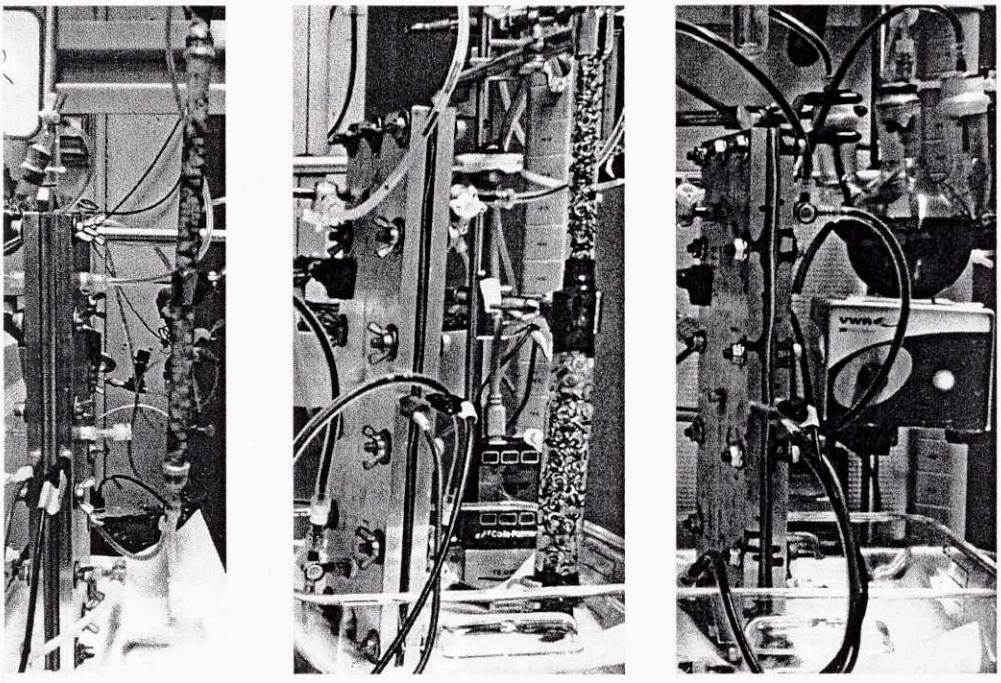

Figure 6-11. Pictures of the EMAR 4 cell with the Teflon packed column (left), the stainless steel lock washer packed column (middle), and the stirred flask absorber (right).

The packed column, which most closely resembles an industrial scale absorber, was difficult to design correctly. The column was constructed from 12 inches of a 1/2" diameter glass tube. Two different types of packing were attempted: 1/8" segments of cut Teflon tubing and 316 stainless steel size 6 lock washers. The Teflon tube segments provided significantly less surface area and were inferior compared to the lock washers. When packed with the lock washers, however, the gas flow area was reduced and flooding occurred on a few occasions. It was determined that the column was not suitable for a proof-of-concept

system because the gas and liquid flow rates were ill-defined. The packed column lacked the versatility to operate effectively under a wide range of conditions.

The stirred flask system was composed of a 250 mL three-neck flask with 24-40 ground glass joints and a Teflon stir bar. The flask was placed on top of a small VWR magnetic stirrer. The stirrer was always set high enough to generate a vortex in the flask. Typically, the flask was operated with about 200 mL of fluid. Higher liquid volumes in the flask were preferable because it leads to higher residence times, and hence, better absorber performance. This system was superior to the packed column because it could operate effectively for a wide range of gas and liquid flow conditions.

Gas/Liquid Separator

The gas/liquid separator used was a 250 mL three-neck flask with 24/40 glass ground joints. The flask was not stirred during operation. The flash was simply designed to operate as a flash tank. The liquid would exit through one outlet, and the gas through another. It was assumed that the majority of gas had already evolved from the sorbent solution by the time the bubbly mixture entered the gas/liquid separator. Hence the liquid level was kept low, since increasing the residence time was not expected to be helpful. Keeping the liquid level low was desirable from a safety perspective because it lowered the possibility of an overflow in the system. The flask typically operated with about 25 to 50 mL of solution.

One constant challenge when operating both flasks was to keep the liquid level constant. Inconsistencies in the loading of the tubing into the peristaltic pump and differences in pressure drop across the two sides of the EMAR 4 cell caused small imbalances in the liquid flow rates into the two flasks. The addition of a level meter into the next generation systems will greatly increase their accuracy, safety, and long-time operating stability.

Other Peripherals

The CO_2 injection into the absorption flask was controlled by a Labview interface. The program controls two 10-1000 sccm Aalborg mass flow controllers (MFC's). One MFC is connected to a nitrogen gas

cylinder, and the other is connected to a CO_2 gas cylinder. The composition and flow rate of the gas entering into the absorber can be easily manipulated using this setup.

The liquid flow was controlled by a Masterflex L/S digital drive capable of simultaneously pumping two channels. The dual-channel pumping was achieved through the use of a two-channel pump head for low flow rates (0-20 mL/min) and also through connecting two single-channel pump heads in series for higher flow rates. The former setup allowed for smaller tubing, which reduced flow pulsation, but was also more prone to imbalanced flow between the two channels. Masterflex C-Flex peristaltic tubing was used and found to be chemically stable with respect to the aqueous amine solution.

The current, or in a few rare cases, voltage of the system was controlled by a BK Precision 9110 power supply. Either a target current or voltage could be consistently applied to the system using the power supply. When a constant current was specified, the voltage was measured through connecting the positive and negative terminals of the power supply to a National Instruments USB-6008 data acquisition module. The potentials were then recorded using National Instrument's Signal Express software. Upgrading from a variable power supply to a potentiostat will significantly increase range of techniques for analyzing the electrochemical cell performance.

The CO_2 flow rate from the system was measured in a variety of ways over the course of the experiments. Originally, the outlet of the gas/liquid separator was combined with a nitrogen stream, precisely controlled by a MFC, and sent to a Gas Chromatogram (GC). Based on the composition obtained from the GC analysis and the known nitrogen flow rate, the CO_2 flow rate was calculated. The disadvantage of this system was the relatively slow measurement rate of once per every two minutes.

A 0-10 sccm Cole-Parmer volumetric flow meter (VFM) was purchased to replace the GC measurements. This was effective measurement strategy with fast measurement rates and 0.01 sccm precision. The VFM operates by measuring the pressure drop of the gas through the meter. One disadvantage of this strategy is that it necessitates a larger pressure drop across the meter compared to a mass flow meter. The data was recorded by connecting the 0-5 Vdc output to the USB-6008 data acquisition module. Unfortunately, after a month, the VFM failed spontaneously. A second VFM had also

been purchased to measure the outlet CO_2 rate from the absorber, it also failed after a few months. It is unclear if the failures are related to the corrosion from aqueous amine vapors or poor design.

After the failure of the VFM's, an Omega mass flow meter (MFM) was purchased. The MFM has by far the fastest measurement times and the greatest accuracy. MFM's operate by measuring the thermal capacity of the gas flowing through the meter. The data for the MFM was recorded through the included software. After a month of operation, the MFM was still operating effectively. Future systems, especially those operating at elevated temperatures, should consider the inclusion of solvent traps to prevent any corrosive amines from condensing in the gas flow meters.

Proof-of-Concept Experiments

Operating Conditions

As mentioned previously, all experiments were operated at ambient temperature and pressure conditions. Experiments were only run with ethylenediamine (EDA). The solutions always contained 1M EDA, 1M $NaNO_3$ and either 0.25M $Cu(NO_3)_2$ or 0.25M $CuCl_2$. Approximately 300 mL of solution would be recirculated through the system during an experiment. After charging the system with a fresh solution, CO_2 was bubbled into the system overnight at 10 sccm to saturate the amine solution completely. Solutions would be used for approximately two weeks before replacement with a fresh solution. No deterioration in performance was ever noticed due to the age of a solution. Upon addition of CO_2, a color change would gradually occur in amine solution, regardless of whether copper was also present.

Liquid flow rates of 5 to 60 ml/min were tested. The superficial velocity of the solution, U, can be calculated from the volumetric flow rate, Q_{flow}, and the width and height of the channel.

$$U = \frac{Q_{flow}}{W\,H} \tag{6-1}$$

For the 1/32" gasket used for the flat plate experiments, the flow rate in cm/s as a function of volumetric flow rate (in ml/min) is given by Eq. 6-2.

$$U = 2.48\,Q_{flow} \tag{6-2}$$

Before the start of an experiment, both the absorber and gas/liquid separator flasks would be purged with CO_2. During operation of the system, the absorber was constantly saturated using a 100 sccm stream of CO_2. Lower concentration streams were not used because of the significant losses in output due to physical solubility. These losses would not be expected during operation at higher temperature or in larger devices, but are significant at the small proof-of-concept scale.

The expected loss in CO_2 output from the gas/liquid separator, Q_P, due to physical solubility can be calculated as a function of the liquid flow rate, the partial pressure of CO_2 entering the absorber, P_F, and the partial pressure of CO_2 in the anode, P_A.

$$Q_p = \frac{Q_{flow}}{RT\,H_{CO_2}\,v_m}\left(1 - \frac{P_A}{P_F}\right) \tag{6-3}$$

H_{CO2} is the Henry's Law coefficient, assumed to be near that for pure water, and v_m is the molar volume of the solution, which can also be estimated with the pure water value. Eq. 6-3 shows that if the partial pressures in the absorber and anode are equal, there is no loss of CO_2 flow from the gas/liquid separator.

If, however, a 15% CO_2 stream were used with a liquid flow rate of 20 mL/min, the expected loss would be 12.5 sccm. That value is greater than the highest output generated with the proof-of-concept device! Therefore, operating with low percentage CO_2 inlets would entirely overshadow the performance of the EMAR system. As was shown in Chapter 3, an EMAR system operated at higher temperature and a much wider range of copper loadings would have extremely minimal losses from physical solubility. Because all experiments were performed with a pure CO_2 stream into the absorber (P_F = 1 atm), the losses due to physical solubility will be omitted for the rest of the chapter.

The expected rate of generation of CO_2, Q_E, can be calculated as a function of the current, I, assuming each electron releases one molecule of CO_2 from its chemical bond with EDA.

$$Q_E = \frac{P_A}{RT}\frac{I}{F} \tag{6-4}$$

The Faradaic efficiency, ε_F, which defines the efficiency in which electrons release molecules of CO_2, is calculated by dividing the observed rate of CO_2 generation, Q_{CO2}, by the expected value.

$$\varepsilon_F = \frac{Q_{CO_2}}{Q_E} = \frac{Q_{CO_2}}{I}\frac{FRT}{P_A} \tag{6-5}$$

The work of capture, W_{CO2}, which is calculated in units of kJ/mole, is calculated by dividing electrical power requirement of the system, IV, by the observed rate of CO_2 generation.

$$W_{CO_2} = \frac{IV}{Q_{CO_2}}\frac{RT}{P_A} \tag{6-6}$$

The RT/P_A is required to convert the volumetric measurement of CO_2 generation to a molar flow rate. Note that V represents the applied voltage, not a volume. The efficiency cannot be calculated for the work of capture since the inlet gas stream into the absorber and the outlet from the gas/liquid separator are both pure CO_2. Therefore, no actual thermodynamic work is being performed, and hence, the efficiency, with respect to work, of the system would be zero in every experiment.

In the following sections, the performance in terms of the Faradaic efficiency and the work of capture will be presented for a variety of different configurations of the proof-of-concept device. Both porous electrode and flat-plate electrode systems were tested. Systems with nitrate salts and chloride based salts were both tested with the flat-plate electrode system. Different flow rates and current densities were also investigated. Some qualitative observations about copper powder generation and electrode stability will also be provided.

Flat Plate Electrode – Stability and Reproducibility

The first experiment performed with the EMAR system using flat plate electrodes was electrochemical impedance spectroscopy (EIS). The results are shown in the form of Nyquist and Bode plots in **Figure 6-12**. The measurements were taken with no gas or liquid flow through the system. The amplitude of the applied sinusoidal voltage waves was 25 mV and the waves were centered on the open-circuit potential. The frequency was varied from 10 kHz to 1 Hz. At high frequencies, the impedance approaches 0.6 Ohms

(6 $m\Omega/m^2$), which represents the resistance of ion transport through the solution and membrane. This also increased by any contact resistances that may exist between the current collectors and the potentiostat cables. At low frequencies the slope of the Nyquist plot approaches 0.5, which is expected for a transport limited system. Future EIS experiments should be performed with varying liquid flow rates to investigate transport effects.

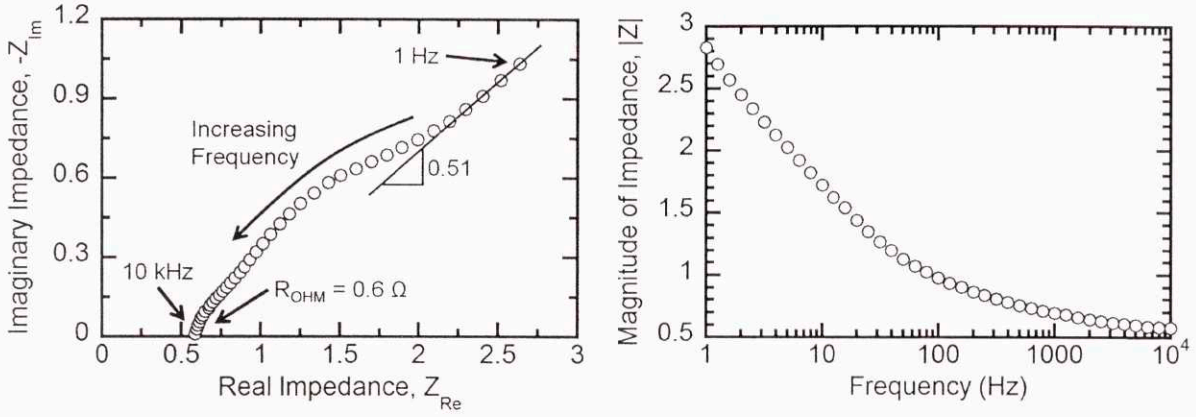

Figure 6-12. Nyquist (left) Bode (right) plots of impedance spectroscopy results for the flat-plate EMAR system with no flow. Solution was CO_2-saturated with 1M EDA, 0.25M $Cu(NO_3)_2$, and 1M $NaNO_3$. Impedances are in units of Ohms.

The next set of experiments performed was designed to test the stability and reproducibility of the EMAR experimental setup. Long duration continuous experiments and cycling experiments, in which the current was cycled on and off every half hour, both demonstrated effective long-term stability. The results of the experiments can be seen in **Figure 6-13**. In the future, increased automation of the EMAR system will be required to run experiments longer than a few hours.

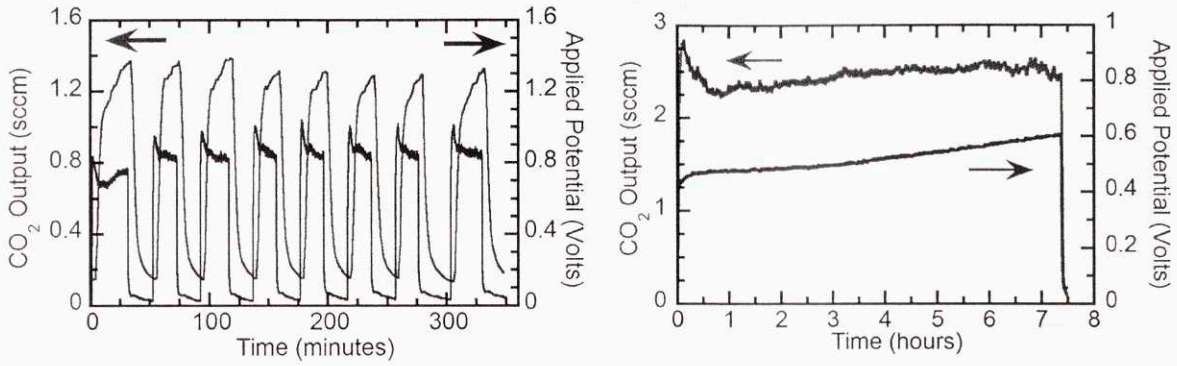

Figure 6-13. Bench-scale cycling (left) and long duration (right) experiments with the EMAR proof-of-concept system. Both experiments done at 0.25A, 20 mL/min liquid flow rate, and with a solution of 1M EDA, 0.25M $Cu(NO_3)_2$, and 1M $NaNO_3$.

Figure 6-13 also highlights the difficulty of reproducing results with the proof-of-concept system. After running the cycling experiment, the system had been disassembled, cleaned, and reassembled. This caused a significant change in the performance. Before reassembly the system was achieving only 30% Faradaic efficiency. Afterwards, the system was operating above 60% efficiency. The condition of the membrane and the flow properties change significantly over time, making reproducibility of the EMAR proof-of-concept system quite poor. Reproducibility will be drastically improved by the creation of a system with a better designed flow profile and which no longer needs the fabric separator to prevent membrane/electrode contact.

The final set of experiments performed to determine the stability of the flat plate electrode system was cycling with polarization reversal. In this experiment, the polarity of the electrodes was repeatedly reversed. In a real EMAR system, polarity reversal is necessary to prevent accumulation of copper on the cathode and loss of copper on the anode. Results for experiments with $Cu(NO_3)_2$ and $CuCl_2$ are shown in the left and right plots of **Figure 6-14**, respectively. Each dip in the CO_2 output and voltage represents one reversal of the polarity.

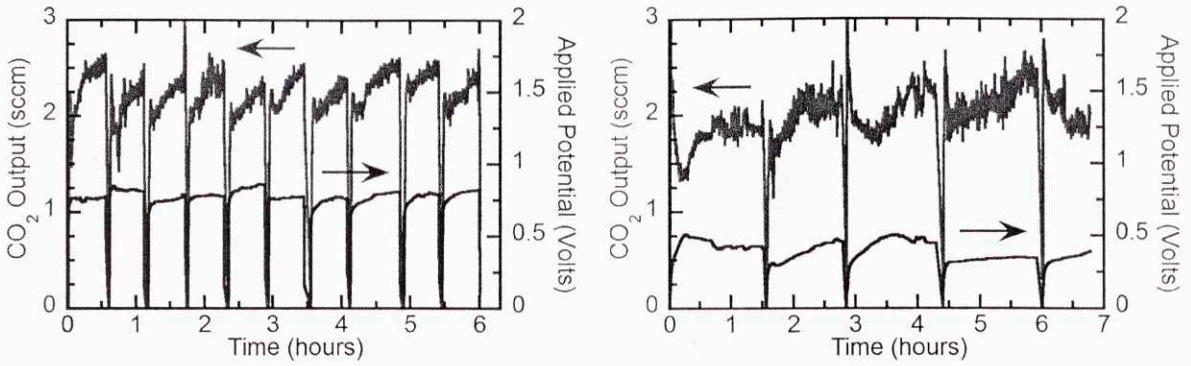

Figure 6-14. Polarity cycling experiments at 0.25A and 10 mL/min liquid flow rate for solutions of 1M EDA, 1M $NaNO_3$, and 0.25M $Cu(NO_3)_2$ (left) or 0.25M $CuCl_2$ (right).

Systems with both nitrate and chloride salts appeared to be relatively stable over 5 to 10 polarity reversals. The nitrate systems appear to be more stable and have higher Faradaic efficiency. The higher efficiency, however, could be a result of the significant shifts in system performance over time. One conclusive result that can be observed is the dramatically lower required potential for the chloride system. This is expected based on the significantly enhanced kinetics of chloride salt systems, as was shown in the Kinetics Chapter.

Flat Plate Electrode – Current Density and Flow Rate Effects

Experiments with varying flow rates and current densities were performed to determine their effect on Faradaic efficiency and the work of capture, defined in Eqs. 6-5 and 6-6, respectively. Experiments with nitrate salts showed Faradaic efficiencies consistently between 60% and 80%. While the Faradaic efficiency was a weak function of current density and flow rate, the work of capture was a strong function of both.

Figure **6-15** shows results from an experiment where the current was varied every 45 minutes and the CO_2 output was measured in two ways. The outlet gas from the gas/liquid separator was combined with a nitrogen sweep gas and sent to a GC for composition analysis. A volumetric flow meter (VFM) was also placed at the exit of the absorber, and the change in CO_2 leaving the absorber was measured over time. Both methods yield similar results, as would be expected from a mass balance on CO_2 in the system. The liquid flow rate for this experiment was 20 mL/min.

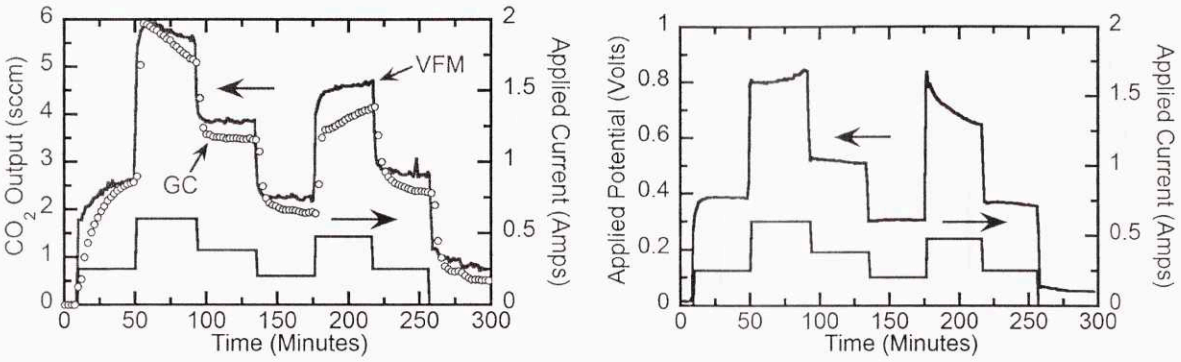

Figure 6-15. CO_2 output (left) and voltage (right) results from the proof-of-concept system with 1M EDA, 0.25M $Cu(NO_3)_2$, and 1M $NaNO_3$, with current varied from 0.2 to 0.6 Amps. The CO_2 output was measured using a GC to analyze the gas leaving the G/L separator and a VFM measuring the change in CO_2 leaving the absorber.

Based on the VFM measurements, which appeared to be more reliable, the Faradaic efficiency and work of capture were calculated for each current. The results are shown in **Figure 6-16**.

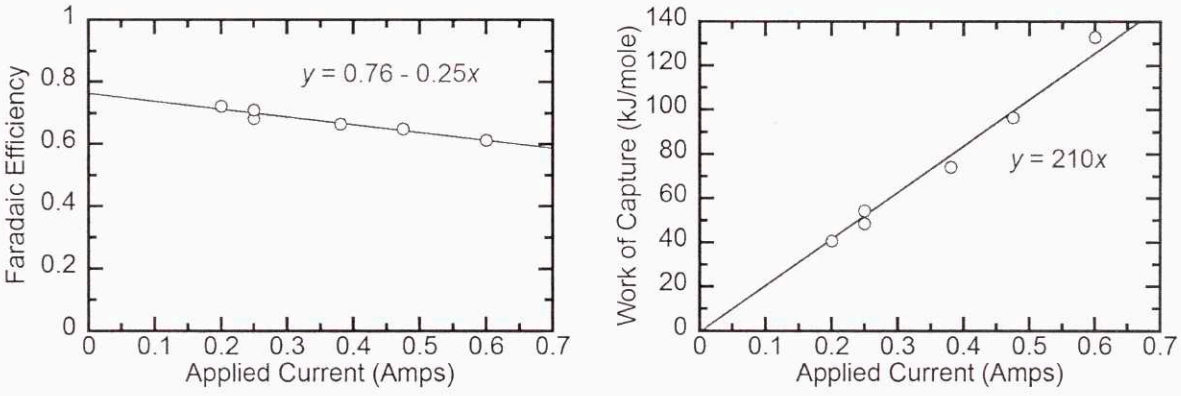

Figure 6-16. Faradaic efficiency (left) and work of CO_2 capture (right) based on the data from **Figure 6-15**.

The Faradaic efficiency declined in a linear fashion with increasing current, though only from 70% at 0.2A to 60% at 0.6A. The work of capture increased in a linear fashion from 41 kJ/mole at 0.2A to 133 kJ/mole at 0.6A. These results show that the EMAR system, with extremely little optimization, can capture CO_2 at for 100 kJ/mole at a current density of 50 A/m^2, which is only an order of magnitude below the target current density for an EMAR.

Further experiments were run at different flow rates and current densities for systems with only nitrate salts and systems with some chlorides salts in the form of $CuCl_2$. The results of the nitrate systems

can be seen in **Figure 6-17**. These results are plotted as a function of CO_2 capture rate, which is the most industrially relevant methodology.

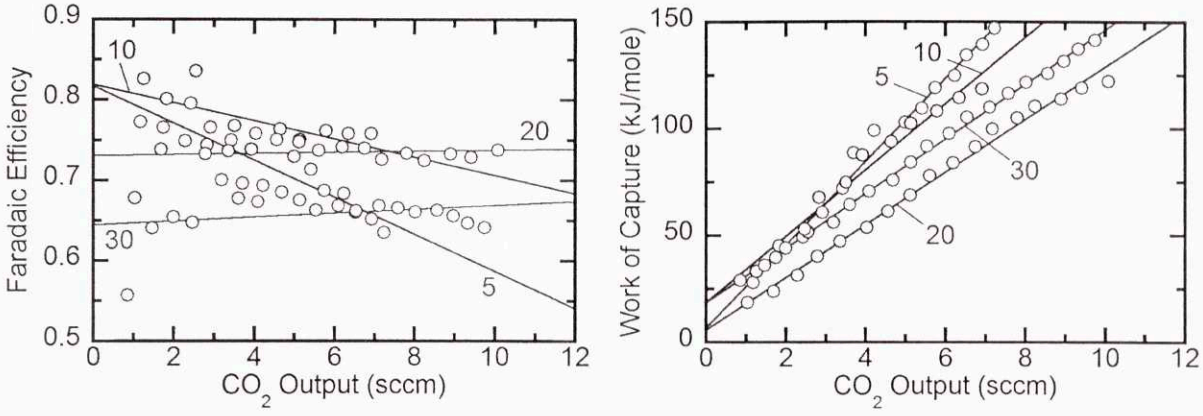

Figure 6-17. Faradaic efficiency (left) and work of CO_2 capture (right) as a function of CO_2 generation rate for 1M EDA, 0.25M $Cu(NO_3)_2$, 1M $NaNO_3$ systems. The numbers in the plots represent the liquid flow rate of the experiment in mL/min.

Figure 6-17 shows that at flow rates from 5 to 30 mL/min, the Faradaic efficiencies remain above 60% and even can reach 80% at very low CO_2 fluxes and moderate flow rates. The lower flow rates show exceptionally good performance at low currents, but their performance declines significantly as the currents increase. The higher flow rates show a nearly constant Faradaic efficiency from 0 to 100 A/m^2. The results also indicate that there is an optimum flow rate in the range near 20 mL/min.

Experiments run at 20 mL/min showed the lowest required work of CO_2 capture for a given CO_2 flux. Lower flow rates appeared to show faster increases in the work of capture, presumably because of increased transport resistances and greater concentration polarization between the two sides of the electrochemical cell.

To further investigate the performance of the proof-of-concept EMAR system as a function flow rate, experiments were run with constant currents, and the flow rates were varied over time. The results from those experiments can be seen in **Figure 6-18**.

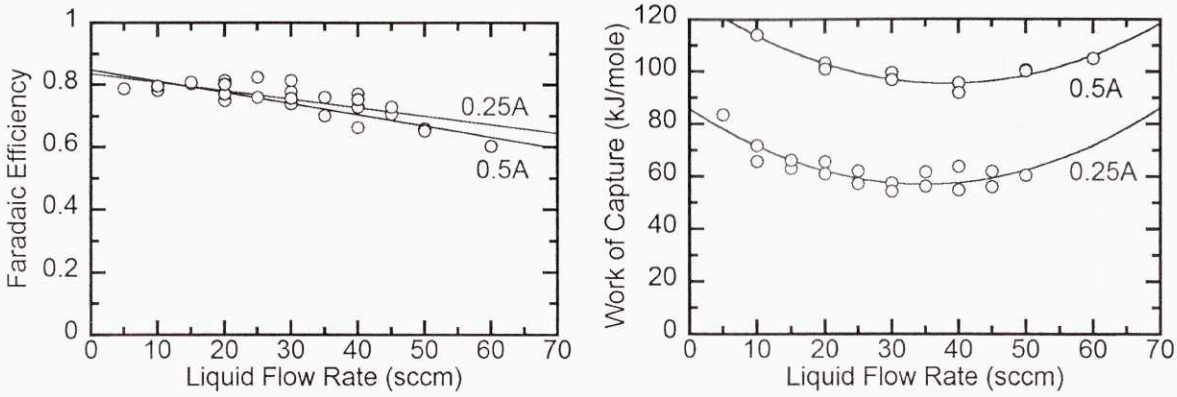

Figure 6-18. Faradaic efficiency (left) and work of CO_2 capture (right) as a function of the sorbent flow rate for a EMAR system with 1M EDA, 0.25M $Cu(NO_3)_2$, and 1M $NaNO_3$. Numbers represent the applied current during the experiment. Lines for efficiency and work of capture are linear regressions and 2nd order regressions, respectively.

The parabolic shape of the work of capture curve agrees with trend from **Figure 6-17** that showed the best performance for moderate flow rates. In contrast to **Figure 6-17**, the ideal flow rates are in the range of 30 to 40 mL/min, rather than 20 mL/min. This difference is most likely a function of the inherent variability of the proof-of-concept system.

The higher performance of moderate flow rates compared to low or high flow rates can be explained by the competition of transport effects and inefficiencies due to low loadings. In the previous chapter on transport phenomena, the importance of fluid velocity can be seen by its effect on the Peclet number. Higher velocities improve transport to the surface, reducing concentration overpotentials. Increasing the velocity also decreases the difference of copper and amines concentrations across the system, which causes open-circuit potential differences. For both of these reasons, as the liquid flow rate is increases, the required voltage is reduced for a given current density.

However, at very high flow rates, the change in the copper loading from the inlet to the outlet of the anode becomes quite small. Eventually, the release of CO_2 is so small that the level of super-saturation is metastable, and hence, bubbles do not spontaneously form. The expected change in CO_2 concentration, $\Delta[CO_2]$, can be calculated as a function of the volumetric liquid flow rate and the current.

$$\Delta[CO_2] = 2\left(\Delta\left[Cu^{2+}\right]\right) = 2\left(\frac{I}{2F}\frac{1}{Q_{flow}}\right) = \frac{I}{Q_{flow}F} \tag{6-7}$$

The change in the physical CO_2 saturation, $\Delta\gamma_{CO2}$, of the aqueous solution is calculated by dividing the expected change in concentration by the CO_2 physical solubility at the anode pressure and temperature.

$$\Delta\gamma_{CO_2} = \frac{\Delta[CO_2]}{\frac{P_A}{H_{CO_2} v_m}} = \frac{I}{Q_{flow} F} \frac{H_{CO_2} v_m}{P_A} \tag{6-8}$$

At room temperature and pressure, the change in CO_2 saturation, which is equivalent to the super-saturation, drops below 10% at liquid flow rates of 50 mL/min when running at 0.25A. At such low super-saturations, it is not surprising that the CO_2 release from the solution becomes inefficient. **Figure 6-19** shows all of the efficiencies from that data in **Figure 6-17** and **Figure 6-18** as a function of the expected system super-saturation. While more data below 10% super-saturation would make the results more conclusive, the trend of decreasing Faradaic efficiency for super-saturations below 15% is statistically significant.

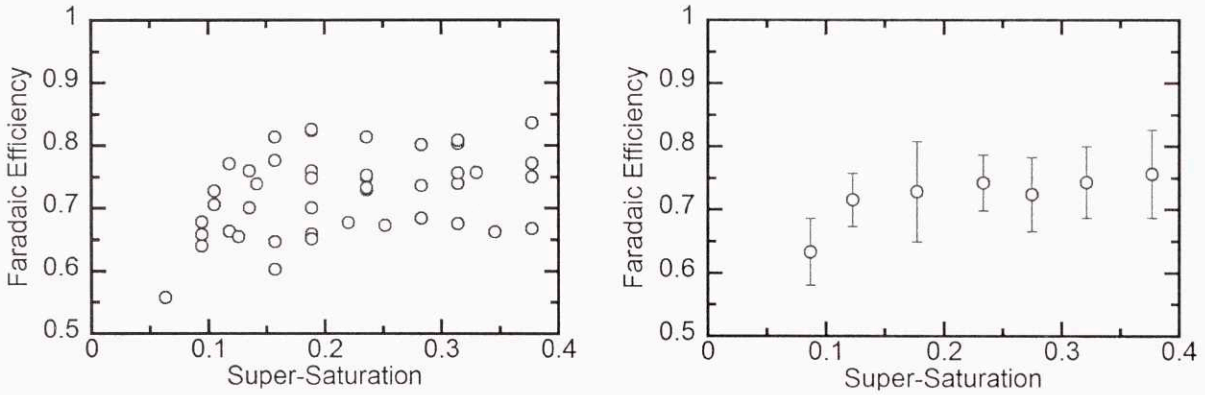

Figure 6-19. Faradaic efficiency as a function of super-saturation for all the results shown in Figures 6-17 and 6-18. In the right plot, the results for every 5% bin of super-saturation have been combined. Error bars represent one standard deviation.

The results indicate that 800 sccm/m^2 of CO_2 can be captured for 100 kJ/mole of electricity using the EMAR system at the optimal flow conditions. This is despite operating well below the ideal operating temperature and with little optimization to the system geometry.

Similar experiments were attempted using systems with $CuCl_2$ in place of $Cu(NO_3)_2$, but the experiments gave inconsistent results. The EMAR system showed significant signs of corrosion when chloride salts were used for extended periods of times, which may be the cause for the poor results. The

measured Faradaic efficiencies, shown in **Figure 6-20**, were in agreement with the results from **Figure 6-14**, but the required voltages, and hence the work of CO_2 capture, were significantly higher than expected.

The increased voltages can be explained by the formation of thick aluminum oxide layers between the aluminum and copper plates, which would add a significant contact resistance. Precipitated aluminum salts clogged the inlets and outlets of the system on multiple occasions and were easily visible all over the device. Difficulties with the electrical connections to the copper through the aluminum plates were experienced during these experiments, but were never encountered during experiments with all nitrate salt systems. Future systems should not be designed with aluminum to avoid the problems of galvanic corrosion.

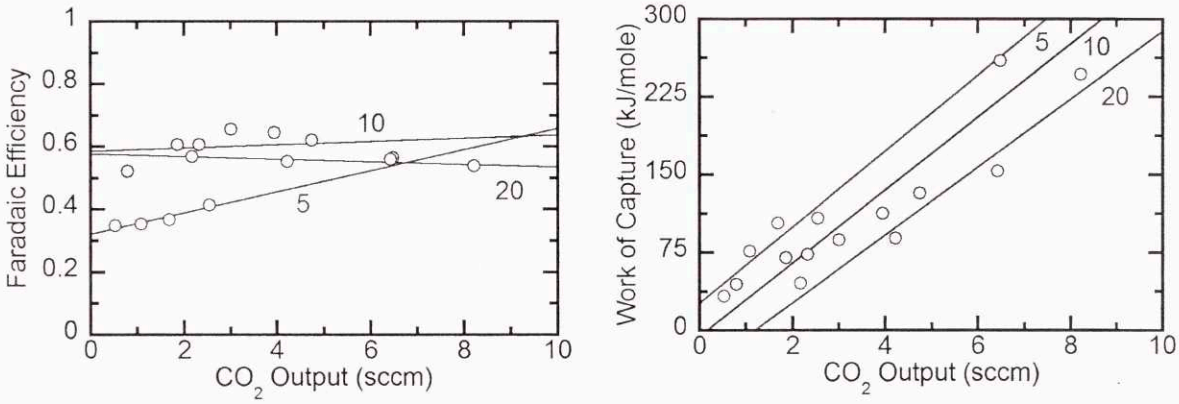

Figure 6-20. Faradaic efficiency (left) and work of CO_2 capture (right) as a function of CO_2 generation rate for 1M EDA, 0.25M $CuCl_2$, 1M $NaNO_3$ systems. The numbers in the plots represent the liquid flow rate of the experiment in sccm.

Porous Electrodes

Prior to the experiments with the flat plate electrode system with 1/32" flow channels, 1/8" porous electrodes were used in 1/8" flow channels for the EMAR experiments. The porous electrodes were obtained from the aerospace company, ERG. The 1/8" thick foams were the thinnest available and had a pore density of 20 pores per inch. The porosity of the foams is over 90% with a surface area of approximately 1000 m^2/m^3. Vitreous carbon foam (glassy carbon) electrodes were also purchased with the intent to plate them with copper and use them in the proof-of-concept system. The electrodes can be

purchased with higher surface areas and very high porosities. Due to the problems with the copper foam electrodes, however, the vitreous carbon electrodes were never tested.

The porous electrodes were first tested using electrochemical impedance spectroscopy (EIS) as shown in **Figure 6-21**. The solutions for these experiments had EDA and $Cu(NO_3)_2$ concentrations 10 times less than the flat plate experiments. The $NaNO_3$ concentration was half of the concentrations used in the flat plate experiments. Despite the significantly lower ionic strength, the solution resistance, which is equal to the x-intercept in the Nyquist diagram, is significantly less than the solution resistance in the flat plate system. This demonstrates the superior properties (i.e., lower resistances) of the porous electrode system. At lower frequencies, the EIS experiments with dilute solutions in porous electrodes still maintain lower resistances because the higher surface area reduced transport limitations.

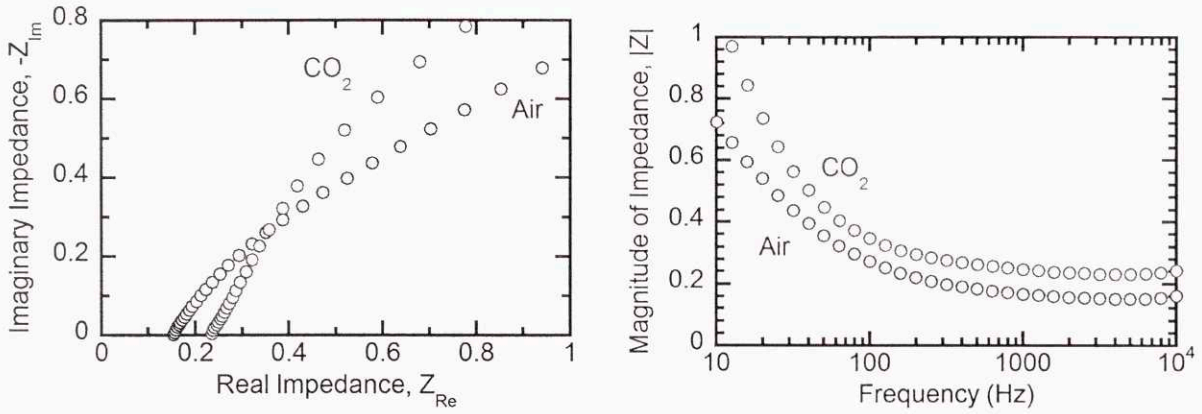

Figure 6-21. Nyquist (left) and Bode (right) diagrams from EIS measurements on 0.1M EDA, 0.025M $Cu(NO_3)_2$, 0.5M $NaNO_3$ solutions under air and CO_2-saturated conditions.

Because the porous electrode experiments were the preliminary tests done with the EMAR system, the voltage measurement scheme had not yet been setup. Therefore, only approximate voltage values based on direct readings of the power supply are available. The concentration of the sorbent solution was also still being optimized; the solutions used with the porous electrode were less concentrated than the solutions used in the flat plate experiments. Finally, the flow rates of CO_2 into the system were at 25 sccm, rather than the 100 sccm for the majority of the flat plate experiments.

The reason porous electrodes were not more thoroughly investigated is because of concerns with bubble entrapment in the pores and the instability of the porous network after many deposition and

dissolution cycles. The latter was difficult to measure in the small proof-of-concept device that lacked the automation capability to operate continuously for long periods of time, but the former was observed through on/off cycling experiments. **Figure 6-22** shows results from two representative experiments with porous electrodes in the EMAR system.

The results show impressively high current efficiencies that even approach unity. Unfortunately, as can be seen in the right plot of **Figure 6-22**, over time the performance of the porous electrode systems significantly decline. It was observed that the electrochemical cell was filling with gas bubbles because the liquid levels elsewhere in the system were all increasing over the duration of the experiment. Several strategies were tested to try and reduce bubble entrapment including faster flow rates and pulsating flow. Unfortunately, neither strategy appeared to prevent bubble entrapment.

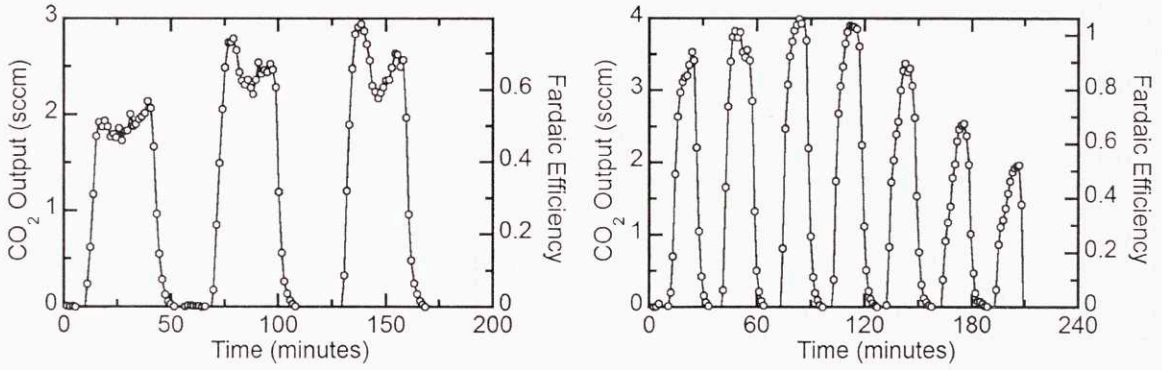

Figure 6-22. CO_2 output and Faradaic efficiency during on/off cycle experiments with porous electrodes in the EMAR system. The composition of the solutions were 0.5M EDA, 0.125M $Cu(NO_3)_2$, and 1M $NaNO_3$ (left) and 0.1M EDA, 0.025M $Cu(NO_3)_2$, and 0.5M $NaNO_3$ (right).

EMAR electrochemical cells with porous electrodes do warrant further study. It is possible that manipulation of some of the operating conditions, such as the temperature, may alleviate the problem. Operation at pressure over 50 bar may also allow operation under conditions with minimal bubble formation. Finally, different types of high surface area copper structures could be investigated. The effort to use a porous copper electrode is worthwhile considering the significantly reduced overpotentials that were predicted in the previous chapter.

Electrode Stability

In a one case, the EMAR system was operated intermittently for weeks without changing of the solution, changing the polarity of the electrodes, or disassembling of the device. After the approximately 30 hours of operation, the device was disassembled, and pictures of the different components were taken. A selection of these photographs can be seen in **Figure 6-23** and **Figure 6-24**.

In the cathode, where the copper is constantly being deposited, significant quantities of copper buildup were observed. Much of the copper was only loosely bound to the copper plate, and was wiped off easily. The cheesecloth, which was placed to prevent contact of the membrane with the electrode surface, was embedded into the plate and extremely difficult to remove.

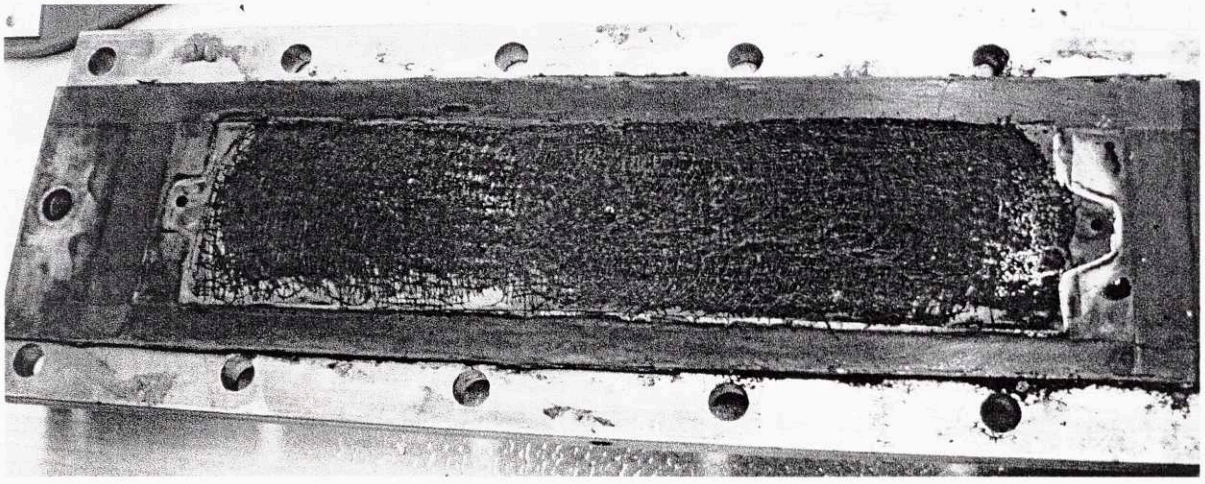

Figure 6-23. A picture of the flat plate copper cathode on top of the aluminum chassis with the cheesecloth spacer after approximately 30 hours of operation. The copper has grown significantly around the cheesecloth.

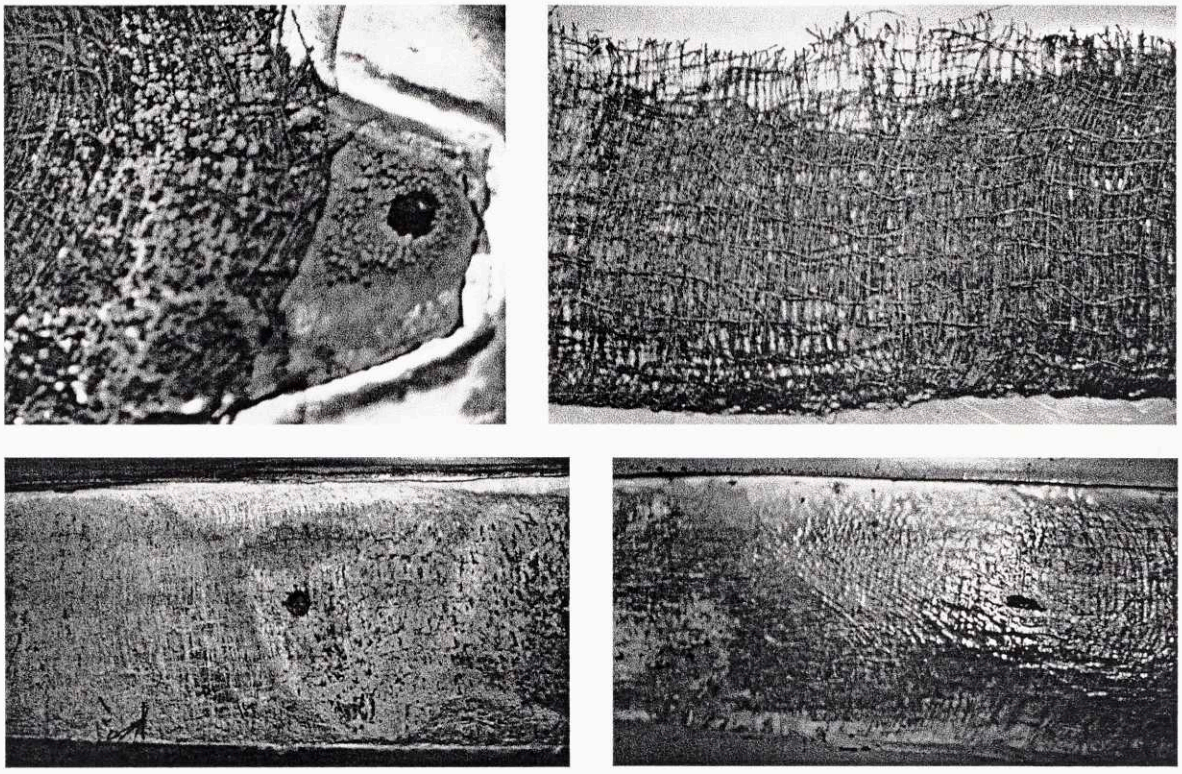

Figure 6-24. (Top Left) A picture of the flow inlet of the on the copper cathode. Significant copper metal buildup surrounds the entrance. **(Top Right)** Picture of the cheesecloth once separated from the copper anode. **(Bottom Left)** A picture of the copper anode after removal of the cheesecloth. **(Bottom Right)** A picture of the Celgard membrane showing significant copper growth. All pictures taken after approximately 30 hours of operation.

In the anode, where copper was being removed, some loose copper discovered on the electrode surface, but significantly less than was on the cathode. The cheesecloth in the anode was not embedded into the electrode and could be easily removed. Both surfaces showed the presence of some copper oxide species. The membrane was stained with copper powder, but did not show the distinctive shiny copper metal growth that was seen in Figure **6-9**. This indicates that the cheesecloth did successfully reduce copper growth through the membrane.

Conclusions from the Proof-of-Concept System

- A proof-of-concept EMAR system was designed and constructed based on several prior iterations of electrochemical cells designed for CO_2 capture processes.

- The system was operated with porous electrodes, but stable cycling could not be achieved due to bubble entrapment. Faradaic efficiencies near unity were achieved before performance the deteriorated.
- The system was operated with flat plate electrodes and a 1/32" flow channel. Stable on/off and polarity cycling was achieved. Experiments with durations of 7 hours were also successful.
- Experiments showed that if CO_2 super-saturations above 15% were generated in the anode, Faradaic efficiencies in flat plate systems could reach 80%.
- Under ideal operating conditions, 800 sccm per m^2 of membrane area could be separated for 100 kJ/mole CO_2 of electricity.
- Chloride systems were tested, but showed poor results. The high required voltages, however, were most likely a function of aluminum oxidation problems, not a failure of the chloride chemistry. Further study with a more corrosion resistant system is warranted.
- After 30 hours of intermittent operation with constant-polarity, significant copper buildup was observed throughout the system, but especially in the cathode.

Chapter 7

Design of Future EMAR Systems

Based heavily on experience gained from the proof-of-concept system and the theory regarding thermodynamics, kinetics, and transport developed in Chapters 3-5, designs for the next generation system and future industrial systems are proposed. A successful design will require consideration of operational requirements, such as sufficient membrane surface area, and engineering requirements, such as the correct choice of materials. The systems will need to be able to operate under elevated pressure and temperature conditions, but also need to be modular to allow for the cleaning and replacement of electrodes and membranes. Implementation of significant automation and control strategies will be necessary to allow for long continuous runs without the need for user intervention.

This chapter will start with a focus on designing the next bench-scale system. A specific design for the electrochemical stack and suggestions for peripherals is provided. A series of addition concerns are addressed, which range from material selection to different operating strategies. At the end of the chapter, a techno-economic assessment of three different industrial EMAR designs is performed to demonstrate the expected performance of the EMAR systems with different configurations. The flat plate electrode design appears the most promising due to its reasonable efficiencies and simple design.

Electrochemical Stack Design

The design of future electrochemical stacks should closely resemble a cross between a fuel cell and a redox flow battery. Many similarities with electrodialysis systems will also exist. In the electrochemical stack design of all these systems, the majority of the fluid flow is internal to the stack. This is necessary for reducing the requirements for piping and supporting structures. The stacks will be composed of three main elements: electrodes, flow channels, and membranes. The order of the construction will be:

Electrode || Flow Channel || Membrane || Flow Channel || Electrode

Each electrode will be bipolar; acting as an anode on one side and a cathode on the other. Hence, the electrode will be simultaneously being dissolved on one side and extended, through deposition, on the other. The electrodes will be composed of thin sheets of copper, most probably alloy 101 with >99.99% copper. Sheets of 1 to 3 mm should be sufficient depending on operating times between reversals. The required thickness of the copper, δ_{Cu}, as a function of the operating parameters can be calculated by Eq. 7-1.

$$\delta_{Cu} = F_S \frac{i_{max}}{2F} \frac{M_W}{\rho} t_{switch} \tag{7-1}$$

Where:

F_S = Safety factor

i_{max} = Maximum current density

M_W = Molecular weight of copper (63.55 g/mol)

ρ = Density of copper (8960 kg/m^3)

t_{switch} = Time between anode/cathode switches

If each cycle causes the loss of some fraction of the electrode, Eq. 7-1 could be multiplied by a plating efficiency, ε_P, to the n^{th} power, where n is the number of cycles the copper plate is expected to last. The enhanced equation is shown in Eq. 7-2.

$$\delta_{Cu} = F_S \frac{i_{max}}{2F} \frac{M_W t_{switch}}{\rho} (\varepsilon_P)^n \tag{7-2}$$

Careful design will be required to ensure that erosion of the copper structure over time does not occur. As was mentioned in the transport modeling section, the deposition and dissolution rates will not be uniform, and may not perfectly match between the cathode and the anode sides. This will lead to the slow copper dissolution in some places and buildup in others. Using copper sheets that are quite thick (>5 mm) provides more material for erosion and buildup, and may lead to more difficulties with blockages of the flow channel.

Using a composite electrode structure, where two thin sheets of copper sandwich a conductive but inert barrier, could be a way to minimize copper erosion problems. A thin sheet of stainless steel foil or graphite placed between the two pieces of copper would prevent the solution from leaking into the chamber on the opposite side even if all the copper on one side dissolves. When the polarity is eventually reversed, copper could re-deposit on the inert material, reversing much of the erosion.

The membranes, which are required to allow ion migration while inhibiting diffusion, could be either a porous polyolefin or an ion-selective ionomer. The former has the advantage of robust physical properties and very low cost. Through surfactant coating of the polyolefin, good wetting can be achieved. Celgard 3401 and 3501 membranes have both been used effectively in the bench-scale system.

Ionomers, by virtue of being non-porous, are superior diffusion barriers while maintaining excellent ionic conductivities. Either cation-exchange or anion-exchange membranes would be useable, but anion-exchange would be more desirable since they would prevent the migration of charged cupric species. Membranes used in electrodialysis processes would be a cheaper alternative to the expensive fluorinated ionomers like Nafion.

The flow channels will most likely employ some type of serpentine design in order to increase the residence time of the fluid flowing over each plate. The required path length, L_p, for an EMAR system can be calculated by,

$$L_p = U\Delta C_{Cu} H \frac{2F}{\langle i \rangle} \tag{7-3}$$

Where:

U = Average flow velocity

ΔC_{Cu} = The change in copper concentration across the entire system

H = The channel height

$< i >$ = Average current density of the system

The flow channel material must be constructed of an electrically-insulating, chemically-inert, and rigid gasket-type material that can handle significant compressive stress. Silicone and PTFE have both been used successfully in the bench scale system. Other common rubbers and plastics including polyurethane

and polyethylene could also be considered for gaskets. Chemical stability experiments should be performed before using new materials.

Figure 7-1 shows a schematic diagram of the first 5 elements of possible electrochemical stack design. This includes two copper electrodes, two gaskets with cut flow channels, and a membrane. The first copper electrode is backed with a sizeable metal (steel or aluminum) plate, which is essential for providing the system with rigidity.

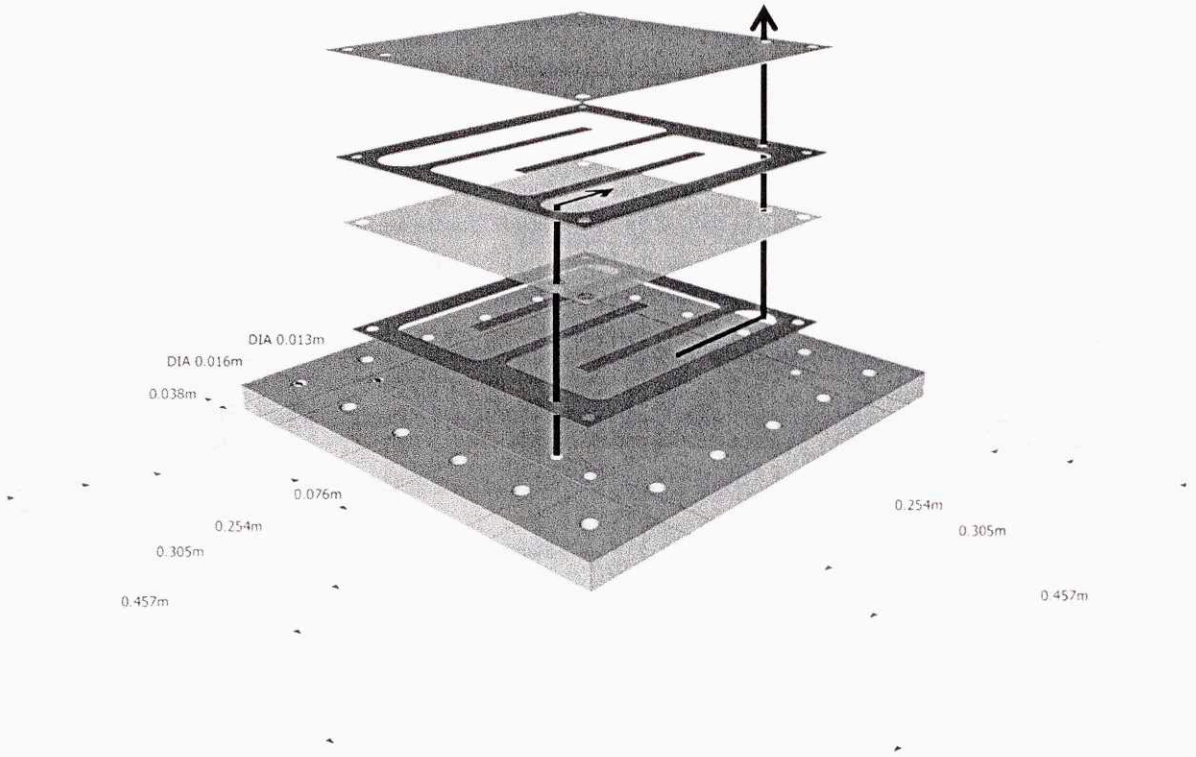

Figure 7-1. Schematic diagram of the first five elements of an electrochemical stack for an EMAR system. Black lines represent the paths of fluid travel.

It may be preferable to electrically insulate the metal from the copper to avoid galvanic corrosion. This could be easily accomplished by adding a thin plastic or rubber film between the metal and copper. The holes in the metal plate will be used to pass bolts through to connect with an identical metal plate on the opposite side of the system. Through bolt and nut construction, significant pressure can be applied to the device to prevent leaks. Inlets, outlets, and electrical connections can be added on the back side of the metal plate.

The black lines give indications of how the fluid will flow internally within the stack structure. After passing horizontally through the serpentine flow channel, the fluid would travel vertically through the membrane, the next gasket, and the next copper plate to reach the 2nd gasket, where it would again enter a horizontal serpentine flow channel. The vertical travel would occur through small holes cut near the outside of the membrane, gasket, and copper plate.

Design of Peripherals

The electrochemical stack will only be one piece of the entire EMAR system. **Figure 7-2** shows a schematic of the whole experimental setup.

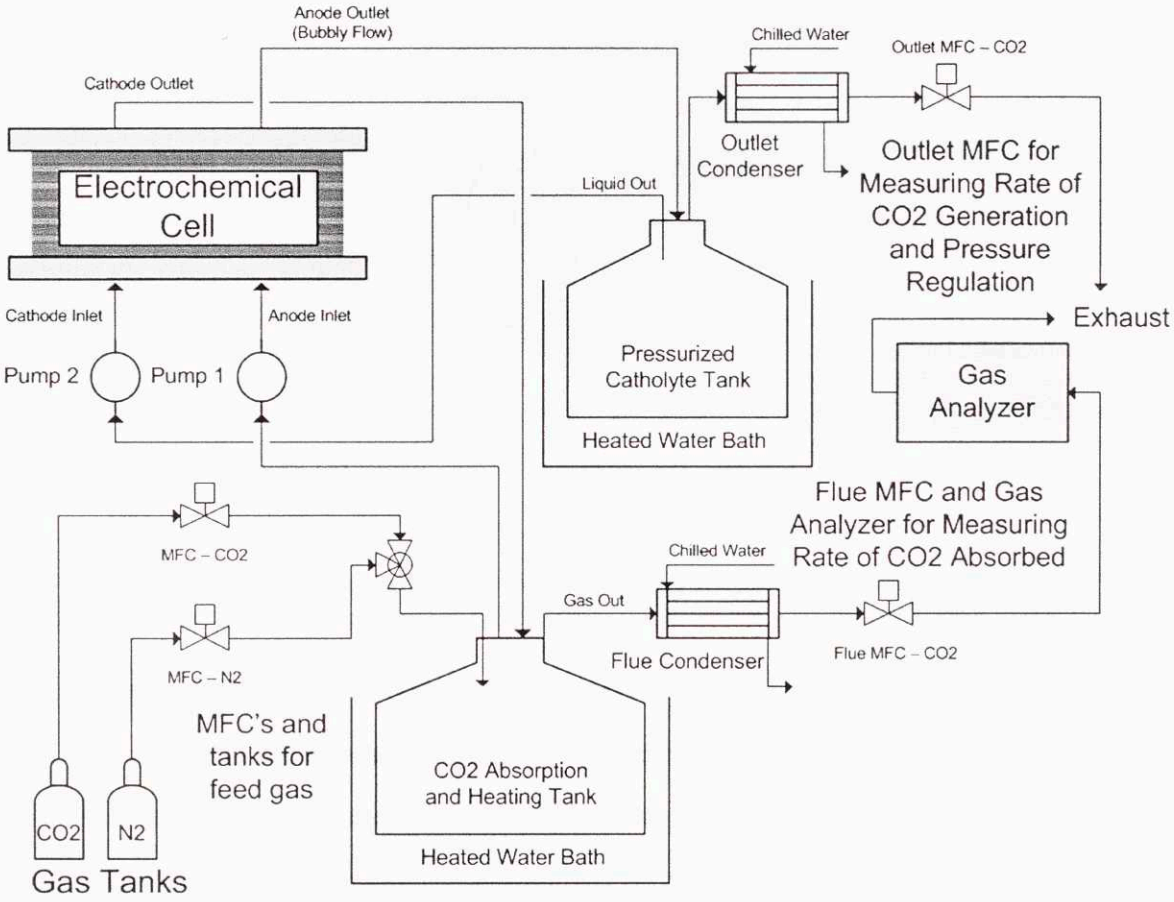

Figure 7-2. Schematic diagram of the important elements of an EMAR experimental setup.

The setup includes the electrochemical stack, a CO_2 absorption vessel, a catholyte tank that also acts as a gas/liquid separator, pumps, condensers, and gas flow and composition measurement devices. All of the equipment shown would be controlled through a computer with access to temperature, pressure, flow, and level measurements at specific points in the system. The computer would also control a potentiostat, which would vary the current or potential across the electrochemical cell. The system would have the capability of automated polarity reversals, which include switching the liquid flows and currents across the system. This section will provide specific advice for implementation of these peripheral pieces of equipment.

Absorption Flask (After Cathode)

During experiments with the initial bench scale system, it was apparent that the design of the absorber significantly affected the overall performance. If the absorber is incapable of absorbing CO_2 at the same rate of desorption, than the CO_2 concentration of the solution will slowly decline until the driving force of absorption increases and the system reaches a steady state. We can model the rate of absorption, N_{abs}, in the flask by use of a simple overall mass transfer coefficient (from the gas to liquid phase), k_{abs} based on the gas phase and liquid phase concentrations of CO_2.

$$N_{abs} = k_{abs}\left(C_{CO_2}^{gas} - C_{CO_2}^{liq}\right) \tag{7-4}$$

Under the conditions of the original bench scale system (room temperature and small changes in copper loading), the absorption of CO_2 is mostly physical. For a larger system operated at higher temperatures, the main mechanism of absorption will switch from physical to chemical, and the mass transfer coefficient will increase sharply. Increasing the volume, and hence residence time, of the absorption flask is also an effective way to increase the CO_2 concentration in the sorbent headed to the anode.

In a heated system, the absorption tank is an excellent location to heat the solution, since heating the electrochemical cell would be difficult. Two strategies could be employed for keeping the absorber supplied with CO_2 while quantifying the rate of absorption. The first would be to constantly flow CO_2

into the system at a greater rate than the system can absorb it while measuring the inlet and outlet flow rates. The rate of absorption would equal the difference in the flow rates.

The second strategy would be to constantly monitor the pressure in the absorber, and only add CO_2 to maintain the pressure in the vessel. The rate of absorption in this setup is equal to the rate of CO_2 being added to the vessel. This strategy has the distinct advantage of having no outlet. At high temperatures, significant evaporative losses could occur from the absorber, necessitating a condenser on any outlet. By eliminating the outlet, the complexity of the system is greatly reduced. While the first strategy would of require two mass flow controllers and a condenser setup, the second strategy only requires one mass flow controller. If, however, it is desirable to add a mixture of nitrogen and CO_2 to simulate flue gas, the first option would be the only feasible strategy.

Including ports for pH probes, other ion-selective probes, or UV-Visible fiber optic probes in the absorption flask will allow for constant monitoring of the solution condition. A port for removing small samples for external analysis may also be helpful. The absorption flask is the logical choice for these ports, since the catholyte tank will be under significant pressure, and less amenable to such attachments.

Catholyte Tank (After Anode)

The catholyte tank, or gas/liquid separator, is where the two-phase mixture of copper loaded sorbent solution and gaseous CO_2 flow to after the anode. This vessel will need to be able to hold pressure, and hence, will most likely be a stainless steel bomb. This vessel will need to be heated in order to operate the system at elevated temperatures. Because of the added complexity (and cost) of the pressurized vessel, the number of ports on the catholyte tank should be kept to a minimum. A mass flow controller connected to the gas outlet of the catholyte tank will have the dual responsibility of measuring the CO_2 generation rate and maintaining the pressure in the anode side of the stack.

An alternative to using a flash tank design to separate the CO_2 from the sorbent liquid is to use inverted bucket steam traps. This would simplify the catholyte tank by removing the need for a gas outlet. Without the gas outlet, there is no need for a vessel. The heating of the liquid solution could be achieved

by flowing the liquid through coiled stainless steel tubing submerged in an oil bath. The efficacy of these steam traps for separating the gas/liquid mixture must be tested, however, before this strategy can be employed.

Potentiostat and Control Systems

The specific potentiostat chosen to manipulate and measure the current and potential through the system will be a critical decision. Gamry offers potentiostats with the ability to measure the potentials of multiple electrodes simultaneously in stacked systems like the one shown in **Figure 7-1**. The ability to run impedance spectroscopy will also be important for characterizing the resistances in the system as a function of many operating parameters, such as the flow rate. Gamry potentiostats can also be controlled through National Instruments' LabView software, which is the logical software choice for the rest of the control and measurement systems.

National Instruments offers modular data acquisition hardware that can take a variety of inputs and produce many different outputs. Temperatures will likely be measured through RTD's or thermocouples; pressure transducers generally provide 0-5 volt outputs. Mass flow controllers will often provide 0-5V or 0-10V outputs and accept the same input. Three way flow values, which will be important for automated polarity reversals, can be easily controlled through solid-state relays. All of this can be controlled from a single LabView visual interface, which will be responsible for controlling and recording all of the process parameters during an experiment. The exception to this will be the heated baths for the absorber vessel and catholyte tank; the temperature of these baths will most likely be controlled by a simple temperature controller, rather than the LabView program.

Liquid and Gas Control Strategies

Maintaining the flow rates, pressures, and liquid levels throughout the system will require implementation of several measurement and control strategies. For simplicity, two single input single output control loops should be employed rather than a single multi-input multi-output control strategy. A diagram of the gas and liquid control scheme can be seen in **Figure 7-3**.

The flow rates of the incoming nitrogen and CO_2 into the CO_2 absorption vessel are controlled simply from initial set points (SP) and not part of any larger control loop. The outlet of the absorber is only measured, and is not controlled. If a small gauge pressure were desired in the absorption vessel, a control loop with a pressure transducer input could be installed. The CO_2 outlet from the catholyte tank is controlled to maintain the pressure in the anode of the device. Therefore, if the pressure drops in the anode, the CO_2 outlet flow rate will be slowed until the pressure increases.

The liquid flow rate through the system is nominally set by the flow rate set point controlling pump 2. The flow rate of pump 1 is controlled to maintain the fluid level in the absorption vessel. Therefore, if the level in the absorber drops, the flow rate exiting the absorber will decrease until the level achieves the target height.

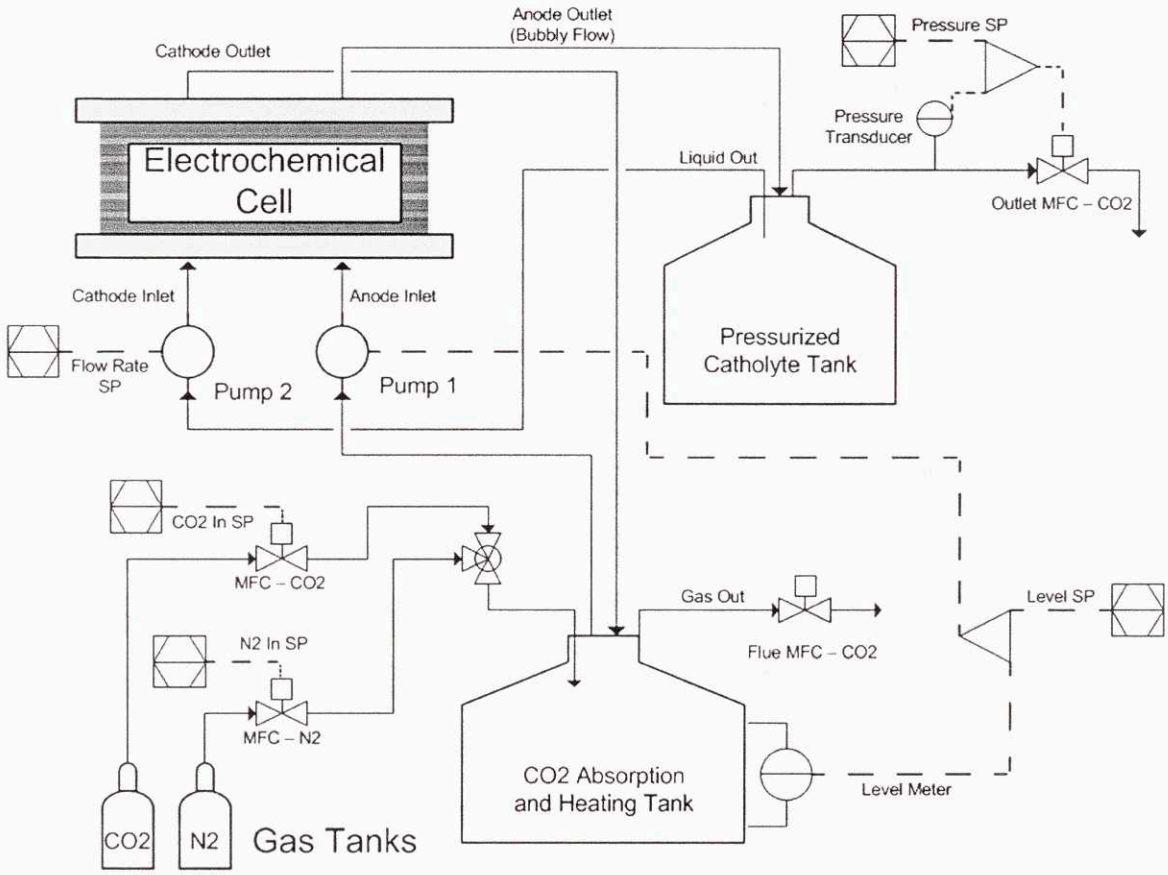

Figure 7-3. Measurement and control schematic of the proposed EMAR experimental setup. Equipment unimportant to the control scheme is omitted.

In addition to the two closed loop control schemes, a timing routine will be setup to automatically change the flows during polarity reversals. This can be achieved through three-way solenoid valves connected to solid-state relays. When the polarity is to be reversed, four three-way valves will switch configurations such that the anode inlet and outlet becomes the cathode inlet and outlet, and vice versa. It is important to put the valves after the pumps such that the absorber level control scheme is not affected. The activation of the three-way valves combined with switching the direction of the current applied by the potentiostat will constitute a full polarity reversal.

With the control schemes and the timing routine, the system should be capable of operating continuously for extended periods of time with no need for operator manipulation. Alarms could also be added if unsafe pressures are detected.

Additional Concerns

Materials of Construction

When designing an EMAR system, the inherent corrosiveness of the amine working solution must be considered. Chloride salts, which have been shown to enhance kinetics and appear to reduce the formation of passivating oxide layers, significantly increase the potential for corrosion. Aluminum, which is stable in most amine solutions, becomes susceptible to galvanic corrosion in the presence of chloride ions. For this reason, it is advisable to limit the contact of the supporting metallic structure (which will presumably be either steel or aluminum) with both the copper and the working solution. Different grades of stainless steel should be tested for their resistance to corrosion for use in fittings. Marine grade stainless steel, SAE 316, has shown good performance, type 18 has not, SAE 304 is untested.

Plastic parts can be safely constructed with polypropylene, PTFE (Teflon), or acetal (Delrin). Parts constructed with polycarbonate will fail after a few weeks of contact and should not be considered for pressurized systems. Tygon tubing has shown lasting resistance and Masterflex C-Flex (a mixture of Tygon and silicone) has been effective in peristaltic pumping applications. One concern with silicone

tubing would be the high CO_2 permeability. For pressure applications, SAE 316 stainless is probably the best option for fittings and tubing.

Thermal Considerations

Understanding the absorption and release of heat throughout the system will be important for designing large systems, which without proper construction, could experience a significantly non-isothermal temperature distribution. The temperature of the absorber, without intercooling, will rise do to the exothermic absorption of CO_2. For EDA, the heat of reaction is approximately -85 kJ/mole. In the electrochemical cell, where the CO_2 is being desorbed, the release of CO_2 will cause an equal and opposite cooling effect. This will be offset, to some extent, by the electrical heat being dissipated into the electrochemical cell. The change in temperature for the absorber and electrochemical cells can be approximated roughly by the following:

$$\Delta T_{Absorber} = 2\frac{\left(-\Delta H_{CO_2}\right)\Delta C_{Cu}}{c_p} \tag{7-5}$$

$$\Delta T_{Cell} = 2\frac{\left(\Delta H_{CO_2} + F\Delta V\right)\Delta C_{Cu}}{c_p} \tag{7-6}$$

For the electrochemical cell to operate isothermally, a cell potential of nearly a volt would need to be applied. For a system requiring 0.5 volts, the swing in cupric ion concentrations would have to be kept below 0.5M, to keep temperatures drops below 10°C. This limits the maximum useful amine concentrations below 2M.

Using the incoming hot flue gas to heat the electrochemical cell could offset some of the temperature swing. As was shown in the thermodynamic chapter, the electrochemical cell requires less energy at higher temperatures. Therefore, using any available waste heat for heating the electrochemical cell will yield efficiency gains.

Solution Composition

As can be seen from the thermal considerations, the concentration of the amine in the working solution has many secondary effects, including the size of the temperature swings. Additionally, low amine loadings lead to lower viscosities, which can improve conductivities and absorption rates significantly. Therefore, using lower concentrations of amines may be advisable, despite the need to increase circulation rate.

In the kinetics section, the significant impact of chloride salts was described. It is likely that some intermediate complexing species can be added to greatly enhance the kinetics, with little downside. Chloride salts, due to their aforementioned enhancement of corrosion, may not be the best choice. Investigation into other halides and small organics (ammonia, acetate, citrate, ascorbate) may lead to a better additive.

Higher concentrations of electrolytes will improve conductivity but increase viscosity. Only a detailed model, which can account for both effects, can determine the correct balance. Reasonably high conductivities can be achieved with 1M solutions of electrolyte without significant viscosity implications.

Copper Loadings

The operational copper loadings will significantly impact the process efficiency. High copper loadings exiting the anode and low loading exiting the cathode will lead to increased overpotentials near the respective exits. As was shown in the electrochemical kinetics results, overpotentials are most sensitive to high copper loadings. For this reason, copper loadings at the exit of the anode should not exceed 0.9. Loadings of 0.1 or below exiting the cathode should be achievable with low energy penalties provided there is sufficient mass transport in the electrochemical cells to prevent excessive concentration polarization.

Another operational strategy, which would avoid high copper loadings and reduce the open-circuit cell potentials, would be to target a maximum copper loading of 0.5. With this strategy, the reaction in the cathode would switch from:

$$Cu(EDA)_2^{2+} + 2e^- \rightleftharpoons Cu + 2EDA \tag{7-7}$$

to

$$Cu(EDA)_2^{2+} + 2(EDA\text{-}CO_2) + 2e^- \rightleftharpoons Cu + 2EDAH^+ + 2EDACO_2^- \tag{7-8}$$

At loading of 0.5, only half of the CO_2 is released; the remaining half participates in the cathode as shown above. Since CO_2 is present on both sides of the electrochemical cell, the activity of the amines is more similar, which will promote a smaller open-circuit potential. The kinetics chapter, however, demonstrated that operating the cathode with CO_2 will increase overpotentials. Additionally, only desorbing half the CO_2 will decrease absorption kinetics.

Degradation of amines or copper

Instability of the sorbent or the copper electrodes requires significantly more research. Oxygen will be present in the system, via the flue gas, and will react with both the amines (oxidative degradation) and the metallic copper electrodes (corrosion). It is unclear if either oxidative degradation or corrosion is preferable over the other. It has been previously reported that cupric ions can catalyze oxidative degradation, but the effect of such high concentrations is unknown. The extent of copper ion catalysis for such strongly chelating polyamines is also unclear since it is similar amines, such as ethylendiaminetetracetic acid (EDTA), are added as corrosion inhibitors for ethanolamine scrubbers. Degradation of the amine is the most likely concern since significant contact with the flue gas occurs in the scrubber. The copper electrodes are exposed only to the oxygen that dissolves into the solution, which will only be on the order of 10μM.

With normal operation, the system should be able to reach outlet cupric ion concentrations of 10mM. Beyond this, an additional porous electrode setup for reducing the cupric ion concentration below 0.1mM could be added. Furthermore, if 10mM of EDTA is added to the system, this may inactivate the low concentration of cupric ions in the absorber.

Ion chromatography is an effective technique for measuring amine degradation. Most small amines will eventually degrade to form small organic ions, such as acetate, which can be readily

measured over time. Some form of HPLC analysis may also work. Gas chromatography would be difficult due to the high fraction of non-volatile salts in the working sorbent.

Zero-Bubble Operation

Bubbles are one of the primary reasons that porous electrodes, which would perform much better from a kinetics and transport perspective, are difficult to employ in a realistic system that must operate robustly for long periods of time. If the system was operated at a high pressure, the water in the anode would absorb the electrochemically released CO_2 physically rather than allow bubbles to form. The CO_2 could then be flashed off in a subsequent tank at lower pressure. The downsides of such an operating strategy would be the added cost of pumping and the increased open-circuit potential required due to the increased pressure of CO_2 in the anode. Operation at lower temperatures, where the thermodynamics, kinetics, and transport are less favorable, may be necessary to increase the physical solubility.

As was shown by the derivations from the thermodynamics chapter, the difference in open-circuit $\Delta V^{Open}(P_1,P_2)$ potential as a function of pressure can calculated by,

$$\Delta V^{Open}(P_1, P_2) = \frac{RT}{F} \ln\left(\frac{P_2}{P_1}\right) \tag{7-9}$$

At 50°C, this would be approximately 44 mV, which is not excessive when compared to the expected reductions in overpotentials. The difficulty that must be overcome for this strategy is the relatively low physical capacity of CO_2 in water. At 50°C with a pressure swing from 60 bar to 10 bar, a 0.7M CO_2 swing can be achieved.[153] This means that for a 2M EDA solution, two to three release stages would be necessary to prevent any bubble formation.

Another significant drawback could be the permeance of CO_2 across the membrane. Effective membranes that prevent CO_2 diffusion would be necessary. Porous polyolefin membranes would most likely be insufficient at preventing CO_2 diffusion. Nafion membranes have also been shown to have relatively high permeability to CO_2, which is not surprising since fluorinated polymers like Teflon, the

backbone of Nafion, are relatively permeable to CO_2. Ionomers not based on Teflon, may meet this requirement.

Preliminary Techno-Economic Assessments

Three techno-economic assessments will be presented in this section: one for a flat plate system, one for a porous electrode system with bubble formation, and one for a porous electrode system operating under zero-bubble conditions. Based on the thermodynamic, kinetic, and transport experiments and modeling, reasonably accurate predictions can be made for the electricity demands for the system under normal operating conditions.

Long-term operating concerns, including electrode stability and the amine stability are difficult to predict. Capital costs of designing an EMAR system are also poorly-defined. The working sorbent is 2M EDA with 2M NaCl supporting electrolyte. **Table 7-1** shows estimates of all the input parameters necessary for the techno-economic assessment. While an optimization or sensitivity analysis would be an ideal way to examine the relative importance of all the parameters, the large number of inputs and complex models make that type assessment difficult at this point. For this analysis, the parameters were chosen based on engineering approximations of reasonable operating conditions. Sensitivity analyses will be necessary in the future to accurately assess the potential of an EMAR system.

Estimates for the molecular diffusivity and conductivity of the solution are obtained using the Stokes-Einstein equation shown in Eq. 7-10,

$$D = \frac{kT}{6\pi\mu r_H} \tag{7-10}$$

Where k is the Boltzmann's constant and r_H is the hydrodynamic radius of the molecule.

Calculation of the diffusivity with Eq. 7-10 is challenging without accurate estimates of the hydrodynamic radius. It is, however, easy to calculate the diffusivity, D, at a given temperature, T, with a known viscosity, μ, if the viscosity and diffusivity are known at a reference temperature, T_0.

$$D = D_0\left(\frac{T}{T_0}\right)\left(\frac{\mu_0}{\mu}\right) \tag{7-11}$$

The conductivity can be calculated in an identical fashion. Standard state diffusivities and conductivities of copper sulfate systems are readily available in literature.[171,168,172] The viscosity of aqueous EDA solutions at a range of temperatures is also available.[59,173] The viscosity, μ, of an aqueous amine solution with copper salt is estimated by multiplying the viscosity of water, μ_W, by the specific viscosities (actual viscosity over the viscosity of water) of EDA, μ_{EDA}, and copper salt systems, μ_{Cu},. Values for μ_W, μ_{EDA}, and μ_{Cu} can be found in literature.

$$\mu = \mu_W\left(\frac{\mu_{EDA}}{\mu_W}\right)\left(\frac{\mu_{Cu}}{\mu_W}\right) \tag{7-12}$$

The first four parameters of **Table 7-1** are based on the plant specifications. The next 19 parameters are specifications of the capture plant. The final 16 parameters are chemical properties of the EDA sorbent under the operating conditions.

The plant specifications represent typical values for a 500 MW_e supercritical coal-fired power plant.[28] Both new power plants designed with carbon capture systems or existing power plants worth retrofitting would likely be supercritical. This analysis, however, will emphasize the economics of retrofitting existing plants, which is the most attractive aspect of the EMAR technology.

To assess the total impact on the cost of electricity (COE), some estimates must be made with regard to capital costs. Two cases will be considered:

Case 1: The capital cost of installing an EMAR system is equivalent to the cost retrofitting an existing plant with a thermal amine carbon capture system.

Case 2: The capital cost of installing an EMAR system is equivalent to the additional cost of including a thermal amine carbon capture system in a built for purpose plant.

Because of the simplicity of the EMAR system and low level of required integration, Case 2 may be the more accurate representation.

Table 7-1. Inputs of parameters for the techno-economic assessment of three different EMAR configurations. Plant specifications based on a sub-critical coal-fired power plant.

Parameter	Abbrev.	Flat Plates		Porous		Zero-Bubble	
		Value	Unit	Value	Unit	Value	Unit
CO_2 Mass Flow Rate	F_{CO2}	466	Mg/hr	420	Mg/hr	420	Mg/hr
Flue Gas CO_2 Partial Pressure	P_F	0.11	bar	0.11	bar	0.11	bar
CO_2 Capture Fraction	x_{CO2}	0.9		0.9		0.9	
Incoming Flue Gas Temperature	T_F	55	°C	55	°C	55	°C
Membrane Current Density	j_M	500	A/m^2	500	A/m^2	500	A/m^2
Absorber Pressure	P_{abs}	1	bar	1	bar	1	bar
Anode Pressure	P_A	10	bar	10	bar	60	bar
Desorption Pressure	P_{out}	8	bar	8	bar	8	bar
EDA Concentration	$[EDA]_0$	2	mol/L	2	mol/L	2	mol/L
Flow Channel Thickness	H	1	mm	2	mm	2	mm
Superficial Flow Rate	U	0.1	m/s	0.1	m/s	0.1	m/s
Flat Plate Electrode Remix Length	L_R	0.1	m				
Porous Electrode Surface Area	S			1000	m^2/m^3	1000	m^2/m^3
Electrode Porosity	ε_{pore}	1.0		0.9		0.9	
Darcy's Law Permeability	k_D			5×10^{-9}	m^2	5×10^{-9}	m^2
Lean Copper Loading	x_{low}	0.1		0.1		0.1	
Heavy Copper Loading	x_{high}	0.9		0.9		0.9	
Faradaic Efficiency	η_F	0.9		0.9		0.9	
Compressor efficiency	η_C	0.7		0.7		0.7	
Pump Efficiency	η_P	0.7		0.7		0.7	
Effective Operating Temperature	$Tsys$	70	°C	70	°C	60	°C
Maximum Gas Fraction in Anode	y_{max}	0.5		0.5		0	
Effective Membrane Thickness	d_{mem}	0.25	mm	0.25	mm	0.25	mm
CO_2 Binding Constant	K_{CO2}	145		145		360	
SS Anode Exchange Current Density	i_0^A	56	A/m^2	56	A/m^2	33	A/m^2
SS Cathode Exchange Current Density	i_0^C	152	A/m^2	152	A/m^2	89	A/m^2
Anode Electron Transfer Coefficient	α_A	0.35		0.35		0.35	
Cathode Electron Transfer Coefficient	α_C	0.35		0.35		0.35	
Henry's Law Constant	H_{CO2}	3800	bar	3800	bar	3300	bar
Molar Volume	v_m	0.02	L/mol	0.02	L/mol	0.02	L/mol
Lean Solution Viscosity	μ_L	0.65	mPa*s	0.65	mPa*s	0.75	mPa*s
CO_2 Loaded Solution Viscosity	μ_{CO2}	1.3	mPa*s	1.3	mPa*s	1.5	mPa*s
Cu^{2+} Loaded Solution Viscosity	μ_{Cu}	1.3	mPa*s	1.3	mPa*s	1.5	mPa*s
Lean Solution Diffusivity	D_L	1.2×10^{-9}	m^2/s	1.2×10^{-9}	m^2/s	1.0×10^{-9}	m^2/s
CO_2 Loaded Solution Diffusivity	D_{CO2}	0.6×10^{-9}	m^2/s	0.6×10^{-9}	m^2/s	0.5×10^{-9}	m^2/s
Cu^{2+} Loaded Solution Diffusivity	D_{Cu}	0.6×10^{-9}	m^2/s	0.6×10^{-9}	m^2/s	0.5×10^{-9}	m^2/s
Lean Solution Conductivity	κ_L	22	S/m	22	S/m	19	S/m
CO_2 Loaded Solution Conductivity	κ_{CO2}	11	S/m	11	S/m	9	S/m
Cu^{2+} Loaded Solution Conductivity	κ_{Cu}	22	S/m	22	S/m	19	S/m

Based on these input parameters, the dimensions of the necessary EMAR cell can be readily calculated. The required membrane area is a function of the membrane current density, the Faradaic efficiency, and the rate of CO_2 capture.

$$A_{mem} = F\frac{F_{CO_2}x_{CO_2}}{M_W^{CO_2} j_M \eta_F} \tag{7-13}$$

The path length of the EMAR cell can be calculated using Eq. 7-3 with the low and high copper loadings in lieu of the ΔC_{Cu} term as shown in Eq. 7-14.

$$L_p = [\mathrm{EDA}]_0 \frac{U H F \varepsilon_{pore}}{j_M}\left(x_{high} - x_{low}\right) \tag{7-14}$$

The EMAR cell width, W, which is the total width of all the parallel channels required, is calculated by dividing the total membrane area by the path length. The volume of all the flow channels is calculated by multiplying the membrane area by the channel thickness and the porosity.

$$W = \frac{A_{mem}}{L_p} \qquad V_{cell} = A_{mem} H \varepsilon_{pore} \tag{7-15}$$

The diffusivity and conductivity in the anode are calculated by the average of the CO_2 and copper loaded values. The diffusivity and conductivity in the cathode are calculated by the average of the copper loaded and lean values. The dispersion, or effective diffusivity, in the porous electrode systems is estimated to be one order of magnitude higher than the molecular diffusivity because agitation caused by flowing through a porous matrix. The dispersion in the flat plate system is predicted to be twice the molecular diffusivity because flow profile through the channels will not have time to fully develop.

The open-circuit potential is calculated by a modified form of Eq. 3-6 shown in Eq. 7-16. The higher values of P_A and K_{CO2} in the zero-bubble case lead to an increased open-circuit potential.

$$\Delta E = \frac{RT}{F}\ln\left[1 + K_{CO_2}\frac{P_A}{P_0}\right] \tag{7-16}$$

The anodic and cathodic overpotentials are based on the Butler-Volmer equation presented in Eq. 4-6. The values for the exchange current densities are only the standard state values (i.e. $[\mathrm{EDA}]_0$ = 1M and

$[Cu^{2+}]_0$ = 0.25M). In chapter 4 it was shown that the exchange current density scales linearly with the non-copper complexed EDA concentration, [EDA], and with the square root of the copper ion concentration. **Figure 7-4** shows the kinetic overpotentials as a function of the copper loading in the system. The average values are reported in **Table 7-2**.

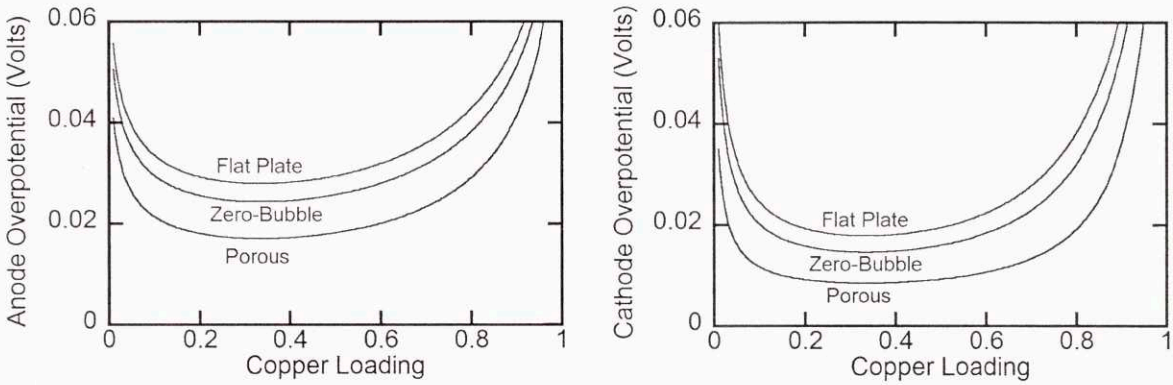

Figure 7-4. Anodic (left) and cathodic (right) kinetic overpotentials as a function of copper loading for the three configurations compared in the techno-economic assessment. Lines are solid when in the operating range of copper loading.

The overpotentials shown in **Figure 7-4** reflect only the overpotentials due to electrode kinetics. The flat plate requires the highest overpotentials because it has less electrode surface area compared to the porous electrode systems. The zero-bubble system requires higher overpotentials than the normal porous electrode system because of the lower operational temperature, which results in lower exchange current densities. Note that the range of copper loadings shown in **Figure 7-4** is larger than the operational range. The values reported in **Table 7-2** are the averages within the operational range.

To incorporate the transport limitations highlighted in chapter 5, the flat plate and porous electrode models must be used. **Figure 7-5** shows the overpotentials caused by the combined transport and kinetic effects. **Table 7-2** reports the transport overpotential, which is defined as the combined overpotential minus the purely kinetic overpotential. The loadings of the flat plate system are narrower than in the porous electrode systems because of the mass transport is incapable of obtaining the fluxes required at extreme loading conditions. Because the required potentials for the porous electrode systems

are in the borderline applicability region between the linear and Tafel models, a numerical solver was used to solve Eqs. 5-25 and 5-26 without simplifying assumptions.

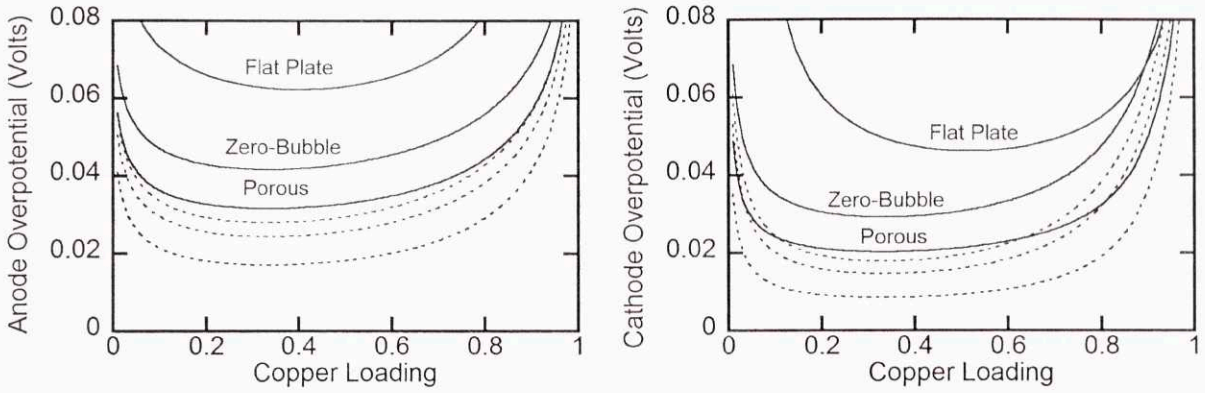

Figure 7-5. Anodic (left) and cathodic (right) overpotentials as a function of copper loading for the three configurations compared in the techno-economic assessment. Solid lines represent combined kinetic and transport overpotentials. Dashed lines represent overpotentials without transport limitations.

Figure 7-5 shows that the addition of transport limitations increases further the disparity in overpotentials between the different configurations. The flat plate electrode system shows dramatic increases in the required overpotential due to concentration polarization at the electrode surface. The lower conductivities in the zero-bubble configuration, which result from the lower operating temperature, produce larger transport overpotentials when compared to the standard porous electrode case. In a real system, requiring a constant current density across the whole range of copper loadings is not ideal. Instead, the required membrane current densities should be correlated with the exchange current densities of the solution.

The solution overpotential, E_S, represents the resistance of ion transport across the flow channel in the flat plate electrode system. The ionic transport resistance in the porous electrode system is already accounted for in the transport model, and thus no additional solution resistance is required. The solution overpotential in the flat plate system is a function of the conductivity, κ, as shown in Eq. 7-17.

$$E_S = \frac{j_M H}{\kappa} \tag{7-17}$$

The solution overpotential in **Table 7-2** represents the sum of solution potentials for the cathode and anode flow channels. At 52 mV, the solution overpotential is a significant inefficiency. To calculate the membrane overpotential, an effective membrane length, d_M, is used to represent the resistance to ion

migration through the membrane. The resulting overpotential can be calculated using Eq. 7-18, which closely resembles Eq. 7-17.

$$E_M = \frac{j_M d_M}{\kappa} \tag{7-18}$$

To account for the below unity porosity and tortuosity of the membrane, and effective length of 10 times the standard membrane thickness of 25 μm is used. An average of the anode and cathode conductivities is used for calculating the membrane overpotential.

The total potential per cell, ΔE_{net}, can be calculated as the sum of the open-circuit potential, the kinetics potentials, the transport potentials, the solution potentials, and the membrane potential; all of these values are reported in **Table 7-2**. The flat plate and zero-bubble systems require similar potentials of 0.35 and 0.37 volts respectively. The range of copper loadings, however, is wider for the zero-bubble porous electrode case, which increases the required potential. The standard porous electrode system shows significantly better performance at 0.29 volts.

The required volumetric sorbent flow rate can be calculated from the dimensions of the EMAR system and the superficial velocity. Using Eq. 7-13 through Eq. 7-15, the volumetric flow rate can also be calculated in terms of the process parameters.

$$F_S = HUW = \frac{F_{CO_2} x_{CO_2}}{[\text{EDA}]_0 \varepsilon_{pore} \left(x_{high} - x_{low}\right) M_W^{CO_2} \eta_F} \tag{7-19}$$

The pressure drops across the system are calculated either Poiseuille equations for laminar flow between parallel plates or using the Darcy's law permeability coefficient, k_D. For a flat plate system, the pressure drop, ΔP is calculated with Eq. 7-20. For the porous electrode system, the pressure drop is calculated with Eq. 7-21.

$$\Delta P = -12 \frac{F_S \mu L_P}{W H^3} = -12 \frac{U^2 \mu}{H} \frac{F \varepsilon_{pore}}{j_M} \left(x_{high} - x_{low}\right)[\text{EDA}]_0 \tag{7-20}$$

$$\Delta P = -\frac{\mu F_S L_P}{k_D W H} = -\frac{\mu U^2}{k_D} \frac{H F \varepsilon_{pore}}{j_M} \left(x_{high} - x_{low}\right)[\text{EDA}]_0 \tag{7-21}$$

The results, which are shown in **Table 7-2**, demonstrate the dramatically lower pressure drops of a flat plate system compared to a porous electrode system. Lowering the velocity in the porous electrode systems by 50% would reduce the pressure drop by a factor of 4. This should be strongly considering in any sensitivity analysis or design optimization of porous electrode systems.

Table 7-2. Calculated system properties for the three configurations examined in the techno-economic analysis.

Parameter	Abbrev.	Flat Plate		Porous		Zero-Bubble	
		Value	Unit	Value	Unit	Value	Unit
EMAR Membrane Area	A_{mem}	0.51	km^2	0.51	km^2	0.51	km^2
EMAR Cell Path Length	L_p	24.7	m	55.6	m	55.6	m
EMAR Cell Width	W	20.5	km	9.1	km	9.1	km
EMAR Flow Cell Volume	V_{cell}	404	m^3	1011	m^3	1011	m^3
Electrode Area/Membrane Area	S^*H	1		2		2	
Anode Dispersion	D_A	1.2×10^{-9}	m^2/s	0.6×10^{-8}	m^2/s	0.5×10^{-8}	m^2/s
Cathode Dispersion	D_C	1.8×10^{-9}	m^2/s	0.9×10^{-8}	m^2/s	0.8×10^{-8}	m^2/s
Anode Conductivity	κ_A	17	S/m	17	S/m	14	S/m
Cathode Conductivity	κ_C	22	S/m	22	S/m	19	S/m
Open-Circuit Potential	ΔE_{OC}	0.215	Volts	0.215	Volts	0.287	Volts
Anode Kinetic Overpotential	E_k^A	0.034	Volts	0.022	Volts	0.030	Volts
Cathode Kinetic Overpotential	E_k^C	0.026	Volts	0.013	Volts	0.021	Volts
Anode Transport Overpotential	E_T^A	0.026	Volts	0.015	Volts	0.017	Volts
Cathode Transport Overpotential	E_T^C	0.039	Volts	0.012	Volts	0.015	Volts
Membrane Overpotential	E_M	0.007	Volts	0.007	Volts	0.008	Volts
Solution Overpotential	E_S	0.000	Volts	0	Volts	0	Volts
Total Cell Voltage	ΔE_{net}	0.347	Volts	0.284	Volts	0.377	Volts
Sorbent Flow Rate	F_S	1.64	m^3/s	1.64	m^3/s	1.64	m^3/s
Pressure Drop Across Cell	ΔP	0.53	bar	11.4	bar	13.1	bar
Number of CO_2 Release Steps	N_R	5		5		2	
Pressure Drop for Release	ΔP_R	1	bar	1	bar	25	bar

The number of CO_2 release steps is another important design factor. This determines how many times the solution may have to be removed from the electrochemical stack, which requires significant piping and instrumentation. When the solution is pumped back into the stack, the pressurization requirement is estimated by ΔP_R. Because of the high anode pressure in the zero-bubble case, it is costly to repressurize the sorbent. It is assumed that 50% of the pressure can be recovered through turbines.

To calculate the number of release steps, we first calculate the volume of CO_2 captured, V_{CO2}, per volume of solution, V_S, per cycle through the system.

$$\frac{V_{CO_2}}{V_S} = [\mathrm{EDA}_0]\left(x_{high} - x_{low}\right)\frac{RT_{sys}}{P_A} \tag{7-22}$$

This ratio divided by twice the maximum gas ratio, y_{max}, yields the number or release stages, N_R.

$$N_R = \frac{1}{2y_{max}}[\mathrm{EDA}_0]\left(x_{high} - x_{low}\right)\frac{RT_{sys}}{P_A} \tag{7-23}$$

For the zero-bubble system, where the maximum gas fraction is zero, we must consider the physical solubility. Therefore, we the divide the moles of CO_2 captured per liter of solution by the difference in moles per liter of CO_2 physical solubility from the anode pressure to the desorption pressure. The difference in solubility is difficult to theoretically represent as a function of temperature and pressure, but can found in tables and charts from literature. Based on the conditions described in **Table 7-1**, the difference in physical solubilities is approximately 0.7 moles/L, which necessitates 2 release steps. Each step is costly due to the significant amount of lost pump work during the depressurization.

Table 7-3 shows the different parasitic electrical demands required to operate the EMAR scrubber. Additionally, the cooling duty required by the absorber and the heat duty required by the EMAR cell to maintain isothermal operation are reported. The electric demand of the flue gas blower, W_B, is calculated by an empirical equation.

$$W_B = \frac{1.45\ \mathrm{MW}}{100{,}000\ \mathrm{kg\ CO_2\ per\ hour}} \tag{7-24}$$

The pump demand is calculated assuming 70% efficiency. The compressor work is calculated assuming 70% isentropic efficiency using the Peng-Robinson equation of state described in Chapter 2.

The absorber cooling duty is calculated by subtracting the heat that can be removed by the increase in temperature of the flue gas from the heat released by the absorption of CO_2. A gas heat capacity, c_P, of 1 kJ/kg/°C and an enthalpy of sorprtion, ΔH_{rxn}, of 85 kJ/mole CO_2 are assumed.

$$Q_C = F_S\left[\text{EDA}\right]_0\left(x_{high} - x_{low}\right)\left(-\Delta H_{rxn}\right) - \frac{F_{CO_2}}{P_F} c_P\left(T_{sys} - T_F\right) \tag{7-25}$$

The heat requirement for the electrochemical cell can be calculated by a similar equation. It is assumed all of the energy from the electrochemical and pump inputs eventually heats the fluid in the electrochemical cell.

$$Q_H = F_S\left[\text{EDA}\right]_0\left(x_{high} - x_{low}\right)\left(-\Delta H_{rxn}\right) - W_{EC} - W_P \tag{7-26}$$

Table 7-3. Parasitic energy requirements for the three EMAR configurations in the techno-economic analysis.

Parameter	Abbrev.	Flat Plate		Porous		Zero-Bubble	
		Value	Unit	Value	Unit	Value	Unit
Electrochemical Electricity Demand	W_{EC}	87.7	MW	71.7	MW	95.4	MW
Pump Electricity Demand	W_P	1.2	MW	3.7	MW	8.9	MW
Compressor Electricity Demand	W_C	23.2	MW	23.2	MW	21.7	MW
Flue Gas Blower Electricity Demand	W_B	6.0	MW	6.0	MW	6.0	MW
Total Electricity Demand	W_{net}	118	MW	105	MW	132	MW
Power Plant De-rating		23.6	%	20.9	%	26.4	%
Absorber Cooling Duty	Q_C	207	MW	207	MW	217	MW
EMAR Cell Heating Duty	Q_H	134	MW	147	MW	118	MW

The heating and cooling demands for the absorber and electrochemical cell are large, which substantially erodes the advantage of an electrochemical system. However, if non-isothermal operation is considered, where temperatures are allowed to vary approximately 10°C within both units, the required heat and cooling duties become manageable. The necessary temperature swing for adiabatic operation, ΔT_{ad}, of one of the units can be calculated by Eq. 7-27. A heat capacity for the sorbent of 4 kJ/kg/°C is reasonable. More dilute working solutions and amines with lower heats of reaction would also reduce the heating and cooling duties.

$$\Delta T_{ad} = \frac{Q}{\rho F_S c_P} \tag{7-27}$$

All three configurations tested in the techno-economic analysis yield power-plant de-ratings between 20.9% and 26.4%, which is a relatively narrow range considering the high levels of uncertainty about many of the important chemical and design parameters. The zero-bubble system performs the worst due

to the high pump work required to re-pressurize the solution after the intermediate release step. The zero-bubble system also suffers from operating at a lower temperature, which is necessary to keep the release steps to just one intermediate step and the release step at the end of the anode.

The difference in kinetic and transport overpotentials between the flat plate system and the porous electrode system becomes somewhat minor compared to the final electrical demand. The flat plate systems also benefit significantly from the much reduced pressure drop across the system. If a spacer material is required for structural support, however, that could add to the pressure drop of the system.

When compared with the estimated 36% de-rating of supercritical retrofits using conventional scrubbing technologies and an estimated 31% de-rating for the installation of an oxy-fuel system, the EMAR scrubber shows tremendous potential.[28] For a purpose built system, however, there is no significant efficiency advantage for using an EMAR scrubber over the other technologies.

The calculated de-ratings can be used to calculate a levelized cost of electricity (COE) based on several previous techno-economic analyses done by EPRI and Alstom, which were normalized in the MIT *Future of Coal* report.[28,174,175] The COE is based on 2005 dollars. Operation and maintenance costs were assumed linearly correlated to total capital costs between the power plant and the capture plant.

Two cases were considered to predict the capital cost of an EMAR system. Case 1 assumes the cost of the EMAR capture plant is equal to the cost of a retrofit thermal amine scrubbing plant. Case 2 assumes the cost of the EMAR capture plant is equal to the cost of including a thermal amine scrubbing plant in a built-for-purpose capture plant. Based on the MIT report, the capital cost in Case 1 is $17/MWh of gross electrical capacity (i.e., before considering the parasitic losses due to the capture plant). For Case 2, the cost is $8.2/MWh. **Figure 7-6** shows the COE for the base case supercritical plant with no capture, for new and retrofit thermal scrubbers, and for a flat plate EMAR system under both cases. Because of the drop-in nature of the EMAR system, the capital cost of the capture plant is not expected to be significantly different for retrofits or new built-for-purpose plants.

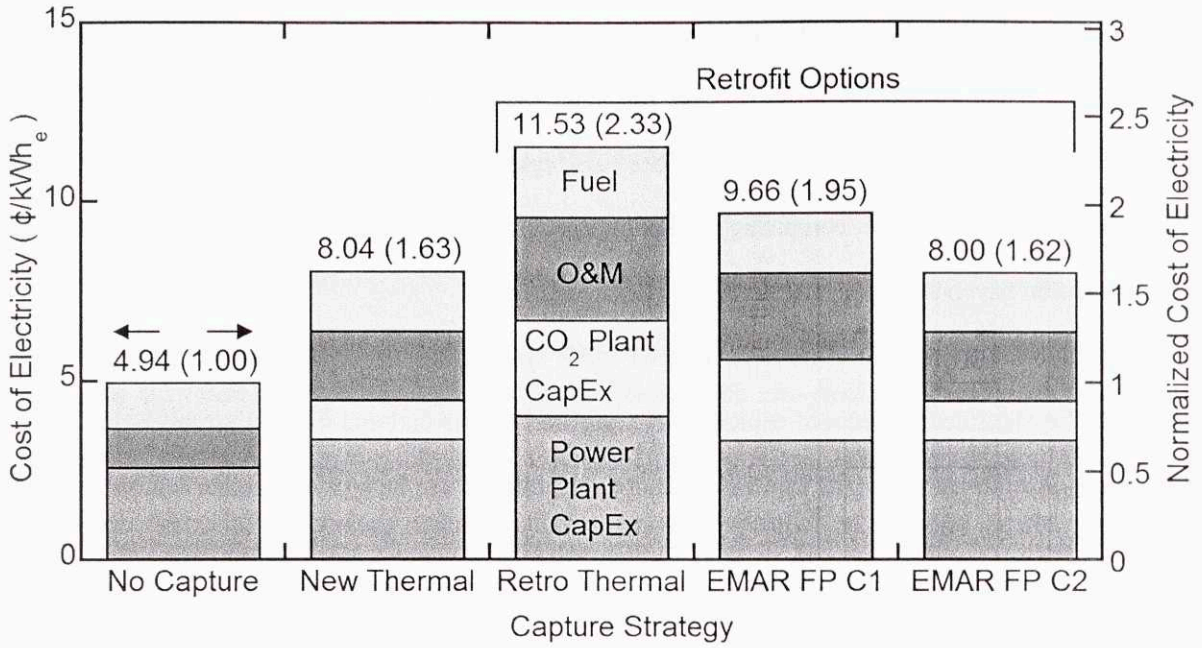

Figure 7-6. Comparison and breakdown of the COE for the base case supercritical plant, new and retrofit thermal scrubbing systems, and both cases the flat plate EMAR system.

Figure 7-6 shows that the COE increases by 133% if a retrofit thermal scrubbing system is installed. The flat plate EMAR systems, however, only show a 95% and 62% increase for Case 1 and 2, respectively. For Case 1, the EMAR system would be the best choice for retrofits, but less desirable than a new plant with a built-for-purpose thermal scrubbing system. For Case 2, the EMAR system is the best option, whether it is for a new plant or for a retrofit. For a porous electrode system, the increases in COE are 89% and 56% for Case 1 and 2, respectively.

Case 2 is a reasonable approximation, because while the cost of the copper is in the 10's of millions of dollars, the capital savings from the reduced compressor requirements is comparable. For a flat plate system initially with 0.75 mm thick copper plates on each electrode, the cost of copper would be about $37 million for 5.1 million kg. This represents 56 times the quantity of copper on the Statue of Liberty but only 0.4% of the annual production in the United States. Applying this technology to 10's of plants a year would not significantly disrupt the global copper market.

When compared with the estimated 37% de-rating of retrofits using conventional scrubbing technologies and an estimated 36% de-rating for the installation of an oxy-fuel system, the EMAR

scrubber shows tremendous potential. For a purpose built system, however, there is no clear efficiency advantage for using an EMAR scrubber over the other technologies. It is implicitly assumed in this analysis that a stable and robust EMAR system can be designed to last decades without significantly more maintenance than the other competing technologies. This will require further development and experimentation beyond what has been currently demonstrated.

In addition to the high efficiencies of the EMAR system, the "drop-in" format of the technology may allow for significantly reduced capital costs compared to conventional thermal scrubbers in retrofit applications. Additionally, EMAR systems are more versatile and can be applied to other industries, such as cement, steel, and aluminum. EMAR systems may also be effective for smaller-scale applications such as producing CO_2 for bio-refineries or even removal of CO_2 from enclosed areas in spacecrafts or submarines.

Chapter 8

Conclusions and Recommendations

Summary

This thesis has made a compelling argument for further research into electrochemically-mediated amine regeneration scrubbers for post-combustion carbon dioxide separations. In the introduction, the need for an electric "drop-in" technology capable of less invasive retrofits of existing power plants was highlighted. Furthermore, a capture technology of this form would be effective for carbon capture from other large point-source emitters such as cement, steel, and aluminum plants.

The specific chemistry chosen for the EMAR process was developed and optimized in the second chapter through screening of 13 different metals and 14 different amines. Operational benefits of the process, which included high pressure desorption, reduced absorber size, and the ability to use polyamines that are poorly suited for thermal systems, were also discussed.

The thermodynamics and kinetics that govern the performance of an EMAR capture system were explored through experimentation and modeling in Chapters 3 and 4. The thermodynamic limit of the system efficiency was determined to be 70% at open-circuit conditions. Analysis of the electrochemical reaction kinetics demonstrated a significantly more facile process than would have been predicted by conventional theories on dissociative electron transfer. Derivation of a new theory based on a consecutive two-electron transfer process, where the intermediate is stabilized by the complexing agent justifies the enhanced kinetics.

Using the experimentally determined thermodynamics and kinetics, the performance of real systems was predicted using transport models for flat plate electrode and porous electrode systems. In both cases, the partial differential equations (PDE) governing the transport phenomena are simplified through a detailed analysis based on reasonable approximations. For the flat plate system, the employed

integral solution strategy converts the PDE to an ordinary differential equation (ODE). For the porous electrode system, the coupled PDE based on the Nernst-Planck equation can be solved entirely by a set of two non-linear algebraic equations.

A proof-of-concept device was constructed to demonstrate the ability for an EMAR scrubber to successfully capture CO_2 at the bench scale. The system achieved up to 80% Faradaic (current) efficiency despite limited optimization of the system design. Stable cyclic operation was achieved and experiments up to 7 hours showed no deterioration of performance over time. Experiments with nitrate salts systems achieved CO_2 capture at a rate of 800 sccm/m^2 with an electricity demand of 100 kJ/mole CO_2. This was achieved despite the limitation of the operating conditions to ambient temperature and pressure. Experiments with chloride salt systems were inconsistent due to significant corrosion problems with the aluminum frame of the device. Copper powder formation in the solution occurred along with loose copper film formation on the electrode surface; the long-term implications of these phenomena are not known.

Recommendations for the next generation bench-scale system were provided in Chapter 7 based on experience from operating the proof-of-concept system. A specific design for future electrochemical cell stacks and suggestions for peripheral equipment and control strategies were provided. Additional concerns including material stability, electrochemical stack heating, and sorbent solution composition were also discussed.

Based on the best available thermodynamic, kinetic, transport, and operational experience, a thorough techno-economic analysis (TEA) is provided. The TEA shows that several different EMAR configurations could achieve below 30% de-ratings on a sub-critical coal-fired power plant. This performance is a significant improvement over traditional thermal scrubbing system, which would cause a 42% de-rating. The 20% to 30% de-ratings for an EMAR system, however, are not a significant improvement over other technologies when considering a built-for-purpose power plant with CO_2 capture.

Directions for Future Research

While this thesis has shown that an EMAR system has the potential to drastically reduce the cost of retrofitting an existing plant, many significant technical challenges must be considered before the process could be ready for application in industry.

At the forefront of these concerns is operational stability. It must be proven that an EMAR system could operate continuously for weeks or months without failure of the electrodes. The mode of failure could be oxidation due to dissolved oxygen, poor cyclic plating, or passivation. The rate of degradation of the amine sorbent must also be considered. Cupric ions have been shown to increase the rate of oxidative degradation in amines; the concentration of cupric ions in the EMAR system, however, is far greater than has been tested previously. The extent of the catalysis at these higher concentrations requires investigation. The effects of flue gas impurities, primarily sulfur dioxide (SO_2), are also a significant concern. If the EMAR system can successfully regenerate amines complexed with SO_2, it will represent a tremendous advantage of the EMAR strategy over traditional thermal scrubbing.

More advanced tools for optimization and sensitivity analysis of EMAR systems must be developed. To accomplish this, all of the calculations described in the TEA need to combine in a comprehensive computer code. This will greatly improve the ability to perform techno-economic analyses that consider the optimum design of these systems. The ability to quickly optimize a design will also be necessary to effectively model the capital cost of a system. Since the capital expense will be extremely sensitive to the size of the system, it is impossible to effectively assess the capital costs without integration with a detailed capture plant performance model.

Further research is warranted on the performance of aminoethylethanolamine, which shows promising kinetics and reasonable thermodynamics. The kinetic effects of different additives, including halides and small organics, should be explored. Investigation of chloride salts demonstrated a combination of impressive catalysis of the electrochemical reactions with undesirable tendencies towards reduced Faradaic efficiencies and copper powder formation.

Confirmation of the transport results from Chapter 5 is also necessary. While the thermodynamic and kinetic models were confirmed with experimental results, the developed transport models were not experimentally validated. Construction of small analytical test cells followed by experiments with varying currents, potentials, and flow rates is the most straightforward approach. To minimize the complexity of these systems, the CO_2 generation rate, which is more challenging to measure than the current or potential, should not be measured. The diffusive flux of different species through the membrane materials should also be investigated.

The development of this technology for other applications beyond post-combustion CO_2 capture should also be explored. In the Appendix, several examples of pH-modulation using EMAR-like systems are described. Separations of other gases or CO_2 from non-combustion sources could be a useful application. Separations of CO_2 and hydrogen sulfide from natural gas are becoming more important with the recent boon in natural gas production. Liquid-phase separations may also be possible but will likely be more complicated. Electrochemical separations of various organic pollutants have been shown previously, but have never been industrially relevant. The competitive complexation strategy that was introduced in this thesis and proven effective in EMAR, may allow for the development of more successful electrochemical separation processes in the future.

Appendix

A) Experimental Techniques

Chemicals

Stock solutions were prepared with distilled and deionized 18 MΩ water using a Milli-Q system. Almost all chemicals used were purchased from Sigma-Aldrich with a few purchased from VWR and a few from Alfa-Aesar. Background electrolytes used were sodium nitrate ($NaNO_3$, purity >99%), potassium nitrate (KNO_3, purity > 99%) and sodium chloride (NaCl, purity > 99%). Cupric ions were added to solutions through the addition of copper nitrate semi(pentahydrate) ($Cu(NO_3)_2$, purity>98%), copper sulphate ($CuSO_4$, purity>99%), or copper chloride ($CuCl_2$, purity>97%) . All amines used were of at least 99% purity. For TETA, which was purchased as a solid hydrate, the supplier-provided Karl-Fischer titration data were used to determine the true molecular weight of the hydrated complex. Sulfuric acid solutions were prepared from a 2.5 M solution purchased from Sigma-Aldrich. Ag/AgCl reference electrodes were purchased through BASi (West Lafayette, IN). Copper 101 alloy (purity > 99.99%) was used for the copper plate electrodes and the copper wire.

Solution Preparation

Stock solutions were prepared using volumetric flasks ranging from 10 mL to 500 mL. First, the desired weights of amines, copper salts, and electrolytes would be added to the volumetric flask. Then water would be added until the solution reaches the target volume. Typical stock solutions included:

- 4N amine solutions (i.e., 2M EDA, 2M AEEA, 1M TETA, 1.33M DETA)
- Copper salts: 2M $Cu(NO_3)_2$, 1M $CuSO_4$, 4M $CuCl_2$
- Electrolytes: 5M $NaNO_3$, 4M NaCl, 3M KNO_3

Experiments were often run at 2 N amine, hence the choice for a 4 N stock solution. The concentrations of the copper salts were generally as high as possible without forming precipitate. It was difficult to store

copper chloride stock solutions; a frothy layer would form after a few days. In general, solutions not saturated with CO_2 were assumed to be stable indefinitely. No results ever indicated otherwise.

Solutions for specific experiments were prepared under the assumption that there would be no change in excess volume due to mixing. Since experimental solutions were never prepared directly from pure amines or concentrated acids, this assumption should be reasonable.

B) pH-Modulating Flow Systems

If one considers the target of the basic ligand in an EMAR-like process to be a proton rather than CO_2, the net effect of the oxidation of inert metals into acidic cations will be a sharp decrease in pH. Chemistries capable of pH control are not new. Lead-acid batteries decrease the pH when $PbSO_4$ is converted to PbO_2 through the release of two protons per electron transferred. Preliminary experiments based on the transition from copper to cupric oxide, from lead to lead dioxide, and from hydroquinone to quinone all demonstrate the ability to electrochemically modulate the pH with the need to electrolyze water. Schematics of how systems like this could be designed can be seen in **Figure 9-1**.

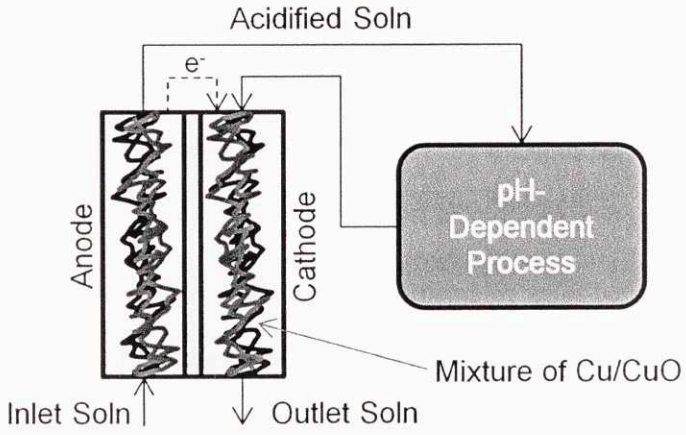

Figure 9-1. Schematic diagram of a possible pH-dependent process operated via electrochemical pH-modulation.

In this process, an incoming solution can be acidified by passing through an anode chamber where copper metal, Cu, is being constantly oxidized to copper oxide, CuO. This process requires the breakdown of water to yield the oxygen, leaving one proton in the solution per electron passed. The acidified solution

can then be sent to a new vessel to undergo some acid-catalyzed process. Once that process is complete, the solution can be sent to the cathode of the electrochemical cell, where the copper oxide is being continuously reduced to copper metal and thereby absorbing protons from the solution. If the system is operated correctly, the outlet solution should leave at approximately the same pH as the inlet entered. This avoids the need to add either salt or electrolyze water to achieve pH swings.

Avoiding the electrolysis of water has many practical advantages. Electrolysis requires large overpotentials or expensive catalysts, which are cost prohibitive. There are also applications where acidic environments in the absence of water are desired. The production of biodiesels through transesterfications is one such example of a process, which organic solvents rather water. The transesterfication process is acid catalyzed, but homogenous catalysis is difficult due to the need to neutralize the acid after the reaction is complete. Electrochemical modulation of the pH could allow for the acidification of the solution followed by neutralization without adding any chemicals. One example of how this could be achieved would be the reversible oxidation and then reduction of hydroquinone to release protons then reabsorb them.

Actuation of mechanical switches through the control of pH-dependent polymers is another possible application of electrochemically-modulated pH environments. Technologies based on water splitting have previously been considered for hydroponic applications where the constant addition of acids and bases to the plant environment leads to the detrimental buildup of salt concentrations. Microbiological bioreactors could be another system where pH control without salt accumulation is desirable.

Several experiments, based on lead, quinone, and copper chemistry, were performed as part of a patent application filed in August, 2012 (still pending as of September, 2013). The experiments used the 2nd generation electrochemical cell seen in **Figure 9-2**.

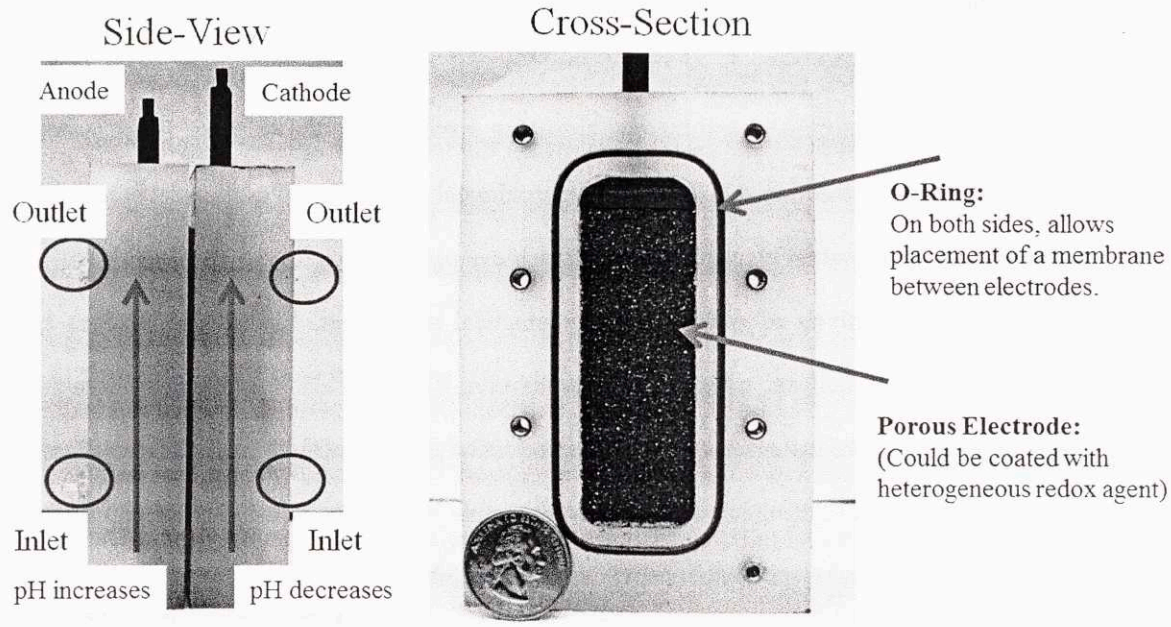

Figure 9-2. 2nd generation electrochemical flow cell uses for pH-modulation experiments.

Copper Example:

Anode: $Cu + H_2O \rightleftharpoons CuO + 2e^-$

Cathode: $CuO + 2H^+ + 2e^- \rightleftharpoons Cu + H_2O$

For this experiment, a two-compartment flow cell with each compartment having approximately 20 mL of volume was used. One compartment contained a copper (Cu) electrode while the other contained a partially oxidized copper electrode. Partial oxidation was achieved via soaking the copper in a concentrated potassium hydroxide solution for several days. A black layer of copper oxide (CuO) was observed on the surface of the oxidized electrode. The two chambers were separated by a Nafion 117 membrane previously soaked in a potassium nitrate solution with a 20 cm^2 working area. The chamber was flushed with copious amount of deionized water then 0.1 molar potassium nitrate.

A 0.1 molar potassium nitrate solution was injected into both sides of the flow cell simultaneously at 1 mL/min in each side for 50 minutes. A 10 mA current (0.5 mA/cm^2 current density) was applied via a potentiostat to the system. Voltages increased from approximately 0.7 to 0.8 volts during the course of the experiment. The pH of each outlet stream was fractionated into 5 mL samples

and the pH of each fraction was measured and recorded. A plot of pH versus time based on the 5 mL fractionation of the two outputs can be seen in **Figure 9-3**.

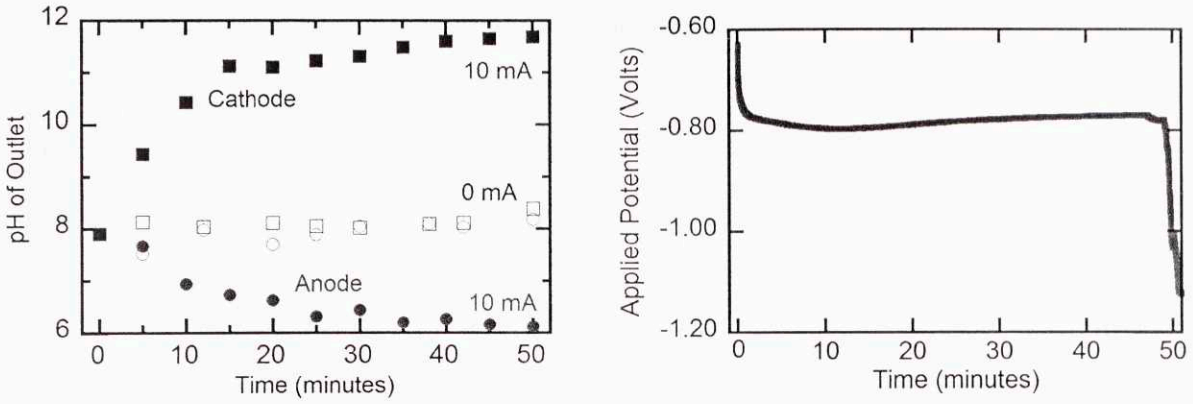

Figure 9-3. (Left) pH of fractionated outlet samples from the copper system with no current (open symbols) and 10 mA of current (closed symbols). **(Right)** Applied potential during the 10 mA experiment.

Lead Example:

Anode: $Pb + 2H_2O \rightleftharpoons PbO_2 + 4H^+ + 4e^-$

Cathode: $PbO_2 + 4H^+ + 4e^- \rightleftharpoons Pb + 2H_2O$ & $PbO_2 + 4H^+ + SO_4^{2-} + 2e^- \rightleftharpoons PbSO_4 + 2H_2O$

For this experiment, a two-compartment flow cell with each compartment having approximately 20 mL of volume, each containing lead (Pb) electrodes, which had been partially oxidized. Oxidation was achieved via a potentiostat that applied a 2.5 volt potential difference between the lead electrode and piece of platinum foil for several hours. A dark brown layer of lead dioxide (PbO_2) was observed on the outside of the electrodes. The two chambers were separated by a Nafion 117 membrane previously soaked in a concentrated sodium chloride solution with a 20 cm^2 working area. The chamber was flushed with copious amount of deionized water then 0.3 molar sodium sulfate to remove any remaining chloride ions. A 0.3 molar sodium sulfate solution was injected into both sides of the flow cell simultaneously at 1 mL/min in each side for 50 minutes. A 10 mA current (0.5 mA/cm^2 current density) was applied via a potentiostat to the system. Voltages increased from approximately 2 volts to 3 volts during the course of the experiment. After the experiment, the anode showed significant quantities of lead dioxide and the cathode showed the presence of lead sulfate ($PbSO_4$), which indicates that the lead transformation, and

not water hydrolysis, was the dominant electrochemical process during the experiment. The pH of each outlet stream was fractionated into 5 mL samples and the pH of each fraction was measured and recorded. A plot of pH versus time based on the 5 mL fractionation of the two outputs can be seen in **Figure 9-4**.

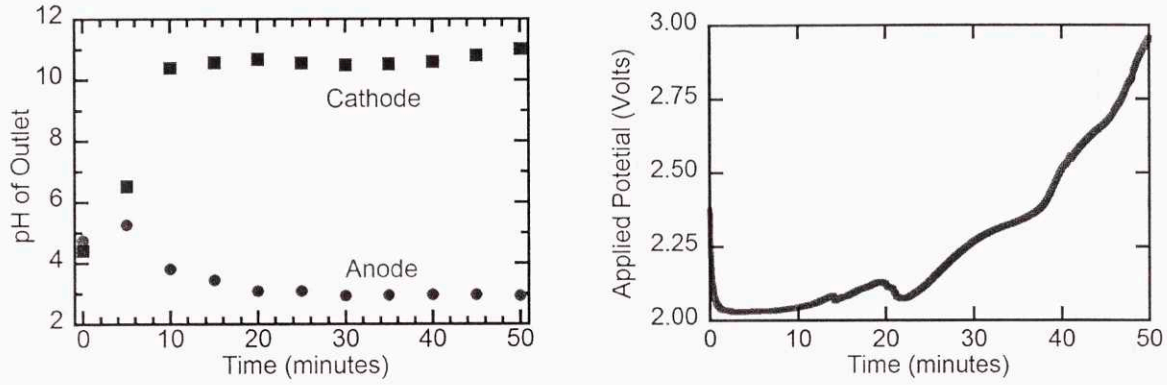

Figure 9-4. (Left) pH of fractionated outlet samples from the lead system with 10 mA of current. **(Right)** Applied potential during the 10 mA experiment.

Quinone Example:

Anode: $BQH_2 \rightleftharpoons BQ + 2H^+ + 2e^-$

Cathode: $BQ + 2H^+ + 2e^- \rightleftharpoons BQH_2$

For this experiment, a two-compartment flow cell with each compartment having approximately 20 mL of volume, each containing vitreous carbon foam electrodes, and being separated by a Nafion 117 membrane previously soaked in a concentrated sodium chloride solution was used. The chamber was flushed with copious amount of deionized water then 1 molar sodium chloride before being filled with the working solution. The working solution was contained 1 molar sodium chloride, 0.01 molar benzoquinone (BQ), and 0.01 molar hydroquinone (BQH_2).

The working solution was injected into both sides of the flow cell simultaneously at 1 mL/min in each side for 40 minutes. A 10 mA current (0.5 mA/cm^2 current density) was applied via a potentiostat to the system. Voltages increased from approximately 0.3 to 0.5 volts during the course of the experiment. The pH of each outlet stream was fractionated into 5 mL samples and the pH of each fraction was measured and recorded. A plot of pH versus time based on the 5 mL fractionation of the two outputs can

be seen in **Figure 9-5**. The pH did not increase significantly in the cathode because of the rapid base-catalyzed degradation of the quinone species at high pH values. Evidence of such degradation could be seen by a distinct darkening of the cathode outlet and noticeable precipitate.

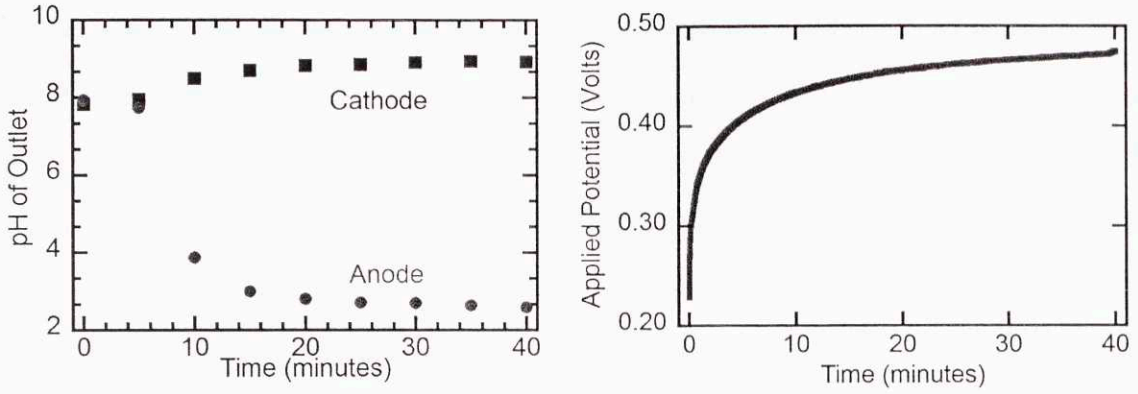

Figure 9-5. (Left) pH of fractionated outlet samples from the quinone system with 10 mA of current. **(Right)** Applied potential during the 10 mA experiment.

C) Aqueous Quinone CO_2 Capture

Our initial study into electrochemical CO_2 capture involved the use of redox-active quinones. The use of quinodal carriers for CO_2 capture, however, had the significant drawback of requiring organic solvent environments. Organic solvents, even ones with low vapor pressure, would be difficult to employ for large scale CO_2 capture due to loss of the solvent through evaporation and entrainment in the flue gas. Attempting to use quinones for CO_2 capture in aqueous systems had never been previously tried, but would be a solution to the organic solvent problem. The three quinones investigated for aqueous capture can be seen in **Figure 9-6**.

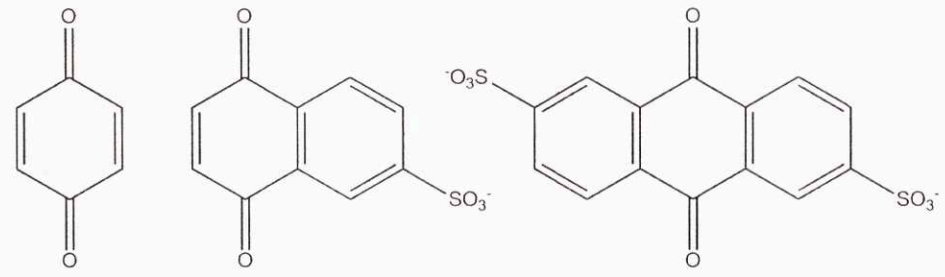

Figure 9-6. Quinones investigated for use in aqueous electrochemical CO_2 capture systems.

To start, we considered the using benzoquinone in an aqueous system. The electrochemistry of benzoquinone under inert gases in aqueous environments has been previously studied. Benzoquinone is sparingly soluble in water, which would be insufficient for an industrial process, but was suitable for initial investigations into the feasibility of such a process. The addition of sulfonic acid groups, however, raised the solubility of naphtha- and anthra- quinones sufficiently to allow for up to 1 M solutions. When studying the stability of the quinones in the aqueous environments buffered at pH 9, benzoquinone and naphthaquinone systems showed poor stability as seen in **Figure 9-7**. Benzoquinone degraded on the orders of hours, while naphthaquinone sulfonic acid degraded on the length scale of days. Measurements of anthraquinone disulfonic acid showed no change over several days even at higher pH's.

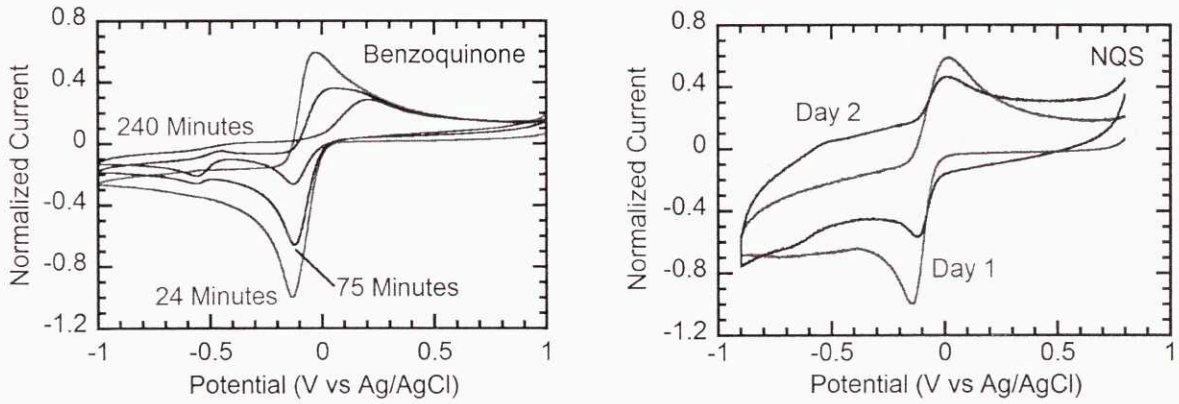

Figure 9-7. Cyclic voltammagrams of BQ (left) and NQS (right) in pH 9 buffered water over time. Solutions contained 0.1 M NaCl. The sweep rate is 0.1 volts/second.

It was determined that in aqueous systems, even ones saturated with CO_2, the predominant form of the reduced quinone species was hydroquinone (protonated) form rather than a CO_2-containing adduct. Therefore, the CO_2 capture would occur through the formation of bicarbonate ions from the reaction of the dissolved CO_2 and hydroxyl groups generated from water during the electrochemical formation of the hydroquinone from the oxidized quinone. This, however, was impossible to observe in an aqueous benzoquinone system because the quinones degrade quickly in even a slightly basic environment. In the stable AQDS system, cyclic voltammagrams in unbuffered solutions show a slight difference between

argon and CO_2 environments as seen in **Figure 9-8**. This difference indicates that reduction of AQDS somehow interacts with the dissolved CO_2.

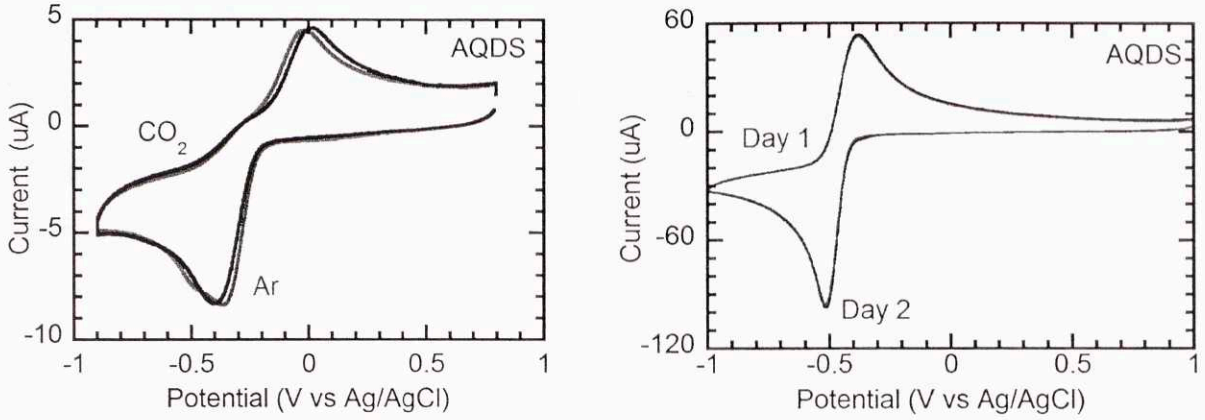

Figure 9-8. (Left) CV of AQDS in unbuffered solution under argon and CO_2 atmospheres. **(Right)** CV of AQDS at pH 9 over time showing negligible degradation over 1 day.

Unfortunately, the reduced form of the AQDS, however, did not appear to be stable in the presence of oxygen. It was this difficulty, which eventually led to the exploration of other chemistries and the abandonment of the aqueous quinone systems.

D) Quantum chemical modeling of Quinones in non-aqueous system

Introduction:

The use of quantum chemical simulations to predict both redox transitions and complexation energies has been well established. Hartree-Fock (HF), density functional theory (DFT), and higher order methodologies have been used effectively for these reaction energies. DFT, however, has become a favored method when dealing with many atom organic molecules because of its impressive scaling characteristics when compared to Moller-Plosset (MP) or cluster-continuum approaches.

For quinones, specifically, several groups have attempted to predict their redox potentials in aqueous, and non-aqueous solvents. Additionally, prediction of their affinity to bind protons (and hence their pKa) have also been investigated computationally. While gas phase calculations of their ionization

energies (IE) and electron affinities (EA) can be performed effectively, significant doubt has been placed on the ability to correctly address their solvation energies correctly.

Polarized continuum models (PCM) have been used to predict their solvation energies, but make many assumptions about the solvation cavity that limit their applicability to systems with strong electronegative or electropositive areas. Inclusion of explicit solvent molecules has been used to improve the incorporation of specific solvent interactions. Hybrid quantum mechanical and molecular mechanics may offer the best chance for an accurate and computationally tractable representation of the solvents.

Methods:

All simulations were performed using Gaussian 03 on a 56 core Linux cluster. Reaction energies and redox transition energies were calculated by separately evaluating the gas phase and solvent contribution as has been done previously. All geometries were optimized and frequency calculations were done using mpw1pw91 6-31+G(d,p) formalism. Gas phase energies were calculated using mpw1pw91 6-311++G(3df,3pd). Solvation energies were calculated using CPCM reaction field with HF/6-31+G(d,p) basis sets using the UAHF solvent radii. The DFT approach towards calculating the gas phase energies was used instead of MP methods because of their ability to effectively model the radical species. Using the MP2 method, the spin-contamination, $\langle S^2 \rangle$, greatly exceeded the desired value of 0.75, which highlights the method's ineffectiveness.

Simulations were performed to ascertain the redox potentials for transition (with respect to the absolute standard hydrogen electrode thought to be approximately 4.36 volts) and the reaction free energies of the quinone species with CO_2. Because the interactions between the quinone in the radical state and CO_2 are non-covalent, the mpw1pw91 DFT methodology was chosen in lieu of the more common B3LYP do to its asymptotically correct predictions of longer range dispersion interactions. All reported energies assume a standard state concentration of 1 mole/dm^3 and a temperature of 298.15 Kelvin. Gas phase basis set superposition errors were corrected using the counterpoise method. These

errors were small, however, due to the large basis sets used. Electrostatic potential maps of benzoquinone in its neutral, dianion, and di-CO_2 complexed dianion adduct can be seen in **Figure 9-9**.

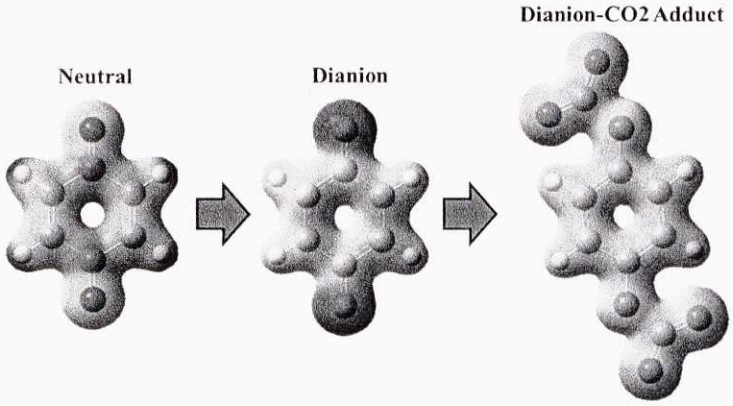

Figure 9-9. Electrostatic potentials mapped onto electon isodensity surfaces for benzoquinone. Red denotes high electronegativity whereas blue denotes an electropositive surface.

Results:

Prediction of the redox states of the quinones has been done previously, and no new strategies were employed for these calculations other than the use of a different DFT functional form. Previous computational studies have focused more on the first redox transition, whereas only a few papers have shown predictions of the second transition. **Table 9-1** includes results for the solvation free energies, gas phase energies, and predicted redox potentials for several quinones. A parity plot of predicted values as a function of experimental values can be seen in **Figure 9-10**. Excellent agreement is shown between the predicted and experimental values with a mean average deviation below 0.1 volts.

Table 9-1: First and second redox potentials versus the SHE of various quinones. Also included is the disproportionation equilibrium constant

Quinone	E_1	E_2	$E_2 - E_1$	K_d
BQ	-0.20	-1.16	-0.96	6.6E-17
NQ	-0.46	-1.22	-0.77	1.3E-13
oNQ	-0.29	-0.98	-0.69	2.2E-12
PQ	-0.36	-1.11	-0.75	2.4E-13
AQ	-0.78	-1.43	-0.65	1.3E-11
BQCl4	0.36	-1.01	-1.37	8.9E-24
dtBBQ	-0.56	-1.72	-1.17	2.5E-20

When predicting CO_2 complexation energies, both gas phase binding energies and changes in the solvation energy were calculated separately and then combined to predict the overall free energy change. Instead of using a simulated value for CO_2 solvation, the Henry's Law solubility was used to calculate a free energy of solvation for CO_2 of 1.15 kcal/mole. Additionally, a correction also needs to be added to account for the entropic penalty associated with the binding of CO_2. Most of this entropic penalty can be understood as the replacement of a translational degree of freedom with a vibrational degree of freedom. Gas phase frequency calculations of the complexation of benzoquinone with a single CO_2 molecule indicate a free energy penalty of approximately 9 kcal/mole at room temperature. Frequency calculations of all the quinones were performed but showed only slight variation. **Table 9-2** shows the calculated solvation and binding free energies along with the predicted equilibrium coefficients of the reactions of several quinones with one and two molecules of CO_2.

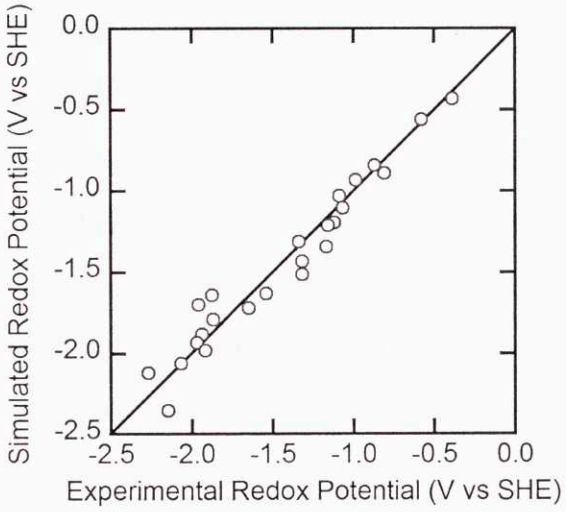

Figure 9-10. Parity plot of simulated redox potentials of various quinones versus experimental under inert atmospheres in DMF.

To minimize the errors inherent to the simulation procedure, we can look at the results in a relative sense rather than as absolute values. We can do this by fixing the free energy for a known reaction of quinones with CO_2, and then consider all of the reactions as exchanging the CO_2 as shown in Eq. 1.

$$[PQ \cdot CO_2]^{2-} + Q^{2-} \rightleftharpoons [Q \cdot CO_2]^{2-} + PQ^{2-} \quad (9\text{-}1)$$

Here PQ represents phenanthraquinone, whose complexation reactions with CO_2 have been reported in literature, and Q represents any other quinone. When comparing the experimentally determined value for phenathraquinone (oAQ) to the predicted value from the quantum simulations, we find a disagreement of -8.7 kcal/mole. By adding this difference to all of the simulated values, we arrive at an adjusted free energy value that reduces the systematic error of the simulation procedure.

Table 9-2: Binding free energies and their associated equilibrium constants

	First CO_2 Binding				Second CO_2 Binding			
Quinone	**ΔG_{gas}**	**ΔG_{solv}**	**K_1**	**K_1^{adj}**	**ΔG_{gas}**	**ΔG_{solv}**	**K_2**	**K_1^{adj}**
BQ	-33.79	20.55	1.0E+10	2.5E+16	-18.93	15.36	8.3E+02	2.1E+09
NQ	-26.50	17.50	7.9E+06	2.0E+13	-12.62	10.97	3.2E+01	8.0E+07
oNQ	-23.73	17.21	1.2E+05	3.0E+11	-7.12	8.46	2.1E-01	5.2E+05
oAQ	-17.73	10.73	2.7E+05	6.7E+11	-4.74	8.55	3.2E-03	8.0E+03
AQ	-19.50	10.31	1.1E+07	2.7E+13	-5.04	8.44	6.4E-03	1.6E+04
BQCl4	-14.56	9.60	8.7E+03	2.2E+10	-0.97	7.49	3.3E-05	8.3E+01
dtBBQ	-27.69	14.04	2.0E+10	5.0E+16	N/A	N/A	N/A	N/A

By combining the results of **Tables 9-1** and **9-2**, the effect of adding CO_2 to the solution on the redox potentials can be determined. Assuming a saturated solution at 1 bar of CO_2 pressure, the equilibrium potentials of the solutions can be calculated. Benzoquinone shows significantly higher binding affinity for CO_2 than the larger aromatic naphtha- and anthra- quinones. Additionally, para-quinones appear to have significantly higher equilibrium coefficients than ortho-quinones. Electron withdrawing side groups, such as chlorine atoms, reduce CO_2 affinity by pulling electronegativity away from the oxygen anions. Alkyl side groups, such as methyl or tert-butyl groups, increase CO_2 affinity by donating electronegativity to the oxygen anions. Binding of the second CO_2 is significantly weaker since the first CO_2 molecule stabilizes the dianion by drastically increasing the resonance possibilities for the pi electrons. Values for the second binding of CO_2 for (2,6)-di-tertbutyl-benzoquinone (dtBBQ) is not shown since the structure is significantly hindered. These results agree with experimentally reported trends, but it is impossible to make more quantitative claims due to the difficulty of measuring these equilibrium values.

The reactivity of several other flue gas components with the dianion quinones were also investigated and the results are shown in **Table 9-3**. Reactions were classified based on the behavior of the molecules. Strong acid gases such as CO_2, SO_2, and SO_3 formed covalent bonds. Highly oxidized species including oxygen and NO_2 oxidized the dianion species to form superoxides and nitrite, respectively. Neither CO nor NO appeared to have any significant interaction. From these results, it is believed that CO_2, SO_2, SO_3, and H_2S could be scrubbed effectively by quinodal dianions.

Table 9-3: Rough approximations of equilibrium binding constants of various gases with dianion quinones.

Gas	Reaction Mechanism	Strength (K_{rxn})	Comment
CO_2	$Q^{2-} + CO_2 \Leftrightarrow (Q\text{-}CO_2)^{2-}$	10^{20}	Covalent
SO_2	$Q^{2-} + CO_2 \Leftrightarrow (Q\text{-}CO_2)^{2-}$	10^{30}	Covalent
SO_2	$Q^{2-} + SO_2 \Leftrightarrow Q^{-} + SO_2^{-}$	10^{10}	Oxidation
SO_3	$Q^{2-} + SO_3 \Leftrightarrow (Q\text{-}SO_3)^{2-}$	10^{50}	Covalent
H_2O	$Q^{2-} + H_2O \Leftrightarrow (Q\text{-}H_2O)^{2-}$	10^{5}	Hydrogen
H_2S	$Q^{2-} + H_2S \Leftrightarrow QH^{-} + HS^{-}$	10^{10}	Protonation
O_2	$Q^{2-} + O_2 \Leftrightarrow Q^{-} + O_2^{-}$	10^{5}	Oxidation
NO_2	$Q^{2-} + NO_2 \Leftrightarrow Q^{-} + NO_2^{-}$	10^{20}	Oxidation
CO	$Q^{2-} + CO \Leftrightarrow (Q\text{-}CO)^{2-}$	Negligible	Dipole
NO	$Q^{2-} + NO \Leftrightarrow (Q\text{-}NO)^{2-}$	Negligible	Dipole

References

1. NOAA National Climatic Data Center, *State of the Climate: Global Analysis for Annual 2012*, 2012.
2. S. A. Marcott, J. D. Shakun, P. U. Clark, and A. C. Mix, *Science (80-.).*, 2013, **339**, 1198–1201.
3. R. Rohde, R. A. Muller, R. Jacobsen, E. Muller, S. Perlmutter, A. Rosenfeld, J. Wurtele, D. Groom, and C. Wickham, *Geoinfor Geostat*, 2013, **1**, 1–7.
4. NCADAC, *Federal Advisory Committee Draft Climate Assessment Report Released for Public Review*, 2013.
5. M. L. Parry, O. F. Canziani, J. P. Palutikof, P. J. Van Der Linden, and C. E. Hanson, Eds., *Climate Change 2007: Impacts, Adaptation and Vulnerability, Contribution of Working Group II to the Fourth Assessment Report of the IPCC*, Cambridge University Press, Cambridge, 2007.
6. National Research Council, *America's Climate Choices*, 2011.
7. EPA, *Draft Inventory of U.S. Greenhouse Gas Emissions and Sinks: 1990-2011*, 2013.
8. MIT, *Retrofitting of Coal-Fired Power Plants for CO2 Emissions Reductions. An MIT Energy Initiative Symposium*, 2009.
9. US Energy Information Administration, *Annual Energy Outlook 2011: With Projections to 2035*, 2011.
10. S. Chu, *Science (80-.).*, 2009, **325**, 1599.
11. B. Metz, O. R. Davidson, P. R. Bosch, R. Dave, and R. Meyer, Eds., *Climate Change 2007: Mitigation of Climate Change, Contribution of Working Group III to the Fourth Assessment Report of the IPCC*, Cambridge University Press, Cambridge, 2007.
12. P. DiPietro, P. Balash, and M. Wallace, *A Note on Sources of CO2 Supply for Enhanced Oil Recovery Operations*, 2012.
13. US Energy Information Administration, *Form EIA-860 Annual Electric Generator Report*, 2013.
14. International Energy Agency, *Key World Energy Statistics*, 2012.
15. M. Finkenrath, J. Smith, and D. Volk, *CCS Retrofit: Analysis of the Globally Installed Coal-Fired Power Plant Fleet*, 2012.
16. International Energy Agency, *Energy Technology Perspectives 2010: Scenarios and Strategies to 2050*, 2010.
17. L. Hanle, K. Jayaraman, and J. Smith, *CO2 emissions profile of the US cement industry*, 2004.
18. D. Gielen, *Energy Convers. Manag.*, 2003, **44**, 1027–1037.
19. J. Harnisch, I. S. Wing, H. Jacoby, and R. Prinn, *Policy Anal.*, 1998.
20. G. T. Rochelle, *Science (80-.).*, 2009, **325**, 1652–4.
21. J. T. Cullinane and G. T. Rochelle, *Chem. Eng. Sci.*, 2004, **59**, 3619–3630.
22. R. J. Hook, *Ind. Eng. Chem. Res.*, 1997, **36**, 1779–1790.
23. R. Idem, M. Wilson, P. Tontiwachwuthikul, A. Chakma, A. Veawab, A. Aroonwilas, and D. Gelowitz, *Ind. Eng. Chem. Res.*, 2006, **45**, 2414–2420.
24. V. Darde, K. Thomsen, W. J. M. van Well, and E. H. Stenby, *Energy Procedia*, 2009, **1**, 1035–1042.
25. A. Portugal, J. Sousa, F. Magalhaes, and A. Mendes, *Chem. Eng.*, 2009, **64**.
26. S. Freguia and G. Rochelle, *AIChE J.*, 2003, **49**, 1676–1686.
27. D. Singh, E. Croiset, P. L. Douglas, and M. A. Douglas, *Energy Convers. Manag.*, 2003, **44**, 3073–3091.
28. J. Katzer, E. Moniz, J. Deutch, S. Ansolabehere, J. Beer, and others, *The future of coal: an interdisciplinary MIT study*, 2007.
29. A. Kothandaraman, L. Nord, O. Bolland, H. J. Herzog, and G. J. McRae, *Energy Procedia*, 2009, **1**, 1373–1380.
30. K. Z. House, C. F. Harvey, M. J. Aziz, and D. P. Schrag, *Energy Environ. Sci.*, 2009, **2**, 193.
31. M. Zhao, A. Minett, and A. Harris, *Energy Environ. Sci.*, 2013, **6**, 25–40.
32. B. J. P. Buhre, L. K. Elliott, C. D. Sheng, R. P. Gupta, and T. F. Wall, *Prog. Energy Combust. Sci.*, 2005, **31**, 283–307.

33. M. Okawa, N. Kimura, T. Kiga, S. Takano, K. Arai, and M. Kato, *Energy Convers. Manag.*, 1997, **38**, S123–S127.
34. C. E. Powell and G. G. Qiao, *J. Memb. Sci.*, 2006, **279**, 1–49.
35. M. Ho, G. Allinson, and D. Wiley, *Ind. Eng. Chem. Res*, 2008, **46**, 1562–1568.
36. M. Ho, G. Allinson, and D. Wiley, *Ind. Eng. Chem. Res*, 2008, **47**, 4883–4890.
37. H. Herzog, J. Meldon, and T. A. Hatton, *Clean Air Task Force*, 2009.
38. D. M. D'Alessandro, B. Smit, and J. R. Long, *Angew. Chem. Int. Ed. Engl.*, 2010, **49**, 6058–82.
39. X. Hu, J. Tang, A. Blasig, Y. Shen, and M. Radosz, *J. Memb. Sci.*, 2006, **281**, 130–138.
40. J. E. Bara, D. E. Camper, D. L. Gin, and R. D. Noble, *Acc. Chem. Res.*, 2010, **43**, 152–9.
41. P. N. Seevam, J. M. Race, M. J. Downie, and P. Hopkins, *Proc. IPC2008*, 2008, 1–13.
42. J. Rhodes and D. Keith, *Biomass and Bioenergy*, 2005, **29**, 440–450.
43. S. Kaldis, *Fuel Process. Technol.*, 2004, **85**, 337–346.
44. E. J. Granite and T. O'Brien, *Fuel Process. Technol.*, 2005, **86**, 1423–1434.
45. J. C. Abanades, E. S. Rubin, and E. J. Anthony, *Ind. Eng. Chem. Res.*, 2004, **43**, 3462–3466.
46. S. M. N. Hassan, University of Waterloo, 2005.
47. H.-H. Cheng, J.-F. Shen, and C.-S. Tan, *Int. J. Greenh. Gas Control*, 2010, **4**, 525–531.
48. S. Xu, Y. W. Wang, F. D. Otto, and A. E. Mather, *Chem. Eng. Sci.*, 1996, **51**, 841–850.
49. B. Arstad, R. Blom, and O. Swang, *J. Phys. Chem. A*, 2007, **111**, 1222–8.
50. N. Ramachandran, A. Aboudheir, R. Idem, and P. Tontiwachwuthikul, *Ind. Eng. Chem. Res*, 2006, **45**, 2608–2616.
51. K. Shen and M. Li, *J. Chem. Eng. Data*, 1992, 96–100.
52. M. Gupta, E. F. da Silva, A. Hartono, and H. F. Svendsen, *J. Phys. Chem. B*, 2013, **117**, 9457–68.
53. A. Hartono and H. F. Svendsen, *Energy Procedia*, 2009, **1**, 853–859.
54. S. Zhou, X. Chen, T. Nguyen, A. K. Voice, and G. T. Rochelle, *ChemSusChem*, 2010, **3**, 913–918.
55. O. Trass and R. Weiland, *Can. J. Chem. Eng.*, 2009, **4**, 773–781.
56. R. Weiland and O. Trass, *Can. J. Chem. Eng.*, 1971, **4**, 767–772.
57. J. Li, A. Henni, and P. Tontiwachwuthikul, *Ind. Eng. Chem. Res*, 2007, 4426–4434.
58. H. Hikita, S. Asai, H. Ishikawa, and M. Honda, *Chem. Eng. J.*, 1977, **14**, 27–30.
59. M. Saleh, M. Ahmed, and M. Islam, *Phys. Chem. Liq.*, 2002, 477–490.
60. H. Lepaumier, D. Picq, and P.-L. Carrette, *Ind. Eng. Chem. Res.*, 2009, **48**, 9068–9075.
61. I. Kim and H. F. Svendsen, *Ind. Eng. Chem. Res.*, 2007, **46**, 5803–5809.
62. S. Ma'mun, H. F. Svendsen, K. a. Hoff, and O. Juliussen, *Energy Convers. Manag.*, 2007, **48**, 251–258.
63. S. Ma'mun, J. P. Jakobsen, H. F. Svendsen, and O. Juliussen, *Ind. Eng. Chem. Res.*, 2006, **45**, 2505–2512.
64. F. Khalili, R. AV, A. Henni, A. East, and P. Tontiwachwuthikul, in *In Recent Advances in Post-Combustion CO2 Capture Chemistry: ACS Symposium Series*, ed. M. Attalla, American Chemical Society, Washington, DC, 2012, pp. 43–70.
65. A. Hartono, K. A. Hoff, T. Mejdell, and H. F. Svendsen, *Energy Procedia*, 2011, **4**, 179–186.
66. A. Hartono, E. F. da Silva, and H. F. Svendsen, *Chem. Eng. Sci.*, 2009, **64**, 3205–3213.
67. J.-M. G. Amann and C. Bouallou, *Energy Procedia*, 2009, **1**, 909–916.
68. J.-M. G. Amann and C. Bouallou, *Ind. Eng. Chem. Res.*, 2009, **48**, 3761–3770.
69. C. Brockman and J. Mote, *Trans. Electrochem. Soc.*, 1938, **61**, 371–376.
70. C. L. Aravinda, S. M. Mayanna, and V. S. Muralidharan, *Proc. Indian Acad. Sci.*, 2000, **112**, 543–550.
71. C. Shih, Y. Wang, and C. Wan, *J. Appl. Electrochem.*, 2003, **33**, 403–410.
72. R. Drissi-Daoudi, A. Irhzo, and A. Darchen, *J. Appl. Electrochem.*, 2003, 339–343.
73. A. Darchen, R. Drissi-Daoudi, and A. Irzho, *J. Appl. Electrochem.*, 1997, **27**, 448–454.
74. L. Di Palma and P. Ferrantelli, *J. Hazard. Mater.*, 2005, **122**, 85–90.
75. D. Voglar and D. Lestan, *J. Hazard. Mater.*, 2010, **180**, 152–7.
76. H. Laitinen, E. Onstott, B. JC, and S. Swann, *J. Am. Chem. Soc.*, 1949, **71**, 1550–1552.
77. J. F. Fisher and J. L. Hall, *Anal. Chem.*, 1967, **39**, 1550–1556.
78. R. S. Subrahmanya and K. Srinivasan, *J. Electroanal. Chem.*, 1971, **31**, 233–244.
79. G. H. McIntyre, B. P. Block, and W. C. Fernelius, *J. Am. Chem. Soc.*, 1959, **81**, 529–535.
80. R. Keefer, *J. Am. Chem. Soc.*, 1946, **68**, 2329–2331.
81. J. Bjerrum, *Acta Chem. Scand.*, 1987, **41**, 328–334.
82. E. Casassas, L. Gustems, and R. Tauler, *J. Chem. Soc., Dalt. Trans.*, 1989, 569–573.
83. J. Hall and W. Dean, *J. Am. Chem. Soc.*, 1958, **80**, 4183–4188.
84. I. Sovago and A. Gergely, *Inorganica Chim. Acta*, 1976, **20**, 27–32.

85. F. Cotton and F. Harris, *J. Phys. Chem.*, 1955, 1203–1208.
86. E. Mattsson and J. O. Bockris, *Trans. Faraday Soc.*, 1959, **55**, 1586–1601.
87. J. Newman and K. Thomas-Alyea, *Electrochemical Systems*, John Wiley & Sons, Hoboken, New Jersey, 3rd edn., 2004.
88. J. Healy, D. Pletcher, and M. Goodenough, *J. Electroanal. Chem.*, 1992, **338**, 155–165.
89. P. M. Vereecken, R. a. Binstead, H. Deligianni, and P. C. Andricacos, *IBM J. Res. Dev.*, 2005, **49**, 3–18.
90. A. Vicenzo and P. Cavallotti, *J. Appl. Electrochem.*, 2002, 743–753.
91. A. Ramos, M. Miranda-Hernández, and I. González, *J. Electrochem. Soc.*, 2001, **148**, C315.
92. S. Aksu and F. M. Doyle, *J. Electrochem. Soc.*, 2002, **149**, B340–B347.
93. H.-H. Strehblow and H.-D. Speckmann, *Mater. Corros. und Korrosion*, 1984, **35**, 512–519.
94. G. Faita, G. Fiori, and D. Salvadore, *Corros. Sci.*, 1975, **15**, 383–392.
95. a. a. El Warraky, *Anti-Corrosion Methods Mater.*, 2003, **50**, 40–46.
96. G. Kear, B. Barker, and F. Walsh, *Corros. Sci.*, 2004, **46**, 109–135.
97. G. Bianchi and P. Longhi, *Corros. Sci.*, 1973, **13**, 853–864.
98. J. M. Saveant, *J. Am. Chem. Soc.*, 1987, **109**, 6788–6795.
99. C. P. Andrieux, I. Gallardo, J. M. Savaent, and K. B. Su, *J. Am. Chem. Soc.*, 1986, **108**, 638–647.
100. R. A. Marcus, *J. Phys. Chem.*, 1963, **67**, 853–857.
101. R. A. Marcus, *Annu. Rev. Phys. Chem.*, 1964, **15**, 155–196.
102. J. Euler and W. Nonnenmacher, *Electrochim. Acta*, 1960, **2**.
103. J. S. Newman and C. W. Tobias, *J. Electrochem. Soc.*, 1962, **109**, 1183.
104. F. Posey, *J. Electrochem. Soc.*, 1964, **111**.
105. R. C. Alkire, E. a. Grens, and C. W. Tobias, *J. Electrochem. Soc.*, 1969, **116**, 1328.
106. a. M. Johnson and J. Newman, *J. Electrochem. Soc.*, 1971, **118**, 510.
107. D. Bennion and J. Newman, *J. Appl. Electrochem.*, 1972, **2**, 113–122.
108. J. Newman and W. Tiedemann, *AIChE J.*, 1975, **21**, 25–41.
109. M. Fleischmann, J. W. Oldfield, and L. Tennakoon, *J. Appl. Electrochem.*, 1971, **1**, 103–112.
110. R. Sioda, *Electrochim. Acta*, 1968, **13**, 375–382.
111. R. E. Sioda, *Electrochim. Acta*, 1970, **15**, 783–793.
112. E. Fenech and C. Tobias, *Electrochim. Acta*, 1960, **2**, 311–325.
113. G. Wranglen, *Acta Chem. Scand*, 1959, **13**, 830–831.
114. J. Bazan and A. Arvia, *Electrochim. Acta*, 1964, **9**, 17–30.
115. R. Alkire and P. K. Ng, *J. Electrochem. Soc.*, 1974, **121**, 95.
116. R. Alkire and A. A. Mirarefi, *J. Electrochem. Soc.*, 1973, **120**, 1507.
117. T. Nguyen, C. Walton, and R. White, *J. Electrochem. ...*, 1986, 1130–1138.
118. L. Klatt and W. Blaedel, *Anal. Chem.*, 1968, **879**.
119. F. Posey and S. Misra, *J. Electrochem. Soc.*, 1966, **113**, 608–614.
120. L. Klatt and W. Blaedel, *Anal. Chem.*, 1967, **39**, 1065–1072.
121. H. Vogt, *Electrochim. Acta*, 1980, **25**, 527–531.
122. A. A. Shah, M. J. Watt-Smith, and F. C. Walsh, *Electrochim. Acta*, 2008, **53**, 8087–8100.
123. H. Al-Fetlawi, A. A. Shah, and F. C. Walsh, *Electrochim. Acta*, 2009, **55**, 78–89.
124. A. A. Shah, H. Al-Fetlawi, and F. C. Walsh, *Electrochim. Acta*, 2010, **55**, 1125–1139.
125. D. P. Scamman, G. W. Reade, and E. P. L. Roberts, *J. Power Sources*, 2009, **189**, 1220–1230.
126. T. Fuller, M. Doyle, and J. Newman, *J. Electrochem. Soc.*, 1994, **141**.
127. T. Evans, T. Nguyen, and R. White, *J. Electrochem. Soc.*, 1989, **136**, 328–339.
128. J. Newman and W. Tiedemann, *J. Electrochem. Soc.*, 1997, **144**, 3081–3091.
129. C. Y. Wang and W. B. Gu, *J. Electrochem. Soc.*, 1998, **145**, 3407–3417.
130. W. Ward, *Nature*, 1970, **227**, 162–163.
131. T. Younos and K. E. Tulou, *J. Contemp. Water Res. Educ.*, 2009, **132**, 3–10.
132. J. Winnick and M. P. Kang, *J. Appl. Electrochem.*, 1985, **15**, 431–439.
133. N. Jemaa, R. D. Noble, H. Walls, C. A. Koval, and D. Wedman, *AIChE J.*, 1993, **39**, 867–875.
134. N. Jemaa, R. D. Noble, C. A. Koval, and J. Yu, *Chem. Eng. Sci.*, 1991, **46**, 1017–1026.
135. N. Jemaa, R. D. Noble, and C. A. Koval, *Chem. Eng. Sci.*, 1992, **47**, 1469–1479.
136. J. Winnick, R. D. Marshall, and F. H. Schubert, *Ind. Eng. Chem. Process Des. Dev.*, 1974, **13**, 59–63.
137. P. Scovazzo, D. L. Dubois, J. Poshusta, C. A. C. Koval, and R. D. Noble, *J. Electrochem. Soc.*, 2003, **150**, D91.

138. D. L. DuBois, A. Miedaner, W. Bell, and J. C. Smart, *Electrochemical and Electrocatalytic Reactions of Carbon Dioxide*, Elsevier Science Publishers, Amsterdam, 1993.
139. A. M. Appel, R. Newell, D. L. DuBois, and M. Rakowski DuBois, *Inorg. Chem.*, 2005, **44**, 3046–56.
140. M. Rakowski Dubois and D. L. Dubois, *Acc. Chem. Res.*, 2009, **42**, 1974–1982.
141. P. A. Terry, H. J. Walis, R. D. Noble, and C. A. Koval, *AIChE J.*, 1995, **41**, 2556–2564.
142. M. D. Eisaman, L. Alvarado, D. Larner, P. Wang, B. Garg, and K. a. Littau, *Energy Environ. Sci.*, 2011, **4**, 1319.
143. M. D. Eisaman, L. Alvarado, D. Larner, P. Wang, and K. a. Littau, *Energy Environ. Sci.*, 2011, **4**, 4031.
144. H. W. Pennline, E. J. Granite, D. R. Luebke, J. R. Kitchin, J. Landon, and L. M. Weiland, *Fuel*, 2010, **89**, 1307–1314.
145. P. A. Terry, R. D. Noble, D. Swanson, and C. A. Koval, *AIChE J.*, 1997, **43**, 1709–1716.
146. P. Paoletti, *Pure Appl. Chem.*, 1984, **56**, 491–522.
147. L. Öjefors and L. Carlsson, *J. Power Sources*, 1978, **2**, 287–296.
148. J. W. Tester and M. Modell, *Thermodynamics and Its Applications*, Prentice Hall, Upper Saddle River, New Jersey, 3rd Editio., 1997.
149. K. a. Smith, J. H. Meldon, and C. K. Colton, *AIChE J.*, 1973, **19**, 102–111.
150. J. H. Meldon and M. a. Morales-Cabrera, *Chem. Eng. J.*, 2011, **171**, 753–759.
151. S. a. Freeman, R. Dugas, D. Van Wagener, T. Nguyen, and G. T. Rochelle, *Energy Procedia*, 2009, **1**, 1489–1496.
152. M. C. Stern, F. Simeon, H. Herzog, and T. A. Hatton, *Energy Environ. Sci.*, 2013, **6**, 2505–2517.
153. L. W. Diamond and N. N. Akinfiev, *Fluid Phase Equilib.*, 2003, **208**, 265–290.
154. J. Carroll, J. Slupsky, and A. Mather, *J. Phys. Chem. Ref. Data*, 1991, **20**, 1201–1209.
155. H. B. Jonassen, R. B. LeBlanc, and R. M. Rogan, *J. Am. Chem. Soc.*, 1950, **72**, 4968–4971.
156. R. Pflaum and W. Brandt, *J. Am. Chem. Soc.*, 1955, **76**, 6215–6219.
157. R. S. Nicholson and I. Shain, *Anal. Chem.*, 1964, **36**, 706–723.
158. R. S. Nicholson, *Anal. Chem.*, 1965, **37**, 1351–1355.
159. R. S. Nicholson and I. Shain, *Anal. Chem.*, 1965, **37**, 178–190.
160. R. S. Nicholson, *Anal. Chem.*, 1965, **37**, 667–671.
161. D. Macdonald, *Electrochim. Acta*, 2006, **51**, 1376–1388.
162. P. Mauracher and E. Karden, *J. Power Sources*, 1997, **67**, 69–84.
163. J. C. Myland and K. B. Oldham, *Anal. Chem.*, 2000, **72**, 3972–80.
164. V. Marathe and J. Newman, *J. Electrochem. Soc.*, 1969, **116**, 1704–1707.
165. N. V. Rees, R. a. W. Dryfe, J. a. Cooper, B. a. Coles, R. G. Compton, S. G. Davies, and T. D. McCarthy, *J. Phys. Chem.*, 1995, **99**, 7096–7101.
166. Á. Molina, F. Martínez-Ortiz, and E. Laborda, *Int. J. Electrochem. Sci*, 2009, **4**, 1395–1406.
167. W. M. Deen, *Analysis of Transport Phenomena*, Oxford University Press, New York, 1998.
168. A. Emanuel and D. Olander, *J. Chem. Eng. Data*, 1963, **8**, 31–32.
169. J. Shu, B. P. a. Grandjean, and S. Kaliaguine, *Ind. Eng. Chem. Res.*, 1997, **36**, 1632–1636.
170. A. Mohanty and R. Das, *AIChE J.*, 1982, **28**, 830–833.
171. J. T. Hinatsu, *J. Electrochem. Soc.*, 1989, **136**, 125.
172. W. M. Haynes, Ed., *CRC Handbook of Chemistry and Physics*, CRC Press, New York, New York, 94th Editi., 2013.
173. M. a. Saleh, S. Akhtar, and M. Shamsuddin Ahmed, *Phys. Chem. Liq.*, 2004, **42**, 103–115.
174. C. Bozzuto, N. Nsakala, G. Liljedahl, M. Palkes, and J. Marion, *Engineering feasibility and economics of CO2 capture on an existing coal-fired power plant*, 2001, vol. 15236.
175. R. Schoff, J. White, T. Buchanan, and N. Holt, *Updated Cost and Performance Estimates For Fossil Fuel Power Plants with CO2 Removal*, 2002.

3195-57